FLOW FIELD AND THERMAL CHARACTERISTICS INDUCED BY A ROTATIONALLY OSCILLATING HEATED FLAT PLATE

By

Moise Koffi

A dissertation submitted to the Graduate Faculty in Mechanical Engineering in partial fulfillment of the requirements for the degree of Doctor of Philosophy, The City University of New York

2013

This manuscript has been read and accepted for the
Graduate Faculty in Engineering in satisfaction of the
dissertation requirement for the degree of Doctor of Philosophy.

Latif Jiji

Date — Chairman of Examining Committee

Ardie Walser

Date — Executive Office

Yiannis Andreopoulos

Masahiro Kawaji

Francisco Javier Diez, Rutgers, The State University of New Jersey

Gabriel Tardos

Peter Ganatos

Supervisory Committee

THE CITY UNIVERSITY OF NEW YORK

ABSTRACT

FLOW FIELD AND THERMAL CHARACTERISTICS INDUCED BY A ROTATIONALLY OSCILLATING HEATED PLATE

By

Moise Koffi

Advisor: Professor Latif Jiji

Co-Advisor: Professor Yiannis Andreopoulos

The objective of this dissertation is the study the flow and heat transfer in the vicinity of a rectangular flat heated plate of $0.2\text{m} \times 0.3\text{m}$ subject to rotational oscillations. Of interest is the effect of the flow field on the thermal characteristics of the plate's surface. A constant heat flux is applied to both sides while the plate is rotated about a fixed edge at a frequency of 2 rad/s in an infinite domain at atmospheric pressure. A computational simulation of the flow with FLUENT reveals a hooked-shape vortex tube around the free edges of the plate, which is confirmed by the flow visualization with smoke particles. During the flapping cycle, vortices form and grow progressively on one face while they shed from the opposite, until they are completely detached from both surfaces at stroke reversal. A data acquisition system uses a numerical computing and programming software (MATLAB) to track the surface temperature recorded by J- type thermocouples at desired locations on the plate. Both experimental and computational results agree with local surface temperature profiles characterized by a transient unsteady periodic variation followed by a steady periodic phase. These characteristics are

symmetrical about the median plane of the plate, which is normal to its axis of rotation. The cooling rate of the surface, proportional to the frequency of rotation, depends on the angular position of the plate and the spatial location on the plate's surface. However, the highest heat transfer coefficient is recorded at free edges, especially in the corners swept by strong tip vortices shedding in two orthogonal directions. Conclusions of the present study are used to explain the role of ear flapping in the metabolic heat regulation of large mammals such as elephants.

Flow visualization and surface temperature measurements of full size rigid and flexible elephant ear-shape models were carried out. Results indicate improved interaction between the shedding vortex and the model's boundary layer. Therefore the cooling is enhanced using flexible models by 30 percent. However, the huge size of the elephant pinna combined with its large surface to volume ratio and blood perfusion plays a key role in the enhancement of the animal's heat dissipation.

To my wife, Marie

To my children Christiane and David, my parents Koffi Foua, and Yebouet Amoin

And my family members

Your endless love, support and patience have paid off.

ACKNOWLEDGEMENTS

First, I am thankful to the Almighty who gave me the strength and the privilege to achieve such a step toward the completion of my doctoral studies.

I would like to express my deepest appreciation to my advisor, Professor Latif Jiji for his guidance, support and expertise. I am very grateful for his patience and advices throughout my research activity and also his tremendous participation in my education at The City College of New York.

Many thanks go to Professor Yiannis Andreopoulos for his mentorship, patience, and great assistance with his extensive experience and expertise, not only for my research but also in my education at the City College of New York.

My gratefulness goes to the Administration of the Department of Mechanical Engineering for its support during my graduate studies at the City College of New York.

I would also like to thank Dean Ardie Walser for his presence at my presentation andProfessor Francisco Javier Diez, Professor Peter Ganatos, ProfessorMasahiroKawaji and Professor Gabriel Tardos for serving as members of my supervisory committee.

I acknowledge the close collaboration with Dr. Savvas Xhantos, Dr. Pierreides Alexis, in the setting of my apparatus and their advices in many aspects of my experiment. I would like to thank all my colleagues of the Experimental Fluid Mechanics and Aerodynamics Laboratory of the Department of Mechanical Engineering for their friendship and support, in particular, Dr. Amir Elzaway, Dr Doghus Akaydin for generously sharing their time to answer my queries. I owe special thanks to Mr. Louis Hernandez and to the whole team of the machine shop, Chen, Mike, and Robert for their help in the design and the readiness of the apparatus of my project. I greatly appreciate the help of Mr. Mohamed Islam, Mr. Amir Danesh, Mr. Royneal Rayess and

Mr. Julio Ocasio for several aspects of my experiment such as: programming, design and drawing.

I convey my gratitude to Vice President Carlos Molina and Dr Claude Braithwaite for their understanding and support in the completion of my project.

I would like to thank my colleagues Diandra Jugmohan, Jose Mercado, Brieseida Cortez for their understanding and support and patience when it was most needed.

Finally, I would like in particular to express my gratitude to my wife, Marie, for her unconditional and endless support, to my parents, brothers and sisters for their continuing encouragement towards the completion of this project.

To you all, I say Thank you.

TABLE OF CONTENTS

NOMENCLATURE

A area, m^2
$\vec{a}$ force vector
b length, m
C_p specific heat at constant pressure, $J/kg-^oC$
c characteristics length, m
C_D drag coefficient
C_L lift coefficient
E_Y annual energy, J
E_i Infinitesimal, J
E Young's modulus, N/m^2
Eu Euler number
$\vec{F}_P$ pressure force vector
$\vec{F}_v$ viscous force vector
f frequency, $1/s$
f_{ij} matrix terms
G Bulk modulus, N/m^2
g gravitational acceleration, m/s^2
G_r Grashof Number
h heat transfer coefficient, W/m^2-^oC
h_a oscillation amplitude, m
I moment of inertia, $kg-m^2$
I_s structural inertial force, kg/m^2-s^2
I_f fluid inertial force, kg/m^2-s^2
k_{eff} effective thermal conductivity
k thermal conductivity, $W/m-^oC$; reduced frequency
k_{ij} spring constant N/m
L sectional aerodynamics force, N
L Length, m; lift force, N
m mass, kg
M mass, kg
n_i number of nodes i
Nu_x local Nusselt Number
N Number of flaps per minute
n_j^f unit vector for fluid
n_j^s unit vector for structure
p pressure, Pa
$\hat{p}$ dimensionless pressure
P_i pixel tally
Pr Prandtl number
P_t Total number of pixels
p length, m
q length, m
p pressure, Pa
q_r heat radiation rate, W
q_m body energy, J
q'' heat flux, W/m^2
q''' internal energy, J
q_r'' heat radiation flux , W/m^2
Re_x local Reynolds Number
Ra_L Rayleigh number
Re Reynolds number
R the characteristic, m; resistance, Ω
R area of the control surface, m^2
r distance, m
S length, m
S_{ri} slots count for down stroke motion
S_ϕ the source term of ϕ
S_h Enthalpy of the fluid, J
S cross sectional area, m^2
S_{fi} slots count for upstroke motion
S Stokes number
St Strouhal number
S slots count per revolution,
T_i average temperature of isotherm, ^oC
T_∞ ambient temperature, ^oC
T_s surface temperature, ^oC

t time, s
T Torque, m-N
T_f film temperature, ^{o}C
$\hat{t}$ dimensionless time, s
$\vec{u}_g$ grid velocity, m/s
U displacement, m
u_i velocity vectors, m/s
u local velocity, m/s
U_{ref} reference velocity, m/s
$\vec{u}$ velocity vector, m/s
U_r tip velocity, 1m/s
u_i x velocity, m/s
U voltage, V; reference velocity, m/s
u_r radial velocity, m/s
u_θ angular velocity, m/s
u_i^s structure velocity, m/s
$\hat{u}_i^s$ dimensionless, solid velocity, m/s
U_{tip} tip velocity, m/s
$\hat{v}_i^f$ dimensionless fluid velocity, m/s
v_i^f fluid velocity, m/s
V_{tip} tip velocity, m/s
V volume, m^3
V_∞ free Stream velocity, m/s
v induced velocity, m/s
ν kinematics viscosity, m/s^2;Poisson's ratio
$\vec{v}_{c.g.}$ velocity of the center of gravity, m/s
V volume m^3.
$\overrightarrow{x_i}$ position of nodes i, m
x_i Cartesian coordinates, m
$\overrightarrow{x_i}$ position along x, m
$\overrightarrow{x_i}$ position along y, m
$\overrightarrow{x_i}$ position along z, m
$\vec{x}_{c.g.}$ position of the center of gravity, m
x_i position vector, m
$\Delta\vec{x}_i$ displacement of node i, m
$\Delta\vec{x}_j$ displacement of node j, m

Greek Letters

α_T Total angular acceleration, rad/s^2
α angular acceleration, rad/s^2
β coefficient of thermal expansion, 1/K
β dimensionless Stokes number
γ first moment of vortices, N-m
Γ diffusion coefficient
δ_{ij} Kronecker delta
ε emissivity
θ angular displacement, rad
λ, G Lame constants
μ dynamic viscosity, kg/s-m
μ Molecular viscosity, kg/s-m
ρ density, kg/m^3
ρ^f density of fluid
ϕ flow potential; scalar
σ Stefan-Boltzmann constant
σ_{ij}^f Newtonian fluid stress tensor, N/m^2
σ_{ij}^s Structural stress tensor, N/m^2
τ_T Infinitesimal torque, m-N
τ_{ij} viscous stress tensor
$(\tau_{ij})_{eff}$ Deviatory stress tensor
Φ general dissipation function
$\vec{\Omega}_{c.g.}$ center of gravity angular velocity, rad/s
Ω the angular velocity, rad/s
ω Vorticity; angular velocity, rad/s
(ξ, η, ζ) arbitrary coordinate

LIST OF TABLES

LIST OF FIGURES

CHAPTER 1: INTRODUCTION

The applications of rotationally oscillating plates are numerous and expanding to many areas. In bioengineering, researchers are curious about the details of undersea propulsion of aquatic animals [1]. On the quest to find new techniques of locomotion and always trying to improve the efficiency of machines, engineers are inspired by the flapping flight of insects [2] and birds [3]. Rotational oscillating plates are widely used in several applications involving heat transfer enhancement [4].

This research project focuses on the flow and the heat transfer characteristics induced by a heated flat plate oscillating in an infinite medium. The investigation examines the flow field and the surface temperature distribution in the vicinity of the rotationally oscillating heated flat plate. Although interest in flow oscillation problems dates back to the mid-19th century [5, 6], a literature search indicates that this problem has not been fully investigated. The transient nature of the flow around flapping wings involves complex vortex shedding difficult to analyze [7].

A comprehensive research plan is formulated to examine the details of the velocity field, vortex shedding, and temperature distribution over the surface of a rotationally oscillating heated flat plate. The research is both theoretical and experimental. The theoretical investigation is based on a computational solution using ANSYS/FLUENT. This is a commercially available software designed to solve complex flow and heat transfer problems. FLUENT has been recently integrated in the graduate program of the Department of Mechanical Engineering and applied in the solutions of a variety of problems.

To examine the accuracy of the theoretical solutions and their range of applicability, comparisons are made with the experimental investigation. The experimental program was carried out in the Experimental Fluid Mechanics and Aerodynamics Laboratory of the

Department of Mechanical Engineering. A mechanism was designed to control the frequency and the amplitude of oscillations. To examine the effect of vortex shedding on heat transfer enhancement, a rectangular plate with an aspect ratio of 1.5 and an arbitrary model shaped like an elephant ear are tested. Smoke flow visualization is performed to investigate the mechanism of the formation and the shedding of vortices. Heat transfer studies are based on uniform surface heating of the oscillating plate. Electric heaters are cemented on both sides of the plate to provide uniform surface flux. Power input to the heaters is controlled to obtain data at various surface heat fluxes. Surface temperature distribution is mapped using a set of thermocouples attached to the surface of the model. Digital thermometers are utilized to check the temperature readings of thermocouples. A computer controlled data acquisition system is used to record data which are reduced and analyzed off-line. Heat transfer results will be used for the determination of the Nusselt number distribution over the plate, for use in the development of a correlation equation for predicting heat transfer characteristics over the surface of oscillating heated plates.

This dissertation includes four parts: (1) Computational investigation of the flow over a rotationally oscillating heated plate, from 0 degree to 90 degree angle in an infinite medium using ANSYS/FLUENT 6.3. (2) Experimental investigation of the flow and the thermal characteristics of a heated flapping plate with a mechanism designed to control the frequency and the amplitude of oscillations. (3) Discussion and parallel analysis of theoretical and experimental results to verify the validity of the solution of heat transfer characteristics for oscillating plates. (4) Application of the flapping plate study to two models similar to an elephant ear, one rigid and another flexible, with the objective to understand why elephants flap their ears.

CHAPTER 2: APPLICATIONS OF ROTATIONAL OSCILLATING FLAT PLATES

2.1. Biological and related applications

Nature provides several examples of rotationally oscillating surfaces. Birds and insects of various kinds are seen flying as illustrated in Fig. 2.1. It is fascinating to watch hummingbirds (Fig. 2.2) or butterflies (Fig. 2.3) flapping their wings while sucking flowers. Similar to dragonflies, they manage to sustain their body aloft in a quasi-steady equilibrium despite the presence of gravitational forces [8]. An observation of swimming fish in rivers or in aquariums shows their flapping tails during their forward motion as presented in Fig. 2.4. However, as we contemplate the beauty of these natural flying species, our curiosity goes beyond, trying to understand the underlying physics behind their motion. In Biology, animals or birds use rotationally oscillating motions for thrust production or lift force generation [3]. For example, the locomotion of aquatic animals such as fish is facilitated by the unsteady flapping of their tails, overcoming the drag force opposed by the fluid. During power flight, birds and insects use their wings to literally swim in the air because viscous reaction forces help them to balance gravitational forces, and also for propulsion when vortices shed from their wings [8, 9].

Fig. 2.1 Flying bird [10]

Fig. 2.2 Humming bird sucking flower [10]

Fig. 2.3 Flying butterfly [11]

Fig. 2.4 Swimming fish [10]

The shedding of vortices from rotational oscillating surfaces presents several benefits including heat transfer enhancement. The first reaction that comes in humans' mind is to instantaneously flap their fingers when they accidentally get burned as demonstrated in Fig. 2.5. Apparently, a translational motion of the hand in the surrounding medium could be a valid and easy solution to seek comfort. Assigning back and forth translational motions or shaking the hand periodically in its own plane seems to be easier to perform than flapping it. However, the idea of flapping seems to be dictated by nature. A valid explanation for such a natural behavior requires investigations. Perhaps, flapping provides faster cooling rate. In this application, it is easy to guess that rotational oscillations induce a flow of cool air around the hand, which is similar to the case where a flat plate is used as a fan to blow some fresh air, to increase the cooling rate of burned fingers.

In hot environments, humans use fans as means to provide comfort. Here, the main role of the fan is to help the body dissipate more metabolic heat, which is carried away by the induced flow of freshly generated air. However, what is the nature of the flow around fanned bodies? A possible explanation may be that flapping surfaces generate tip vortices that land tangentially on the target body resulting in enhanced cooling. It seems that the tangential motion of the air in the

vortex interacts in such a way as to decrease the thickness of the boundary layer of the body seeking comfort in Fig. 2.6.

Fig. 2.5 Flapping burnt fingers

Fig. 2.6 Fanning for comfort

The traditional technique to activate a fire and improve its combustion reaction consists of just fanning it as illustrated in Fig. 2.7. As we focus on this simple combustion application, we notice that the rotational oscillations of a fan supply more air to keep the fire active. Here the idea is to maintain and improve the reaction of combustion, replacing burned products with fresh air that contains more oxygen. During the upstroke motion of the moving fan, burned gases are pushed away and also removed tangentially by tip shedding vortices. The wake behind the moving surface attracts more oxygen present in the incoming air. The same phenomenon is repeated during the down stroke motion and after several flapping cycles, the fire remains active.

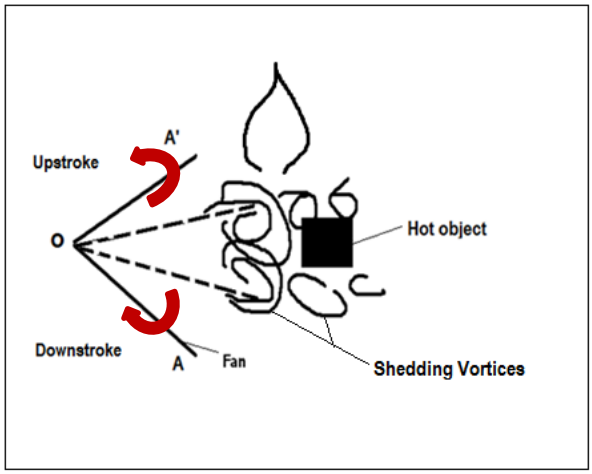

Fig. 2.7 Fanning a fire

An interesting biological example of rotationally oscillating surfaces is observed in large mammals [12] like elephants as shown in Fig. 2.8. In their daily motion in hot environments, African elephants periodically flap their pinnae, with a frequency that can reach 20 flaps per minute, searching for comfort [13, 14]. Besides the biological applications mostly borrowed from nature, flapping plates can be useful in engineering designs.

Fig. 2.8 Elephant heat loss [15]

2.2 industrial applications

2.2.1. Underwater or unmanned air Vehicles

In a society where technology is moving at a very fast pace, trying to help humans in their daily lives, flapping surfaces offer challenging applications for engineering designs [16], motivated by

the observations of biological systems. For example, the design of underwater vehicles uses the principle of thrust production [17] from the flapping tail of the swimming fish. The idea of lift force generation in the design of unmanned vehicles is borrowed from the unsteady flow of birds and insects flight [16, 18]. Flying robots or ornithopters displayed in Figs. 2.9 and 2.10 are used for space exploration, for difficult missions such as spying enemies in military applications or for the maintenance of nuclear power plants [16]. Moreover, flapping wings offer more maneuverability and energy saving capabilities compared to fixed wings. However, they need to be of the size of insects, about 15 mm [18, 19]. Unsteady flapping flight is said to save up to 27% of aerodynamics power requirement compared to steady flight according to a 2D analysis performed by Pesavemto and Wang [20]. They found that such performance improvement is made possible at stroke reversal because the flapping device interacts with the wake created behind. In fact, micro air vehicles are used as intelligence reconnaissance robots that can infiltrate and operate autonomously in narrowed spaces, unsafe or challenging for human access [16, 21]. In Reynolds number flight conditions ranging between 10^4 and10^5, flapping flight is an excellent propulsion technique used by natural flyers. Inspired by the swift, one of the fastest bird flyers, researchers believe that flapping micro air vehicles are more efficient than fixed wing vehicles [22]. The benefits of vortex shedding from flapping devices can be extended to solve flow control problems encountered in aeronautics.

Fig. 2.9 DARPA's Hummingbird Nano Air Vehicle [23]

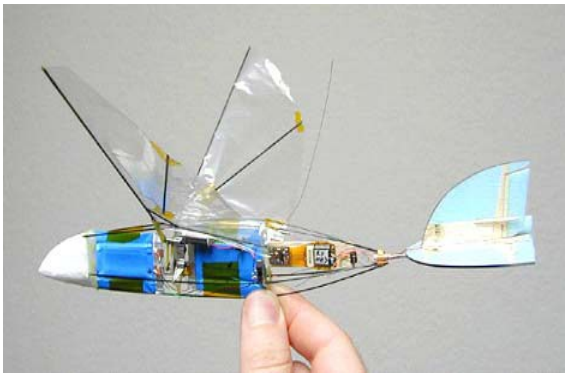

Fig. 2.10 Unmanned flying vehicle [24]

2.2.2 Flapping plate vortex generators

Vortex generators are mostly used in aeronautics applications to solve the problem of flow separation, created by the rise of static pressure on wall boundaries [25].

In a few applications, flapping plates are used as vortex generators, interacting with the boundary layer flow over hot surfaces. Flapping produces an induced velocity with a high circulation vortex in the vicinity of the edge of the boundary layer, which increases heat dissipation from the surface due to a decrease in the thickness of the boundary layer. Stream wise vortices transport the free stream to mix with existing fluid in the vicinity of the boundary layer of the hot surface. Previous researchers found that vortex generators can increase the heat transfer rate from hot surfaces by 50% [26]. As energy is always wasted in engineering designs, rotationally oscillating plates offer the possibility to recover energy that can be used to improve the efficiency of today devices and machines.

2.2.3 Energy Harvesting Applications

a) Piezoelectric cantilever beams energy harvesting

The flow induced by rotationally oscillating plates at a given frequency can become turbulent depending on the flapping rate and the geometry of the device. The forming and shedding of vortices from the detached flow during the upstroke and down stroke motions can result in a formation of downstream Von Karman vortices travelling away from the flapping plate itself [27]. Recent studies show that flapping foils can be used to collect the kinetic energy of an incoming flow by recovering part of the energy of the leading edge vortex and increasing the energy harvesting capacity [27]. A piezoelectric flexible cantilever beam installed inside the boundary layers and wakes of a circular cylinder in a wind tunnel can be used to collect tiny amount of electricity enough to power small electronic devices [28]. Similar results can be

achieved when the cylinder in this application is replaced by a flapping plate, because the moving device can generate a detached flow made of alternatively shedding vortices travelling downstream inside the wind tunnel.

b) Micro energy harvesting from opening and closing doors

Energy can be harvested from the opening and the closing of doors in facilities, which is a direct application of flapping plates as shown in Fig. 2.11. This is such a simple experiment with a large number of occurrences, where a small portion of the energy lost by humans can be recovered. The rotational oscillations of flat doors generate vortices that leave the surface during the upstroke and the downstroke motions. Each time doors are opened or closed, the dynamics of vortices disturb the surrounding medium; therefore the mechanism can be used for proximity detection or for activation of a sensor. Although the energy collected is very small, the summation of several of these amounts will result in a substantial quantity enough to power a few electronic devices. Taking the example of a house of 5 rooms occupied by 5 people and assuming each person will perform this experiment 5 times a day, a minimum possible output power per unit area $P_{min} = 1\mu W/cm^2$ could be generated for each cycle of 3 seconds, with an induced flow velocity of 3m/s. An estimate of the total annual energy produced E_Y is determined using equation (2.1).

$$E_Y = (5\text{rooms}) \times (5\text{persons}) \times (5\text{times/day}) \times (365\text{days}) \times P\,\text{min} \times (\text{time/cycle}) \quad (2.1)$$

The total annual energy collected is estimated to be

$$E_Y = (5) \times (5) \times (5) \times (365) \times (1\mu W/cm^2) \times (3\,\text{seconds}) = 13{,}6875\mu J/cm^2$$

Based on the activity level of all the people living in the facility, the energy consumption could be decreased by at least a little amount, assuming a building with a large number of rooms.

In this technological world, human's displacement and transportation has been facilitated by the modern means of locomotion such as: automobiles, airplanes, and boats, etc., for their daily activities or long distance travels. In large cities, the use of automobiles has become a common practice for the average citizen. Consequently, car doors opening and closing as illustrated in Fig. 2.12 are easy activities performed by passengers several times daily. Opening a car door induces an air flow inside the vehicle due to the pressure gradient between the surrounding medium and the interior of the vehicle. Depending on the circumstances of each passenger, the rotational speed of the door will vary while fluid particles are accelerated by the forming and shedding of vortices around the tip of the car door. A tiny portion of the energy used to operate car doors can be recovered if this technique is used for proximity detection or as power supply to electronic devices inside the vehicle.

In the latter case, the main issue remains the collection of such a small amount of flow energy that needs to be turned into electrical energy.

Fig. 2.11 Micro energy harvesting from door's opening and closing

Fig. 2.12 Micro energy harvesting from car doors'opening and closing

In conclusion, flapping plates are widely used in biological and industrial applications for aerodynamics force generation, energy harvesting, or heat dissipation enhancement. The literature review will provide more findings and applications by previous researchers.

CHAPTER 3: LITERATURE REVIEW

Previous researchers have found interest in the study of the flow induced by flapping a flat plate in an infinite domain because such a flow could be used for thrust production and lift force generation. Another important motivation has been the applications to heat transfer enhancement. However, a few studies focused on the thermal characteristics and the flow induced by rotationally oscillating plates.

Licht et al. [17] used flapping foils of $0.1\text{m} \times 0.4\text{m}$ driven by actuators to design an underwater vehicle. They found that flapping motion provided thrust for the propulsion of the vehicle. In their investigation of propulsive oscillating foils, Guglielmini et al. [29] explained the thrust produced in the locomotion of the fish as generated by vortices that shed in the opposite direction of the forward motion.

A flapping mechanism made with a four bar linkage, driven by an electric motor was designed by Lin et al.[30] for the experimental investigation of the thrust and the lift of ornithopters' wings. The results of their analysis showed that the lift force increases with the flapping frequency but an angle of attack is a requirement for lift force generation. A similar mechanism controlled by a robotic system is designed in chapter 6 of this project for the experimental investigation of the flow around rotationally oscillating plates. The mechanism is driven by a DC motor that provides predictable angular positions of the plate.

A few experimental investigations in biology revealed that flapping motion is responsible for heat transfer enhancement due to the improvement of the convection rate from the surface. Experiments performed by Datta [31] on African elephants showed that these animals use both sides of their pinnae as fins to dissipate significant amount of metabolic heat. According to his study, flapping increases heat loss due to an increase in air flow. However, the heat transfer data

recorded in his experiment is based on an estimate of the effect of the movement of the pinnae combined with vasodilatation. The heat transfer due to the flapping motion alone is not specified. African elephants are large mammals that flap their pinnae while walking and feeding in hot savannas [32], and the flapping rate of their pinnae varies with the surrounding atmospheric conditions [13]. Wright's 1984 study indicates that these animals, due to the large size of their body, produce a huge amount of metabolic heat [32]. In 1936, Benedict calculated the standard metabolic heat transfer rate q_m produced by elephants as a function of their total body mass [33]:

$$q_m = 0.8215 \times (W/kg) \times M(kg) \tag{3.1}$$

The total heat generated by a 2,000kg African elephant is estimated to be about 1,643W; this represents three times the heat produced by its Asian counterparts of 544W [13], still significant. To deal with its body heat, a 4,000kg African elephant in motion is expected to dissipate more than 3,286W while feeding to avoid overheating [32].

Despite all these studies about the elephant's body temperature regulation, one might imagine different venues used by the animal for heat dissipation, which could include: sweating and heat convection or radiation from the surface to the surrounding atmosphere. However, Datta reported that elephants do not have any sweat glands [31]. This eliminates the possibility of heat loss by perspiration, although one gram of sweat could help carry away 2.26kJ of energy [34]. The total surface area of the elephant body as shown in Fig. 3.1 is estimated to be about 20.7m^2 [35], including a negligible portion accounting for the feet. Therefore, it is reasonable to discard the heat loss by conduction to the ground. As elephants spend most of their time eating and drinking [13], they have to find other heat loss alternatives to maintain their body temperature in an acceptable comfort range. Nevertheless, the study by Kinahan et al. [36] indicates that large

mammals like elephants have low surface to volume ratio for substantial heat transfer by natural convection and radiation, compared to small mammals. The pinnae of the African elephant as shown in Fig. 3.2, estimated to be 137cm x 88.9cm [13], represent 20% of the total surface area of the whole body of the animal [32]. In addition, the elephant's ear is made of a huge network of blood vessels and due to its large surface to volume ratio, researchers hypothesize that ear flapping is the animal's main mechanism for heat loss [13, 31, and 37]. However, elephants can also extend their pinnae to use them as a mean of communication whenever they are in danger [38, 39].

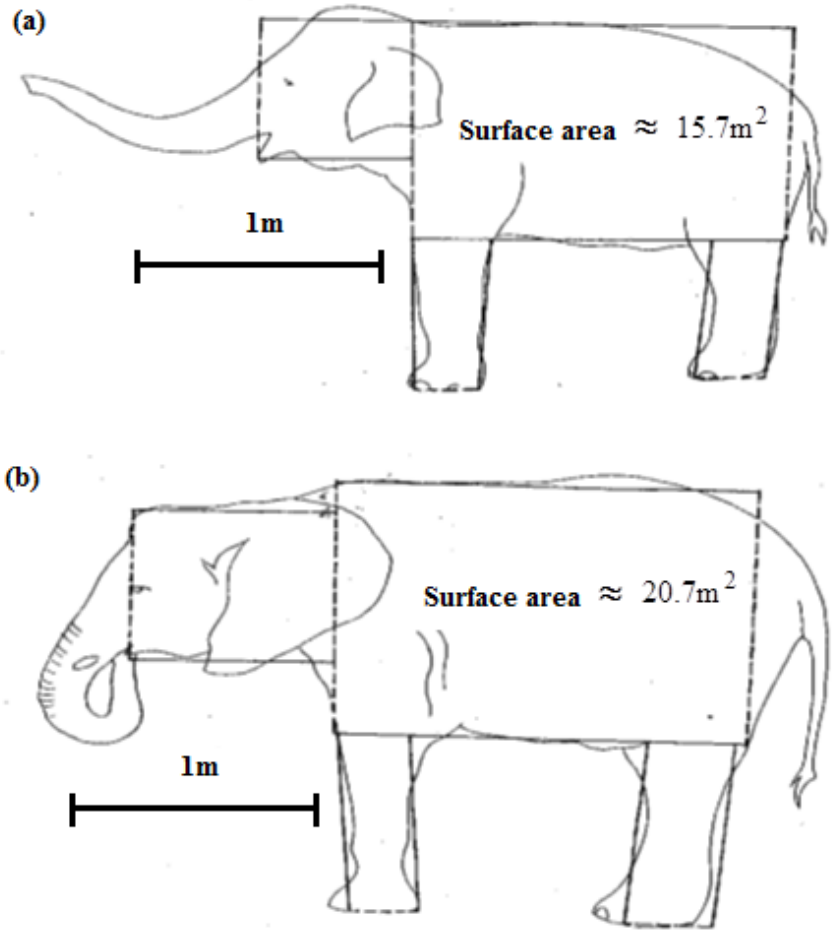

Fig. 3.1 Geometry of the elephant: a) Indian elephant b) African elephant [35]

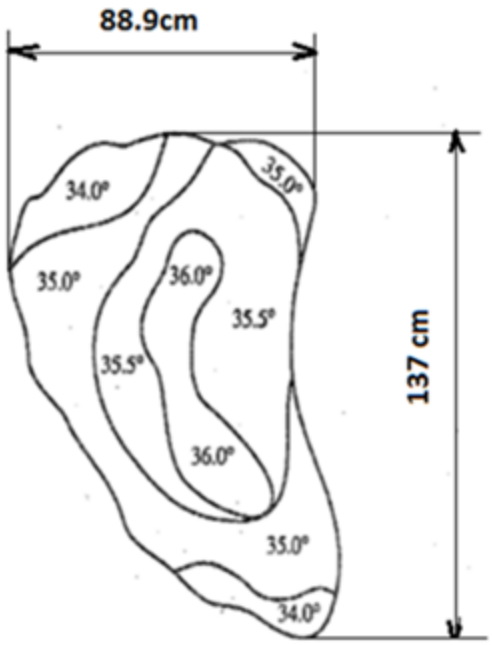

Fig. 3.2 Heat distribution across the surface of the African elephant's pinna at ambient temperature of 32.1°C [13]

Kinahan et al. [36] recorded the daily body temperature of 4 adult elephants every 30 minutes by hand feeding them with I Buttons; the same instrument was used to measure the ambient temperature at chosen locations. Their study illustrated in Fig. 3.3 indicates that the body temperature of elephants oscillates between 35.2°C and 37.5°C regardless of the ambient conditions, by generating internal metabolic heat [36]. Furthermore, Vanitha and Baskaran [40] performed an experimental investigation on Asian elephants in daylight hours, between 6:00 am and 6:00 pm, as displayed in Fig. 3.4. Their study shows that the highest flapping rates of the elephant ear are recorded between 1:00 pm and 2:00 pm, which corresponds to a peak ambient temperature range between 35°C and 40°C [40]. According to their results in Table 3.1 of mean ear-flapping frequencies measured on captive Asian elephants, the highest flapping rates of 9.3 flaps/min and 9.4 flaps/min are recorded between the months of May and August, when ambient temperatures range between 32°C and 36°C [40].

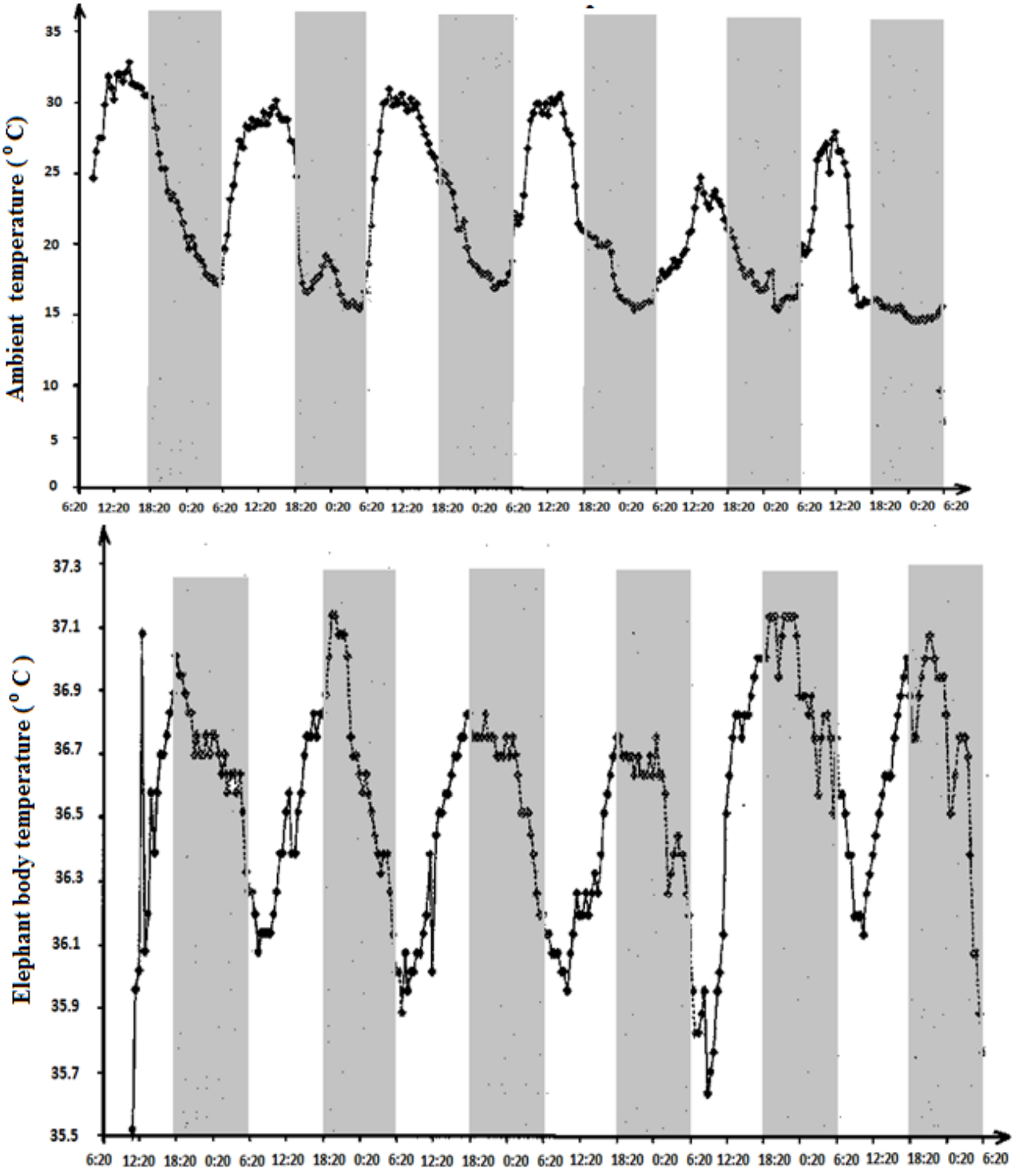

Fig. 3.3 Daily ambient temperature and elephant core body temperature variation [36]

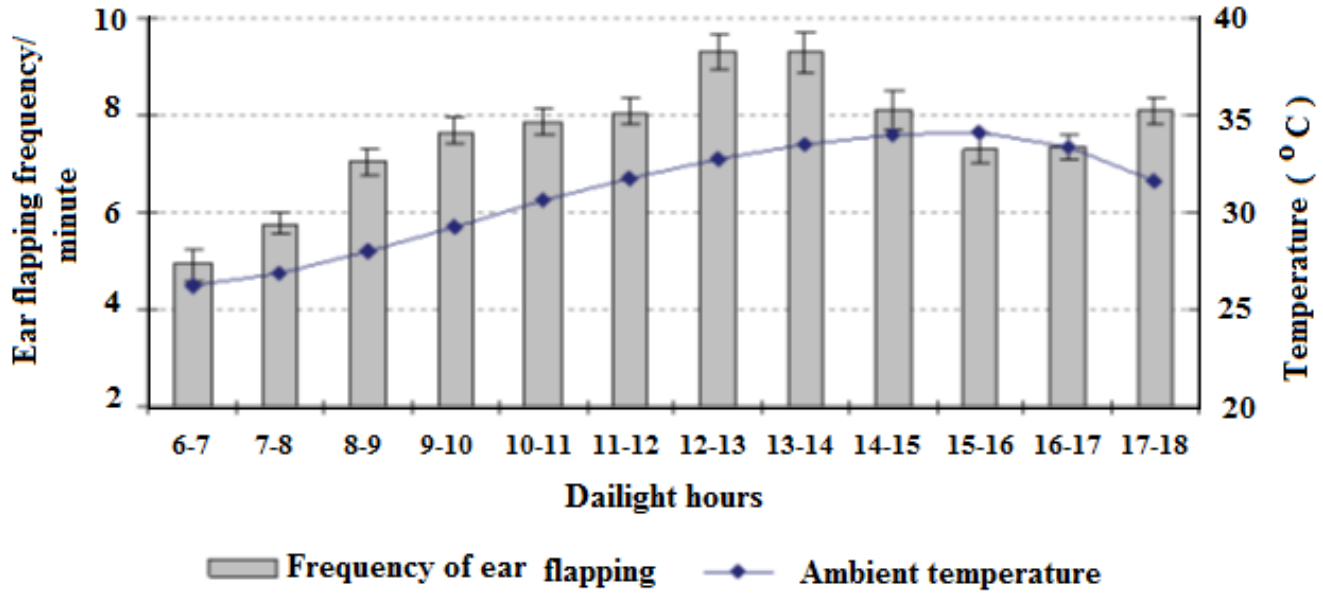

Fig. 3.4 Mean frequency of ear flapping recorded on captive Asian elephants and ambient temperature recorded in relation to daylight hours between May 2007 and April 2008 [40]

Table 3.1

Mean frequency of ear flapping per minute by captive elephants and ambient temperature (°C) recorded during different months between May 2007 and April 2008 [40]

Month	Ear flapping + SD	Temp. + SD
January	6.2 + 4.3	27.8 + 3.7
February	7.3 + 4.3	29.4 + 3.2
March	6.7 + 4.9	29.7 + 3.1
April	7.2 + 5.3	32.0 + 3.4
May	9.0 + 4.7	35.6 + 3.5
June	9.4 + 5.0	36.0 + 3.4
July	8.1 + 5.4	32.7 + 3.4
August	9.3 + 6.0	32.0 + 2.8
September	8.7 + 6.2	31.8 + 2.5
October	7.9 + 6.6	30.1 + 3.4
November	7.7 + 5.2	29.3 + 3.3
December	5.2 + 4.0	28.2 + 3.0

Elephants are large animals with thin and sensitive ears made of a huge network of blood vessels [41] that can facilitate the heat flow from the body of the animal towards the surrounding atmosphere. Similar to a moving fin, the flapping pinna of the elephant induces an air flow that participates in the improvement of the heat transfer rate from the surface of the body by forced convection. Benedict et al. [42] noticed large temperature gradients over the surface of the moving elephant's ear which can turn to a potential site for heat dissipation. They found that the tip of the flapping elephant pinna is the most favorable zone for heat transfer enhancement, nevertheless the outside has better cooling rate than the inside [42]. Moreover, Philip and Heath [13] estimated the total heat loss by convection and radiation from the pinna with equations (3.2) for surface convection and (3.3) for surface radiation. They used the mean surface temperature over the pinna in equation (3.4) determined from infrared thermography.

$$q_c = hA(T_s - T_\infty) \tag{3.2}$$

$$q_r = \sigma \varepsilon A(T_s^4 - T_\infty^4) \tag{3.3}$$

$$T_s = \sum T_i \left(\frac{P_i}{P_t} \right) \tag{3.4}$$

Where

q_c = average heat convection rate from surface, W
q_r = average heat radiation rate from surface, W
A = surface area of plate, m^2
σ = Stefan-Boltzmann constant = $5.67 \times 10^{-8}\ W/m^2 - K^4$
T_S = surface temperature, ^oC
T_∞ = ambient temperature, ^oC
T_i = average temperature of an isotherm, ^oC
P_i = pixel tally of that isotherm
P_t = total number of pixels in the analyzed image

In their flat plate experiment [13], Philips and Heath used infrared thermography to evaluate a heat loss of 1,500W by a 2,000kg elephant. This result represents 91.3% of the animal's standard

metabolic rate of 1,643W which is equivalent to a heat loss of 375W from each side of both ears. The resulting surface temperature is 36°C in a surrounding ambient at 20°C, with a wind velocity of 5m/s as illustrated in Fig. 3.5. According to their model , a heat loss of 75 W coupled with a wind velocity of $0.2\mathrm{m/s}$ would lead to a pinna's surface temperature of $32^{o}\mathrm{C}$ compared to a decrease in the surface temperature to $23^{o}\mathrm{C}$ when the wind velocity is increased to $5\mathrm{m/s}$ .Therefore, higher wind velocity is required for a significant amount of heat loss. Also, they found that the rate of heat transfer increases with the ear flapping rate which is dictated by the surrounding environment. This might explain why elephants move their ears faster in warmer outdoor environments, under the sun, than in cooler indoor conditions [13].

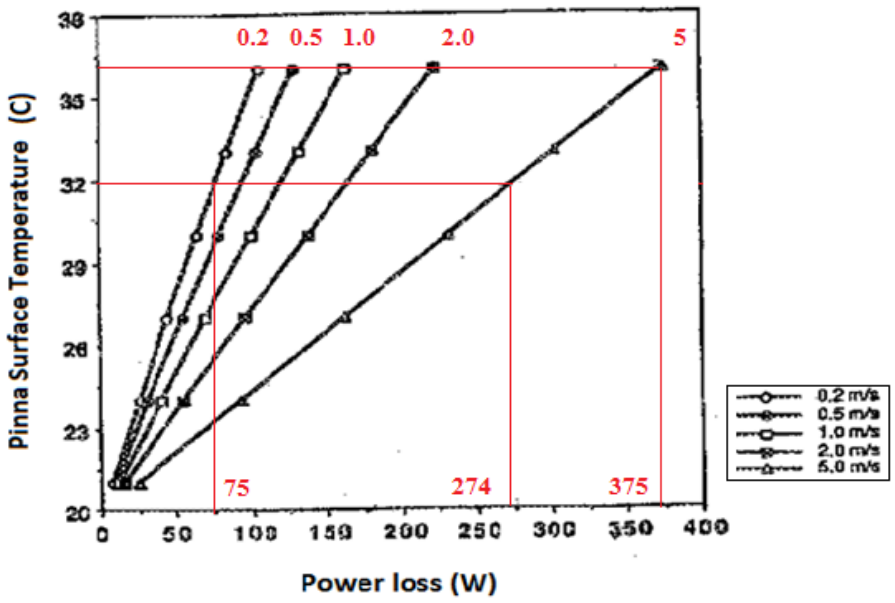

Fig. 3. 5 Flat plate model of heat loss by the pinnae of a 2,000kg African elephant at ambient temperature of 20°C [13]

Overall, experimental results presented earlier in Fig. 3.2 indicate that temperature is not uniform over the whole surface of the elephant pinna, although its local magnitude might change with flapping cycles. Moreover, the study of Philip and Heath [13] provides the spatial variation of

the pinna's surface temperature on one face only, even though heat is removed from both sides. However, these findings do not reveal the transient effect of the flapping motion on the elephant pinna's surface temperature, and mention little about the physics underlying the enhancement of the heat loss from the pinna's surface. The search for comfort through flapping surfaces for heat transfer enhancement are not limited to large mammals but also can be extended to small animals like rabbits[13] or birds[4].

Craig and Larochelle [4] studied the flow around flying domestic pigeons in a wind tunnel. They found that flying pigeons produce 33 watts of metabolic heat which represents 13 times the heat they would produce at rest. Such an amount of thermal energy is likely to increase the body temperature by more than $3^{o}C$. Craig and Larochelle concluded that 99% of the heat produced should be dissipated during flapping flight. Heat loss from the wing depends on other factors such as, stretching that can influence the total heat removed from the wing of the bird. In this study, the temperature distribution over the wings is not known; therefore a rigorous calculation of the heat loss from the wings cannot be achieved.

Ward et al. [43] used infrared thermograph to measure the temperature of starlings flying in a wind tunnel with a free stream velocity ranging from 6 to 14 m/s and an ambient temperature between $15^{o}C$ and $25^{o}C$. Values of heat transfer coefficients calculated for different parts of the bird including each section of the wing are presented in Fig. 3.6. The calculated values in this experiment are based on 2 different methods: the first method consists of treating each section of the body of the bird as a separate flat plate while the second method accounts for the other sections of the total surface including non-flapping parts such as the legs, the tail and the neck as shown in Fig. 3.6. According to Table 3.2, the heat transfer coefficient obtained by the first method is larger than the value provided by the second method .Overall highest values of heat

transfer coefficients are recorded from the 14 sections representing the wing, as a result of heat transfer enhancement due to the flapping motion.

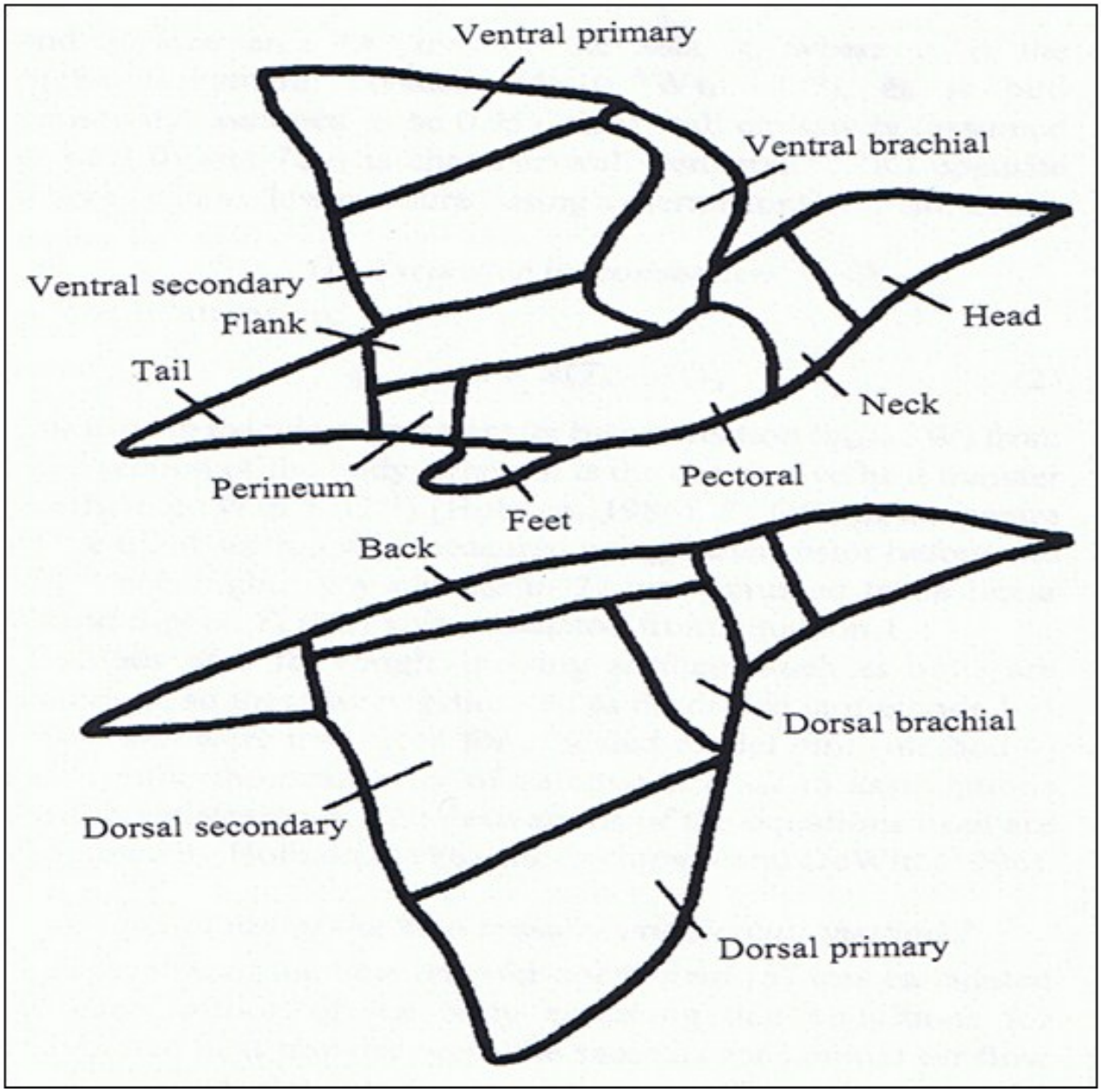

Fig. 3.6 The 14 sections of the surface of a flying starling [43]

Table 3.2

Heat transfer coefficient for the 14 sections of the wing of the bird [43]

	Surface Area $\times(10^3)m^2$	Heat Transfer coefficient, h (W/m^2-°C)		$T_s - T_a$ ($^\circ C$)
		Method 1	Method 2	
Legs	4.2 ± 0.5	78	22	6.8 ± 1.3
Ventral brachials	48.1 ± 2.0	78	78	6.0 ± 075
Head	14.7 ± 0.2	65	65	5.3 ± 0.6
Dorsal brachial	32.7 ± 3.9	91	91	4.7 ± 0.4
Pectoral	37.8 ± 4.2	47	47	4.4 ± 0.4
Flanks	33.0 ± 4.4	53	25	3.8 ± 0.4
Perineum	8.0 ± 0.7	85	22	3.4 ± 0.4
Neck	6.6 ± 0.8	134	31	2.9 ± 0.3
Back	38.7 ± 2.4	45	24	2.8 ± 0.8
Dorsal secondaries	57.4 ± 18.6	50	29	2.5 ± 0.4
Tail	17.5 ± 1.8	52	21	2.4 ± 0.9
Ventral secondaries	53.6 ± 17.4	52	28	2.5 ± 0.4
Dorsal Primaries	71.3 ± 24.7	54	51	2.2 ± 0.5
Ventral Primaries	**65.7 ± 22.8**	**56**	**52**	2.2 ± 0.4

The experimental investigation provides relevant information on the flow field and the thermal characteristics of the flow induced by rotationally oscillating heated plates. However, theoretical studies are necessary to check the validity of these results.

Phillips and Heath estimated the heat loss from the flapping elephant pinna using a theoretical approach for the determination of the heat transfer coefficient [13]. According to their study, the large size of the African elephant's pinna of 137cm x 88.9 cm can turn the flow turbulent;

therefore the resulting heat transfer coefficient is determined using the definition in equation (3.5) with the appropriate correlated local Nusselt numbers [13, 44].

In free convection over a stationary vertical plate, equations (3.6) and (3.7) are utilized in the derivation of the heat transfer coefficient in equation (3.8). In forced convection over a fixed semi-infinite plate, the tip velocity in (3.9) and the corresponding Reynolds number in (3.10) are combined to determine the Nusselt Number in (3.11) which is used to calculate the heat transfer coefficient in equation (3.12).

$$h_x = \frac{Nu_x \cdot k}{x} \tag{3.5}$$

Free convection analysis:

$$Gr_x = \frac{\beta g(T_s - T_\infty)x^3}{\nu^2} \tag{3.6}$$

$$Nu_x = 0.55 \cdot (Gr_x \cdot P_r)^{1/4} \tag{3.7}$$

$$h_x = 0.55k\left[\left(\frac{\beta g}{\nu^2} \cdot \frac{Pr}{x}\right) \cdot (T_s - T_\infty)\right]^{1/4} \tag{3.8}$$

Forced convection:

$$V = 2\pi \times (\frac{2}{3}L) \times (\frac{100}{360}) \times 2 \times (\frac{N}{60}) \tag{3.9}$$

$$Re_x = \frac{V \cdot x}{\nu} \tag{3.10}$$

$$Nu_x = 0.030 Re_x^{4/5} Pr^{1/3} \tag{3. 11}$$

$$h_x = 0.030 \cdot \frac{k}{x} Re_x^{4/5} Pr^{1/3} \tag{3. 12}$$

Where

G_{rx} = local Grashof number

Re_x = local Reynolds number

Nu_x = local Nusselt number

h_x = local heat transfer coefficient, $W/m^2 - ^oC$

Pr = Prandtl number

N = number of flaps per minute

L = width of the elephant ear, m

ν = kinematics viscosity of air, m/s^2
T_s = surface temperature, °C
T_∞ = ambient temperature = 25 °C
x = distance from leading edge, m

A first theoretical approach in the analysis of the local surface temperature of flapping heated plates can be performed with well-known correlation equations found in literature. However, the theoretical study of the flow field will provide more understanding of the temperature field. Karo et al. [45] utilized the discrete vortex model with the conformal mapping method to study the flow around a rotationally oscillating plate starting from rest. The results of calculations compared to flow visualizations provided information on vortex patterns, velocity profiles and unsteady forces on the plate. The two dimensional analysis showed that a pair of vortex clusters is generated below and above the plate during the flapping cycle. The two dimensional study will not reveal all the vortices involved in the flow field. A three dimensional CFD analysis with FLUENT 6.3 presented in chapter 5 will identify the different types of vortices present in the flow field. The analysis will focus on the details of vortex formation and their influence on heat transfer characteristics in the vicinity of the oscillating plate for several amplitudes angles.
Liu and Karachi [46] examined with CFD analysis some important details of the formation of the vortices around flapping wings. They found that a strong leading edge vortex (LEV) having a shape of spiral form causes low pressure on the upper face of the wing during the first half of the down stroke as illustrated in Fig. 3.7. This vortex is followed by another vortex from the leading edge and the latter one forms and runs from the tip to the base due to the low pressure region created by the first vertex. At the transition from down stroke to upstroke, both vortices merge into a hook-shaped vortex that will deform and shed from the trailing edge as shown in Fig. 3.8.

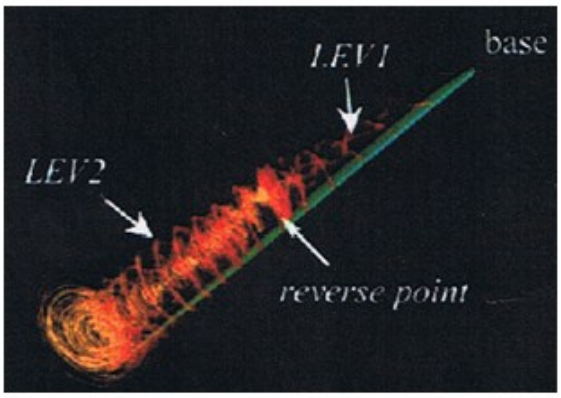

Fig. 3.7 CFD simulation of the unsteady leading edge vortex [46]

Fig. 3.8 Unsteady leading edge vortex as seen from behind and below a MAV wing [47]

Flapping motion observed in birds and insects flights has been found to be responsible for lift generation [5, 47, 48, and 49]. The lift force decreases after a maximum value of 27g during the down stroke motion due to the shedding of vortices from the wing as illustrated in Fig. 3.9. Ho et al. [47] determined that the lift force is a positive quantity, which is predominant during the down stroke of the flapping cycle according to Fig.3.9. The results of these investigations are used in the design of micro air unmanned flying vehicles utilized in military applications or in hazardous environment such as nuclear power plants for maintenance purposes as mentioned in Chapter 2.

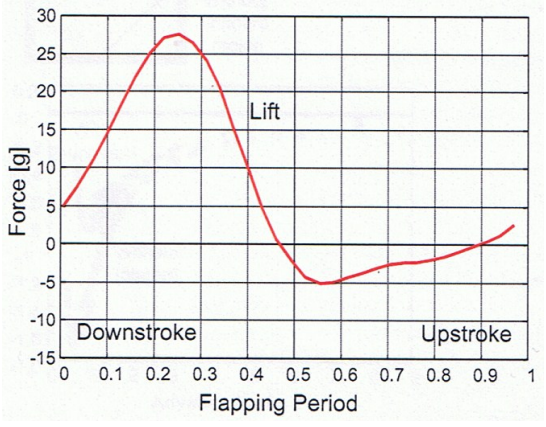

Fig. 3.9 Phase average lift during one flapping cycle [47]

A numerical study of fluid flow around a two-dimensional rigid oscillating plate with Femlab, a finite element analysis software used to model and solve scientific and engineering problems based on partial differential equations, was presented by Lind and Abedian [50]. In their model shown in Fig. 3.10, a straight line representing a wing at constant temperature equal to 295K undergoes sinusoidal angular motion while one end is kept fixed. Air flowing with a bulk velocity U enters the simulation domain and exits at zero relative pressure. They investigated the effect of flapping motion on the heat transfer rate from the plate. Important dimensionless flow parameters used in their study were the reduced frequency $k = \omega L/U$ and the Reynolds number based on flapping frequency $Re_f = \omega L^2/\nu$ with ω the flapping frequency, L the plate length, ν the kinematic viscosity and U the free stream velocity of air in laminar flow. Table 3.3 shows examples of the flow characteristics for typical flying animals.

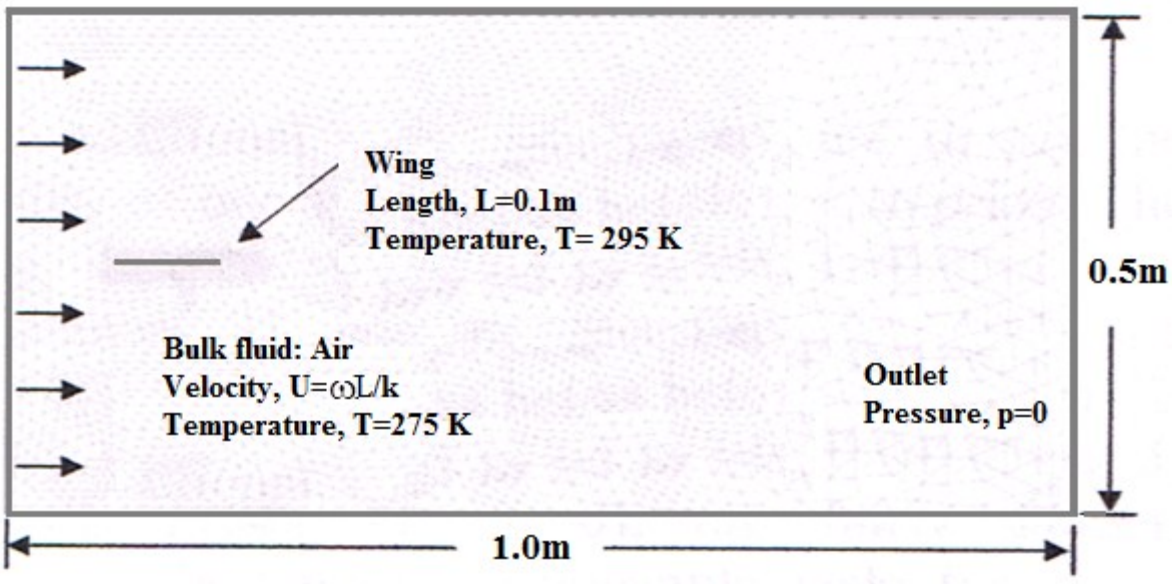

Fig. 3.10 Fem lab meshed model geometry [50]

Table 3.3
Characteristic quantities for typical flying animals [50]

Quantity	Small wasp	Locust	Pigeon
Wing Length, L	0.0006m	0.04 m	0.25 m
Angular frequency, ω	400 rads/s	20 rads/s	5 rads/s
Forward velocity, U	1 m/s	4 m/s	5 m/s
Reduced frequency ωL/U	0.24	0.20	0.25
Reynolds frequency *Ref = $\omega L^2/\upsilon$	10	2,300	22,500

In their study, flapping motion is simulated by assigning oscillatory axial and lateral velocities to the plate. The horizontal and vertical velocities were derived by taking the time derivative of the angular position in Fig. 3.11. The axial velocity has a frequency twice that of the lateral velocity as shown later in Fig. 3.12.

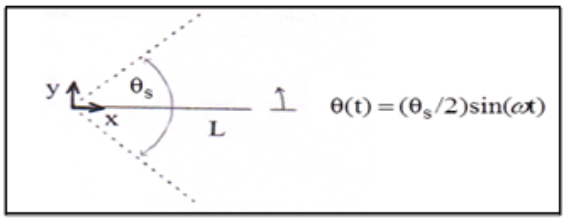

Fig. 3.11 The two dimensional model of a flapping wing [50]

$$u(t) = -A_0 \sin[(\theta_S/2)\sin(\omega t)]\cos(\omega t) \quad (3.13)$$

$$V(t) = A_0 \cos[(\theta_S/2)\sin(\omega t)]\cos(\omega t) \quad (3.14)$$

Where θ represents the angle of a full down stroke or upstroke and ω the angular frequency

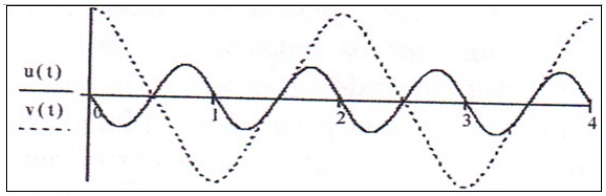

Fig. 3.12 Sinusoidal horizontal, u (t), and vertical v (t), velocity components shown for two periods of oscillations [50]

As conclusion to their simulations, the tip vortices on either side of the plate spin alternatively clockwise and counterclockwise in some ranges of dimensionless parameters. This pair of vortices is likely to significantly improve the heat transfer from the plate. But here the two-dimensionality of the plate model does no give the details of the heat transfer over the whole surface of the plate. Knowledge of the local surface temperature distribution on the plate will make it easier to calculate the heat transfer rate from the plate.

Flapping motion is shared by vertebrates like fish who achieve undulatory propulsion by sending alternating waves down the body towards the tip of the tail. Adkins and Yan [51] proposed a mathematical and numerical model in order to solve viscous flow around a moving fish-like body shown in Fig. 3.13. Unsteady solution to the incompressible Navier- Stokes equations is key to the understanding of such highly unsteady phenomena. A computational system based on the method of three dimensional Navier -Stoke equations solver is developed for the solution to real flow problems. The Reynolds-Averaged Navier-Stokes equation is written in Cartesian tensor form as follows:

$$\frac{\partial \rho}{\partial t} + \frac{\partial}{\partial xi}(\rho u_i) = 0 \tag{3.15}$$

$$\frac{\partial}{\partial t}(\rho u_j) + \frac{\partial}{\partial x_j}(\rho u_i u_j) = -\frac{\partial p}{\partial x_i} + \frac{\partial}{\partial x_j}[\mu(\frac{\partial u_i}{\partial x_j} + \frac{\partial u_i}{\partial x_j} - \frac{2}{3}\delta_{ij}\frac{\partial u_i}{\partial x_i})] + \frac{\partial}{\partial x_j}(-\rho\overline{u'_i u'_j}) \tag{3.16}$$

$$\text{With} \quad \overline{-\rho u'_i u'_j} = \mu_l(\frac{\partial u_i}{\partial x_j} + \frac{\partial uj}{\partial x_i}) - \frac{2}{3}(\rho k + \mu_l \frac{\partial u_i}{\partial x_i})\delta_{ij} \tag{3.17}$$

Where

x_i, x_j, x_l = Cartesian coordinates, m

$u_i, u_j, u_l, u'_i, u'_j, u_l'$ = velocity components, m/s

ρ = density of the fluid, kg/m^3

μ = dynamic viscosity, kg/s-m

t = time, s

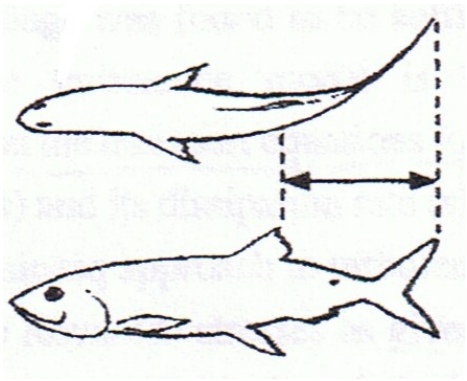

Fig. 3.13 The carangiform motion of a tuna [50]

Another theoretical study was proposed by Moffat and Duffy [52] who modeled the problem of rotating a solid surface at constant pulsation Ω as a two-dimensional stationary viscous flow. They considered two solid surfaces rotating symmetrically with constant pulsation $\Omega/2$ about a given plane as shown in Fig. 3.14. In the case of small Reynolds numbers, the problem is solved by superposition of two linear problems: a solid body rotation and a flow at pulsation $\Omega/2$. It is shown that the solution to the fluid flow equation is reduced to solving a bi-harmonic problem for the stream function $\psi(r,\theta)$ with:

$$\nabla^4 \Psi = 0 \tag{3.18}$$

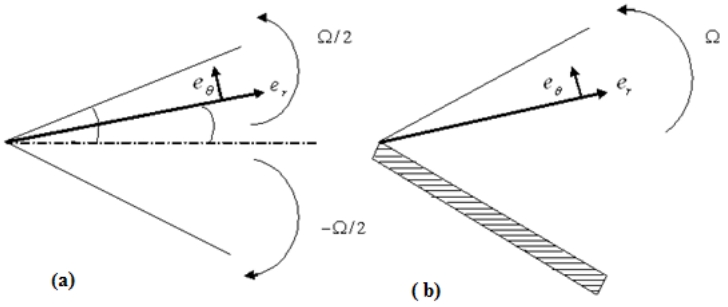

Fig. 3.14 Cylindrical coordinates are considered (a) symmetrical flapping plates (b) one flapping plate attached to a fixed boundary $\Omega r^2 << 1$ [52]

Using cylindrical coordinates to solve this problem, the quasi-steady solution is known to be the stream function $\psi(r,\theta)$ given by equation (3.19) for r << L.

$$\psi(r,\theta) = -\frac{1}{4}\Omega r^2\left(\frac{\sin 2\theta - 2\theta\cos\Omega t}{\sin\Omega t - \Omega t\cos\Omega t}\right) \tag{3.19}$$

Where

Ω = angular velocity of the body, rad/s
θ = angular displacement from the horizontal, rad
t = time, s
r = distance from the origin of the axis of rotation, m
L = total length of the plate, m

This solution is valid for a critical maximal angle α_c =257.45 degrees for the angular displacement Ωt from the origin. If we superimpose the rotation of the rigid body on the flow at pulsation $\Omega/2$, the stream function becomes:

$$\psi(r,\theta) = -\frac{1}{4}\Omega r^2\left(1 + \frac{\sin 2\theta - 2\theta\cos\Omega t}{\sin\Omega t - \Omega t\cos\Omega t}\right) \tag{3.20}$$

The velocity field is derived by taking the derivative of the stream function with respect to r to obtain the radial component $u_r(r,\theta)$ and with respect to θ for the angular component $u_\theta(r,\theta)$ with:

$$u_r(r,\theta) = \frac{1}{r}\partial_\theta\psi = -\frac{1}{4}\Omega r\left(\frac{2\cos 2\theta - 2\cos\Omega t}{\sin\Omega t - \Omega t\cos\Omega t}\right) \tag{3.21}$$

$$u_\theta(r,\theta) = -\partial_r\psi = \frac{1}{2}\Omega r\left(1 + \frac{\sin 2\theta - 2\theta\cos\Omega t}{\sin\Omega t - \Omega t\cos\Omega t}\right) \tag{3.22}$$

The boundary conditions are:

$$\theta = \pm\alpha/2 = \Omega t/2 \qquad \begin{aligned} u_r(r,\pm\Omega t/2) &= 0 \\ u_\theta(r,\Omega t/2) &= \Omega r \\ u_\theta(r,-\Omega t/2) &= 0 \end{aligned} \tag{3.23}$$

The analytical solution is an interesting tool for the calculation of the flow induced by rotationally oscillating plates. The analytical solution alone cannot guarantee the use of the velocity field to predict surface temperature over oscillating plates. No description of vortices was mentioned in the above study; therefore their influence on the heat transfer from the plate is unknown.

Overall, several attempts have been made to investigate either the flow field or the heat transfer characteristics around flapping wings. The main objective has been understanding of the details of the flow field and thermal characteristics involved. Most of the previous work examined the flow characteristics around flapping plates where a fluid of free stream velocity U enters the flow domain, providing an explanation to the aerodynamics of flying animals or flying vehicles [16]. Little work was presented for the case where the rotation of the plate is the only mechanism responsible for inducing the flow. Flapping motion is used for heat transfer enhancement applications such as metabolic heat regulation observed in animals [4, 31]. But these studies are limited to experimental observations. Theoretical analyses are necessary to check the validity of the results obtained. A detailed analysis of the thermal characteristics of flows generated by rotating a plate in a domain where the free stream velocity is equal to zero can help design new techniques such as electronic cooling systems [26]. Previous studies used 2D simulations models for the analysis of flow characteristics in the vicinity of rotationally oscillating plates [16, 46]. Some of them provided qualitative descriptions of the flow field such as the formation and the shedding of vortices: Lind et al. [50] concluded that the shedding of vortices resulted in heat transfer enhancement, but they did not show how to calculate the heat transfer rate from the plate. With a 2D model, vortices are visualized in one direction only. Therefore, information on their behavior in other directions is not provided. Several applications of rotational oscillating plates utilize many flapping cycles: examples include micro air vehicles, birds and insects flights. However, most of the previous work has focused on the study of one cycle only. Such analyses are not sufficient to investigate all the transient effects on the flow and thermal characteristics around flapping plates. Also, some papers presented the position analysis and the kinematics of the moving plate itself [16, 30]. Others derived important dimensionless

parameters, helpful for the analysis of such flows [48]. However, none of these studies has provided a comprehensive work for the development of a correlation to predict surface temperature distribution over rotationally oscillating plates, through a large number of cycles.

The present study starts with a computational simulation of the flow using 2D and 3D models in FLUENT for a detailed analysis of the velocity field, vortex shedding, and the temperature distribution over the surface of a rotationally oscillating heated plate. The experimental investigation follows the computational investigation, to check the validity of the flow and the thermal characteristics over the surface of the plate. The resulting solution will serve in future work to develop correlation equations for the prediction of the flow and heat transfer characteristics in the vicinity of rotationally oscillating heated flat plates. A theoretical background of the computational investigation of the flow induced by the rotational oscillating motion of the plate will be presented beforehand.

CHAPTER 4: COMPUTATIONAL INVESTIGATION OF THE FLOW INDUCED BY A ROTATIONALLY OSCILLATING PLATE WITH ANSYS/FLUENT 6.3

Problem definition

A rectangular flat plate of area 0.2m x 0.3m with a thickness of 4mm is rotated back and forth over amplitude of 90° angle at a frequency ω about a vertical axis, in a semi-spherical domain of radius equal to 5m (Fig. 4.1). A constant heat flux q'' is continuously applied to both sides of the plate during its motion in a flow domain at atmospheric pressure. A convenient method for solving this problem is a simulation of the flow with ANSYS/FLUENT 6.3, a computational fluid dynamic software package designed for flow and heat transfer calculations. This is a moving boundary problem where a user defined function (UDF) assigns the motion to the plate with a computer code, written in the C programming language found in Paragraph 9.3 of the Appendix.

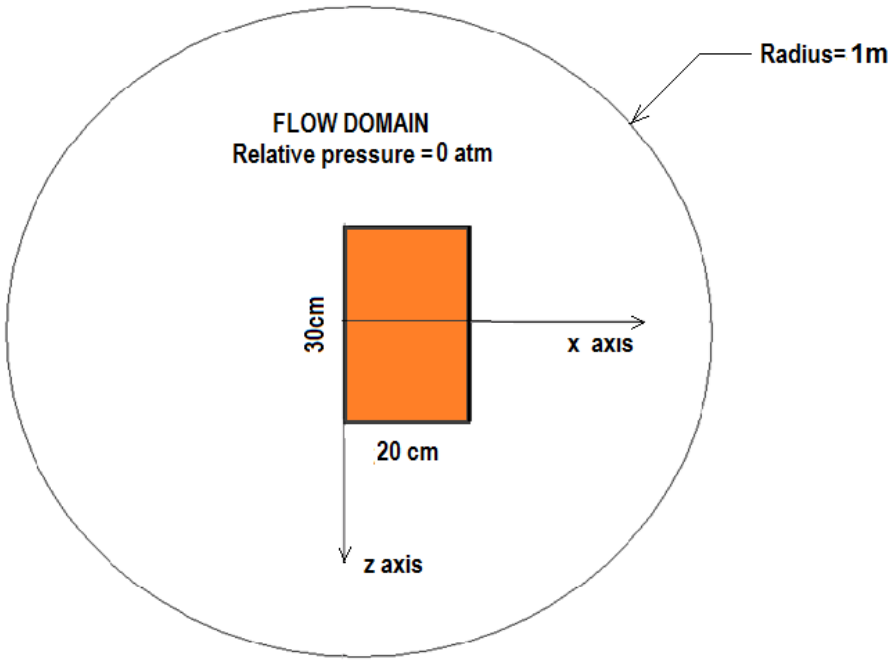

Fig. 4.1 Rectangular flat plate in semi-spherical flow domain

4.1 Theoretical background of the dynamic mesh

In this project, the rotationally oscillating motion of the plate modifies the boundaries of the flow domain after each time step. The computational fluid dynamic (CFD) simulation in FLUENT of such a transient problem requires a dynamic mesh model [53]. This method is based on the conservation equation (4.1) for an arbitrary scalar ϕ:

$$\frac{d}{dt}\int_{\partial V}\rho\phi dV+\int_{\partial V}\rho\phi(\vec{u}-\vec{u}_g)\bullet d\vec{A}=\int\Gamma\nabla\phi\bullet d\vec{A}+\int_{V}S_\phi dV \tag{4.1}$$

Where

ρ = the fluid density, kg/m^3
$\vec{u}$ = the flow velocity vector, m/s
$\vec{u}_g$ = the grid velocity of the moving mesh, m/s
Γ = the diffusion coefficient
S_ϕ = the source term of ϕ

Using a first order backward difference, the time derivative term is written as follows:

$$\frac{d}{dt}\int_{V}\rho\phi dV=\frac{(\rho\phi V)^{n+1}-(\rho\phi V)^{n}}{\Delta t} \tag{4.2}$$

$$\frac{dV}{dt}=\int_{\partial V}\vec{u}_g\cdot d\vec{A}=\sum_{j}^{n}\vec{u}_{g,j}\cdot\vec{A}_j \tag{4.3}$$

$$V^{n+1}=V^{n}+\frac{dV}{dt}\Delta t \tag{4.4}$$

With: $\frac{dV}{dt}$ = the volume time derivative of the control volume

4.1.1 Spring-based smoothing method

The spring-based smoothing method applies to this problem because the flow domain is meshed with tetrahedral elements [53]. The method consists of modeling each edge connecting any two nodes as a spring. Thus the meshed flow field resembles a network of interconnecting springs. A particular node will be in equilibrium if the sum of the forces applied to that node is equal to zero. The force developed in each spring attached to a given node can be calculated using Hooke's Law:

$$\overrightarrow{F_i} = \sum_{j}^{n_i} k_{ij}(\Delta\overrightarrow{x_j} - \Delta\overrightarrow{x_i}) \qquad (4.5)$$

With

$$k_{ij} = \frac{\mathbf{1}}{\sqrt{\left|\overrightarrow{x_i} - \overrightarrow{x_j}\right|}} \qquad (4.6)$$

Where

$\overrightarrow{x_i}$ = position of nodes i , m

$\overrightarrow{x_i}$ = position of its neighbor node nodes j , m

$\Delta\vec{x}_i$ = displacement of node i , m

$\Delta\vec{x}_j$ = displacement of its neighbor node j, m

n_i = number of neighboring nodes connected to node i

k_{ij} = spring constant for the edge connecting node i and node j, N/m

The spring constant factor can be adjusted between 0 and 1 as illustrated in Fig. 4.2 and Fig. 4.3. A value of 0 corresponds to the absence of damping in the spring, while 1 is the default level of damping. During the simulation of a case, the mesh can be degenerated due to the motion of the plate (Fig. 4.2). Therefore, setting the spring constant factor to 0 improves the quality of the tetrahedral elements during the update of the volume mesh.

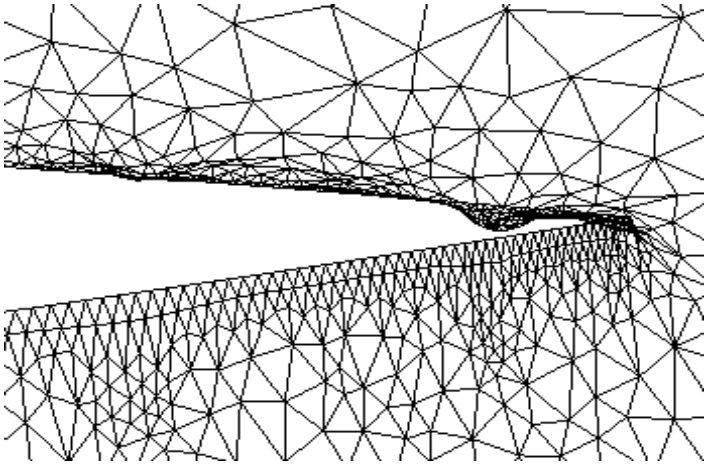

Fig. 4.2 Effect of a spring constant factor of 1 on interior node motion [53]

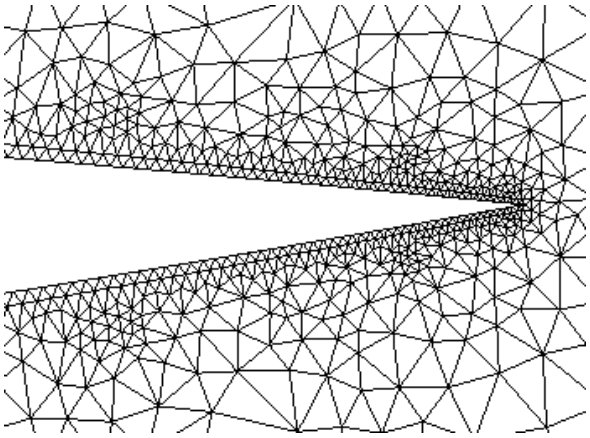

Fig. 4.3 Effect of a spring constant factor of 0 on interior node motion [53]

4.1.2 Solid-body kinematics

The user defined function (UDF) describes the linear and angular velocities of the plate about the center of gravity of the solid body with respect to time. During the simulation of the flow over the moving plate, FLUENT updates the position of the center of gravity after every time step [53].

$$\vec{x}_{c.g.}^{\,n+1} = \vec{x}_{c.g.}^{\,n} + \vec{v}_{c.g.}.\Delta t \tag{4.7}$$

$$\vec{\theta}_{c.g}^{\,n+1} = \vec{\theta}_{c.g.}^{\,n} + \vec{\Omega}_{c.g.}.\Delta t \tag{4.8}$$

Where

$\vec{x}_{c.g.}$ = position of the center of gravity, m

$\vec{\theta}_{c.g.}$ = orientation of the center of gravity, rad

$\vec{v}_{c.g.}$ = linear velocity of the center of gravity, m/s

$\vec{\Omega}_{c.g.}$ = angular velocity of the center of gravity, rad

The position vectors after each time step are updated during the motion of the plate as sketched in Fig. 4.4 and the new position $\vec{x}^{\,n+1}$ is obtained from the previous $\vec{x}^{\,n}$ as defined by equation (4.9).

With:
$$\vec{x}^{\,n+1} = \vec{x}^{\,n} + \Delta\vec{x} \tag{4.9}$$

$$\Delta\vec{x} = \left|x_r^n - \vec{x}_{c.g}\right| \cdot [\sin(\Delta\theta)\hat{e}_\theta + (\cos(\Delta\theta) - 1)\hat{e}_r] \tag{4.10}$$

Where the unit vectors $\hat{e}_r$, $\hat{e}_\theta$ are defined as:

$$\hat{e}_r = \frac{\Omega_{c.g} \times x_r}{\left|\Omega_{c.g} \times x_r\right|} \tag{4.11}$$

$$\hat{e}_\theta = \frac{\Omega_{c.g} \times x_\theta}{\left|\Omega_{c.g} \times x_\theta\right|} \tag{4.12}$$

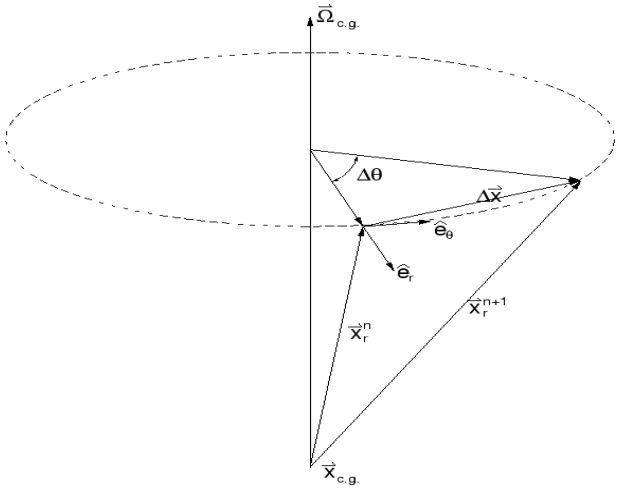

Fig. 4.4 Solid body rotation coordinates [53]

4.1.3 Theoretical calculation of forces and the moment applied to the plate.

The total force F_T on the moving plate in the flow field, expressed in equation (4.13) is composed of pressure and viscous forces. The moment of forces applied to the plate is calculated with equation (4.14) about an arbitrary point as shown in Fig. 4.5.

$$F_T = \vec{a} \cdot \vec{F}_P + \vec{a} \cdot \vec{F}_v \tag{4.13}$$

$$\vec{M}_A = \vec{r}_{AB} \times \vec{F}_P + \vec{r}_{AB} \times \vec{F}_v \tag{4.14}$$

Where

$\vec{a}$ = specified force vector
$\vec{F}_P$ = pressure force vector
$\vec{F}_v$ = viscous force vector

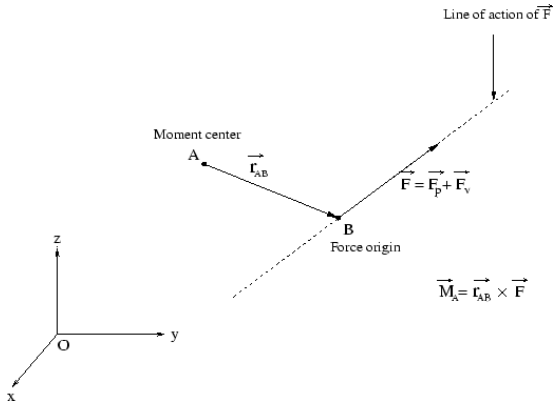

Fig. 4.5 Calculation of forces and moment on plate [53]

4.2 Simulation of the dynamic mesh with ANSYS/FLUENT 6.3

The simulation of the 3D dynamic mesh allows the visualization and the monitoring of the flow and thermal characteristics over the surface of the plate. To facilitate the analysis of these characteristics during the simulation of the flow, small-sized discs are created at desired locations on the plate's surface for study. These surfaces are made during the modeling of the geometry in Gambit or Solid Works prior to the meshing of the flow domain in Fig. 4.6. In this problem, a finer mesh is required for the calculation of thermal characteristics. However, the meshing of the flow domain presents a great challenge as the grids must be refined in order to obtain accurate results. A finer mesh requires a huge number of cells, therefore larger computer storage with a longer computation time to solve the Navier Stokes and the energy equations at each specific node point. During the simulation of the flow with FLUENT, the UDF assigns the rotation to the plate with the tracking point surfaces represented by triangular cells. Each point surface shares its three nodes with neighboring cells within the surface mesh.

The flow field is investigated first because of its impact on the plate's surface thermal characteristics. The time history of the aerodynamics forces and their moments applied to the

moving plate are analyzed throughout the flapping cycle. Results obtained in current simulation are utilized as a guide in the design of the flapping mechanism for the experimental investigation discussed in chapter 5.

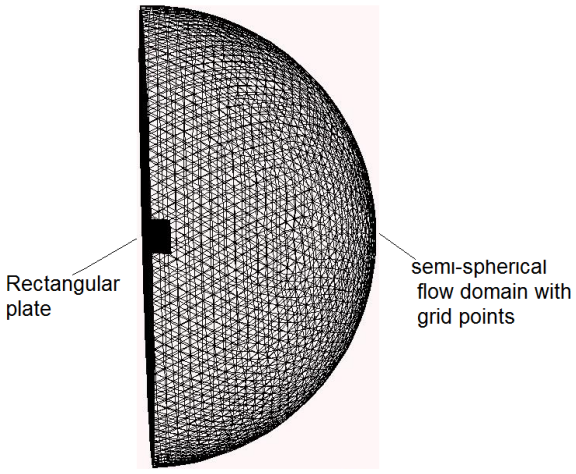

Fig. 4.6 Semi-spherical meshed flow domain

4.2.1 Aerodynamic forces applied to the flapping plate

a) Drag force on the plate

The drag [54] is the force applied to the surface of the plate opposed to the direction of the flow. During flapping flight, part of the weight of insects like dragonflies is supported by the induced drag force [9]. Throughout the simulation of the flow around the moving plate with FLUENT, the drag coefficient of the rectangular flat plate flapping at a frequency $\omega = 2\text{rad/s}$ is monitored as shown in Fig. 4.7 and the drag force is plotted using FLUENT results in Table 4.1. Over a given flapping cycle, there are mainly, pressure and viscous forces acting on the moving device. In this project, the rotation of the plate occurs around a vertical axis, over amplitude of 90° angle called the upstroke, followed by the down stroke motion that brings the moving device to its initial position. But the transition from upstroke to down stroke constitutes a critical phase of the flapping cycle because the flow characteristics change rapidly.

during the inversion process (Fig. 4.7), passing through a peak value of the drag coefficient equal to -0.25. Values of the viscous component of the drag force in Table 4.1 indicate that the pressure force is the major component opposed to the rotation of the plate.

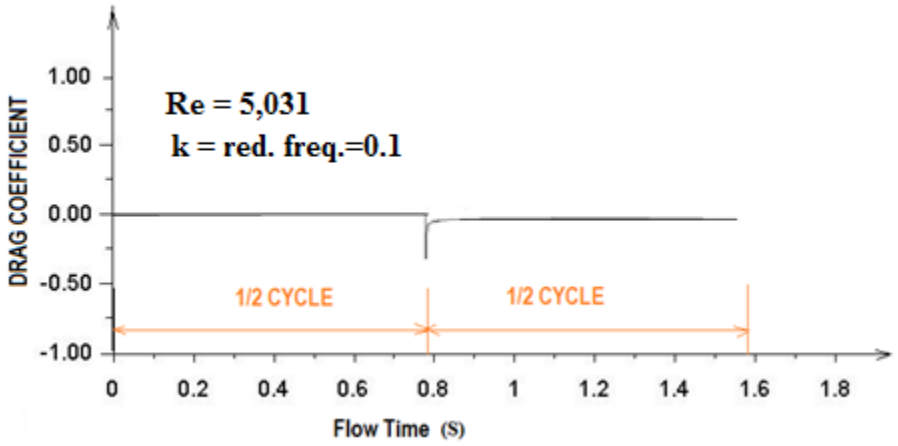

Fig. 4.7 Drag coefficient on the plate over a cycle

Table 4.1
Drag force components on the plate

Time steps	Pressure force (N)	Viscous force (N)	Total force (N)
1	0.09000	0.00185	0.09640
2	0.13292	0.00060	0.13360
3	0.16470	0.00040	0.16511
4	0.18187	0.00037	0.18224
5	0.19672	0.00036	0.19708
6	0.20939	0.00035	0.20975
7	0.22103	0.00040	0.22137
8	0.22961	0.00032	0.22994
9	0.23726	0.00031	0.23757
10	0.24658	0.00029	0.24687
11	0.24810	0.00026	0.24836
12	0.24253	0.00023	0.24276
13	0.24269	0.00018	0.24288

Table 4.1 (Con't)
Drag force components on the plate

Time steps	Pressure force (N)	Viscous force (N)	Total force (N)
14	-0.53626	-0.00068	-0.53633
15	-0.40135	0.00014	-0.40122
16	-0.33640	0.00027	-0.33612
17	-0.29232	0.00037	-0.29194
18	-0.25763	0.00047	-0.25716
19	-0.22628	0.00055	-0.22573
20	-0.19950	0.00064	-0.19886
21	-0.17373	0.00072	-0.17301
22	-0.17373	0.00072	-0.17301
23	-0.15204	0.00083	-0.15121
24	-0.13446	0.00095	-0.13351
25	-0.12573	0.00051	-0.12458
26	-0.13718	0.00153	-0.13565

The total drag force increases as shown in Fig. 4.8, with the projected area and the angular position of the plate in the computational domain. As the pressure drag increases, the viscous drag(very low compared to the pressure drag), which is responsible for fluid rotation, decreases with the stroke angle within the flapping cycle as illustrated in Figs. 4.9 and 4.10.

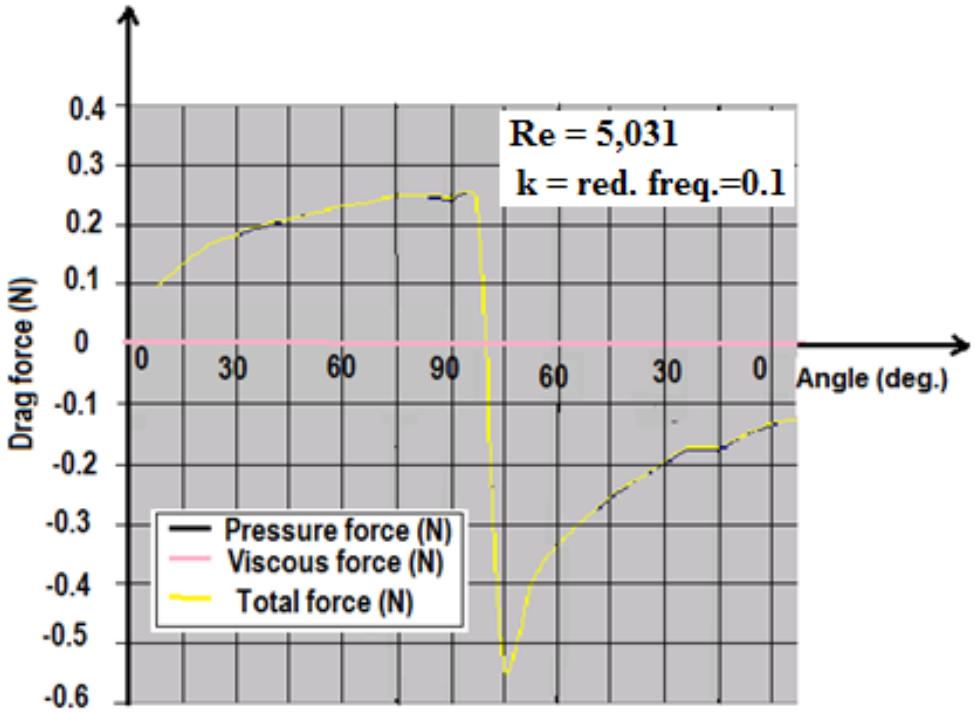

Fig. 4.8 Drag force on the plate over a cycle

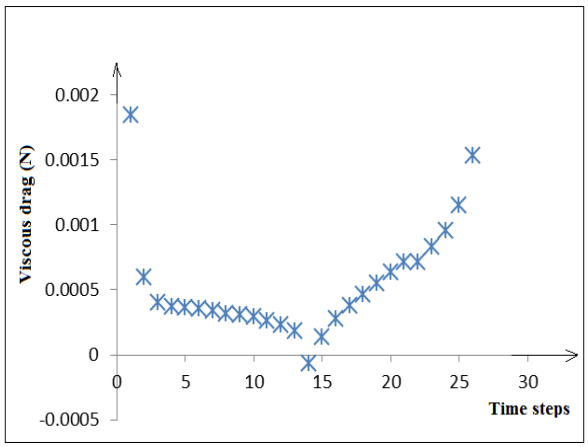

Fig. 4.9 Viscous drag (N) on the plate

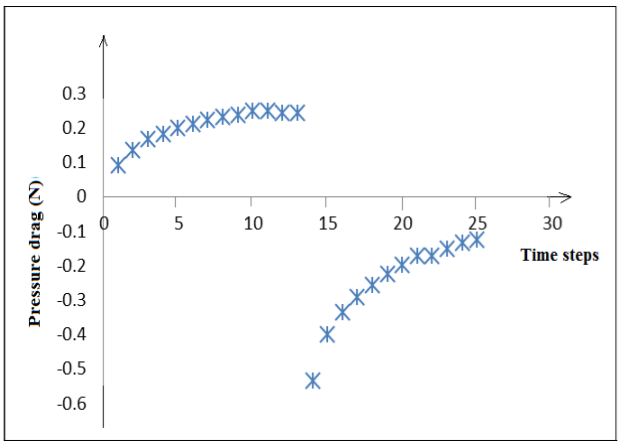

Fig. 4.10 Pressure drag (N) on the plate

b) Lift force on the plate

The lift [54] is defined as the component of the aerodynamic force applied to the plate, perpendicular to the moving fluid stream. The graph displayed in Fig. 4.11 exhibits higher lift coefficient values at end strokes. But the lift coefficient increases from negative to positive values through zero, which corresponds to the mid-stroke of the plate. It appears that the absolute value of the lift decreases with the angular position of the plate, as illustrated in Fig. 4.12. Consequently, the highest lift is observed when the position of the plate is close to 0° angle. In conclusion, when the drag increases, the lift decreases.

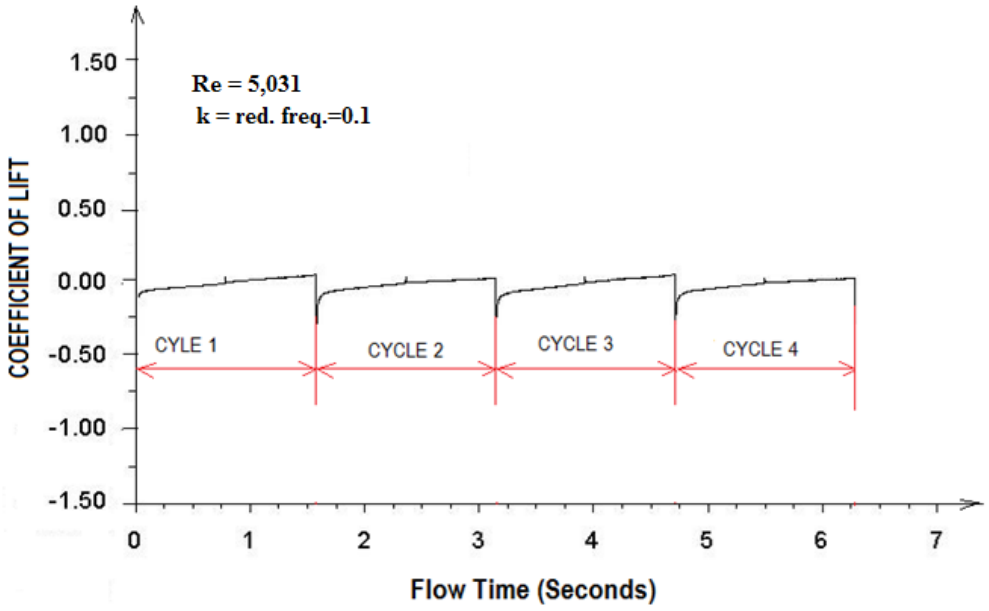

Fig. 4.11 Lift coefficient on the plate over 4 cycles

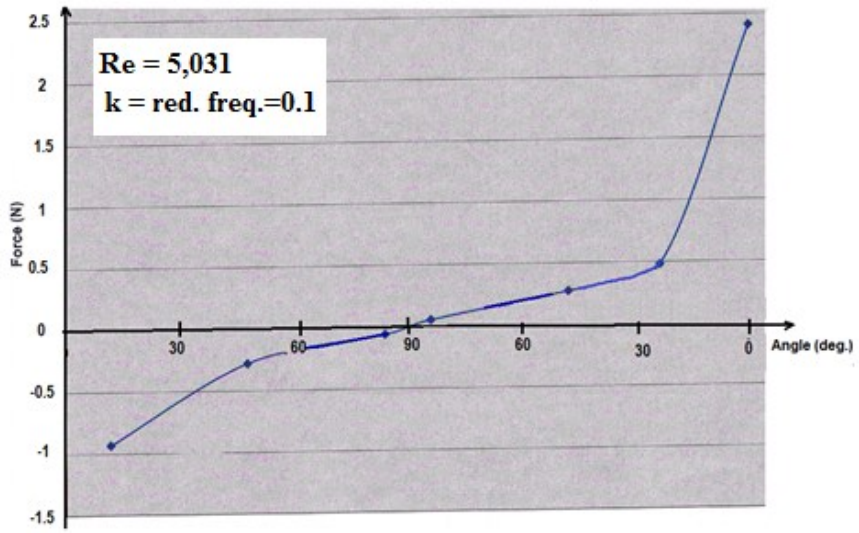

Fig. 4.12 Lift force on the plate over a cycle

4.2.2 Torque applied to the flapping plate

The moment of aerodynamic forces applied to the moving plate represents mainly the moment of pressure forces given by equation (4.14). According to Fig. 4.13, the torque on the moving plate increases with the angular position, similar to the lift, with a maximum value equal to 0.07 N-m. This data will serve as a reference in the design of the mechanism for the experimental investigation of the flow over the rotationally oscillating plate.

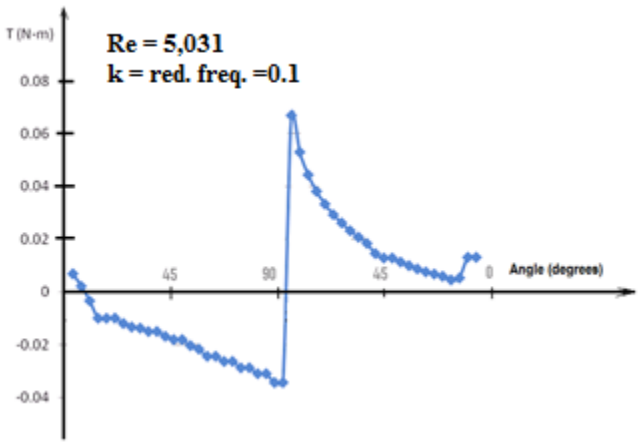

Fig. 4.13 Torque on the plate during the flapping cycle

4.3 Analysis of the flow around flapping plates

4.3.1 2D Simulation of the flow with Fluent 6.3

Due to the complexity of the problem, an initial investigation of the flow around the rotationally oscillating plate in a 2D simulation using ANSYS 13/FLUENT 6.3 is performed over several flapping cycles with the objective of studying the transient variation of the flow and the thermal characteristics over the surface of the plate. This procedure allows a preliminary analysis of the flow field and the distribution of the thermal characteristics over the surface of the plate. The 3D simulation is carried later to examine more details on the local thermal characteristics.

a) 2D Flow field characteristics

The 2D simulation of the flow over the rotationally oscillating heated flat plate is carried out in a flow domain (Fig.4.14) where one of its edges is kept fixed while the device is free to oscillate over an amplitude of 90° angle. Assigning an angular velocity of 2 rad/s to the plate, the simulation is carried out over a total of 9 flapping cycles with a time step size of 0.00058875 seconds. Velocity and pressure contours are plotted in Fig. 4.15 for 3 different angular positions (10°, 30°, and 60°), with the objective to track the variations of the flow characteristics with the stroke angle over a complete cycle.

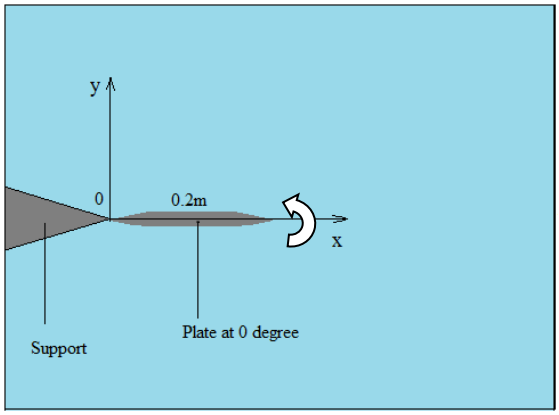

Fig. 4.14 2-Dimensional flow domain

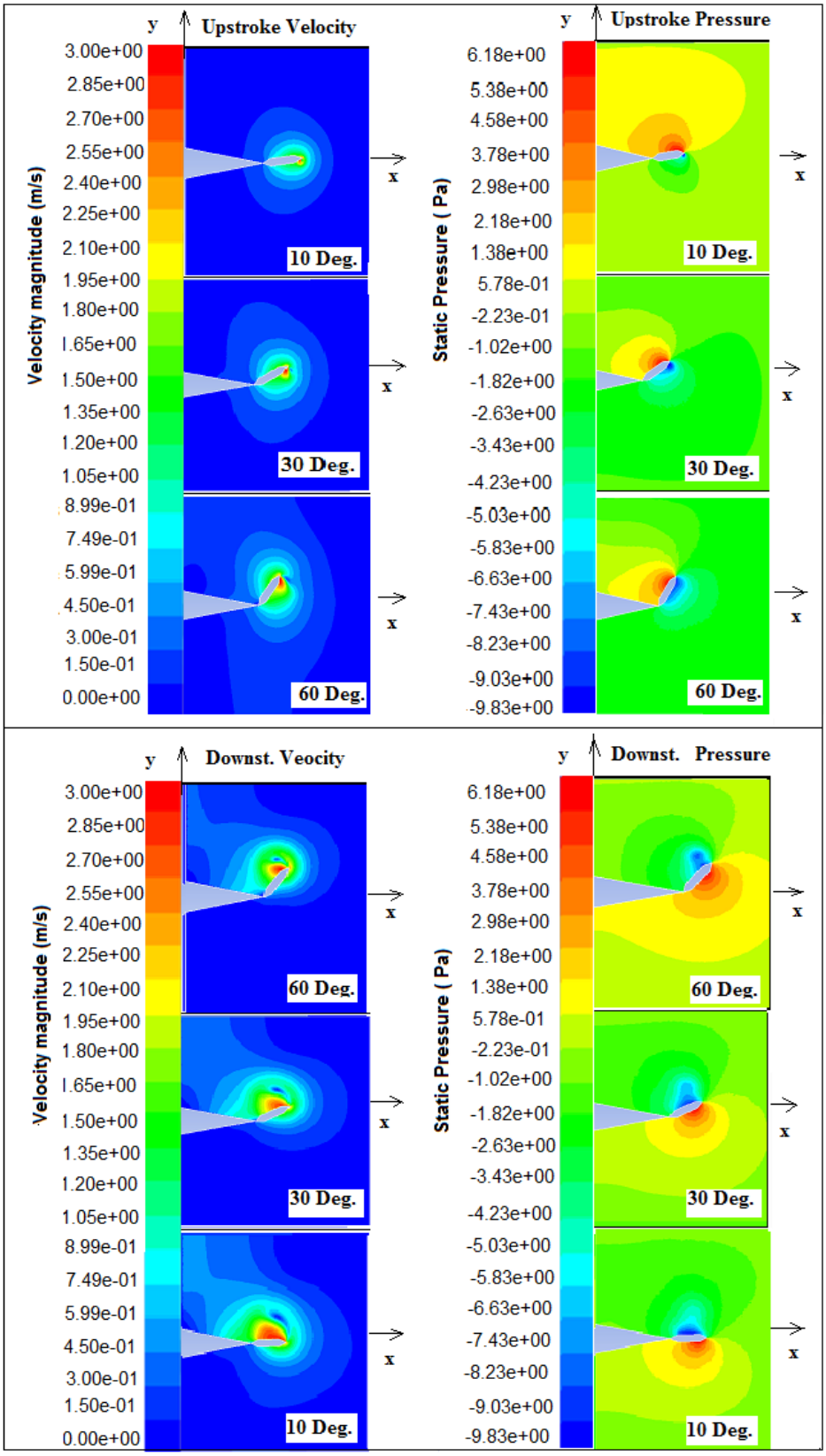

Fig. 4.15 Velocity and pressure contours over a flapping cycle

b) Discussion of 2D fluent results

The nature of the flow around the rotationally oscillating plate depends on the Reynolds number, which is estimated based on the characteristic length of the geometry. Assumption is made that the velocity of the fluid at the tip is taken to be the velocity of the tip of the plate itself subject to solid body rotation. With a boundary condition $q'' = 540 W/m^2$, the surface temperature reading (see Fig. 5.33 in chapter 5) of a thermocouple installed at the tip is 43^oC, giving a film temperature $T_f = 34^oC$. This result is used to determine properties for the calculation of the Reynolds number at the tip of the plate (4.15).

$$Re = \frac{V_{tip} \times r}{\nu} \tag{4.15}$$

$$Re = \frac{0.4 \times 0.2}{16.485 \times 10^{-6}} = 4{,}852.9$$

Where

Re = Reynolds number of fluid at the tip of the plate.

ν = kinematics viscosity of air at the film temperature $= 16.485 \times 10^{-6} m^2/s$

r_{tip} = plate radius = 0. 2m

V_{tip} = tip velocity of moving plate = $V_{tip} = \omega \times r_{tip} = 0.4 m/s$

Here, the contours of flow characteristics at 10° angle in Fig. 4.15 indicate a fluid velocity equal to 2.64 m/s at the tip of the plate, which is different from the velocity due to rigid body motion. Therefore a reasonable approximation of the Reynolds number is reevaluated using the fluid velocity (U_{tip}) at the tip of the plate given by equation (4.16). The computed Reynolds number indicates that the flow is laminar.

$$Re = \frac{U_{tip} \times r_{tip}}{\nu} \tag{4.16}$$

$$Re = \frac{2.64 \times 0.2}{16.485 \times 10^{-6}} = 32{,}029$$

Also, considering the flow field around the moving plate, Bernoulli's equation can be written along the stream-line just above the plate's upper surface [8]:

$$\frac{\partial \phi}{\partial t} + \frac{1}{2}u^2 + \frac{p}{\rho} = \text{const.} \tag{4.17}$$

Where

ϕ = flow potential
u = local velocity, m/s
ρ = density, kg/m^3
p = pressure of the fluid, Pa

Fixing the time in equation (4.17), pressure and velocity vary in opposite directions. The flow around the rotationally oscillating plate is characterized by high pressure zones in the front and a wake in the back as illustrated in Fig. 4.15. During the motion of the plate, the opposing drag force creates an induced flow over the surface around the tip while fluid particles are attracted by the wake behind the plate. Such a negative pressure leads to the separation of the boundary layer on its surface, as particles make a sharp turn around the tip, along circular concentric path lines as shown in Fig. 4.16. At the beginning of the stroke, which corresponds to the acceleration phase of the plate, the diameter of the vortex grows progressively and reaches a critical size prior to its shedding from the surface. As the size of the vortex increases in the back, the boundary layer in the front face of the plate is subject to shearing viscous forces by accelerated fluid particles. The vortex interacts tangentially, decreasing the thickness of the boundary layer with the spinning fluid involved. In reality, fluid streams from both front and back faces merge and form the tip vortex in the back of the plate. According to previous work, the shedding of the tip vortex participates in the generation of lift force [54]. 2 D computational results in Fig. 4.15 indicate that the tip velocity of the accelerated fluid involved in the vortex decreases with the stroke angle until the plate comes to a complete stop where the velocity magnitude jumps to a

peak value at stroke reversal. Such a high velocity will participate significantly in the enhancement of the heat transfer rate at that location.

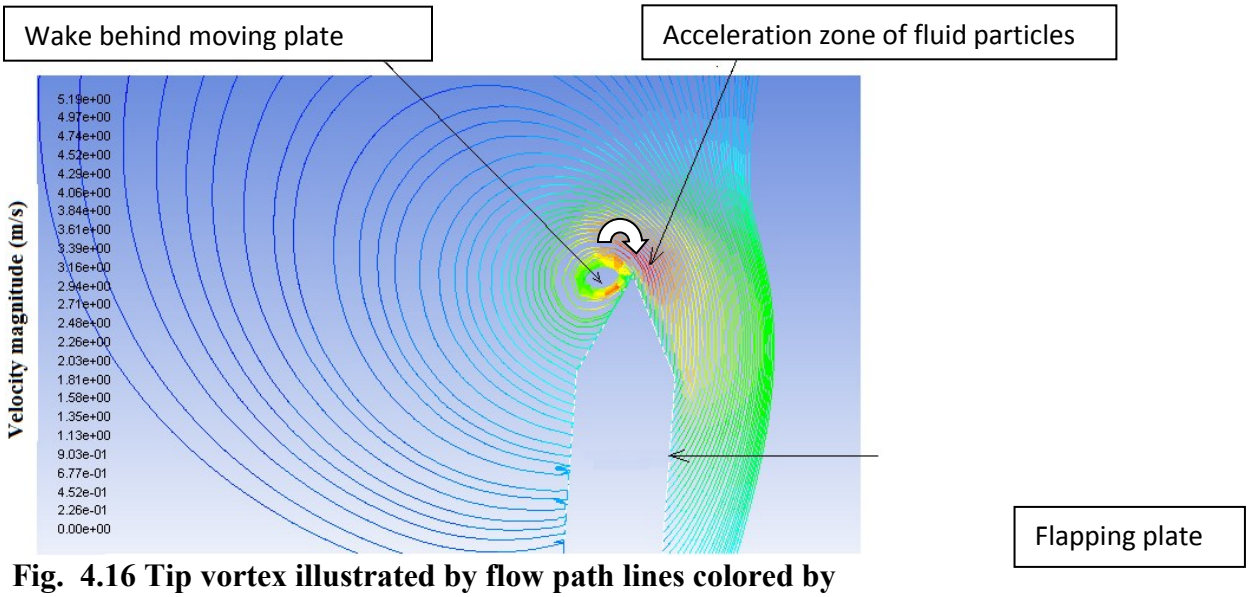

Fig. 4.16 Tip vortex illustrated by flow path lines colored by velocity magnitude for a plate's angular position of 90° angle

Conclusion

The 2D simulation of the flow around oscillating plates provides preliminary information on the flow domain. The static pressure reaches peak values in the front of the moving plate forcing particles under the opposing drag to flow over the surface towards the wake in the back. A tip vortex, similar to a ring, is visualized around the edges of the plate, evidenced by the flow path lines colored by the velocity magnitude in one plane only. However, the current investigation does not show the distribution of the flow and thermal characteristics over the whole surface of the plate. Therefore, a 3D analysis seems to be a more realistic approach of the investigation of the flow over the rotationally oscillating heated plate.

4.3.2 3D Simulation of the flow with Fluent 6.3

a) Analysis of the 3D static pressure on the plate

During the flapping cycle, of interest is the determination of the local pressure distribution around the plate. The static pressure can be measured with an instrument moving with the flow [54]. The upstroke static pressure contours (Fig. 4.17) exhibit a symmetrical distribution about the y axis. The highest value observed at the center of the plate characterizes the stagnation pressure on the surface because at that location the velocity of the flowing fluid decreases to zero. Rear face pressure curves are plotted for 5 different values of z in Fig. 4.18: z = 0 (center of the plate); $z = \frac{1}{4}L$; $z = \frac{1}{2}L$; $z = \frac{3}{4}L$; z =L (edge of the plate). The pressure decreases from the middle of the plate (1.31 Pa) towards the edges (-6.31 Pa) in the z direction but also from the base to the tip. The low pressure at the edges creates a wake behind the plate, confirming the results obtained in the 2D simulation.

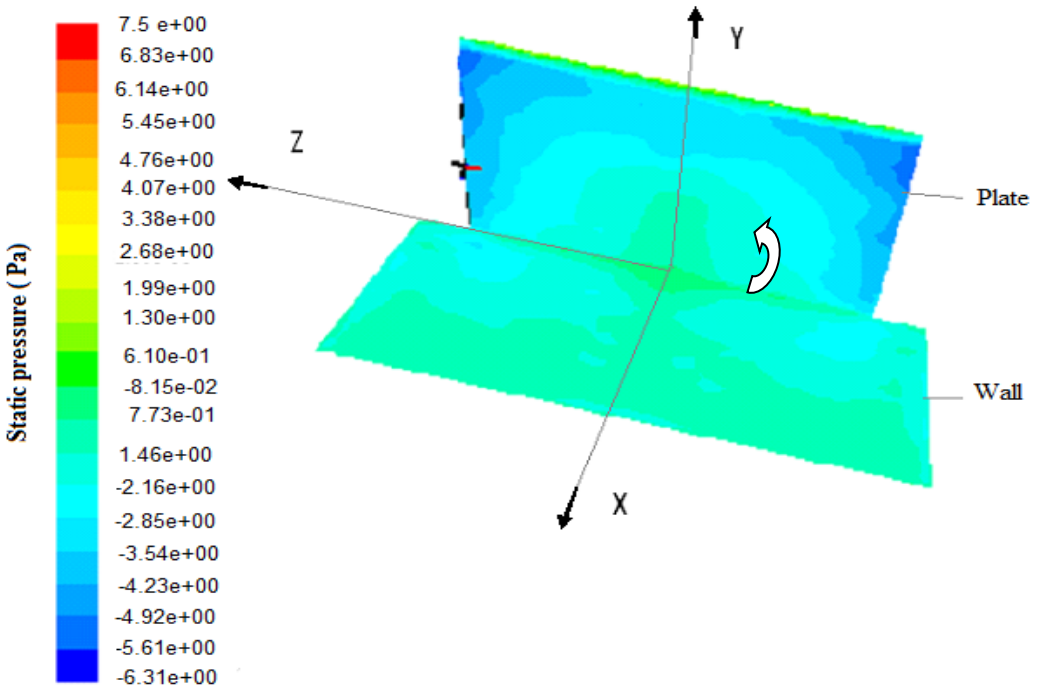

Fig. 4.17 Upstroke static pressure distribution at an intermediate stroke angle

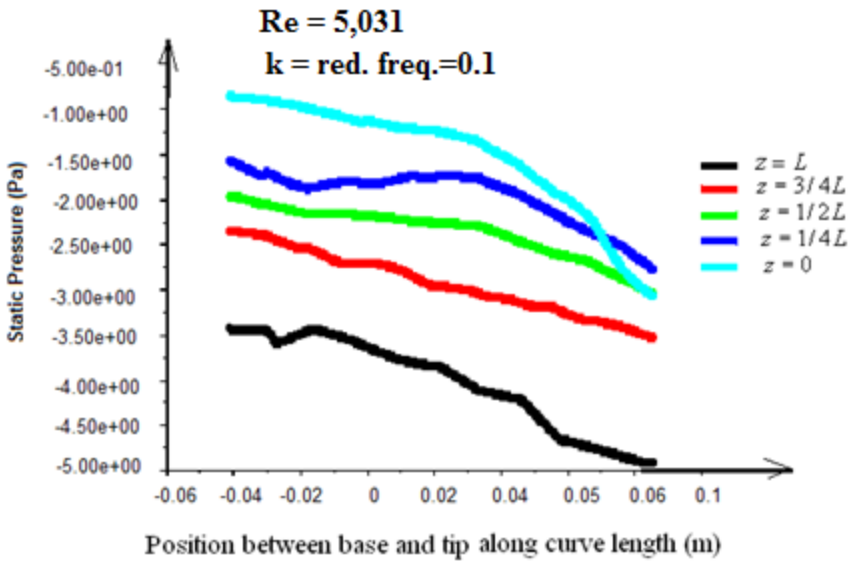

Fig. 4.18 Bottom face upstroke pressure distribution at a 50°angle

The end of the upstroke (90° angle) in Figs. 4.19 and 4.20 shows a pressure distribution similar to the contours at 50° angle. However, the stagnation pressure was relocated towards the tip of the plate and its value increased from 1.31 to 82.1 Pa. Again, the lowest pressure is measured at the edges as shown in Fig. 4.19, due to the shedding of vortices at these locations, according to flow path lines already observed in Fig. 4.16.

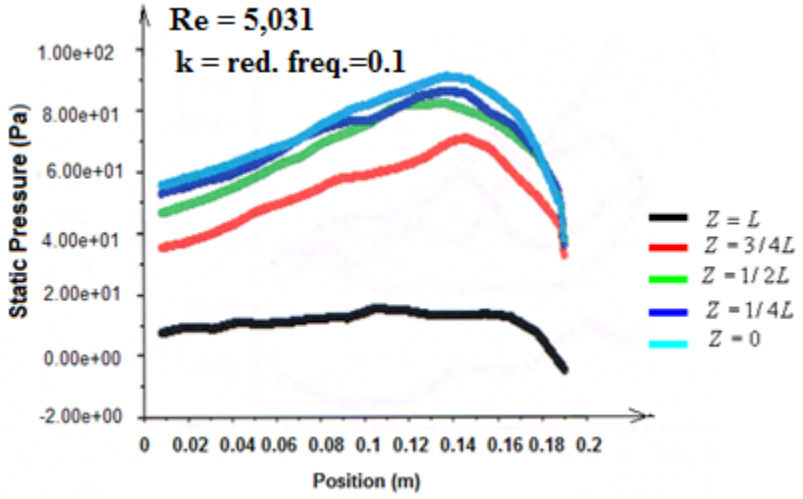

Fig. 4.19 Back face pressure from the base to the tip at 90° angle

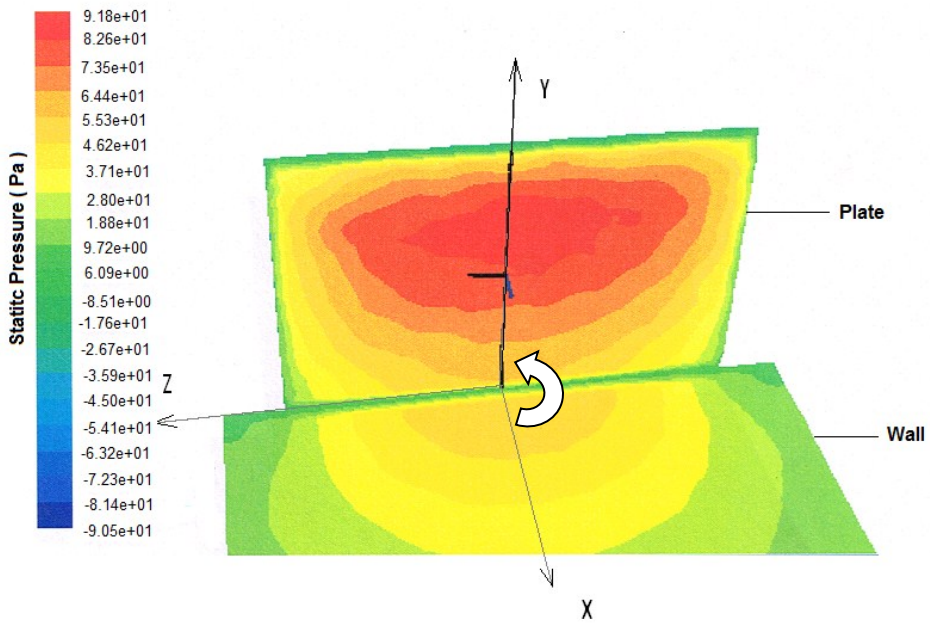

Fig. 4.20 Pressure contour at 90° angle

b) Analysis of the 3D velocity field

The starting of the upstroke induces a flow field characterized by velocity vectors around the tip of the plate (Fig. 4.21) with fluid particles rotating from higher to lower pressure regions. Far away, the velocity of fluid particles is equal to zero, since the moving plate is the only mechanism generating the flow field. Patterns with circular streamlines are visible around the edges, similar to the 2D results (Figs. 4.21 through 4.26). One can visualize the highest magnitude of the velocity at the tip regardless of the angular position or the direction of rotation of the plate. The magnitude of the velocity drops from 3.67 m/s at the start of the upstroke to 2.64 m/s when the plate reaches a 45° angle, before the deceleration phase that occurs at the end of the stroke. The increase in the magnitude of the velocity at end strokes indicates that acceleration and deceleration are the main mechanisms that trigger the shedding of the vortex from the tip of the plate. Path lines in Fig. 4.26 show a symmetrical distribution of the flow about the median plane of the plate, normal to the axis of rotation. The same figure reveals the

3dimensional characteristic of the flow, which leads to the formation of a vorticity tube around the free edges. The behavior of the flow around the moving plate plays a significant role in the distribution of the local surface temperature discussed in the following paragraph.

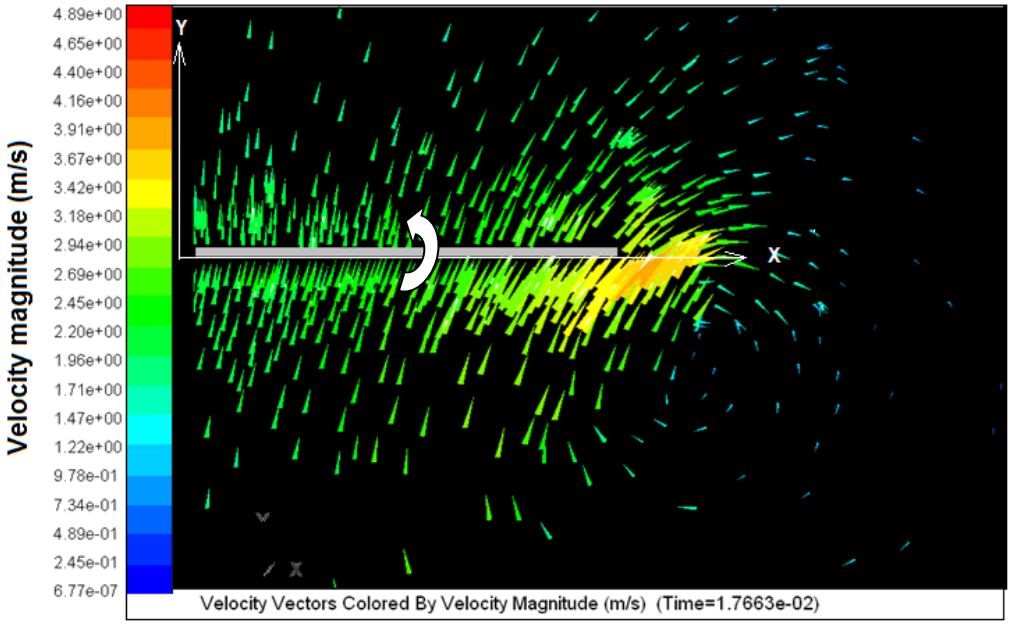

Fig. 4.21 beginning upstroke velocity vectors

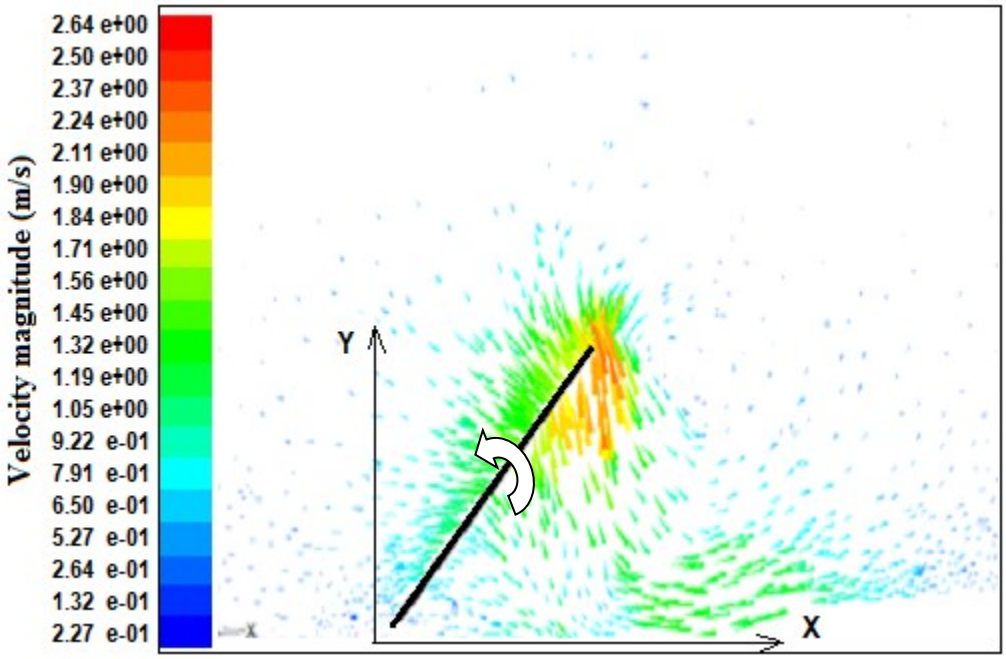

Fig. 4.22 Upstroke Velocity vectors at 45° angle

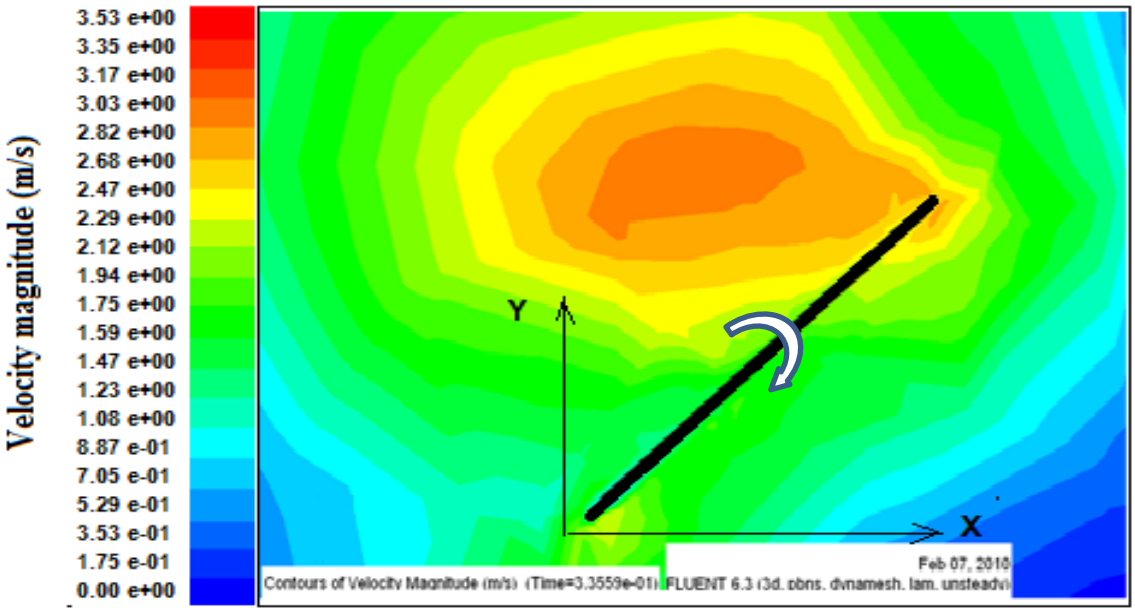

Fig. 4.23 Downstroke velocity countour at 45° angle

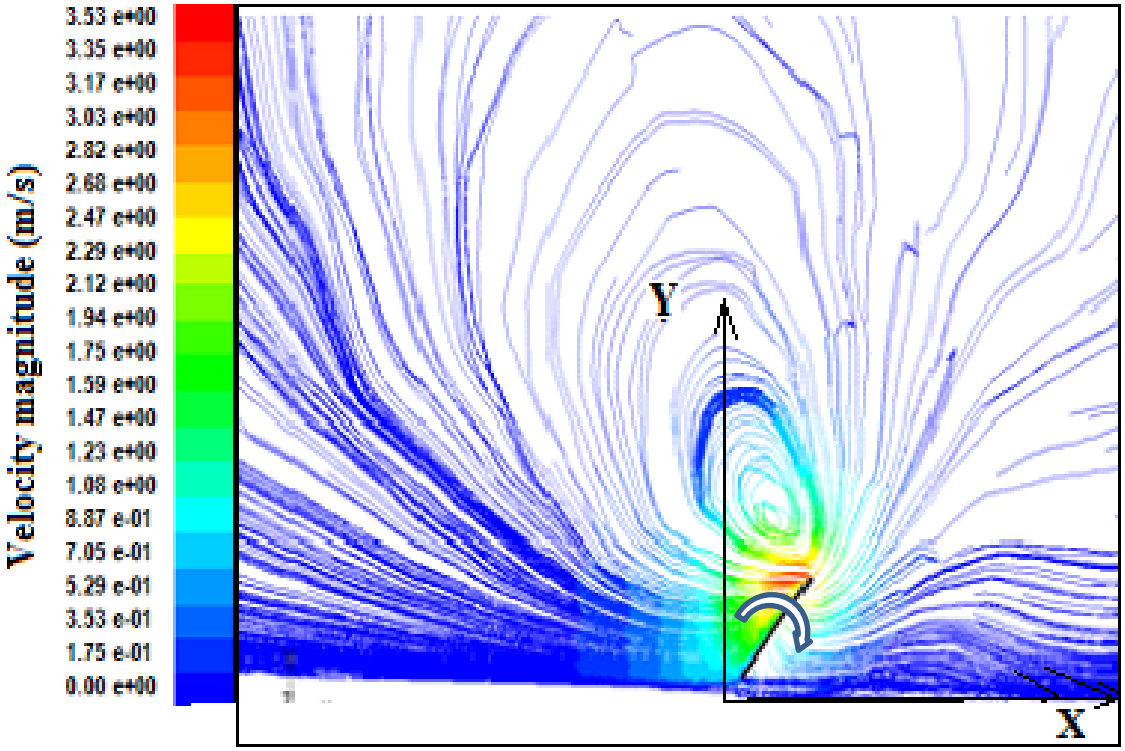

Fig. 4.24 Downstroke velocity pathlines at 45° angle

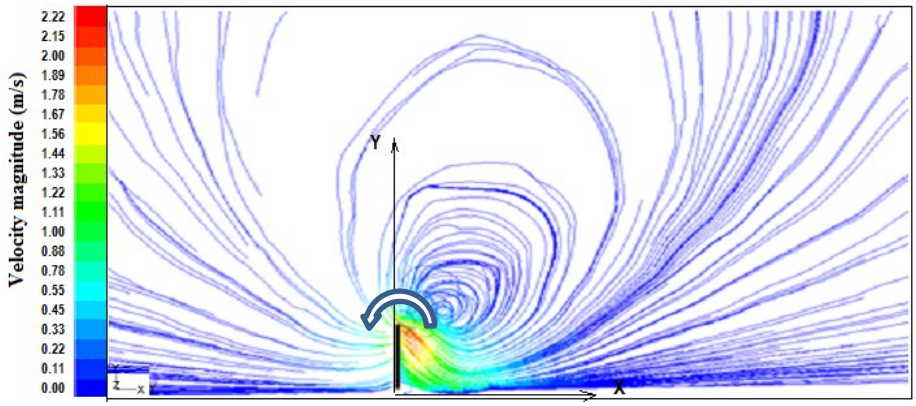

Fig. 4.25 Side view flow pathlines colored by velocity magnitude at 90° angle

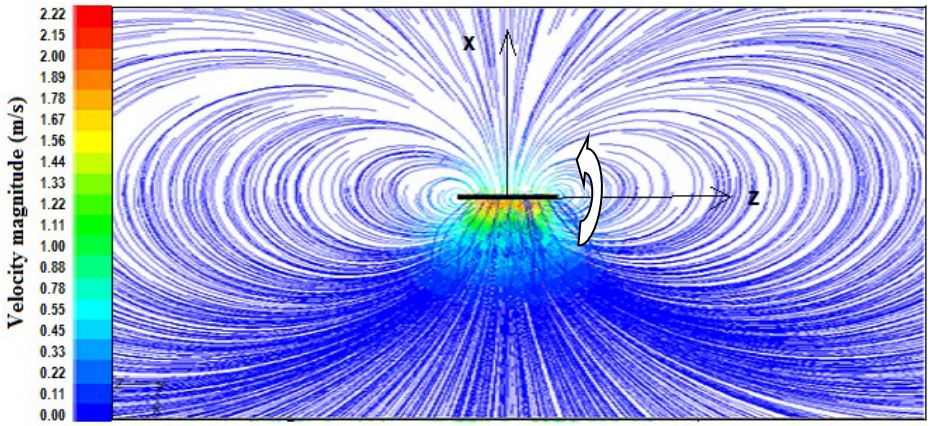

Fig. 4.26 Top view path lines colored by velocity magnitude at 90° angle

4.4 Thermal characteristics induced by rotationally oscillating heated plates

The computational investigation of the flow field around rotationally oscillating plates provides important information on the distribution of flow characteristics, which will be used in the analysis of the temperature distribution over the moving surface, heated at constant flux. The software package FLUENT 6.3 is used to monitor thermal characteristics at desired locations on the surface of the moving plate over several cycles.

4.4.1 2-Dimensional analysis of thermal characteristics over a flapping plate

Point segments are created by splitting the face, which is a segment for a 2D simulation, during the generation of the geometry of the flow domain. Three points—P1 (center), P3 (tip), P5

(base)—separated by a distance of 0.095 m as shown in Fig. 4.27 allow the tracking of the surface temperature over several cycles for a given heat flux. These tiny segments of length equal to 0.0025m are created large enough to include at least 2 node-points in 2D simulations. 2D Fluent results indicate a direct correlation, which is noticeable between the velocity magnitude represented by the first and the fifth cycles and the associated heat transfer coefficient in Fig. 4.28. A peak value of the heat transfer coefficient ($27\ W/m^2-K$), observed at the tip during the 1st cycle matches the highest velocity magnitude (4.1 m/s) at the tip of the plate, recorded at stroke reversal. For a heat flux $q"=540 W/m^2$ applied to the plate's surface, Fig. 4.29 provides the local temperature distribution at P1, P3, and P5 for 9 flapping cycles where surface temperature increases through a transient periodic phase followed by steady periodic oscillations. However, the highest temperature is recorded at the base (P5) and the lowest at the tip (P3) where the flow is detached from the surface of the plate at end strokes.

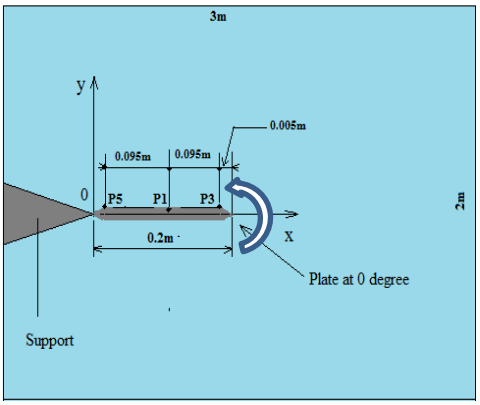

Fig. 4.27 Location of 2D point- segments and heat on the plate's surface

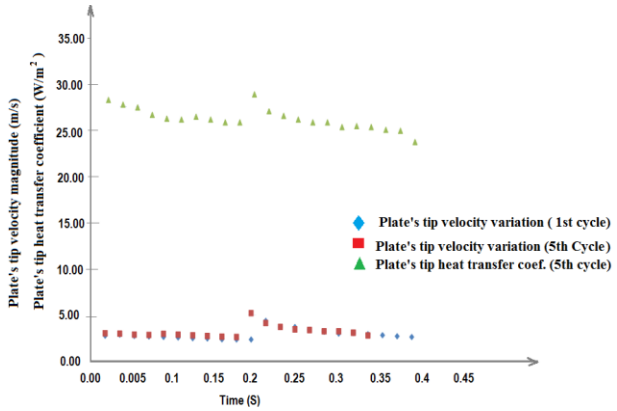

Fig. 4.28 Correlation between tip velocity transfer coefficient variations for 1st and 5th cycles

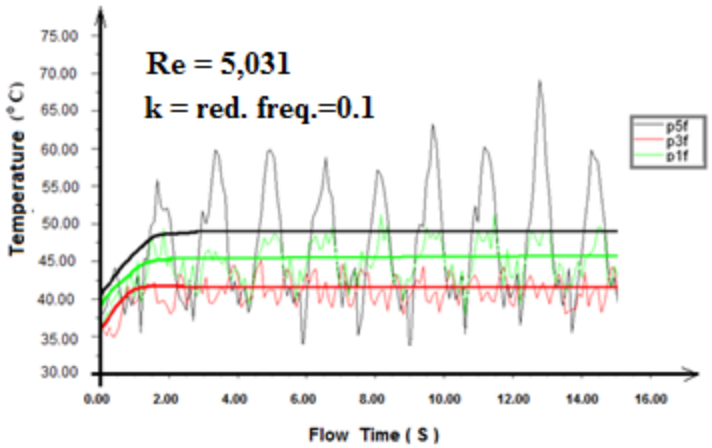

Fig. 4.29 2D transient temperature profiles along the front face for a simulation of 9 flapping cylces at a rate of 2rad/s

4.4.2 3D Thermal characteristics over a flapping plate.

The 3D simulation of the flow around rotationally oscillating heated plates with FLUENT provides the thermal characteristics at chosen locations on the surface. The triangular mesh required to solve this fluid dynamic problem utilizes tetrahedral elements, each represented by 3 node-points that fit in a small disc of radius 0.005m. Averaging the characteristics of the 3 node-points allows plotting the thermal characteristics at different locations on the plate's surface. Here, six distinct tetrahedral elements (P1, P2, P3, P4, P5, and P6) enable to collect time-dependent characteristics over several cycles.

a) Surface temperature contours and profiles

In this example, a surface heat flux of 540 W/m^2 is considered during the 3D simulation of the flow over the rotating plate at 8 rad/s. From the observation in Fig. 4.30, higher temperature values at point surfaces P5, P1, P2, and P4 are concentrated between the base and the center of the plate, while lower values are recorded at free edges at P3 and P6. Temperature contours and plots obtained over 3 consecutive time steps in Figs. 4.30 through 4.32 exhibit a gradual

expansion of the cooler area, from free edges toward the center of the plate. In these figures, the local temperature distribution is symmetrical about the median plane of the plate in the x direction. This information is confirmed via data recorded by P2 and P4, regardless of the applied heat flux and the angular position. Furthermore, one can notice that the local temperature decreases with increasing distance from the center toward the free edges of the plate.

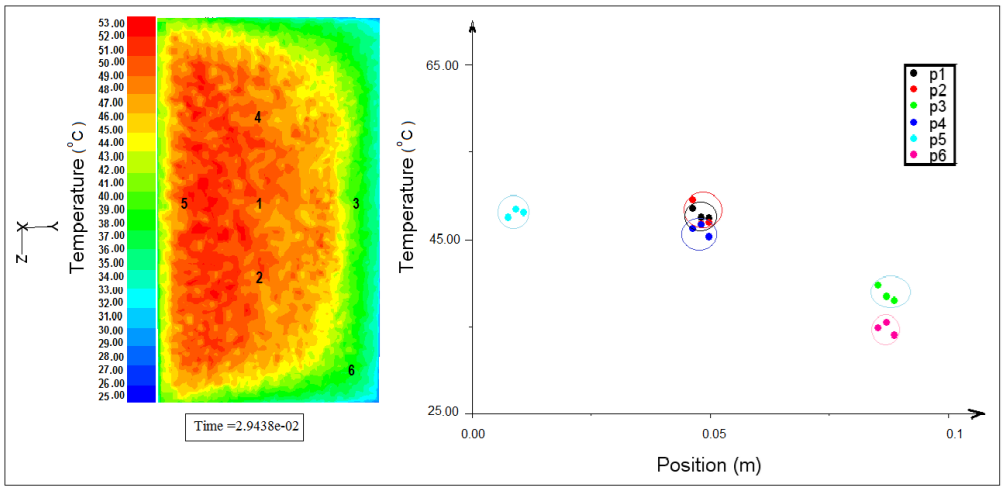

Fig. 4.30 Local surface temperature along x for heat flux 540W/m ^{2}. Time step 1

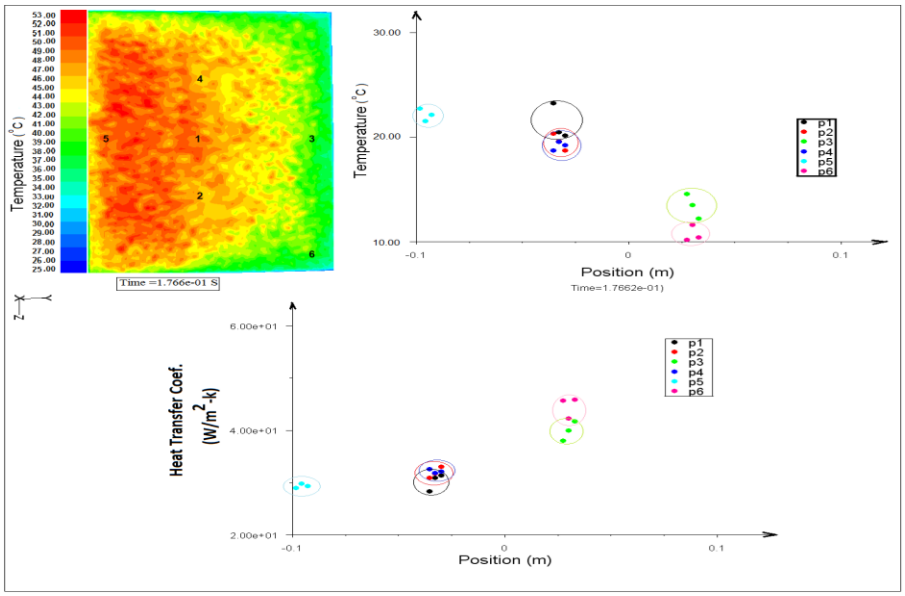

Fig. 4.31 Local surface temperature along x for heat flux 540W/m ^{2}. Time step 2

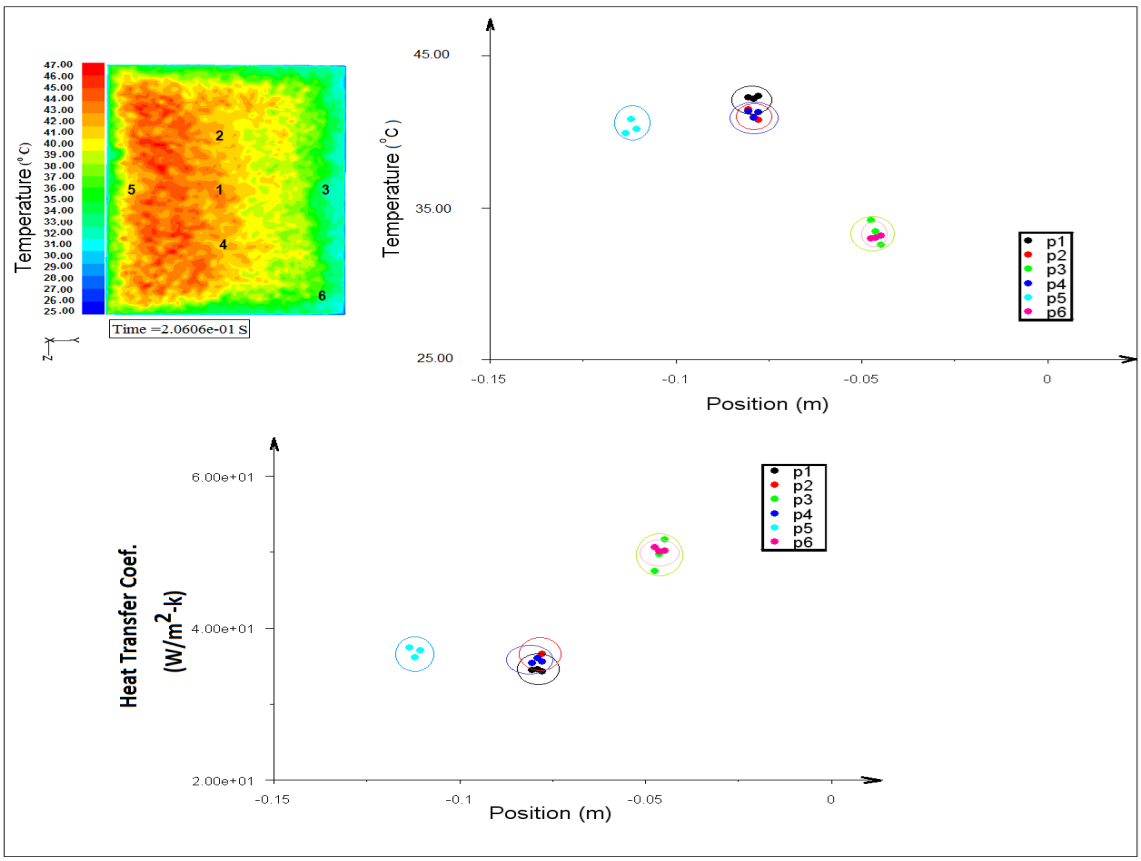

Fig. 4.32 Local surface temperature along x for heat flux 540W/m^2 at stroke reversal

The simulation of the flow over the oscillating plate is repeated at a lower speed equal to 2 rad/s with the same applied heat flux of 540 W/m^2. In this case, temperature contours of both front and back faces are displayed and compared over 4 consecutive angles within the cycle: 30°, 45°, 55°, and 65° (Fig. 4.33). The surface temperature always decreases from the center to free edges of the plate, along normal or parallel lines to the axis of rotation. Contours in Fig. 4.33 indicate that the local temperature distribution over the surface is a function of the angular position of the plate. Moreover, the gradient between two distinct vertices chosen in the vicinity of the center of the plate is close to zero. Nevertheless, the gradient increases significantly when the test points are closer to the free edges of the plate. A comparative analysis between both faces of the plate,

displayed in Fig. 4.34 shows that the peak temperature is always observed on the back face regardless of the angular position of the moving device. Also, it is observed that the total area occupied by the low temperature zones is larger in the front compared to the back face. This result is predictable due to the presence of the drag force in the front, shearing fluid particles as they flow around the tip to the rear of the plate.

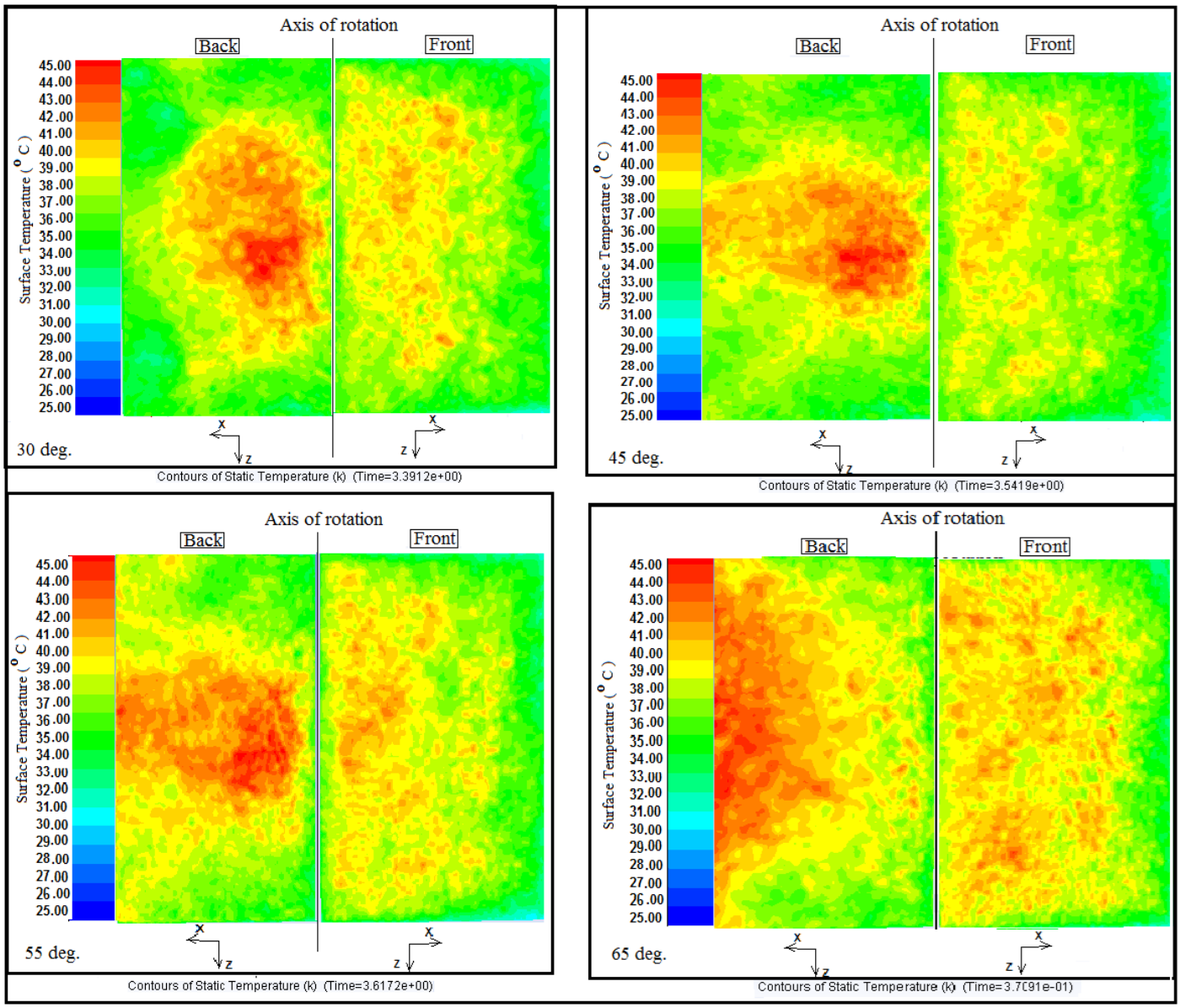

Fig. 4.33 Upstroke temperature contours of front and back faces at 30°, 45°, 55°, 65° angles

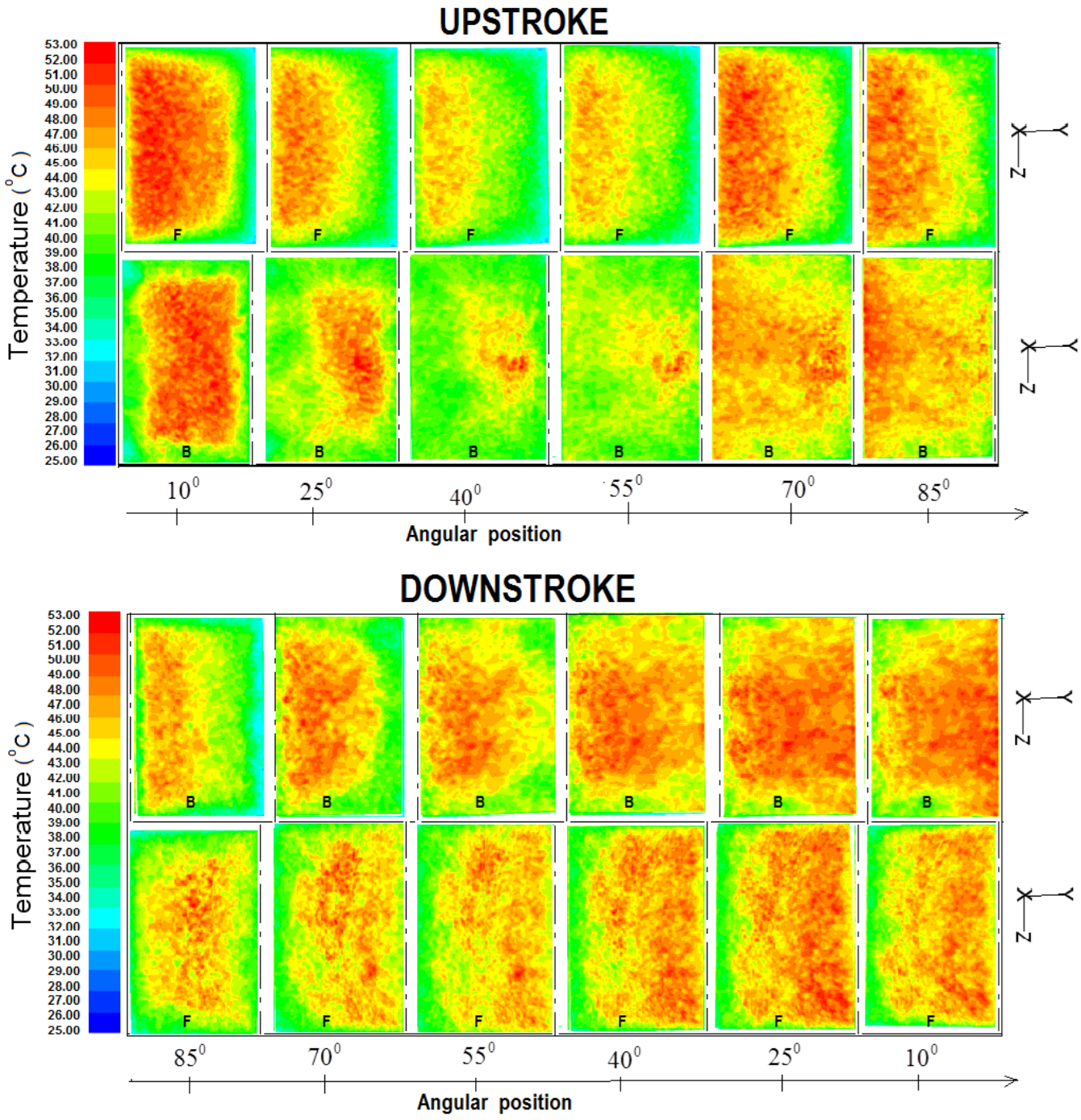

Fig. 4. 34 Temperature contours of front and back faces of the plate over a complete flapping cycle for a heat flux of 540W/m ^{2}

b)Analysis of temperature distribution with lines Line rakes

A heat flux of 540 W/m^2 is applied to the surface of the plate during two simulations performed over several flapping cycles at two different rates of 2 rad/s and 8 rad/s. Local surface temperature are plotted along 2 parallel lines in two orthoghonal directions as illustrated in Fig. 4.35.

According to FLUENT results (Figs. 4.36 through 4.40), surface temperature curves along constant x behave like parabolas with their vertices located in the median plane of the plate in the x-direction. Moreover, profiles along constant z lines are described by parabola branches with their concavities increasing from the center of the plate's surface toward the free edges. Similar observations are made for heat transfer coefficients curves where the concavity of the parabolas are oriented instead in the positive y-direction. Also, in the x-direction, the surface temperature over the plate is described by half parabolas centered on the z-axis. Comparing vorticity profiles (Figs.4.41 and 4.42) with line rakes and singular temperature plots results, it is observed a direct correlation between thermal data and flow field characteristics: peak vorticity magnitudes are noticed at free edges where the heat transfer rate is predominant from the plate's surface.

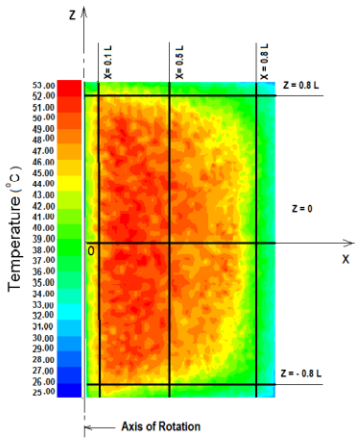

Fig. 4.35 Reference lines for the analysis of thermal

characteristics over the surface of the plate

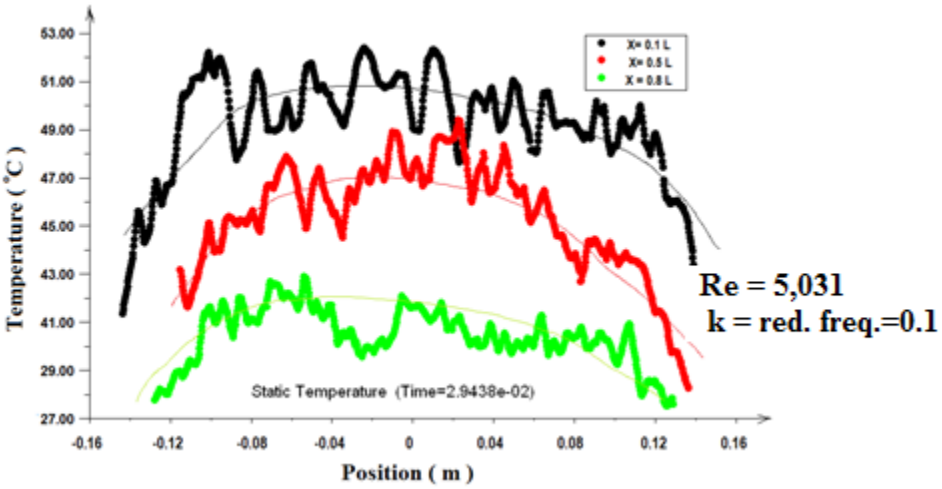

Fig. 4.36 Surface temperature distribution along z-axis for a flapping rate of 2 rad/s and a heat flux of 540W/m ^{2}

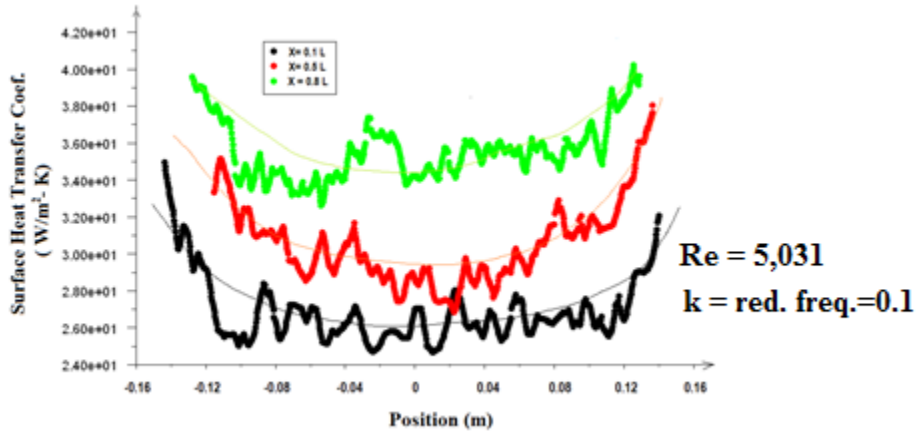

Fig. 4.37 Local surface heat transfer coefficient distribution along z-axis for a flapping rate of 2 rad/s and a heat flux of 540W/m ^{2}

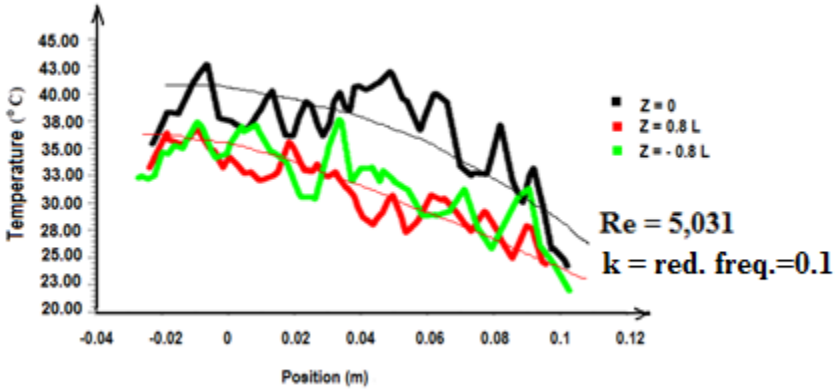

Fig. 4.38 Surface temperature profile along x-axis for a flapping

rate of 2rad/s and a heat flux of 540W/m ^{2}

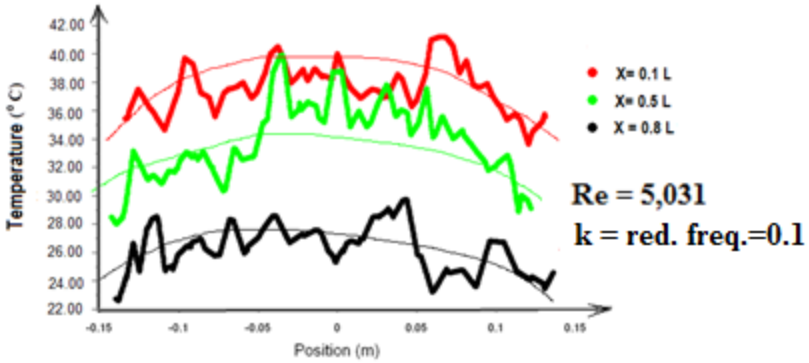

Fig. 4.39 Surface temperature profiles along z-axis for a flapping rate oft 2rad/s and heat flux of 540W/m ^{2}

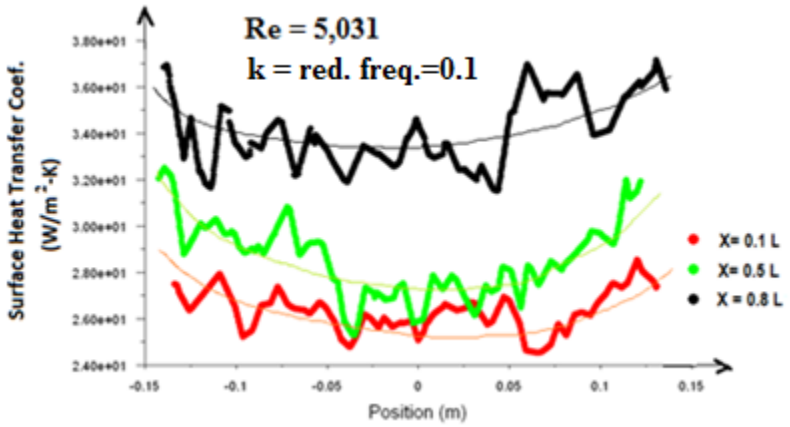

Fig. 4.40 Local surface heat transfer coefficient profiles along z-axis for a flapping rate of 2rad/s and a heat flux of 540W/m ^{2}

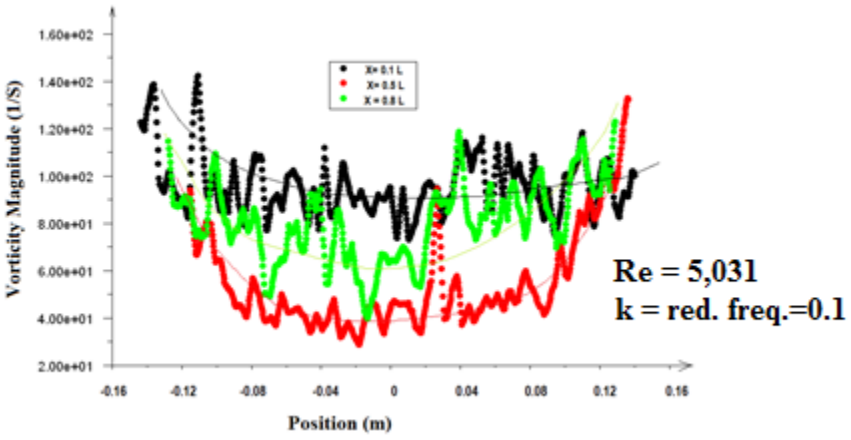

Fig. 4.41 Vorticity distribution over the plate's surface along z-axis for a flapping rate of 8rad/s and a heat flux of 540W/m ^{2}

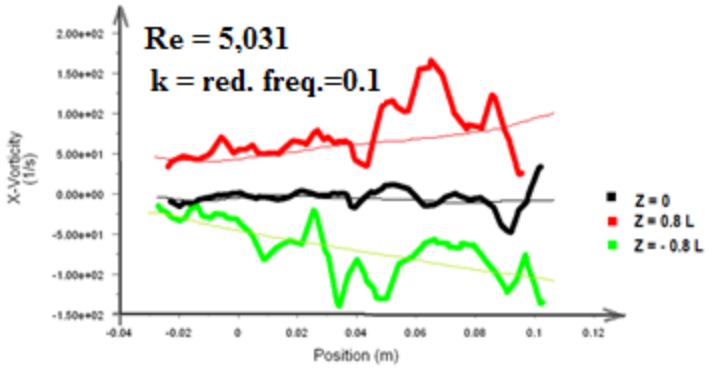

Fig. 4.42 Vorticity distribution over the plate's surface along x-axis for a flapping rate of 2rad/S and a heat flux of 540W/m ^{2}

In conclusion, for a given angular position, the surface temperature distribution over a flat rectangular plate, heated at constant heat flux q" subject to rotational oscillations at a frequency ω, behaves like branches of parabola along constant x and z lines, with decreasing temperature from the center to the the plate's edges as shown in Figs. 4.43 and 4.44. The same behavior is observed for the heat transfer coefficient profiles oriented in the opposite direction of temperature profiles.

The local heat transfer coefficient over the plate can be derived from Newton's law of cooling in equation (4.18).

$$h = \frac{q''}{T_s - T_\infty} \tag{4.18}$$

Where

$q'' =$ heat flux applied to the plate surface, w/m^2

$T_s =$ plate surface temperature, ^oC

$T_\infty =$ ambient temperature, ^oC

$h =$ local heat transfer coefficient, $w/m^2 - K$

Equation (4.18) can be rewritten as:

$$q'' = h \times \Delta T \tag{4.19}$$

where ΔT is the temperature above ambient.

In this problem, the flux is kept constant during the rotation of the plate. According to equation (4.19), the heat transfer coefficient and the surface temperature fluctuate in opposite directions at a given ambient temperature, which confirms the distribution of thermal characteristics profiles discussed earlier in this paragraph. Due to their symetrical distribution about the plane of equaiton z = 0, thermal characteristics over the surface of the plate can be represented by a familly of curves summarized in Fig. 4.45

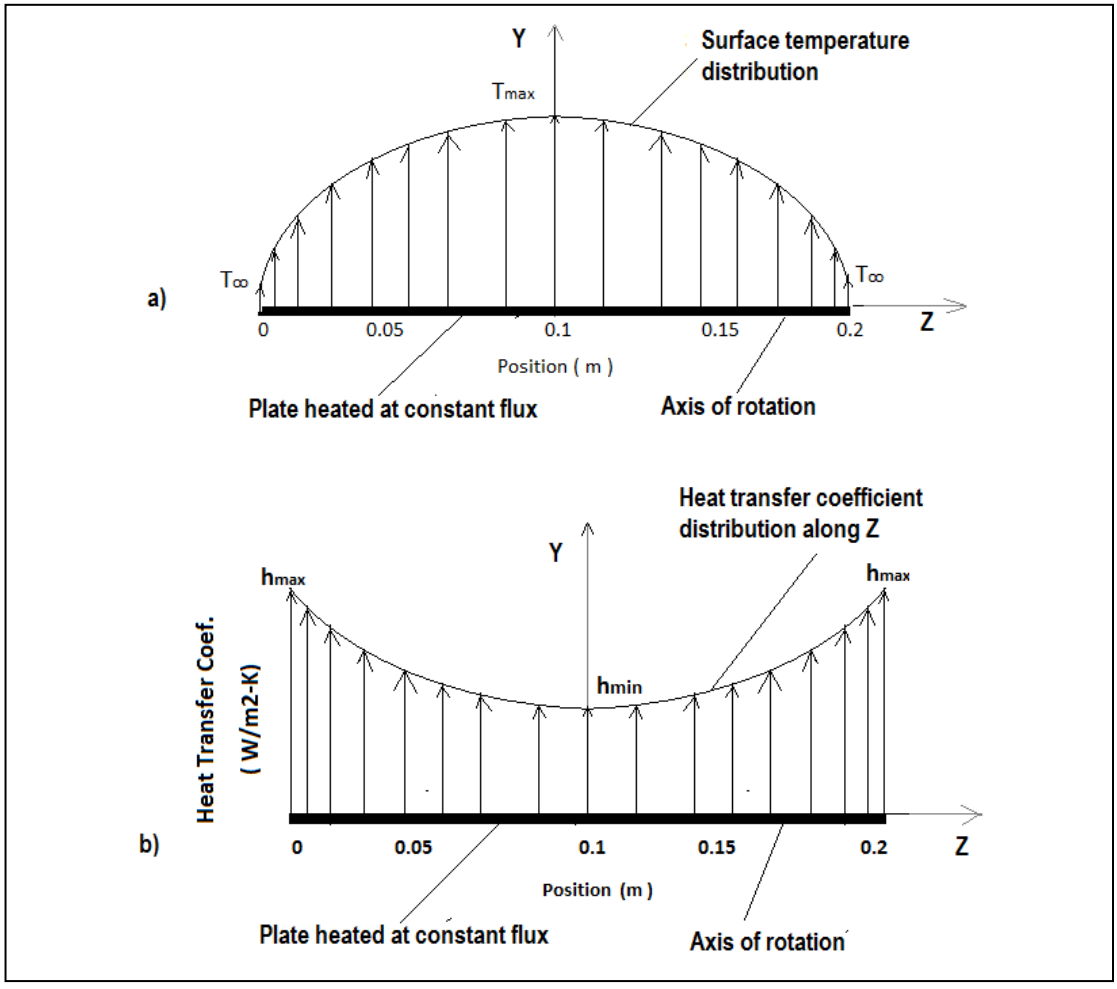

Fig. 4.43 Sectional view of thermal characteristics along z over a rotating heated plate: a) Temperature, b) Heat transfert coefficient

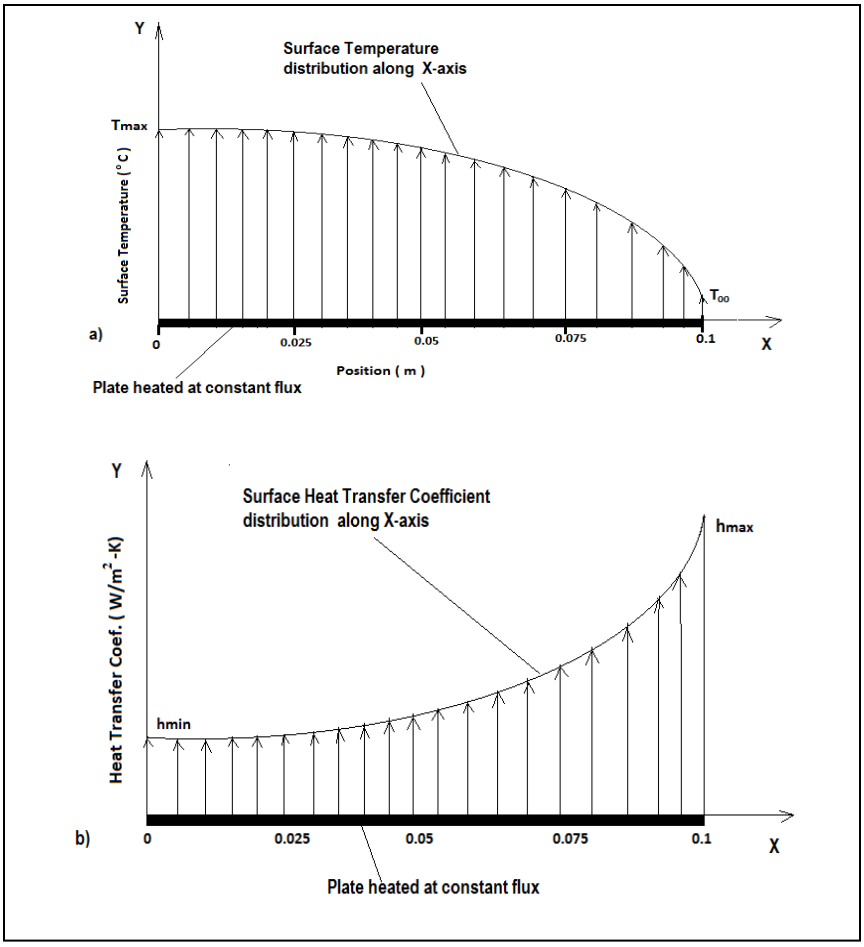

Fig. 4.44 Sectional view of thermal characteristics along x over a flapping flat heated plate : a) Temperature field, b) Heat transfert coefficient

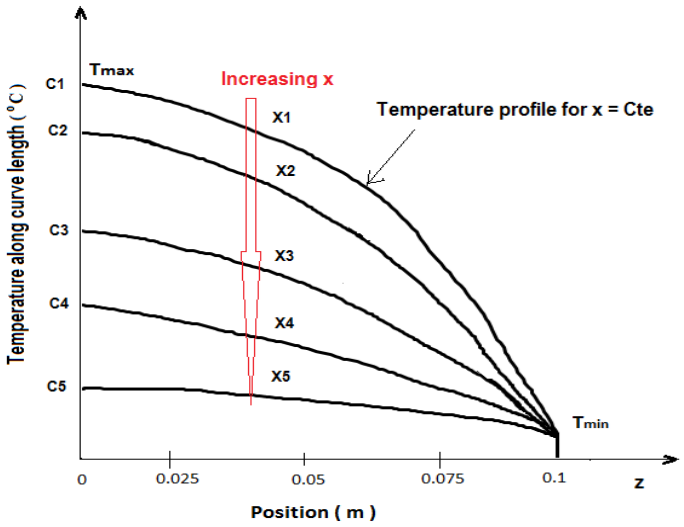

Fig. 4.45 Temperature distribution along surface from plate's center

c) Analysis of transient temperature profiles

Thermal analysis of a complete flapping cycle

In this paragraph, thermal characteristics are tracked at specific locations on the surface of the moving heated plate during the simulation of several cycles. A flapping frequency of 2 rad/s is assigned to the plate for the simulation of 2 cases with the respective applied heat fluxes:

250W/m^2 and 540W/m^2.

The surface temperature is recorded at 5 different locations on the plate, already defined in previous figures: at the base (P5), at the tip(P3), in the center (P1), in the corner (P6) and at 2 other points (P2, P4) positioned on a parallel line to the axis of rotation.

Starting with a flux of $250\text{W}/\text{m}^2$, the tracking of thermal characteristics over a complete flapping cycle shows 5 important phases in the variation of the local surface temperature. At the beginning, the temperature increases at all locations with different slopes depending on the tracking point, for a duration of T/3 where T is the flapping period. The end of the upstroke is marked by a deceleration phase, corresponding to duration of T/6, until the plate comes to a complete stop at 90° angle. The deceleration period is evidenced by a decrease in the slope of the curves, with a nearly constant temperature value over a very short period of time. At the deceleration phase, temperature curves start to flatten at all locations except for the tip temperature profile (P3), where a negative slope matches with the beginning of the shedding of vortices explained in Paragraph 4.4.2.2. The sudden stopping of the plate is followed by the stroke reversal that occurs over a very short period of time (T/10) where the average temperature drop can be estimated to 3° C. This phase marks the beginning of the down stroke motion, which is critical in the flapping cycle of the plate. It is the time when the maximum vortex shedding

occurs, removing a significant amount of heat from the surface. The plate's surface temperature restarts to grow, similar to the upstroke motion, until the end of the cycle. At the completion of the downstroke motion, one can notice again a deceleration phase, marked by a decreasing slope of the temperature curves as the plate prepares to stop. The simulation is repeated at the same frequency of rotation of 2rad/s with a heat flux of 540 W/m^2.

Conclusions from previous paragraphs about the local temperature distributions are confirmed by current results: information from P4 and P2 (Figs. 4.46 and 4.47) indicate a symetrical temperature distribution about the plate's median plane of equation z = 0.

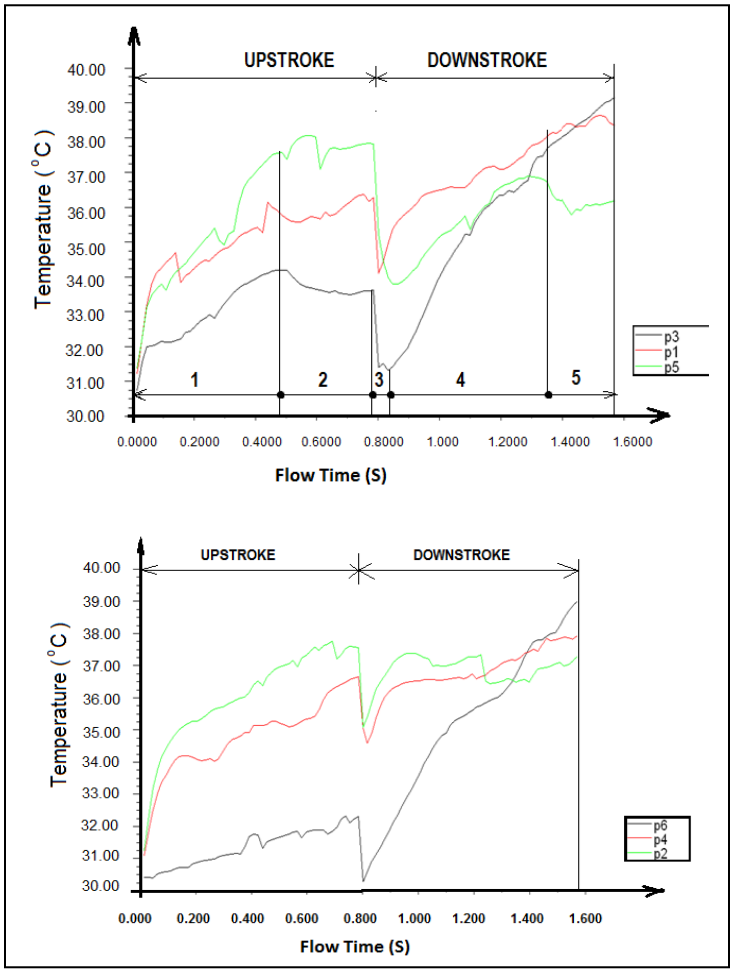

Fig. 4.46 Transient local surface temperature over 1 flapping cycle at 2 rad/s for a heat flux of 250W/m^2

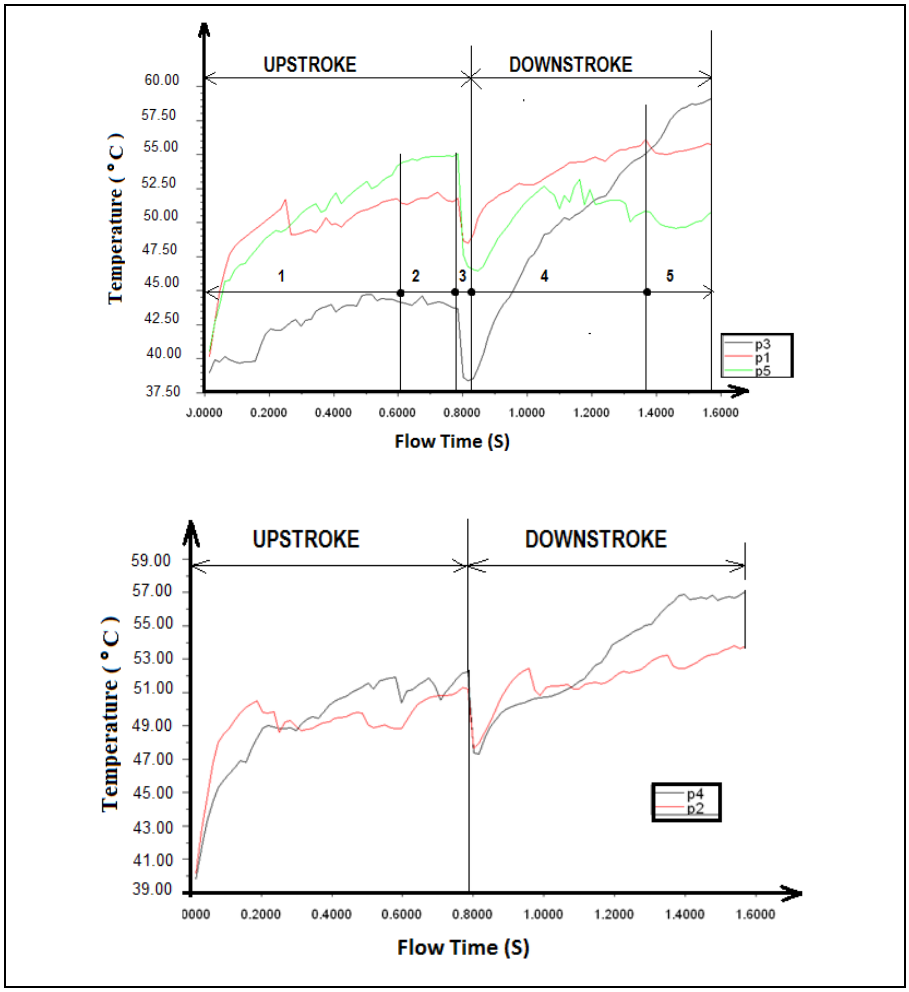

Fig. 4.47 Transient local surface temperature over 1 flapping cycle at 2 rad/s for a heat flux of 540W/m ^{2}

Thermal analysis of several flapping cycles

The investigation of the local surface temperature is now carried out over several flapping cycles.

Observations of temperature curves at different locations over several cycles from Figs. 4.48 through 4.50 still indicate a decreasing temperature from the center towards the free edges of the plate. The flapping frequency is increased from 2 rad/s to 8 rad/s, keeping the same number of cycles with a surface heat flux of 1,000 W/m^2 but the surface temperature is recorded at the tip only for the highest frequency. It is interesting to notice that the increase in the flapping rate

leads to enhanced cooling as shown in Figs. 4.50 and 4.51. It is observed that the spatial distribution of the local temperature is conserved despite the overal increase in temperature magnitudes.

In Figs. 4.52 and 4.53, the simulation is performed over an increased number of cycles with the objective of reaching steady state. But this time, the temperature is recorded at the tip only. The simulation of 13 cycles indicates a negligible temperature increase with time at the end of the simulation. From 13 to 19 cycles, the change is barely noticeable. Carrying out the computation over an increased number of cycles could become tedious, requiring several days. Taking into account the computer storage, we decided to conclude that steady state is reached.

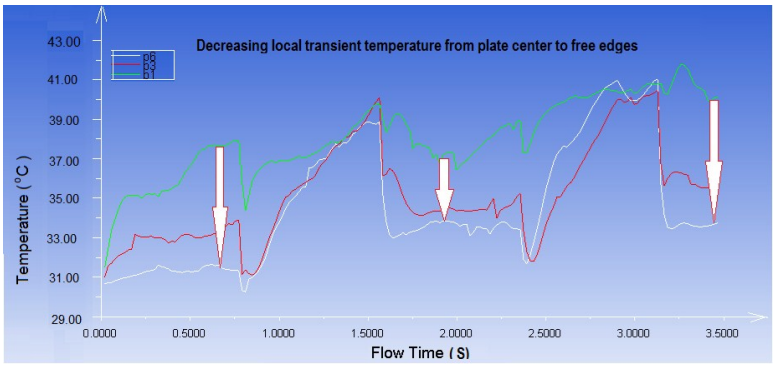

Fig. 4.48 Transient local surface temperature over 2 flapping cycles for heat flux of 250W/m ^{2} at 2 rad/s

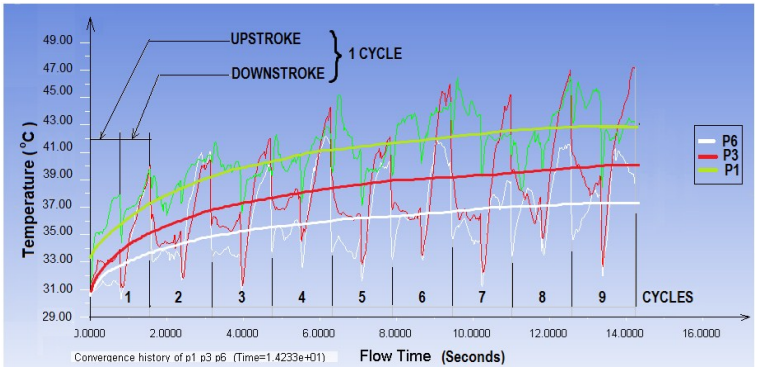

Fig. 4.49 Transient local surface temperature over 9 flapping cycles at a rate of 2 rad/s for a heat flux of 540W/m ^{2}

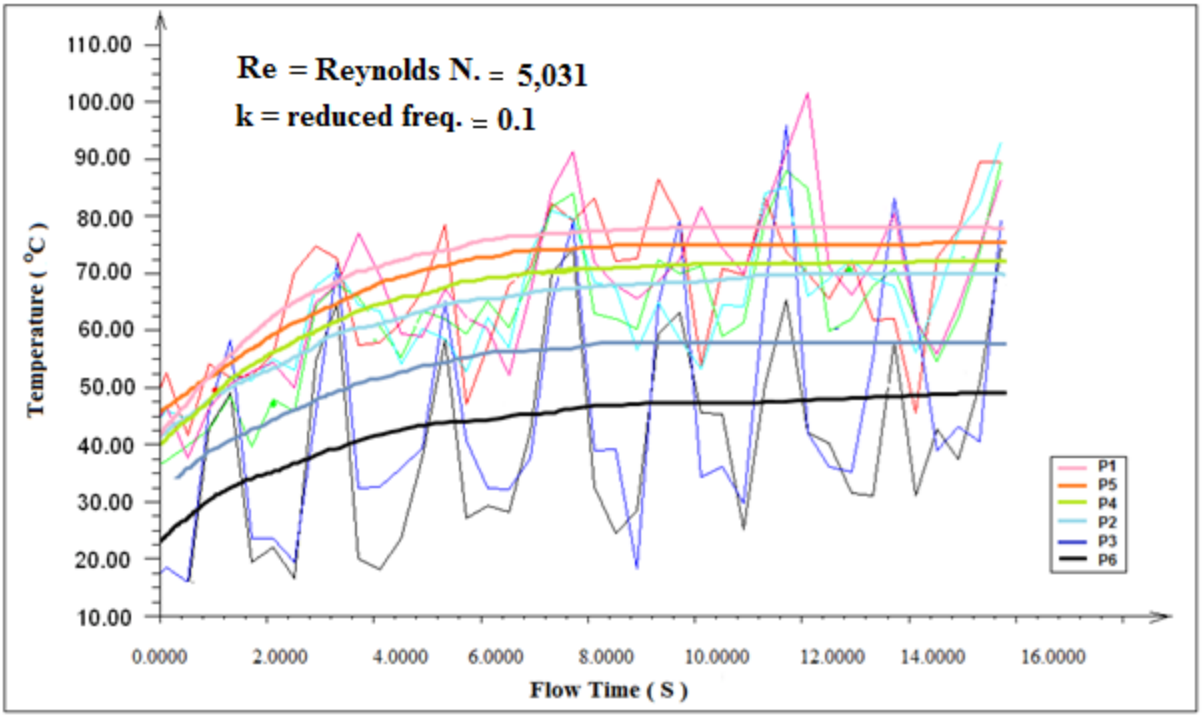

Fig. 4.50 Transient local surface temperature over 9 flapping cycles at a rate of 2 rad/s for heat flux of 1000W/m ^{2}

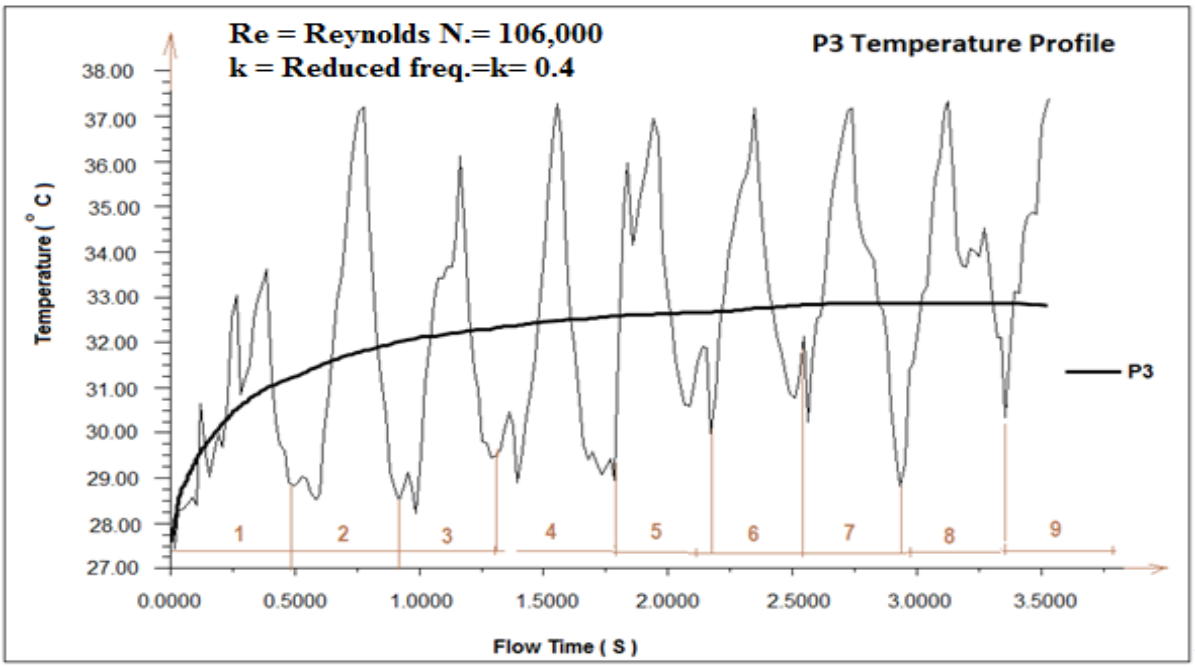

Fig. 4.51 Transient local surface temperature over 9 flapping cycles at a rate of 8 rad/s for heat flux of 1000W/m ^{2} (tip only)

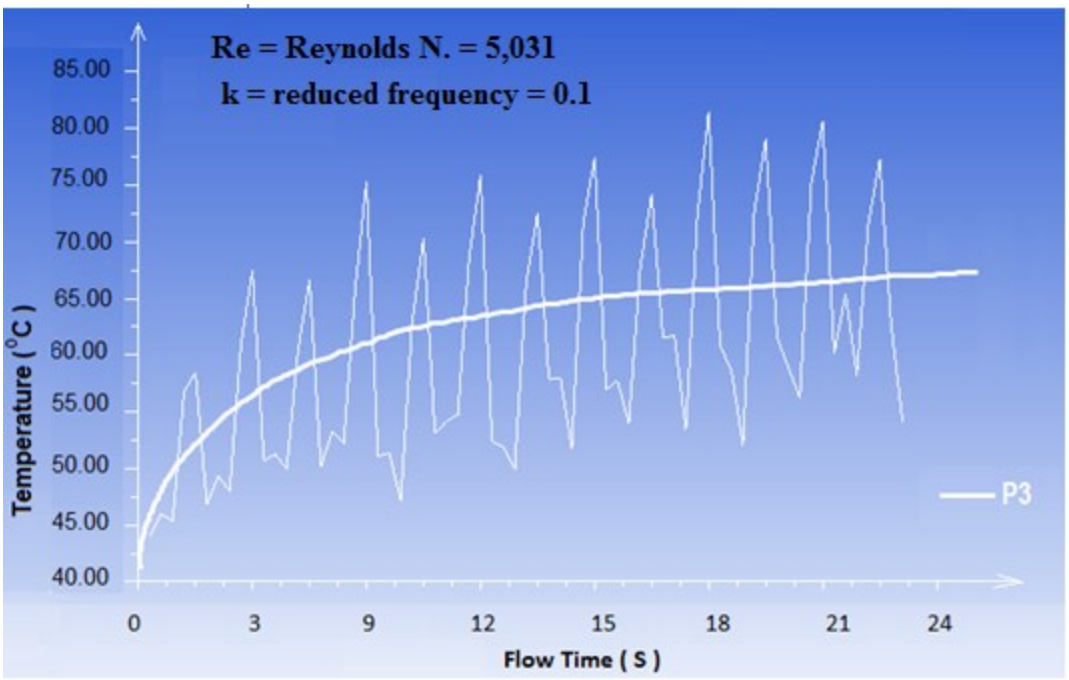

Fig. 4. 52 Transient local surface temperature over 13 flapping cycles for heat flux of 1000W/m ^{2} at 2 rad/s (tip only)

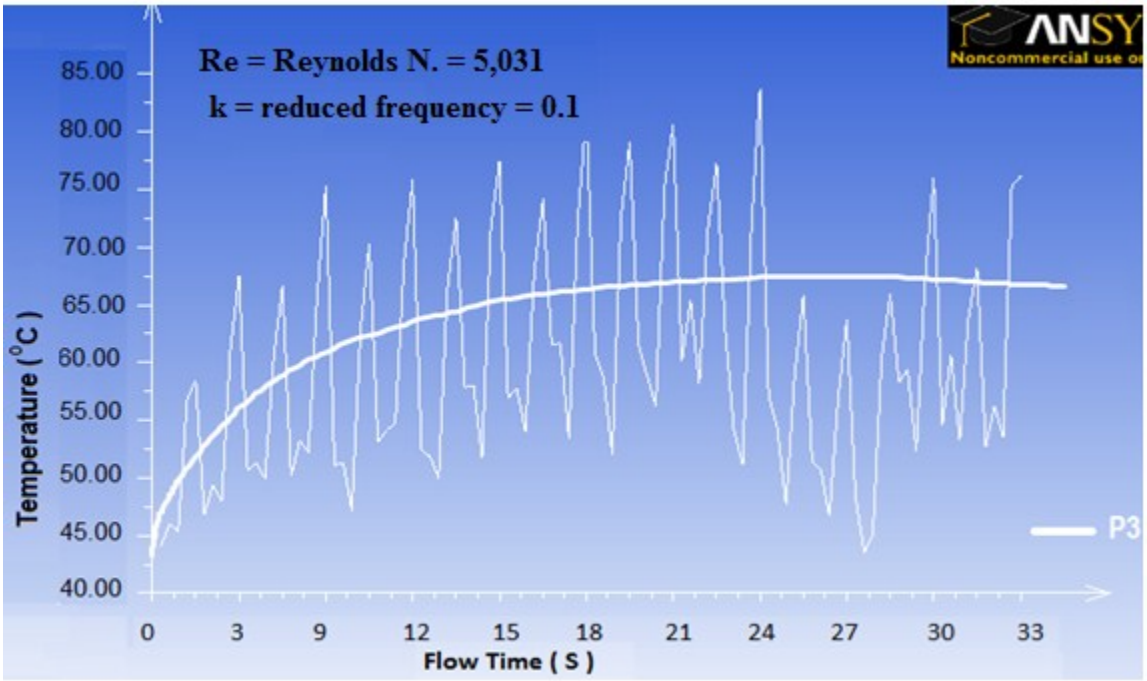

Fig. 4. 53 Transient local surface temperature over 19 flapping cycles for heat flux of 1000W/m ^{2} at 2 rad/s (tip only)

4.5 Conclusion of computational investigation on flapping plates

The results of the computational investigations of the flow around the rotationally oscillating heated plate with FLUENT indicate a close correlation between the flow field and the temperature distribution over the surface. The flow field and the transient thermal characteristics are both symmetrical about the plate's median plan, normal to the axis of rotation. During the flapping cycle, the temperature recorded on the front face increases gradually until the end of the stroke, followed by a sudden decrease over a short period of time at the onset of the down-stroke motion. The stroke reversal constitutes a critical phase in the flapping cycle due to the shedding of the vortex tube that removes a significant amount of heat from the tip of the plate. As the flow detaches from one face, the wake behind attracts surrounding fluid particles inside a back vortex, enhancing the heat transfer rate at these locations. Over several cycles, the local temperature increases through a transient periodic phase, followed by a steady periodic region until the end of the simulation. FLUENT results of temperature profiles indicate that surface temperature decreases from the plate's center toward the free edges. The highest heat transfer coefficients are recorded at these edges regardless of the angular position of the moving plate. Moreover, the heat transfer coefficient is directly proportional to the flapping frequency of the plate. The computational investigation provides relevant information on the flow field and thermal characteristics around heated flapping plates; however, the experimental investigation is required to check the validity of theoretical results.

CHAPTER 5: EXPERIMENTAL INVESTIGATION OF THE FLOW AROUND A ROTATIONALLY OSCILLATING HEATED FLAT PLATE

This chapter focuses on the design of a mechanism that provides rotationally oscillating motion to a rectangular flat plate of 0.3m x 0.2m about a fixed edge at a constant angular velocity ω, low enough to induce a laminar flow field. The plate is rotated back and forth to an arbitrary angular position θ over several cycles. Of interest is the design of a mechanism to control the amplitude of oscillations, the angular velocity and the number of cycles. A uniform heat flux q'' is applied to both faces of the plate and the local temperature distribution over the surface is to be determined.

5.1 Design of the flapping mechanism

5.1.1 Four bar linkage mechanism analysis

In mechanisms, four bar linkages are used for many applications [30, 55] such as path, motion, and function generation. Lin et al. [30] already used this concept illustrated in Fig. 5.1 for the simulation of the flapping motion of birds. In their design, linkage OA drives the mechanism while BD is connected to the wing structure, represented by the plate in this study. The position of the driving and the following linkages are described respectively by angles θ_2, θ_3 and θ_4 where β, λ and ψ are used for kinematics analysis. The four bar linkage is a crank and rocker mechanism where the driving linkage can rotate a complete revolution while the following linkage undergoes a rocking motion. An electrical motor with a constant rotational speed is coupled to the driving linkage OA for the experimental investigation.

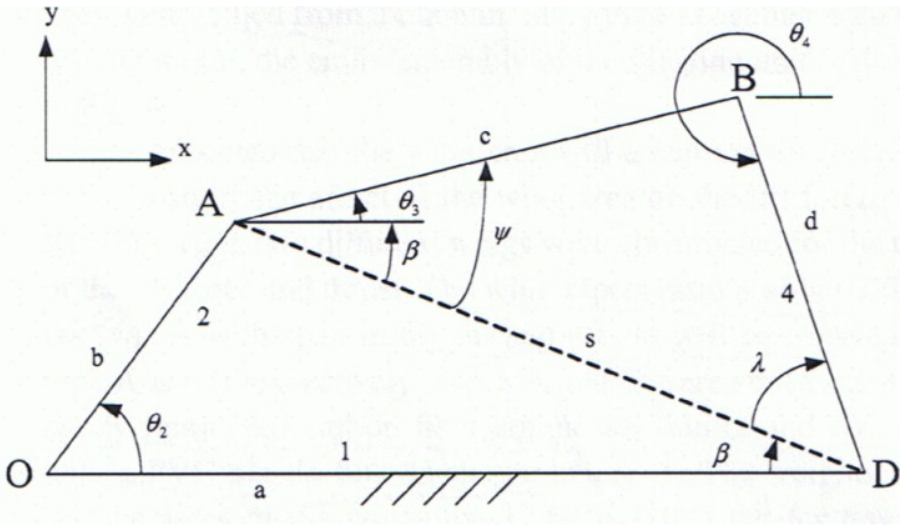

Fig. 5.1 Four bar linkage mechanism [30]

According to Grashof criteria [55], the sum of the shortest and the longest links of a planar four-bar linkage cannot be greater than the sum of the remaining two links, for a continuous motion between the links. Such a statement is illustrated by equation (5.1).

$$l + s < p + q \tag{5.1}$$

Where

l = length of longest link, m

s = length of shortest link, m

p, q = length of other two links, m

Although the four bar linkage mechanism has been used to design flapping mechanisms in several applications, the lengths of linkages need to satisfy some constraints such as the Grashof criteria for the mechanism to operate successfully. The relative motion between rotating parts can generate more frictional surfaces leading to considerable energy loss. Therefore, a smoother mechanism utilizing a robotic system is selected in this project for the simulation of the flapping motion required by the experimental investigation.

5.1.2 Robotics flapping mechanism design

The challenge in this method is to design a simple machine operated by a robot that will assign a rotationally oscillating motion to the rectangular flat plate. The task here is divided into two important stages: the selection of the motor to drive the mechanism and the design of the flapping mechanism to provide oscillating motion to the rectangular flat plate. The design of the robotics mechanism starts with the selection of the motor, followed by a detailed description of the whole mechanism.

a) Selection of the motor to drive the mechanism

Calculation of the torque applied to the plate

The plate is set in rotational oscillations with a maximum angular velocity $\omega = 10$ rad/s about a fixed vertical axis which is 0.12m far apart from the edge as indicated in Fig. 5.2. Of interest is the determination of the torque required to rotate the plate.

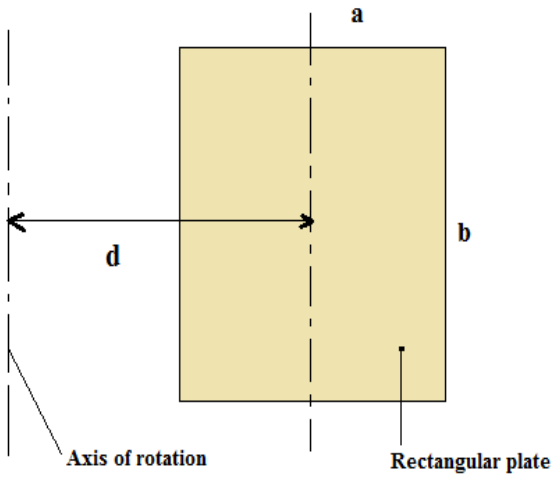

Fig. 5.2 Calculation of the torque applied to the plate

Inertia plays a very important role in this problem due to the rotation of the plate. The moment of inertia of the plate is calculated using the parallel axis theorem [56] since the axis of rotation is

far from the edge of the plate. Then, Newton's law of rigid body motion is used to determine the torque applied to the plate. In this analysis, the viscous moment and the moment of the plate about the axis of rotation are neglected. Assuming an angular acceleration of the plate equal to $\alpha = 10\,\text{rad/s}^2$, the mass of the plate is given by the volume times the density of the plate.

$$m = V \times \rho = (L \times l \times t) \times \rho \tag{5.2}$$

Where

m = mass of the plate, kg
V = volume of the plate in, m^3
ρ = density of the material = 1,800 kg/ m^3
l = width of the plate = 0.2 m
L = Length of the plate = 0.3m
t = thickness of the plate = 0.004m (including the heaters)

$$m = 1800(\text{kg/m}^3) \times (0.2\text{m} \times 0.3\text{m} \times 0.004\text{m}) = 0.432\text{kg}$$

The moment of inertia [57] of an area is a relative measure of the manner in which the area is distributed about any axis of interest. According to the parallel axis theorem, the moment of inertia of an area with respect to any axis is equal to the moment of inertia around a parallel centroidal axis, plus the product of the area and the square of the distance between the two axes.

The moment of inertia of the plate about the axis of rotation is given by the following equation.

$$I = m \times d^2 + \frac{1}{12}(m \times b^2) \tag{5.3}$$

$$I = m \times \left[d^2 + \frac{1}{12} \times b^2 \right] \tag{5.4}$$

Where

I = moment of inertia of the plate, kg-m^2
m = mass of the plate, kg

d = distance between axis of rotation and axis of symmetry of the plate, m

b = length of the plate, 0.3m

$$I = 0.432 \times \left[(0.12)^2 + \frac{1}{12} \times (0.3)^2 \right] = 0.0095 \text{kg} - \text{m}^2$$

The torque is given by Newton's law of rigid body motion applied to the plate and the power of the electric motor is calculated by multiplying the torque by the angular velocity of the plate.

$$T = \sum \tau_T = I \times \alpha_T \quad (5.5)$$

$$P = T \times \omega \quad (5.6)$$

Where

T = Torque on the plate, m-N

τ_T = Infinitesimal torque applied to the plate, m-N

I = moment of inertia of the plate, kg-m^2

α_T = angular acceleration of the plate= 10 rad/s^2

ω = angular rotation of the plate = 10 rad/s

$$T = 0.00950 \text{ kg} - \text{m}^2 \times 10 \text{ rad/s}^2 = 0.095 \text{ N} - \text{m}$$

The power required by the motor for an angular velocity $\omega = 10 \text{ rad/s}$ is calculated as follows:

$$P = 0.095\text{W} \times 10 = 0.95\text{W}$$

A safety factor of 5 is used to account for additional loads and the total number of cycles required by the experiment. A resulting power $P_u = 0.95\text{W} \times 5 = 4.75\text{W}$ is considered in the selection of a motor from Table 5.1. The choice of the geared robotics DC motor with a rotation speed of 93rpm at 12 V (shown in Fig. 5.3) is made for smooth power transmission to the flapping mechanism. The helical aluminum shaft coupling (shown in Fig. 5.4) is made of stainless steel; it is selected for its lightweight to connect the motor to the main shaft of the mechanism, on which the plate is attached. This type of coupling provides flexibility for angular and axial displacements to both rotating shafts. It is used in applications that require precise

positioning for frequent starts and stops with zero backlash. The vibration damper coupling (shown in Fig. 5.5) is made of two steel hubs and a flexible neoprene element. It connects the main shaft supporting the plate to the mechanism with the objective to compensate for misalignments and to absorb vibration shocks that occur at end strokes.

Table 5.1
Selection of the NPC geared robotics motor [57]

Dynamometer Test Results

Test Results at 12V				Test Results at 24V			
torque in in/lbs	Amps	RPM	HP	torque in in/lbs	Amps	RPM	HP
.42	4.0	93	.001	9.64	9.16	174	.03
10	5.47	91	.014	19.78	10.05	172	.05
20	6.78	89	.028	27.76	10.73	171	.08
30	8.19	86	.040	38.70	12.13	169	.10
40	9.55	84	.053	49.70	13.31	167	.13
50	10.96	82	.065	60.10	14.52	165	.16
60	12.42	80	.076	68.70	15.50	163	.18
70	13.75	78	.087	78.80	16.68	161	.20
80	15.14	76	.097	90.60	17.95	159	.23
90	16.50	74	.107	100.90	19.12	157	.25 →
100	17.97	72	.116 →	375	82		
260	56						

Fig. 5.3 NPC geared robotics motor[57]

Fig. 5.4 Aluminum helical beam shaft coupling of 12.7 mm diameter [58]

Fig. 5.5 Vibration damper coupling of 12.7mm diameter [58]

b) Description of the flapping mechanism

In this paragraph, the mechanism sketched in Fig. 5.6 is designed to provide rotationally oscillating motion to the plate over total amplitude of 90° angle. The Vex robot controller in Fig. 5.7 is programmed with the Easy C language using the algorithm (9.3.2 a) and the code (9.3.2b) respectively in Paragraph 9.3 of the Appendix, to assigning rotational oscillating motion to the plate over several cycles. All the electrical components involved in the wiring diagram of Fig. 5.7 including the speed controller VI 84 in Fig. 5.8 are secured in a plastic box as shown in Fig. 5.9. Detailed engineering drawings of the mechanism and its components are available in Paragraph 9.2 of the Appendix.

The plate is rotated by the 12.7 mm-diameter shaft of the geared robotics DC motor with a rotation speed that can be controlled according to the requirements of the experiment. The motor is powered by a 12 V sealed lead acid battery each time the speed controller VI 84 receives a signal from the 7.2 V robot Vex microcontroller. The rotation speed of the plate can be modified using the low speed (Low) or the high speed (High) sensor in Fig. 5.7. Two limiting switches designated CW (clockwise) and CCW (counterclockwise) in the same figure are used to reverse the direction of rotation of the plate; their locations can be adjusted to provide different flapping

amplitudes to the rotating device. The plate's flapping frequency ω is measured using a shaft speed encoder [59], based on the calculation from equation (5.7).

$$\omega = \frac{2\pi \sum_{i=1}^{n} (S_{fi} + S_{ri})}{60 \times S \times t} \tag{5.7}$$

Where

S_{fi} = slots count for upstroke motion

S_{ri} = slots count for down stroke motion

S = slots count per revolution, 90

t = duration of experimentation, s

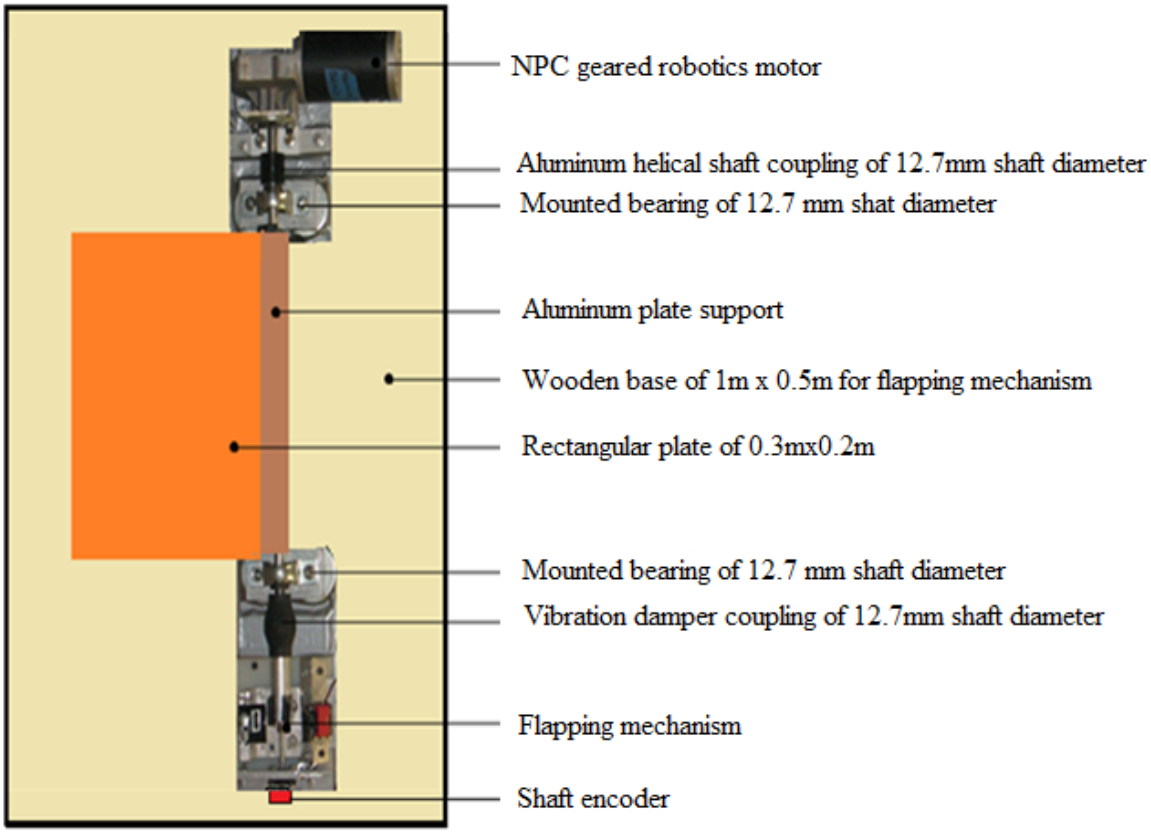

Fig. 5.6 Sketch of flapping mechanism

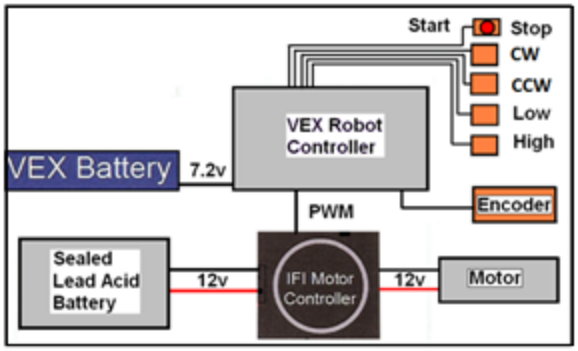

Fig. 5.7 Wiring diagram of flapping mechanism

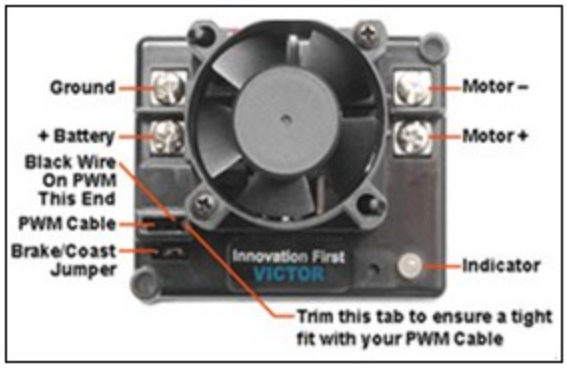

Fig. 5.8 Speed controller VI 84 [60]

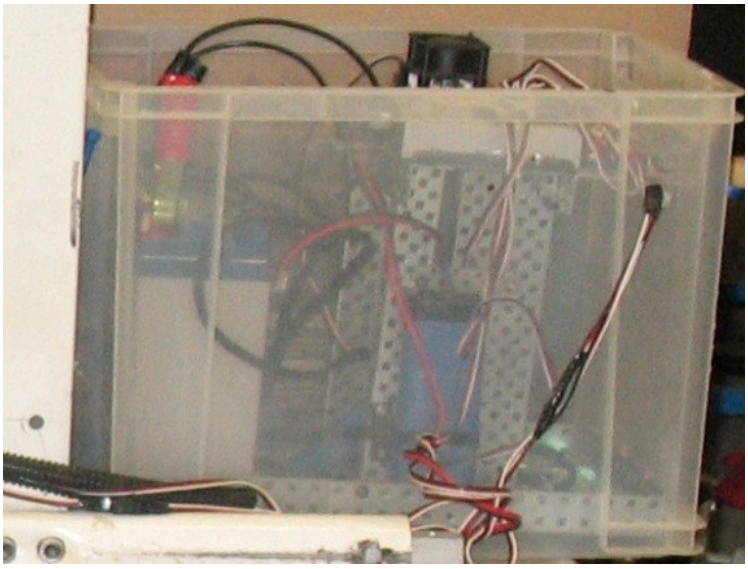

Fig. 5.9 Control box for the robotic electrical components

5.2 Description of the flow visualization experiment with smoke particles

A smoke machine releases particles, trapped temporally inside a container that is open to the testing area, during the flow visualization experiment described in Fig. 5.10. The rotational oscillating motion of the plate induces a flow of smoke particles from the container to the testing area. A double-pulsed laser, with a power ranging from 0.2 to 5.5W, produces a light sheet for the illumination of a section of the flow domain to be analyzed. At the same time, a high-speed

camera set with a resolution of 1280 x 800 and a sampling rate of 5,000 pulses per second (PPS) with an exposure time of 190 microseconds, enables the capture of videos and still images. The flow in the vicinity of the rotating plate is recorded using an optical lens, 50inches in diameter, mounted on the camera. A particle image velocimetry (PIV) computer software called INSIGHT 3G makes it possible to analyze images and videos recorded with the camera.

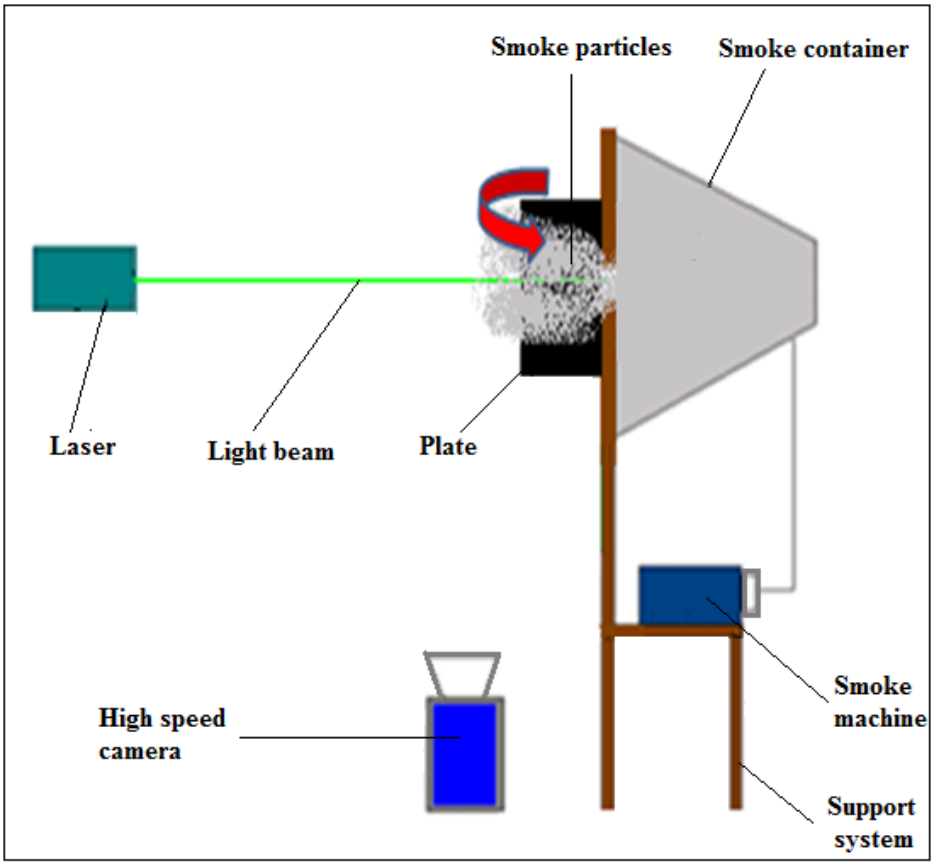

Fig. 5.10 Sketch of experimental setup

First, the mechanism is setup to provide flapping motion to the plate about a horizontal axis as illustrated in Fig. 5.11. The laser sheet illuminates along a section of the flow field, which is orthogonal to the axis of rotation, through the center of the plate as displayed in Fig. 5.12. The down stroke counterclockwise motion of the plate at a rate of 20 flaps per minute (in Fig. 5.13) enables to observe the forming and the shedding vortices behind the flapping plate. As the stroke

angle increases from the horizontal position, it is easy to visualize the center of the vortex and the boundary layer described by smoke particles over the surface of the plate.

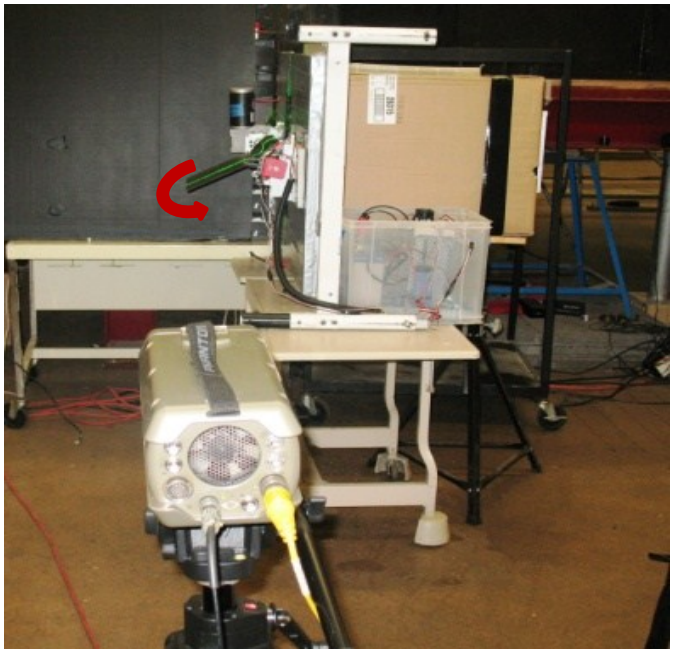

Fig. 5.11 Horizontal flow visualization setup

5.2.1 Flow visualization results for rigid flat plates

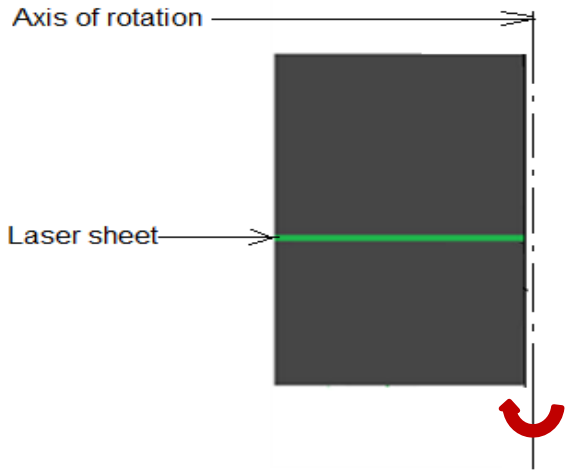

Fig. 5.12 Top view of the plate illuminated with laser beam

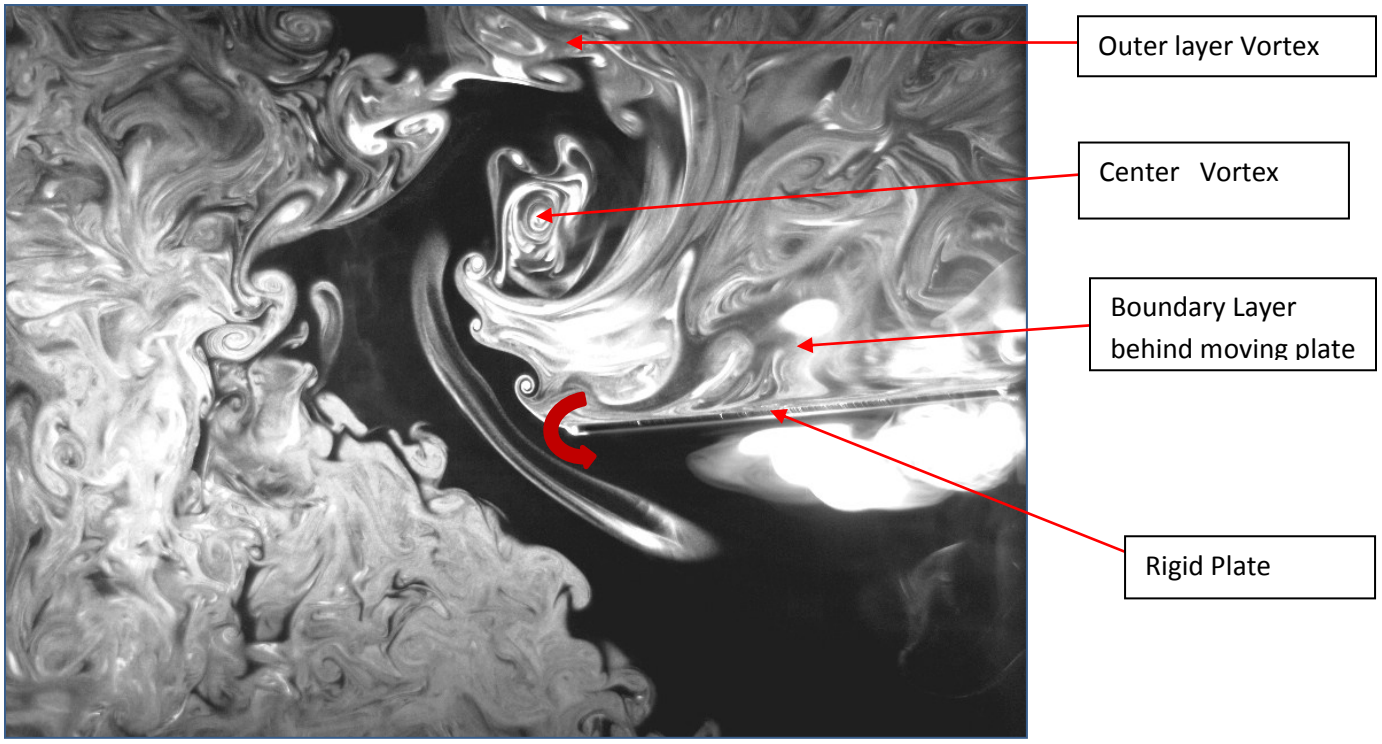

Fig. 5.13 Down stroke vortex behind moving rigid plate

The images in Fig. 5.14 describe the dynamics of vortices generated by the flapping plate at a rate of 20 flaps/min, during the down stroke motion. The vortex starts with a small diameter as shown in Fig. 5.14 A, and its size increases gradually with the stroke angle. At the onset of the second cycle, the history of the preceding vortex can be visualized in the picture of Fig. 5.14 B. Near the end of the stroke, the shape of the vortex becomes oval as the flow prepares to detach, according to the illustration in Figs. 5.15 C, D and E. The reversing phase of the stroke describes a flow with an S shape in Fig. 5.14 F presenting the shedding of the vortex on one side and its forming on the opposite side of the plate. The end of the stroke (as shown in Fig. 5.14 F) is marked by a complete detachment of the flow from the plate.

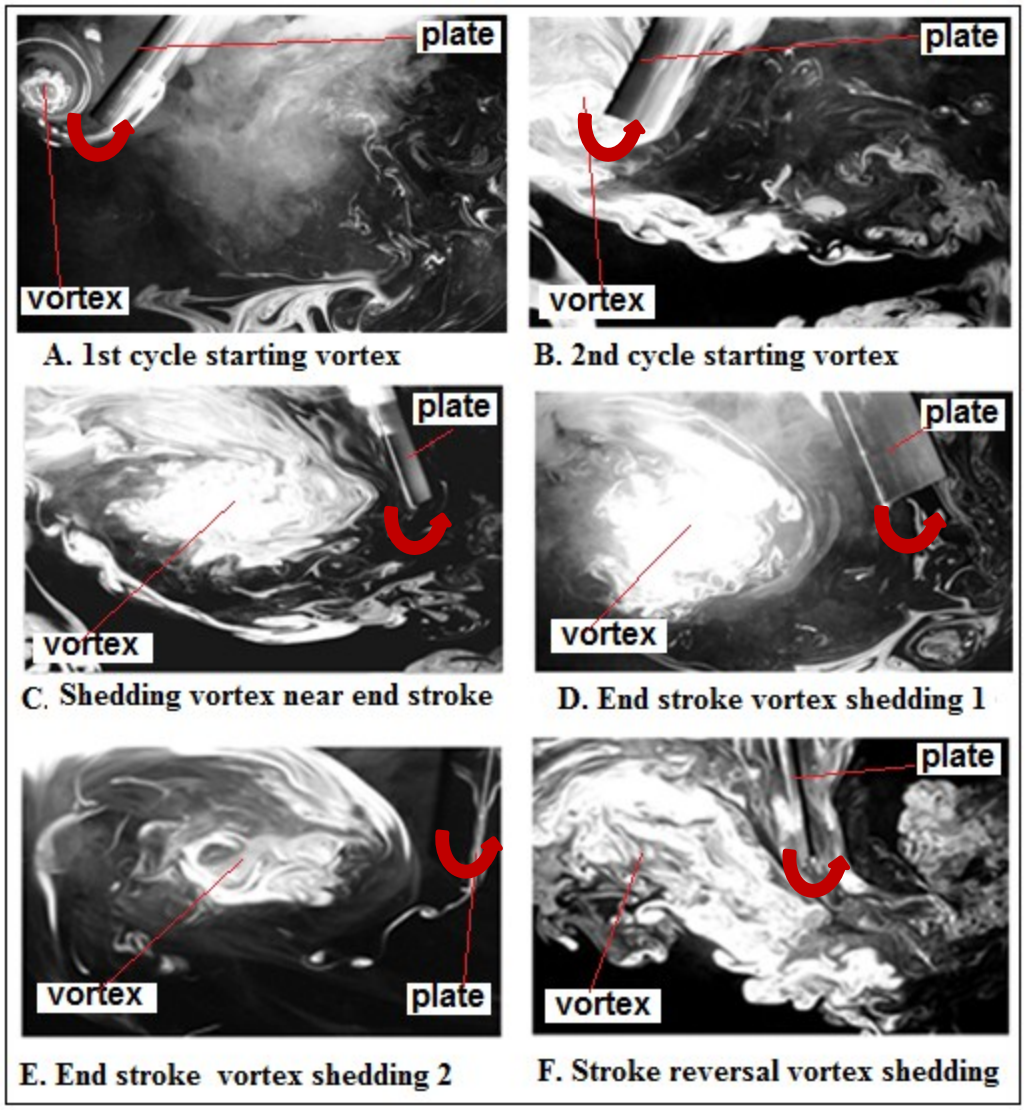

Fig. 5.14 Details of vortex dynamics

Now, the laser sheet illuminates the flow field in the longitudinal direction, parallel to the axis of rotation of the plate as shown in Fig. 5.15. The picture in View A of Fig. 5.16 exhibits the dynamics of vortices similar to the results already discussed in Fig. 5.14 but with a vortex progressing to the center of the plate's surface from the bottom edge. Furthermore, the image in View B displays a nearly symmetrical flow distribution about the median plane of the plate in the lateral direction. One can visualize the presence of an impinging jet of fluid in the back, targeting the center of the moving plate. The clockwise rotation of the plate leads to the stagnation

pressure caused by the impinging jet on the back face and the shedding of counter clockwise vortices from all free edges. Overall, the resulting induced flow field around rigid plates subject to rotational oscillations generates a lift force that can enhance the energy of rotation of the plate. However, the testing of a flexible material in this experiment could probably lead to interesting results that can be used in several applications.

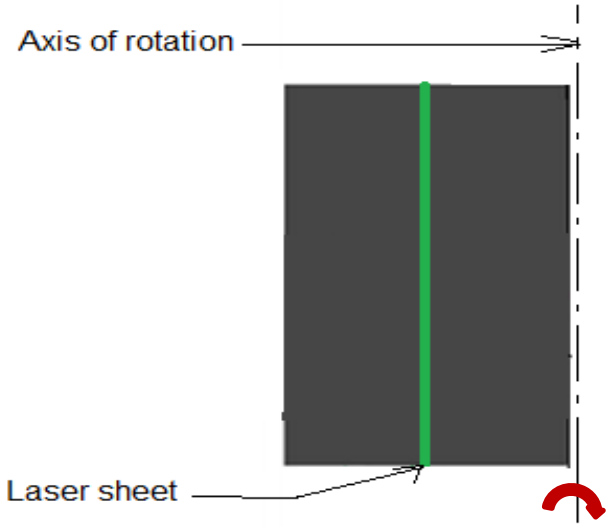

Fig. 5.15 Longitudinal sectional view of flow field

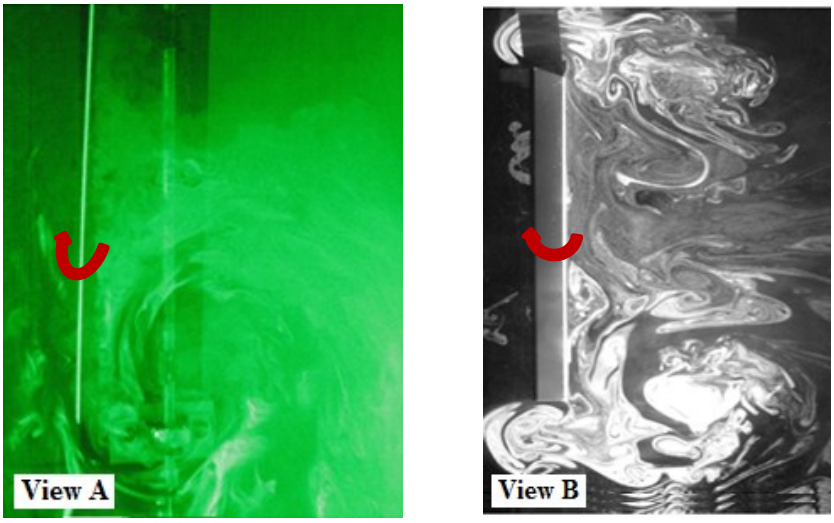

Fig. 5.16 Smoke particles in longitudinal section: Views A and B

5.2.2 Flow visualization results for flexible flat plates

In this experiment, the rigid flat plate is replaced by a piece of synthetic leather of 0.3m x 0.2m with a thickness of 2.5 mm. In this particular case, the plate is curved backward during its rotation making smoke particles travel along circular paths imposed by its current shape, before reaching the tip. At end strokes, the bulk motion of the plate stops suddenly while the tip is flipped from back to front over a relative angle θ which is a function of the flexural strength of the material. The flow visualization result in View A of Fig. 5.17 indicates that the tip vortex forms and covers over 70% of the plate's surface. Because of the deformation of the plate, one can notice a premature detaching flow as illustrated by the picture in view B of Fig. 5.17. However, most vortex shedding occurs at the tip when the flexible plate stops suddenly, accelerating fluid particles due to the relative motion of the tip.

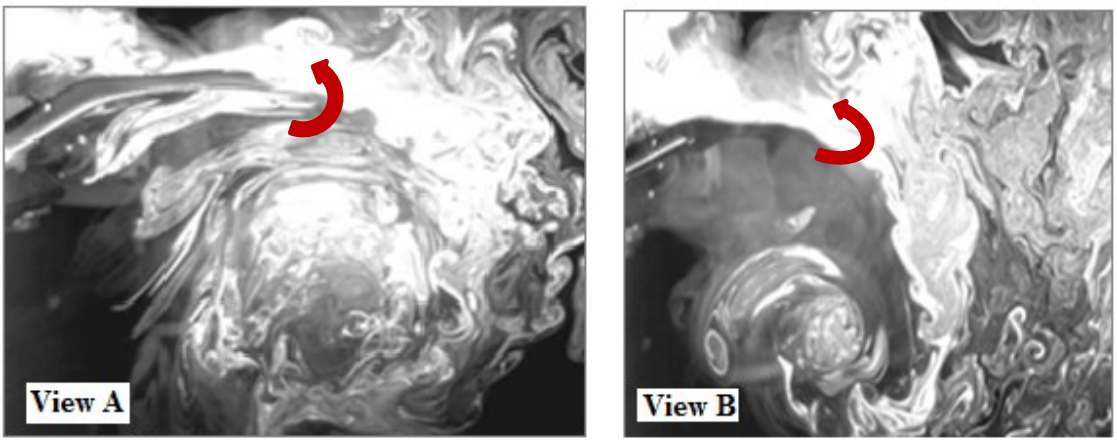

Fig. 5.17 Visualization of tip vortex from a flexible plate: starting stroke (View A) and tip shedding vortex (View B).

In conclusion, the flow visualization experiment shows that vortex shedding occurs in all directions with the presence of a vortex tube around the free edges of the plate during its rotation. In the case of flexible plates, the vortex forms at the tip and continues to grow until it covers most of the surface of the plate before shedding. The analysis of the dynamics of vortices is

essential and will serve in future chapters to explain the impact of the induced flow field in the enhancement of the heat transfer rate from the surface of the moving plate.

5.3 Description of the heat transfer experiment for rigid plates

5.3.1 Plate design for heat transfer experiment.

The heat transfer experiment requires a suitable design of the plate for the assignment of the boundary condition of constant and uniform heat flux over its whole surface. Carbon fiber of the type RO4003 from Rogers's corporation [61] is used to design the plate. Its low thermal conductivity of 0.64 W/m-K as indicated in Table 9.1 (Appendix) is selected to minimize the heat transfer by conduction through the plate's material. A low density of 1,800kg/m3 is chosen to reduce the inertial torque applied to the plate during flapping cycles. The plate is heated with a total power of 480W under a voltage of 110V on both sides. The total heat supply is provided by 0.14cm--thick flexible silicone rubber heaters of 20 cm x 30 cm as shown in Fig. 5.18.

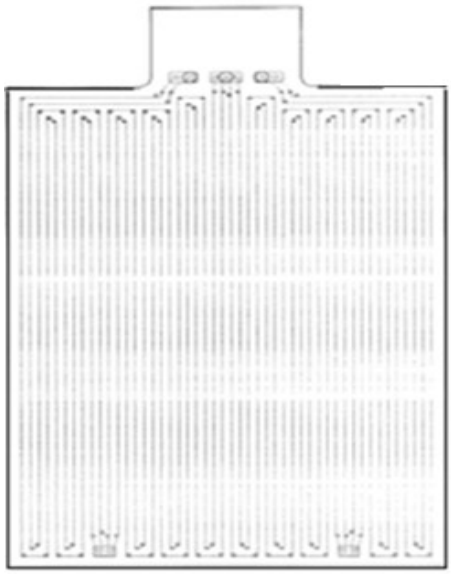

Fig. 5.18 Flexible silicone rubber heater with embedded heating elements[62]

The silicone rubber heaters are cemented on each face of the plate as illustrated in View A of Fig. 5.19 with an appropriate silicone adhesive designed to support the operating temperature that ranges between ambient and $280^{o}C$. The heating wires are embedded inside the silicone rubber with a spacing of 0.3cm to ensure a uniform heat flux over the entire surface of the plate. J type thermocouples are attached to the surface of the plate at desired locations as described in Fig.5.19B for local temperature measurement. The heating system is made of a variable transformer of model N-SC-3H with a maximum power of 300VA and an output voltage in the range of 0 to 130 VAC to control the setting of different heat fluxes. Both heaters of resistant R equal to 30 Ω each are coupled in a parallel electrical circuit as shown in Fig. 5.20.

5.3.2 Surface temperature data acquisition over heated flapping plates

The heat flux q" applied to the plate is determined in terms of the power supply defined in equation (5.8) and the total plate area, using equation (5.9):

$$q = \frac{U^2}{R} \tag{5.8}$$

$$q'' = \frac{q}{A} \tag{5.9}$$

Where

R = equivalent resistance of the heater, 15 Ω

U= voltage supply to the heater, 50 V

A= Total Surface of plate, $1200cm^2$

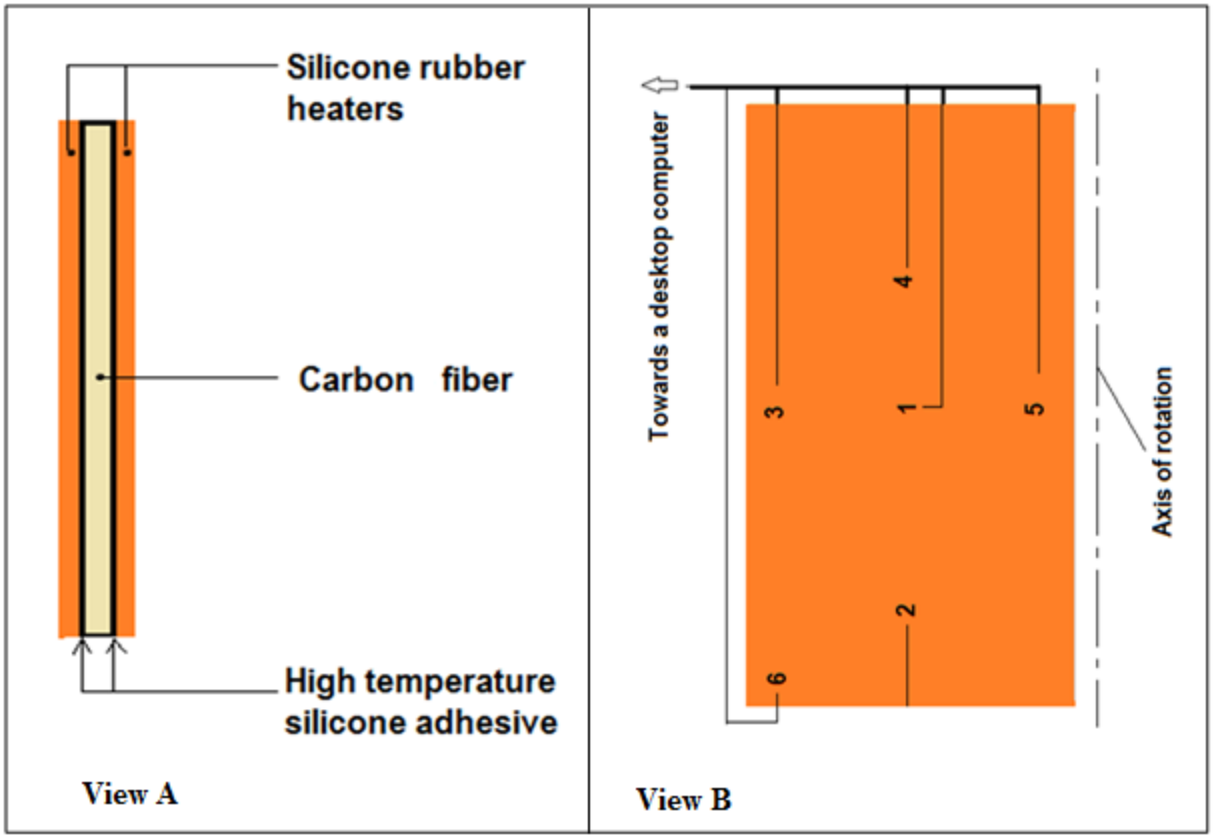

Fig. 5.19 Plate setup for heat transfer experiment

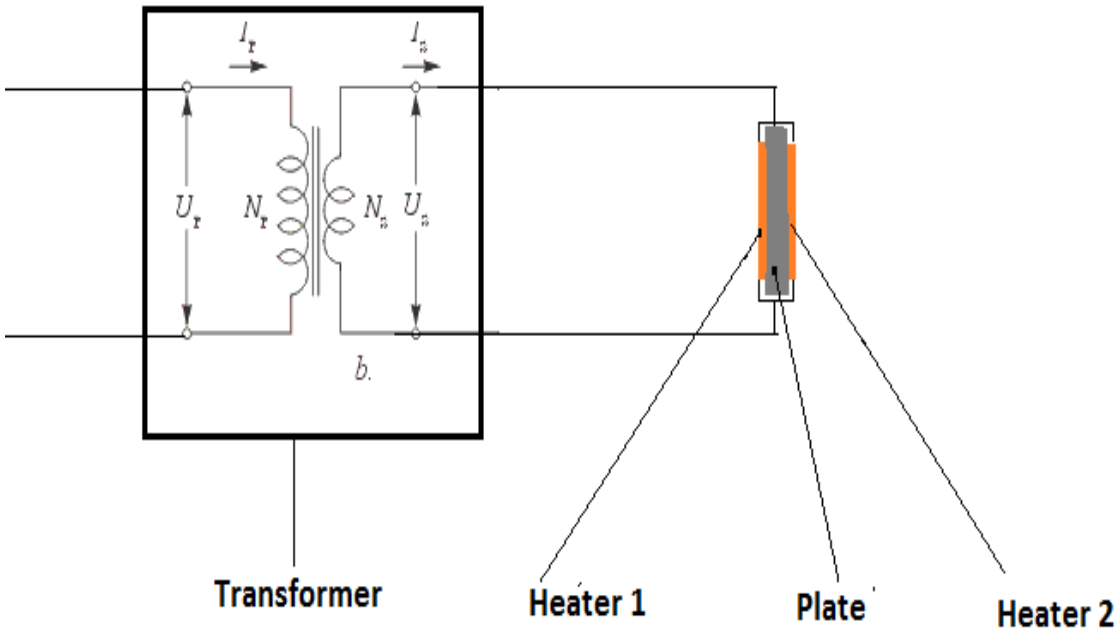

Fig. 5.20 Wiring diagram of silicone rubber heaters

In this problem, the material of the heater is silicone rubber with a thermal emissivity of 0.94, making heat dissipation by radiation to be important at higher temperatures. The following example provides a calculation of the radiative heat loss using the Stefan-Boltzmann law of heat radiation in equation (5.10). The power supply to the heaters is set to an equivalent voltage of 50V controlled by the variable transformer. The reading of the plate's surface temperature at the center is $T_s = 120^o C$, which allows the calculation of the power loss by radiation.

$$q_r = \sigma \varepsilon A(T_S^4 - T_1^4) \tag{5.10}$$

Where

q_r = average heat radiation from surface, W

A = surface area of plate, $0.12 m^2$

σ = Stefan-Boltzmann constant, $5.67 \times 10^{-8} W/m^2 - K^4$

ε = emissivity of silicone rubber = 0.94

T_S = surface temperature, $120^o C$

T_1 = surrounding temperature, $25^o C$

Hence,

$$q_r = (5.67 \times 10^{-8} W/m^2 - K^4) \times 0.94 \times (0.12 m^2)[(120 + 273.15)^4 - (25 + 273.15)^4] = 102 \text{ W}$$

The heat flux q_c'' applied to the plate is determined using the total power q supplied to the heating system and subtracting the heat loss by radiation at higher temperatures. The total heat dissipated by convection q_c is computed in (5.11) and the corresponding heat flux q''_c is determined in equation (5.12).

$$q_c = q - q_r \tag{5.11}$$

$$q''_c = \frac{q_c}{A} \tag{5.12}$$

Therefore, the resulting heat flux from the energy convected from the plate is computed as follows:

$$q = \frac{U^2}{R} = \frac{50^2}{15} = 166.67W$$

$$q''_c = \frac{q_c}{A} = \frac{q - q_r}{A} = \frac{166.67 - 102}{0.12} = 538.92 \ W/m^2$$

5.3.3 Heat transfer experimental investigation over the flapping plate

a) Setup of heat transfer experiment

The plate is rotated in the vertical position as shown in Fig. 5.21 with the thermocouples attached to its surface for the tracking of the local temperature. A desktop computer is utilized to process the thermal data collected with the thermocouples. The plate surface temperature is converted from analogic to digital and transferred through BNC cables to the six-channel National Instrument- BNC-2110 data acquisition block in Fig. 5.22. The data are finally routed to a desktop computer where MATLAB programs in the Appendix are written for the calculation of the plate's surface temperature over several cycles. The code in Paragraph 9.3.3 enables the acquisition of the raw temperature data from the plate's surface. First, the electromotive force (EMF) of each thermocouple is determined using a calibration with ice water as shown in Fig. 5.23. The calibration is facilitated using the program code in Paragraph 9.3.4 of Appendix C. Then the recorded raw data are filtered with the program in Paragraph 9.3.5 that utilizes a Butterworth filter with a cutoff frequency of 0.94. The final electrical temperature data are plotted after conversion to degree Celsius by the same filtering program.

ted after conversion to degree Celsius by the same filtering program.

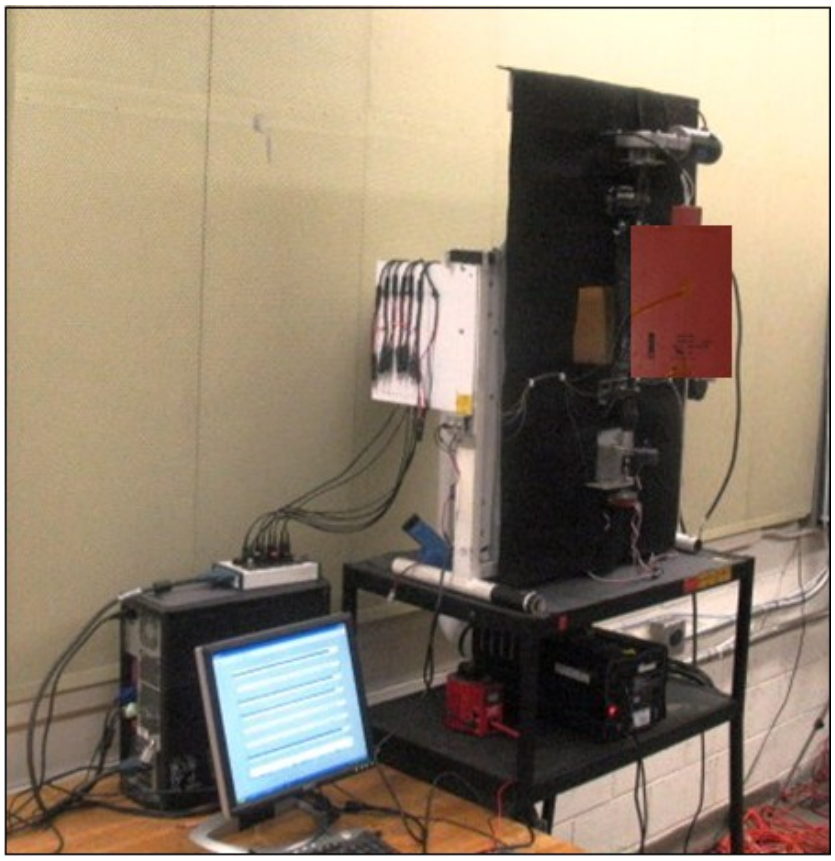

Fig. 5.21 Temperature data acquisition experimental setup

Fig. 5.22 National Instrument - BNC-2110-DAQ connector block [63]

Fig. 5.23 Calibration of thermocouples with ice water

b) Free convection investigation of surface temperature over a vertical heated flat plat

The heat transfer investigation starts with a free convection experiment where a heat flux q'' of $540 W/m^2$ is applied to both faces of the plate and the surface temperature is recorded with the thermocouples over a period of 30minutes. Free convection results will serve as a reference for the analysis of future forced convection surface temperature solutions. Fig. 5.24 provides a map of growing transient temperature magnitudes at all locations from ambient to nearly constant values, when steady state is reached. An increase of the steady state local surface temperature with **y** is observed in the vertical direction, from a value (bottom corner) at T_6 equal to 80^oC to a value (top of the plate) at T_4 equal to 142^oC .Temperature readings from T_1, T_3 and T_5 are very close to each other because the corresponding thermocouples are located at the same altitude (y = 0.15m) from the bottom of the plate.

Another experiment is performed where the free convection test is followed by forced convection analysis with the same applied surface heat flux of $q'' = 250 W/m^2$. The free

convection surface temperature is recorded over a period of 10 minutes, at 5 different locations when steady state is reached. Then, the plate is set into motion at a flapping rate of 35 flaps per minute; this procedure allows a quick and preliminary investigation of the plate's surface temperature map in forced convection. In free convection the highest temperature is read at the top edge of the plate, Fig. 5.25 indicates that the highest point in forced convection is located in the vicinity of the plate's center. Next, the plate is heated at a constant flux of 57 W/m^2 for a period of 30 minutes to reach steady state, before collecting the surface temperature data over a period of 30 additional minutes as shown in Fig.5.26. The free convection surface temperature distribution remained similar with different heat fluxes applied to the plate, with the lowest temperature measured at the bottom and the highest at the top of the plate.

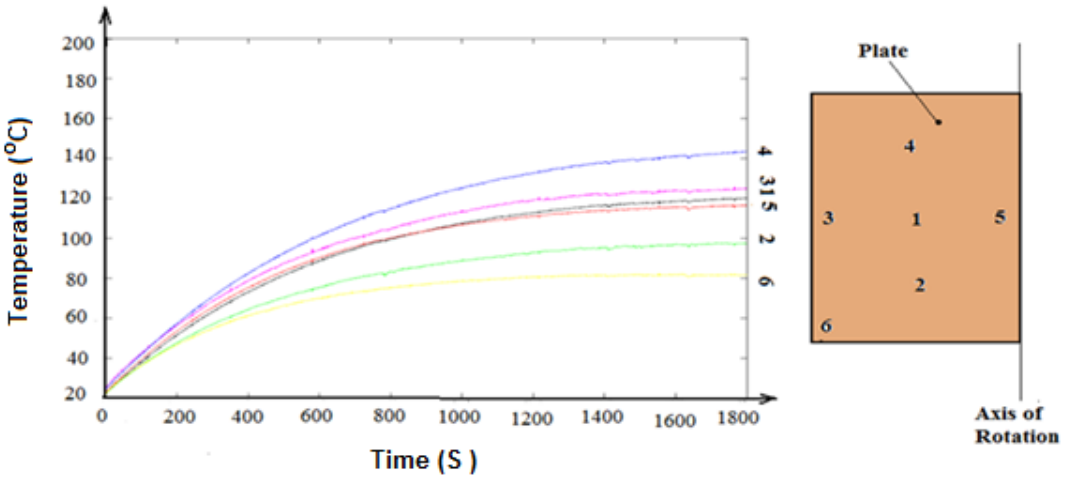

Fig. 5.24 Free convection transient plate surface temperature map for a flux with heat flux $q'' = 540 W/m^2$

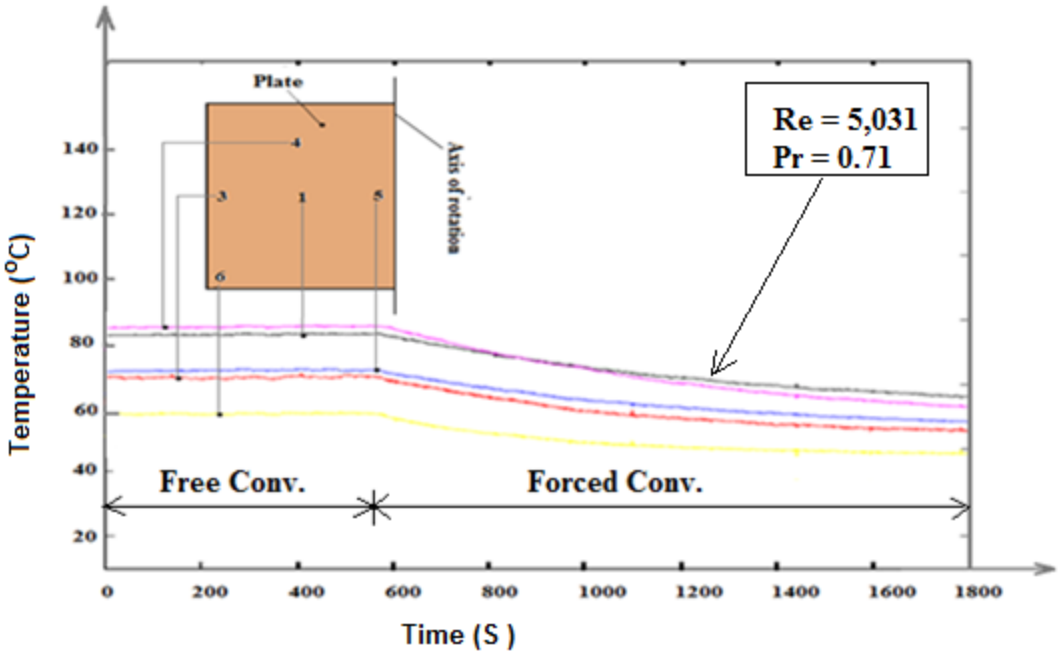

Fig. 5.25 Free convection followed by forced convection transient plate surface temperature map for a flux with heat flux $q'' = 250 W/m^2$

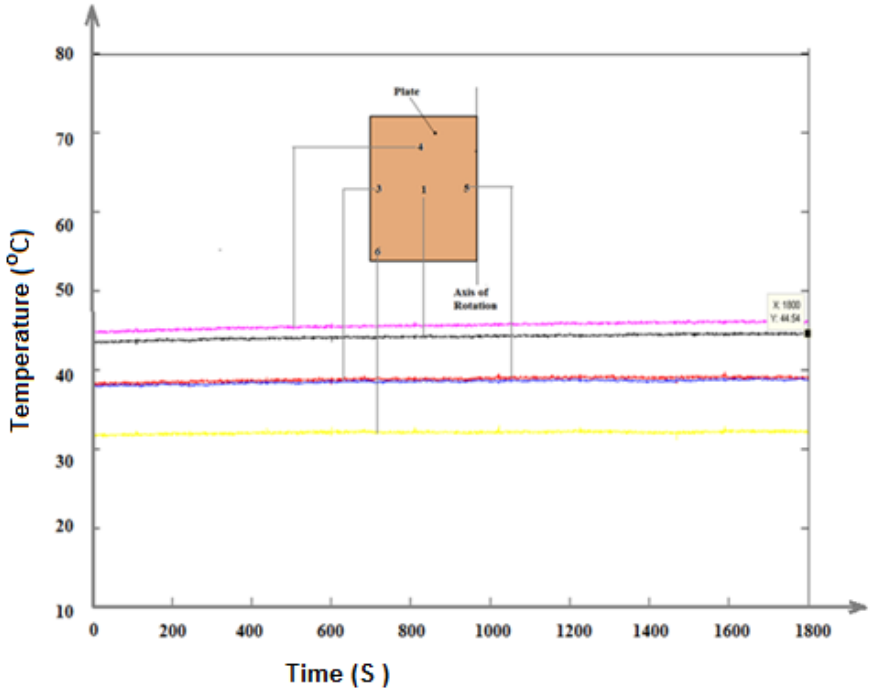

Fig. 5.26 Free convection transient plate surface temperature map for a flux with heat flux $q'' = 57 W/m^2$

In conclusion, the experimental free convection local temperature over the plate's surface increases over a period of 20 minutes before reaching steady state, where the temperature remains constant despite the continuous applied heat flux. Along the vertical direction, the plate's surface temperature rises rapidly from the bottom to the center and then slightly until the top edge. Over the top half of the plate, the thickness of the boundary layer remains nearly constant and so is the local heat transfer coefficient at these locations.

c) Forced convection investigation over a rotational oscillating vertical heated flat plate

The plate is set in a rotationally oscillating motion at rate of 40 flaps/min with an applied heat flux of $57\ \text{W/m}^2$ just after the free convection experiment. Over the flapping cycles, the surface temperature decreases progressively at all locations until steady state is reached as shown in Fig. 5.27. These temperature values are organized in Table 5.2 and plotted in Fig. 5.28 to show the influence of the flapping motion on the overall distribution of thermal characteristics over the plate's surface. A bulk temperature drop ranging from 2^{o}C to 2.8^{o}C is noticeable over the surface of the plate by comparing free convection and forced convection experimental results using the same boundary conditions. The resulting heat transfer coefficients are prepared in Table 5.3 and plotted in Fig. 5.29. The highest heat transfer coefficient of $34.7\ \text{W/m}^2-\text{K}$ is recorded at the edge of the plate compared to a minimum value of $20.6\ \text{W/m}^2$ at the center of the face.

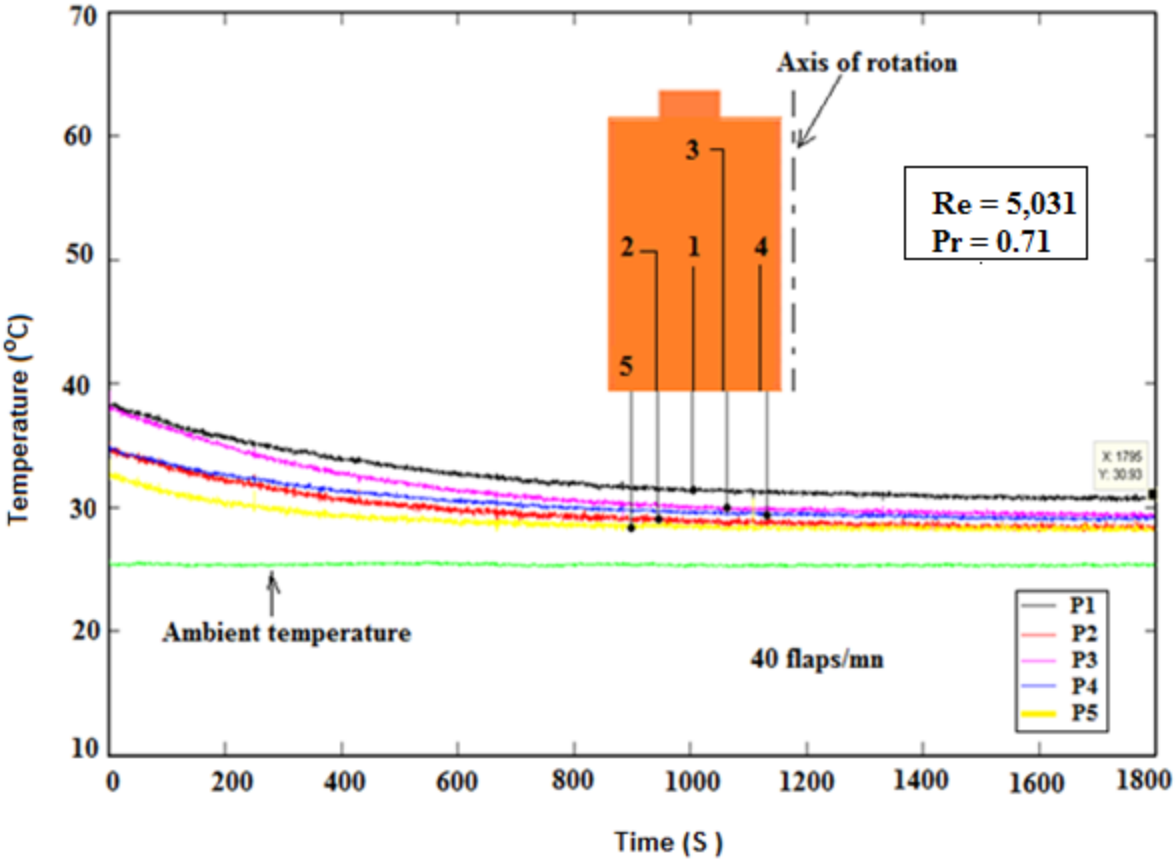

Fig. 5.27 Local plate's surface temperature for a heat flux of 57W/m ^{2}

Table 5.2
Free conv. vs. forc. conv. at 40 flaps/min
Surface temperature (°C)

Thermoc.	Amb.	Free Conv.	Forc. Conv.
TC1	24.60	29.80	27.30
TC2	24.40	29.20	26.60
TC3	24.40	30.00	26.80
TC4	24.50	28.80	26.70
TC5	25.00	28.80	26.60

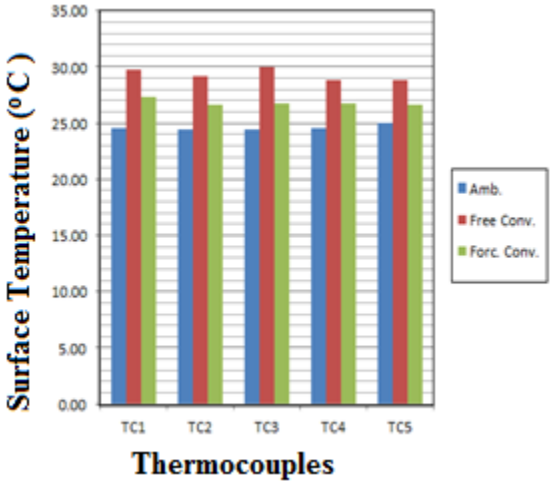

Fig. 5.28 Local plate's surface temperature for heat flux = 57W/m ^{2} Free Convection vs. Forced Convection

Table 5.3 Free conv. vs. forc. conv. at 40 flaps/min Heat Transf. Coef. (W/m^2-K)			
Thermoc.	Amb.	Free Conv.	Forc. Conv.
TC1	24.60	10.67	20.56
TC2	24.40	11.56	25.23
TC3	24.40	9.91	23.13
TC4	24.50	12.91	25.23
TC5	25.00	14.61	34.69

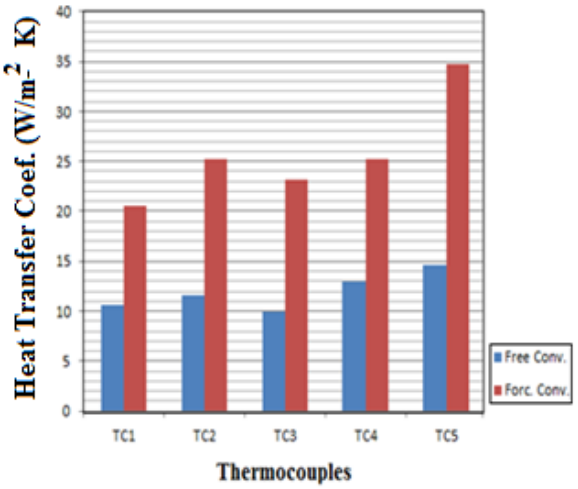

Fig. 5.29 Local plate's surface heat transfer coef. for heat flux = 57 W/m^2

The next experiment is conducted with the objective to check the impact of the variation of the flapping frequency on the thermal characteristics over the plate's surface. Assigning a surface heat flux of 130 W/m^2, a test is performed with the plate's flapping frequency set to 35 flaps/min. This is followed by another experiment, where the plate's flapping frequency was increased to reach 40 flaps/min. Second, 2 other similar experiments are conducted but at this time, the heat flux is increased to 540 W/m^2. Starting with the flux of 130 W/m^2, Table 5.4 and Fig. 5.30 illustrate an overall drop of the surface temperature of about 1 degree Celsius when the frequency changes from 35 flaps /min to 40 flaps /min. As a result, Table 5.5 and Fig. 5.31 show an average increase of the heat transfer coefficient to over 2 $W/m^2 - K$. In conclusion, the local surface heat transfer coefficient rises with the plate's flapping frequency.

Table 5.4

Surf. Temp. with a flux of 130W/m^2 for 2 different frequencies (°C)

Thermoc.	35flaps/min	40flaps/min
TC1	31.69	30.84
TC2	29.23	28.36
TC3	30.28	29.43
TC4	29.78	29.10
TC5	28.52	28.36

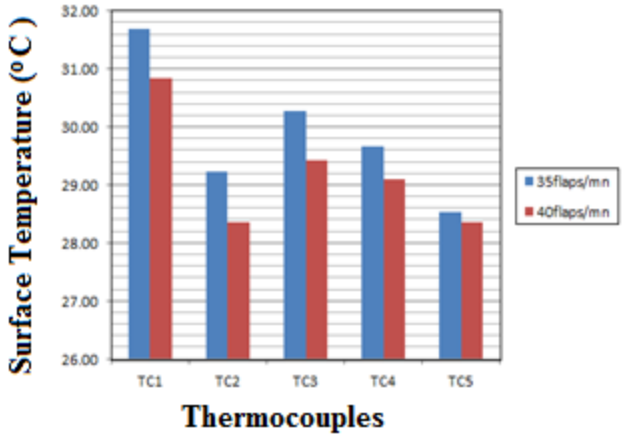

Fig. 5.30 Comparative analysis of local surface temperature for a heat flux of 130 W/m^2

Table 5.5

Heat Transf. Coef. for 2 flapping rates of 35 and 40 flaps/mn with a heat flux of 130 W/m2 (W/m^2-K)

Thermoc.	35flaps/min	40flaps/min
TC1	16.44	18.84
TC2	26.00	32.74
TC3	20.83	24.83
TC4	23.01	26.83
TC5	31.34	32.74

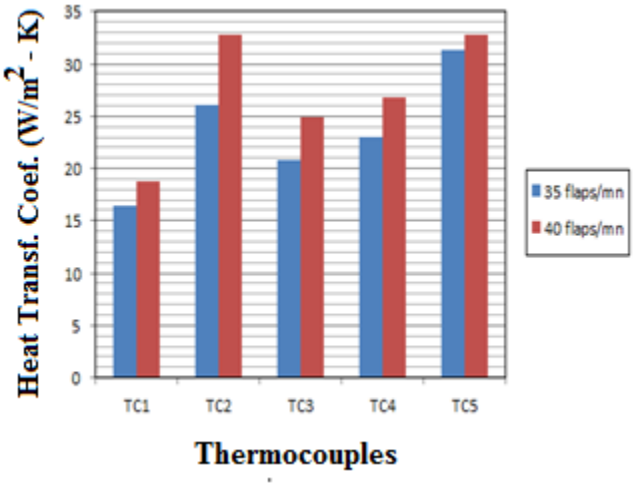

Fig. 5. 31 comparative analysis of local heat transfer coefficient for a heat flux of 130 W/m^2

For the final experiment, the heat flux q" of 540 W/m^2 is applied to the surface of the flapping plate at a rate of 35 flaps/min. The experiment is repeated with a higher flapping frequency equal to 40 flaps/min. The local surface temperature increases through a transient unsteady periodic phase for both flapping frequencies, before reaching steady state at all locations as shown in Fig. 5.32.

Overall, it is interesting to notice that the cooling of the plate's surface is improved in all peripheral zones except for regions located in the vicinity of the fixed edge, about which the rotation of the plate occurs. A decrease in their magnitudes is noticeable although the temperature distribution remains unchanged. The increase in the plate's flapping rate presented in Table 5.6 results in a drop of its overall surface temperature of about 5% as shown in Fig. 5.33. Therefore, the heat transfer coefficient recorded in Table 5.7 is increased by an average value of 13% over the plate's surface as illustrated in Fig. 5.34.

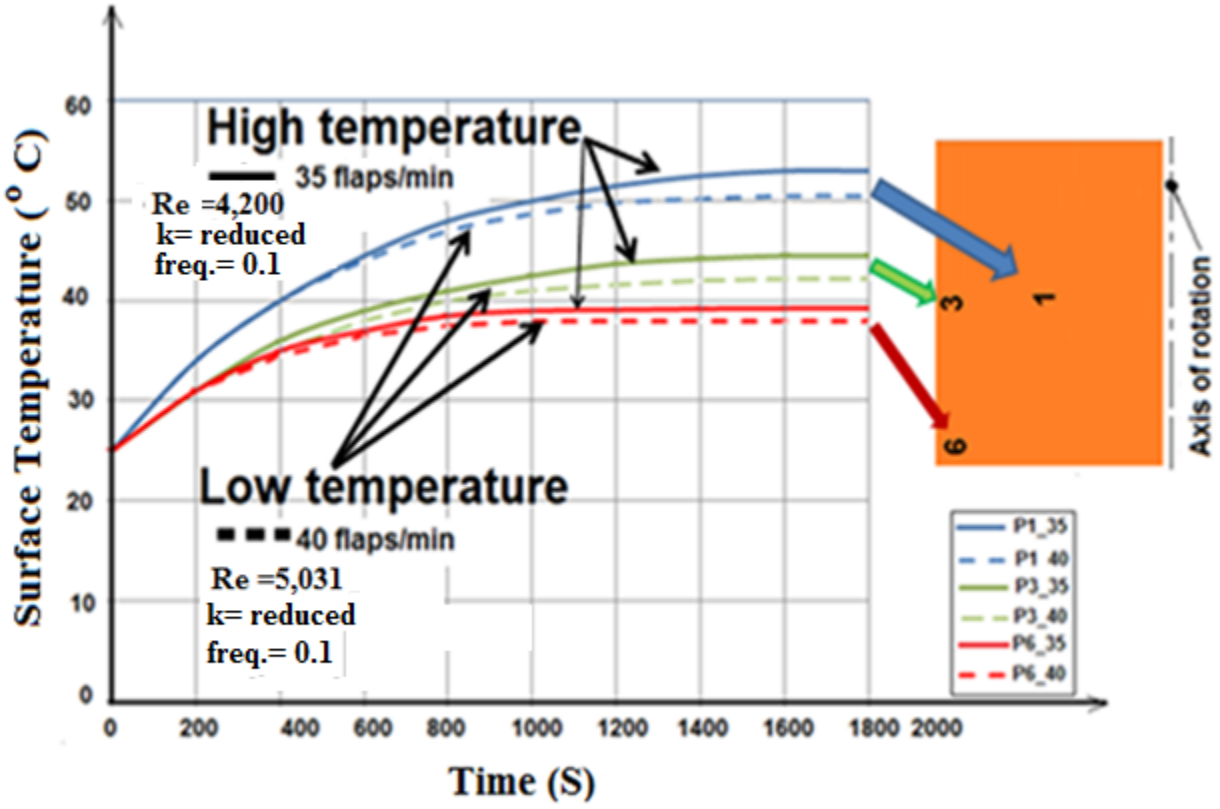

Fig. 5.32 Analysis of local surface temperature for 2 flapping rates (35 and 40 flaps/min) with a surface heat flux of 540 W/m ^{2}

Table 5.6
Surface Temperature for 2 different flapping frequencies (°C)

Thermoc.	35flaps/min	40flaps/min
TC1	53.48	50.35
TC2	44.44	41.95
TC3	50.26	47.38
TC4	46.42	43.95
TC5	39.28	37.64

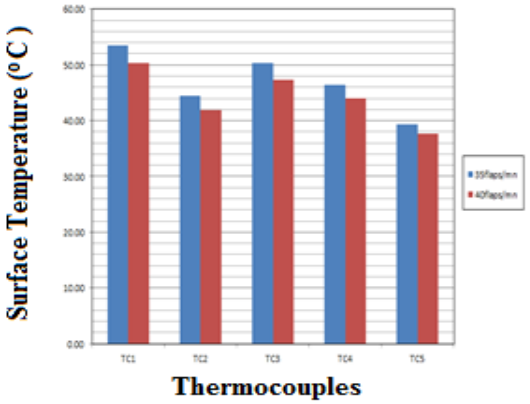

Fig. 5.33 Comparative analysis of local surface temperature with heat flux of 540 W/m^2

Table 5.7
Heat Transfer Coefficient for 2 different flapping frequencies (W/m^2 - C)

Thermoc.	35flaps/min	40flaps/min
TC1	18.96	21.30
TC2	27.78	31.86
TC3	21.38	24.13
TC4	25.21	28.50
TC5	37.82	42.72

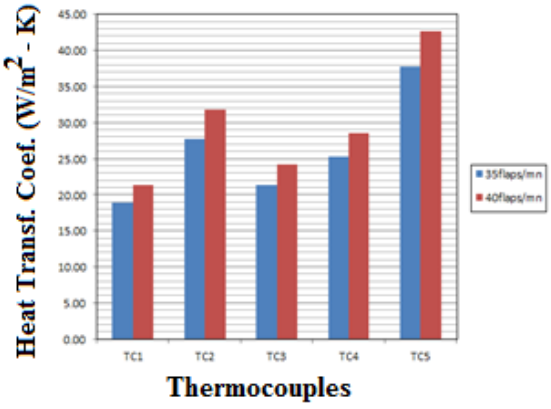

Fig. 5.34 Comparative analysis of local heat transfer Coefficient for a surface heat flux of 540 W/m^2

5.4 Conclusion of the experimental investigation of the flow over flapping plate

During the plate's flapping cycle, the visualization of the flow field with smoke particles shows the presence of tip vortices that form progressively and shed completely at end strokes, consecutive to the sudden stopping of the plate. A tangential vortex tube is created at all free edges of the moving plate and the diameter of the vortex increases until the shedding is proceeded. A parallel analysis between rigid and flexible plates indicates an improved interaction between the vortex and the plate's boundary layer for flexible models. This is due to the

backward bending motion that brings the center of the vortex closer to the center of the moving flexible plate; which is different for rigid flapping counterparts where the vortex dynamics mainly occur at the very tip of the plate.

The investigation of the surface temperature with J-Type thermocouples installed at chosen locations on the surface of the moving plate provides unsteady local temperature maps for free and forced convection experiments. In free convection, the plate's surface temperature always increases from the bottom to the top along the y axis. However, the overall temperature distribution indicates a significant improvement of the forced convection local heat transfer coefficients compared to the free convection case. Collected data show that the heat transfer rate from the plate is particularly enhanced at the free edges where vortices are formed and shed during flapping cycles. The cooling rate of the plate's surface increases with the flapping frequency of the plate. Also, the improved interaction between the tip vortex and the boundary layer of flexible flapping plates results in a higher cooling rate for flexible heated surfaces compared to rigid ones. In addition, the relative angular displacement of the tip at end strokes provides additional opportunity to heated flexible plates for heat transfer enhancement. Overall, the heat transfer coefficient increases with the following paramaters: the distance from the center of the flapping heated plate, the frequency of rotation of the plate, the size of the shedding vortex and the flexural strength of the material of the plate.

While in free convection, the lowest surface temperature is measured at the bottom of the plate due to buoyancy, in forced convection, the highest cooling rate is recorded at all free edges and locations where vortices are shed from the plate.

The next chapter will discuss and correlate experimental and theoretical data, in order to check the validity of the characteristics of the flow around flapping heated plates.

CHAPTER 6: DISCUSSION OF THE FLOW FIELD AND THE THERMAL CHARACTERISTICS INDUCED BY ROTATIONAL OSCILLATING PLATES

6.1. Discussion of the flow induced by rotationally oscillating heated plates

Background

The results of theoretical and experimental investigations of the flow and thermal characteristics induced by a rotationally oscillating heated plate present an interest due to the complexity of the three dimensional flow nature. Because of its unsteadiness, prediction can be made that such a flow will participate in the improvement of the heat transfer rate from the surface of the moving plate. Pohlhausen solved the surface temperature distribution over a flat plate heated at constant temperature, in a laminar flow field. Furthermore, the analytical solution to the flow over a flat plate heated at constant flux is also known [44]. However, a review of literature indicates that the study of the surface temperature distribution of rotationally oscillating plates has not been fully examined. Previous work has shown little experimental three-dimensional data about rotational oscillating plates [64]. Both theoretical and experimental investigations of current study have presented a flow field dominated by the presence of strong tip vortices during the motion of the plate. This chapter will discuss the dynamics of vortices that play a major role in the plate's surface temperature distribution. In fact, their interaction with the boundary layer of the plate increases the cooling rate of the moving surface by forced convection. However, knowledge of the main dimensionless parameters constitutes a significant step in the analysis of the flow and thermal characteristics induced by rotationally oscillating heated plates. First, the conservation equations need to be satisfied at each point of the fluid, in the vicinity of the flapping plate. Tang et al. [65] investigated the flow around rotationally oscillating surfaces using the Navier Stokes equations for incompressible flow in the Cartesian coordinates system, written here in indicial

notation where the conservations of mass and momentum are given respectively by equations (6.1) and (6.2).

$$\frac{\partial \rho}{\partial t} + \frac{\partial}{\partial x_j}(\rho u_j) = 0 \tag{6.1}$$

$$\frac{\partial}{\partial t}(\rho u_j) + \frac{\partial}{\partial x_j}(\rho u_j u_i) = -\frac{\partial p}{\partial x_i} + \frac{\partial \tau_{ij}}{\partial x_j} \tag{6.2}$$

$$\text{With:} \quad \tau_{ij} = \mu\left(\frac{\partial u_i}{\partial x_j} + \frac{\partial u_j}{\partial x_i}\right) - \frac{2}{3}\mu\frac{\partial u_l}{\partial x_l}\cdot\delta_{ij} \tag{6.3}$$

Where

x_i = the position vector, m
t = time, s
u_i = the velocity vector, m/s
p = the pressure, Pa
ρ = fluid density, kg/m^3
μ = fluid viscosity, $kg/s-m$
τ_{ij} =viscous stress tensor

In most applications involving rotational oscillating motion of a flat surface, a free stream already exists in the flow domain, mixing with the flow induced by the moving device. Examples include the flow around the wings of flying birds [3], or in the vicinity of swimming aquatic animals [66]. One of the challenges in the study of such flows is their highly unsteady nature. However, the present study focuses on the case where the motion of the fluid is originated by the rotational oscillating motion of the plate, in the absence of free stream. Here, the momentum equation in (6.2) is rewritten in dimensionless form [65] in (6.4) with the objective to identify the key dimensionless parameters describing the flow, expressed in equations (6.5), and (6.6), using a reference velocity defined in equation (6.7).

$$\frac{k}{\pi}\cdot\frac{\partial}{\partial t}(\overline{u_i}) + \frac{\partial}{\partial x_j}(\overline{u_j}\cdot\overline{u_i}) = -\frac{\partial \overline{p}}{\partial x_i} + \frac{1}{Re}\left(\frac{\partial^2 \overline{u_i}}{\partial x_j^2} + \frac{\partial^2 \overline{u_j}}{\partial x_i^2}\right) \tag{6.4}$$

$$\mathrm{Re} = \frac{U_{ref}\, c}{\nu} \tag{6.5}$$

$$k = \frac{2\pi f\, c}{U_{ref}} \tag{6.6}$$

$$U_{ref} = 2\pi f h_a \tag{6.7}$$

Where

c = characteristics length, m
f = frequency of rotation, $1/s$
h_a = flapping amplitude, m
k = reduced frequency
U_{ref} = reference velocity = tip velocity, m/s
Re = Reynolds number

The dimensionless form of the Navier Stokes equation of motion presents an advantage because it separates the reduced frequency and the Reynolds number, facilitating the analysis of each parameter [67]. Still, further examination of the flow characteristics induced by rotationally oscillating plates is performed for the determination of all relevant parameters describing fluid motion. The Navier Stokes equations of motion applied to a fluid element assuming a continuum and Newtonian fluid is expressed in the Cartesian coordinates system along x, y and z axes respectively in equations (6.8), (6.9), and (6.10) respectively along x, y, and z.

$$\rho\frac{Du}{Dt} = \rho g_x - \frac{\partial p}{\partial x} + \frac{\partial}{\partial x}\left[\mu\left(2\frac{\partial u}{\partial x} - \frac{2}{3}\nabla\cdot\vec{V}\right)\right] + \frac{\partial}{\partial y}\left[\mu\left(\frac{\partial u}{\partial y} + \frac{\partial v}{\partial x}\right)\right] + \frac{\partial}{\partial z}\left[\mu\left(\frac{\partial w}{\partial x} + \frac{\partial u}{\partial z}\right)\right] \tag{6.8}$$

$$\rho\frac{Dv}{Dt} = \rho g_y - \frac{\partial p}{\partial y} + \frac{\partial}{\partial y}\left[\mu\left(2\frac{\partial v}{\partial y} - \frac{2}{3}\nabla\cdot\vec{V}\right)\right] + \frac{\partial}{\partial z}\left[\mu\left(\frac{\partial v}{\partial z} + \frac{\partial w}{\partial y}\right)\right] + \frac{\partial}{\partial x}\left[\mu\left(\frac{\partial u}{\partial y} + \frac{\partial v}{\partial x}\right)\right] \tag{6.9}$$

$$\rho\frac{Dw}{Dt} = \rho g_z - \frac{\partial p}{\partial z} + \frac{\partial}{\partial z}\left[\mu\left(2\frac{\partial w}{\partial z} - \frac{2}{3}\nabla\cdot\vec{V}\right)\right] + \frac{\partial}{\partial y}\left[\mu\left(\frac{\partial w}{\partial x} + \frac{\partial v}{\partial z}\right)\right] + \frac{\partial}{\partial y}\left[\mu\left(\frac{\partial v}{\partial z} + \frac{\partial w}{\partial y}\right)\right] \tag{6.10}$$

Assuming constant viscosity, constant density and neglecting gravity, the x-component of the momentum equation is simplified further, yielding equation (6.11) for a 2D analysis.

$$\frac{\partial u}{\partial t} + u\frac{\partial u}{\partial x} + v\frac{\partial u}{\partial y} = -\frac{1}{\rho}\frac{\partial p}{\partial x} + \nu\left[\frac{\partial^2 u}{\partial x^2} + \frac{\partial^2 u}{\partial y^2}\right] \tag{6.11}$$

Where

$p = \text{fluid pressure, Pa}$

$\vec{V} = \text{velocity vector of moving fluid, m./s}$

$x, y, z = \text{position of fluid in Cartesian coordinate system, m}$

$u, v, w = \text{components of velocity vector, } m/s$

$t = \text{time, s}$

$g_x, g_y, g_z = \text{components of gravitational acceleration field, } N/s^2$

$\rho = \text{fluid density, } Kg/m^3$

$\mu = \text{dynamic viscosity, } kg/s-m$

A dimensional analysis is performed to replace independent and dependent variables $x; y; t; u; v$ and p with dimensionless variables x^*, y^*, t^*, u^*, v^* and p^* using characteristic quantities: the length L, the time T and the velocity U.

Setting: $$t^* = \frac{t}{T}; x^* = \frac{x}{L}; y^* = \frac{y}{L}; u^* = \frac{u}{U}; v^* = \frac{v}{U} \text{ and } p^* = \frac{p}{\rho U^2} \tag{6.12}$$

the x-component of the Navier Stokes equation of motion is now expressed in equation (6.13) in terms of the Stokes number S defined in equation (6.14), after few transformations detailed in Paragraph 9.4.1 of the Appendix.

$$\frac{1}{2\pi}\cdot\frac{\partial u^*}{\partial t^*} + \left(u^*\cdot\frac{\partial u^*}{\partial x^*} + u^*\cdot\frac{\partial u^*}{\partial y^*}\right) = -\frac{\partial p^*}{\partial x^*} + \frac{1}{S^2}\cdot\left(\frac{\partial^2 u^*}{\partial {x^*}^2} + \frac{\partial^2 u^*}{\partial {y^*}^2}\right) \tag{6.13}$$

Where $$S = \sqrt{\frac{\omega L^2}{\nu}} \tag{6.14}$$

The dimensionless Stokes number [68] defined as $\beta = fL^2/\nu$, sometimes called the reduced frequency can be used to measure the degree of unsteadiness of the flow [69].

In this study, important dimensionless parameters have been discussed in the analysis of the flow induced by rotationally oscillating plates. Now, it is important to study the related flow characteristics resulting from theoretical and experimental investigations. Previous chapters have indicated the presence of strong tip vortices that can significantly influence the flow and the

thermal characteristics in the vicinity of the moving plate's surface. Therefore, of interest is the study of the mechanism of vortex dynamics over rotationally oscillating plates.

6.2 Mechanism of vorticity dynamics induced by rotationally oscillating plates.

6.2.1 Introduction

The visualization of the flow with smoke particles has shown a flow field where particles are either attracted or repelled by the moving device, generating strong vortices as a result of the rotation of fluid elements around the tip of the plate. Vorticity ξ is defined [57] as the measure of the rotation of fluid particles during their motion in the flow field; it is expressed in the cylindrical coordinate system using equation (6.15).

$$\vec{\zeta} = \nabla \times \vec{V} = \hat{e}_r\left(\frac{1}{r}\frac{\partial V_z}{\partial \theta} - \frac{\partial V_\theta}{\partial z}\right) + \hat{e}_\theta\left(\frac{\partial V_r}{\partial z} - \frac{\partial V_z}{\partial r}\right) + \hat{k}\left(\frac{1}{r}\frac{\partial r V_\theta}{\partial r} - \frac{1}{r}\frac{\partial V_r}{\partial \theta}\right) \tag{6.15}$$

According to the Stokes theorem, the total vorticity enclosed in a closed contour is equivalent to the circulation Γ around the contour expressed in equation (6.16).

$$\Gamma = \oint_C \vec{V} \cdot d\vec{S} = \iint_A \left(\nabla \times \vec{V}\right)_z dA \tag{6.16}$$

Where

$\Gamma =$ circulation around a closed contour, m^2/s
$\vec{\zeta} =$ vorticity vector, $1/s$
$\vec{V} =$ velocity vector, m/s
$A =$ area encompassed by the contour, m^2
$\vec{S} =$ vector, m
$C =$ closed curve fixed in the flow field
$(r, \theta, k) =$ variable in cylindrical coordinate
$(V_r, V_\theta, V_z) =$ velocity components cylindrical

During the plate's flapping cycles, vortices are transported over the surface in all directions toward the free edges of the moving plate, prior to their shedding. The vorticity transport equation [70] is derived from the momentum equation as detailed in Paragraph 9.4.2 and expressed in symbolic form in equation (6.17).

$$\frac{D\omega}{Dt} = \omega \cdot \nabla v + \nu \nabla^2 \omega \tag{6.17}$$

Where

$\omega =$ vorticity vector, $1/s$
$v =$ velocity of the fluid, m/s
$t =$ time, s

The vorticity transport equation in (6.16) plays the same role as the momentum equation of motion in equation (6.2). However, the pressure term does not appear because vorticity tracks only the effect of viscous forces. Pressure and gravity act at the center of mass of a particle and thus do not directly modify vorticity. Therefore they cannot produce fluid rotation. Vortices are the result of fluid rotation caused by the unbalanced shear stresses acting tangentially at the surface of the particles [70].

6.2.2 Discussion of vorticity dynamics over the rotating plate

With a careful observation of the flow visualization results obtained in chapter 6, the dynamics of vortices can be explained using a sectional view of the flow field, along the median plane of the plate as illustrated in Fig.6.1.The formation of a vortex tube tangent to the plate's surface is observed during the impulsive rotation of the plate from rest. The vortex starts with a circular shape of small diameter generated by accelerated fluid particles around the tip of the moving plate. But during the rotation of the plate, additional fluid layers participate in its growth. Because its diameter increases with the stroke angle, the vortex is brought closer to the center of the plate's surface. This provides a greater opportunity for its interaction with the plate's boundary layer over a larger surface area. It is observed from the flow visualization experiment that while the plate rotates clockwise, the immediate surrounding fluid rolls over the surface along the radius. Therefore, counterclockwise vortices are formed on the back surface until the separation of fluid layers from the plate in the vicinity of the tip.

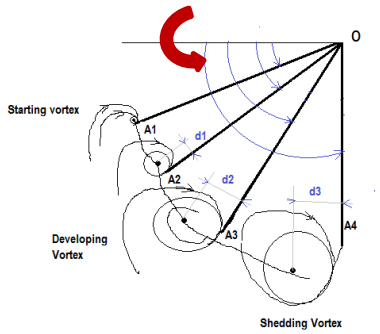

Fig. 6.1 Dynamics of tip vortex during the down stroke motion

A hook-shaped tip vortex is formed as illustrated in Fig. 6.2 as the flowing fluid in the vicinity of the plate's surface spins toward the core of the vortex attracting more particles from the surrounding environment. Along their path, rotating particles describe tangential circles around the tip of the plate, removing fluid layers from its surface. The fluid removed is directed toward the center of the vortex that engages more fresh and cold incoming fluid from the surrounding atmosphere.

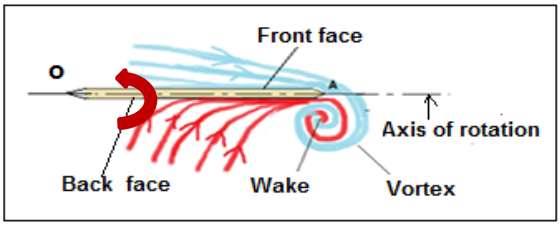

Fig. 6.2 Details of tip vortex during the upstroke motion

Overall, the vortex is first initiated with the acceleration of the plate from rest, develops with the stroke angle and the process continues throughout the cycle as described in Fig .6.3 until its diameter reaches a critical size near the end of the half-cycle. When the plate stops suddenly and reverses its motion, the detached fluid in the rear which is attracted by the wake behind, impacts the surface of the plate. However, due to its size, the vortex is shifted quickly to the opposite side of the moving plate, clearing out regions located at the edges. Such a quick change in the direction of the motion is subject to substantial heat loss from the tip of the plate.

The boundary layer of the flapping surface exerts a retarding unbalanced shear force on fluid particles creating shear layers which are responsible for fluid rotation at the tip of the plate due to the viscosity of the fluid.

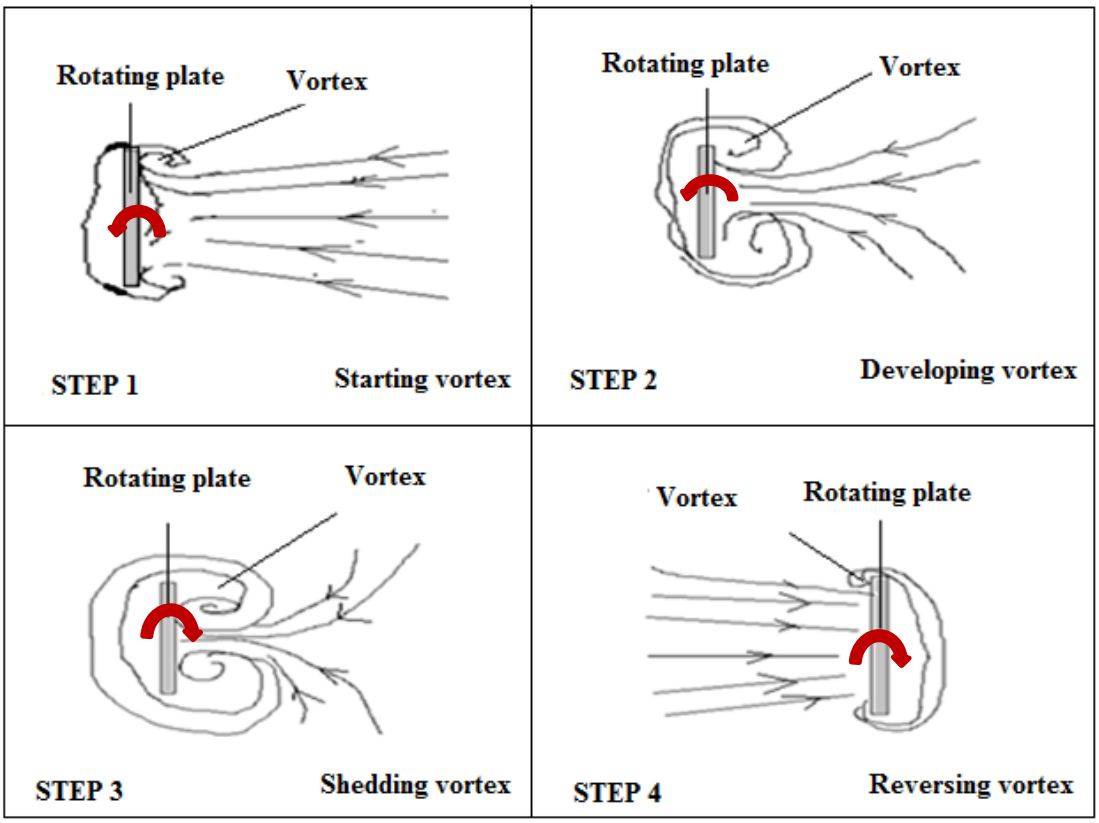

Fig. 6.3 Dynamics of vortices around flapping plate during a complete stroke

An analogy is made for the illustration of the mechanism of vortex shedding where the displacement of fluid elements over the plate's surface is compared to passengers walking inside a moving bus, altogether in the same direction. Any sudden stopping of the vehicle's motion is subject to forward propulsion of passengers out of the vehicle due to inertia, unless they hold a solid surface attached to the vehicle. This image explains the concept of flow separation at end strokes during the rotational oscillations of the plate. In conclusion, the complete shedding of the vortex is triggered by the impulsive stopping of the plate. phenomenon occurs regardless of

the direction of rotation of the plate as illustrated in Fig. 6.4, with a continuous fluid supply from the surrounding atmosphere, participating in the formation of the tip vortex.

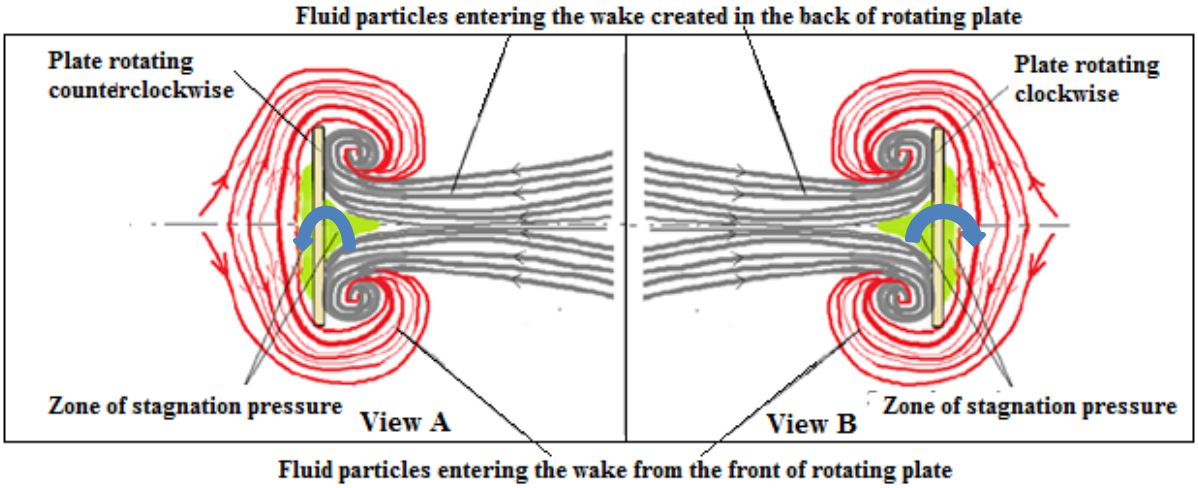

Fig. 6.4 Dynamics of the vortex induced by a flapping plate: View A: Counterclockwise motion. View B: Clockwise motion.

6.2.3 Analysis of computational and experimental results

Throughout the experimental investigation of the flow around the rotationally oscillating plate at a rate of $2 rad/s$, photographs of the flow field were captured during the down stroke motion for three different angular positions at $10, 30$ and 60^{o}. Results are compared to the static pressure and velocity contours obtained from the computational investigational with FLUENT 6.3 as illustrated in Fig. 6.5. According to the flow visualization results, the size of the vortex grows with the angular position. The growth of the tip vortex matches the increase in the area of higher velocity zones on the plate's surface at the tip provided by the computational results. FLUENT results indicate that zones of low pressure located in the vicinity of the flapping device correspond to higher velocity magnitudes. In conclusion, experimental and theoretical results are in good agreement because the tip regions where vortices are generated are characterized by low pressure or high velocity, demonstrating the acceleration of fluid particles at these locations. For a plate's characteristics length of 0.2m, the linear velocity of the tip can be estimated to be

0.4m/s. However, the maximum velocity value of 3m/s read here is the velocity of the fluid induced by the tip of the plate.

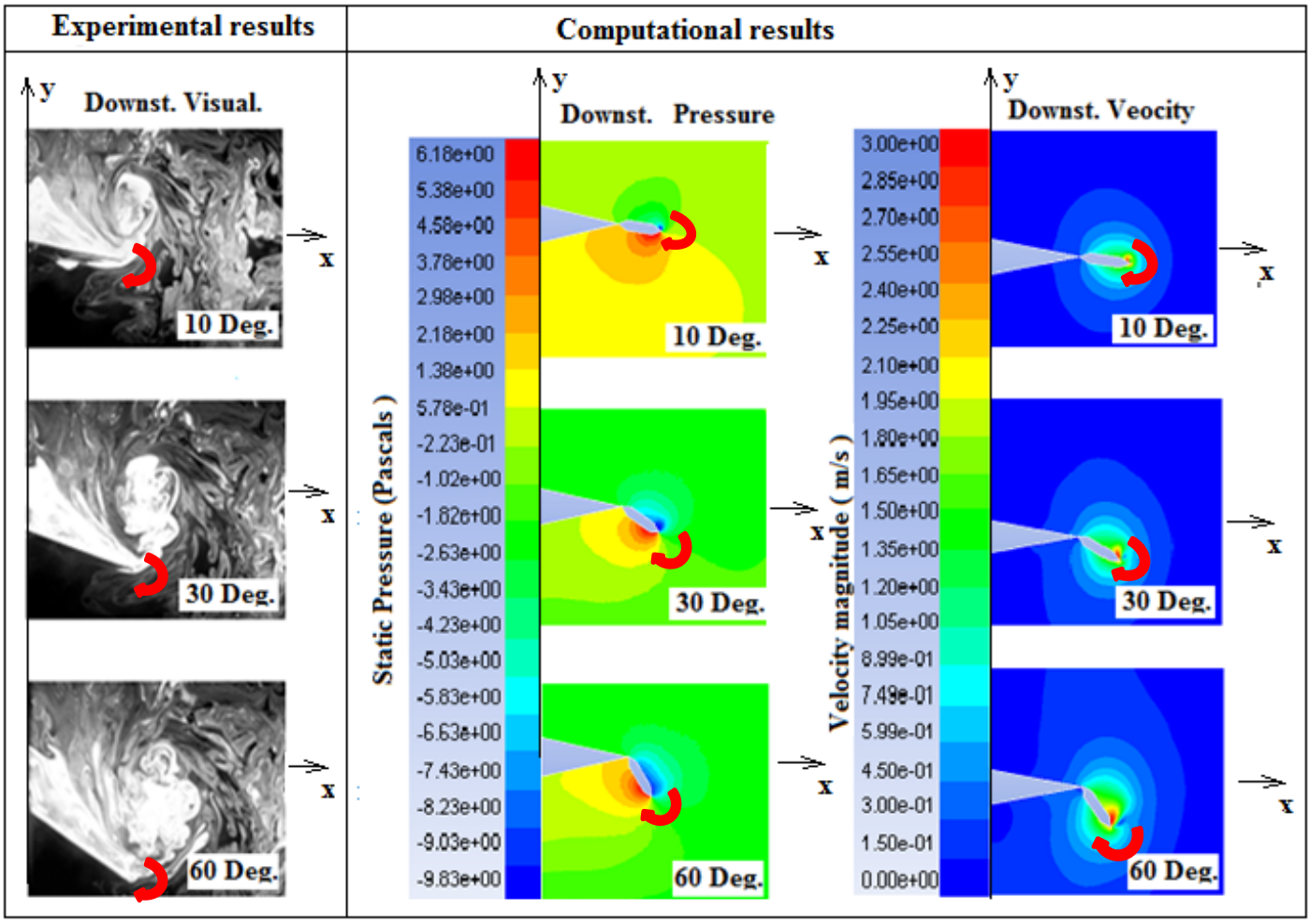

Fig. 6.5 Computational flow field contours vs. experimental flow visualization with smoke particles around a flapping plate at a rate of 2 rad/s

6.2.4 Discussion of the flow induced characteristics

a) Energy distribution behind flapping plate

From the observation of the flow field in the back of the rotating plate illustrated earlier in Fig. 6.4, a sectional cut of the impinging jet of fluid in the vicinity of the plate's surface is characterized by energy zones distributed as sketched in Fig. 6.6. One can distinguish an outer layer made of fluid particles with high kinetic energy induced by the wake at the tip of the plate and a central zone where the energy of fluid particles is the lowest. In the outer layer, particles

are accelerated by the dynamics of tip vortices, which increases their kinetics energy. The high energy of particles in the outer layer is due to the energy of particles that decreases as we move to the core of the jet of fluid. This explains the presence of a stagnation pressure in the central zone of the plate's surface characterized by a quiescent fluid. Consequently, the surface temperature of the flapping plate is the highest at the center of the back face.

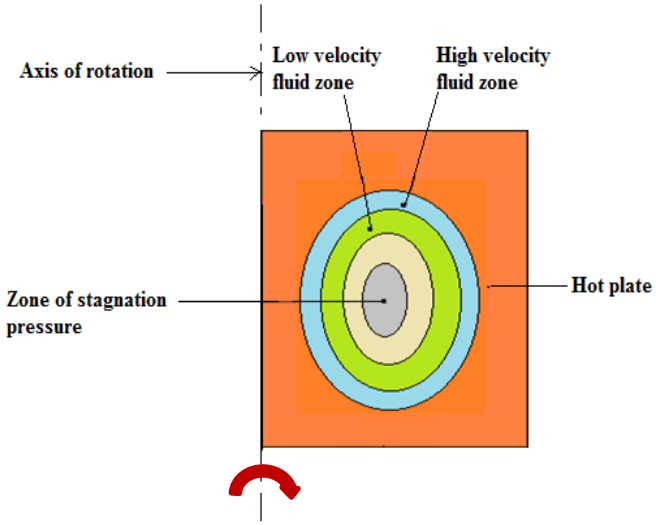

Fig. 6.6 Flow energy distribution of impinging fluid jet behind flapping plate

b) Aerodynamics flow induced characteristics

The main interest in the study of the flow around rotationally oscillating plates is not limited to their heat transfer enhancement applications but also for its participation in the generation of aerodynamics forces induced by vortices, such as the lift and the drag. The lift force is enhanced if the vortex is created in the immediate surroundings of the flapping device [57]. This is the case for flexible flapping plates, discussed in the next paragraph, where forming and shedding vortices are located closer to the plate's surface due to the flexibility of the material. The lift force [57] is derived in equation (6.18) using γ , the first moment of vortices [2] defined in equation (6.19); the induced velocity v generated by the flow is determined in terms of the vorticity vector ω in equation (6.20).

$$L = -\rho \frac{d\gamma}{dt} + \rho \frac{d}{dt} \int_A V dA \tag{6.18}$$

$$\gamma = \int_R r \times \omega dR \tag{6.19}$$

$$v = \frac{1}{4\pi} \int_V \omega \times \frac{r}{r^3} dV \tag{6.20}$$

Where

ω = vorticity vector, $1/s$
L = sectional aerodynamics force, N
ρ = fluid density, kg/m^3
v = induced velocity by the vortex, m/s
r = distance separating induced velocity to vortex, m
V= entire control volume of fluid comprising the plate, m^3
R= area of the control surface surrounding all vortex elements, m^2
A= cross sectional area of the plate, m^2

The aerodynamics forces can be derived from the solution of the Navier Stokes equations of motion where the lift (L) and the drag (D) acting on the moving plate are determined using the definition in equations (6.21) and (6.22):

$$C_L = \frac{L}{0.5\rho U^2 S} \tag{6.21}$$

$$C_D = \frac{D}{0.5\rho U^2 S} \tag{6.22}$$

Where

C_L = Lift coefficient
C_D = Drag coefficient
ρ = fluid density, kg/m^3
S = plate cross sectional area, m^2

In conclusion, the flow characteristics over flapping surfaces are influenced by the vortical structure of the flow field, responsible for the generation of aerodynamics forces and also for heat transfer enhancement by forced convection. Several examples of applications based on rotationally motion are found in nature in insects and bird flights. However in most of these applications, the flapping device is not rigid but flexible. Therefore the flow around flexible

oscillating plates is investigated here for the development of new technological applications and also for the understanding of biological systems.

6.3 Discussion of the flow around flexible flapping plates

6.3.1 Introduction

In the case of flexible flapping plates, the Navier Stokes equations are formulated to account for the solid interacting with the fluid [71] where the motion of the fluid is described by (6.23) and (6.24), and the motion of the solid by (6.25). However, the solid-fluid structure needs to be in equilibrium leading to equation (6.28).

Fluid:
$$\frac{\partial v_i^f}{\partial x_i} = 0 \tag{6.23}$$

$$\rho^f \frac{\partial v_i^f}{\partial t} + \rho^f v_j^f \frac{\partial v_i^f}{\partial x_j} = \frac{\partial \sigma_{ji}^f}{\partial x_j} \tag{6.24}$$

Solid:
$$\rho^s \frac{dv_i^s}{dt} = \frac{\partial \sigma_{ji}^s}{\partial x_j} \tag{6.25}$$

With: σ_{ij}^f the stress tensor for a Newtonian fluid and σ_{ij}^s the Piola-Kirchoff stress tensor for linear isotropic elastic body defined as:

$$\sigma_{ij}^f = p\delta_{ij} + \mu\left(\frac{\partial v_i^f}{\partial x_j} + \frac{\partial v_j^f}{\partial x_i}\right) \tag{6.26}$$

$$\sigma_{ij}^s = \lambda\delta_{ij}\frac{\partial u_k^s}{\partial x_k} + G\left(\frac{\partial u_i^S}{\partial x_j} + \frac{\partial u_j^S}{\partial x_i}\right) \tag{6.27}$$

$$\sigma_{ij}^f \cdot n_j^f + \sigma_{ij}^s \cdot n_j^s = 0 \tag{6.28}$$

Where

u_i = displacement of the solid body, m

v_i = velocity of fluid, m/s

p = fluid pressure, Pa

ρ = fluid density, kg/m^3

μ = fluid dynamics viscosity, kg/s – m
λ, G = Lame constants
δ_{ij} = Kronecker delta
n_j^f ; n_j^s = outward unit vectors for fluid and solid

A dimensional analysis is performed to determine the key dimensionless parameters that govern the flow induced by flexible flapping plates by setting new dimensionless variables in equation (6.29).

$$\hat{u}_i^s = u_i^s/U \; ; \hat{v}_i^s = v_i^s/U \; ; \; \hat{v}_i^f = v_i^f/U \; ; \hat{p} = p/P \; ; \text{and } \hat{t} = t/T \tag{6.29}$$

Using the new variables, equation (6.24) is transformed to give (6.30) which is simplified further, dividing it through by the fluid inertial force I_f due to the convective acceleration. The new expression of the momentum equation with dimensionless parameters is given by equation (6.31).

$$\frac{\rho^f V}{T}\frac{\partial \hat{v}_i^f}{\partial \hat{t}} + \frac{\rho^f V^2}{L}\hat{v}_j^f \frac{\partial v_i^f}{\partial x_j} = -\frac{P}{L}\frac{\partial \hat{p}}{\partial \hat{x}_i} + \frac{\mu V}{L^2}\frac{\partial^2 \hat{v}_i^f}{\partial \hat{x}_j^{\,2}} \tag{6.30}$$

$$St\frac{\partial \hat{v}_i^f}{\partial \hat{t}} + \hat{v}_j^f \frac{\partial \hat{v}_i^f}{\partial \hat{x}_j} = -Eu\frac{\partial \hat{p}}{\partial x_i} + \frac{1}{Re}\frac{\partial^2 \hat{v}_i^f}{\partial \hat{x}_j^{\,2}} \tag{6.31}$$

With: $St = \dfrac{L}{TV}$ = Strouhal number (6.32)

$$Eu = \frac{p}{\rho^f V^2} = \text{Euler number} \tag{6.33}$$

$$Re = \frac{\rho^f VL}{\mu} = \text{ Reynolds number} \tag{6.34}$$

$$I = \frac{\rho^f V^2}{L} = \text{fluid inertial force} \tag{6.35}$$

Where

L = characteristics length of plate, m
V = velocity of solid structure, m/s
U = displacement of solid structure, m
P= Reference pressure, Pa

A similar analysis is performed with the new dimensionless variables defined earlier, transforming equation (6.25) to dimensionless form in (6.36). Further simplification can be achieved, dividing the latter equation by the structural inertial force I_s and replacing U by VT to give (6.37).

$$\frac{\rho^s V}{T}\frac{d\hat{v}_i^s}{d\hat{t}} = \frac{(\lambda+G)U}{L^2}\frac{\partial^2\hat{u}_k^s}{\partial\hat{x}_k\partial\hat{x}_i} + \frac{GU}{L^2}\frac{\partial^2\hat{u}_i^s}{\partial\hat{x}_j\partial\hat{x}_j} \tag{6.36}$$

$$\frac{d\,\hat{v}_i^s}{d\hat{t}} = \frac{(\lambda+G)T^2}{\rho^s L^2}\frac{\partial^2\hat{u}_k^s}{\partial\hat{x}_k\partial\hat{x}_i} + \frac{GT^2}{\rho^S L^2}\frac{\partial^2\hat{u}_i^s}{\partial\hat{x}_j\partial\hat{x}_j} \tag{6.37}$$

With:
$$\lambda = \frac{2G\nu}{1-2\nu} \tag{6.38}$$

$$E = 2G(1+\nu) \tag{6.39}$$

Where

E = Young's modulus of plate's material, N/m^2

G = Bulk modulus of plate's material, N/m^2

ν = Poisson's ratio

Key parameters such as the Reynolds number, the Strouhal number and the Euler number have been identified for the analysis of flexible flapping plates, including the Young's modulus to account for the flexural strength of the material and the Poisson's ratio accounting for the stretching and the contraction of the material as it interacts with the fluid during the rotational oscillating motion of the plate. These parameters will help in the understanding of results obtained from the experimental investigation.

6.3.2 Flow induced by flexible flapping plates

Experimental investigation results have shown that flows induced by rotationally oscillating flexible and rigid plates are quite-similar but not the same. The dynamics of vortices for flexible models exhibit additional features that participate in the improvement of the induced flow and thermal characteristics. During its rotation, the plate is curved to the back due to the drag force on the front surface. The angular rotation of the tip of flexible plates is greater than the one of

rigid models by $2\Delta\theta$, where $\Delta\theta$ is the extra angular displacement of the tip at end strokes, due to the flexibility of the material. Consequently, a relative cycle performed by the tip of flexible plates is added to the regular stroke angle swept by rigid models as described in Fig. 6.7.

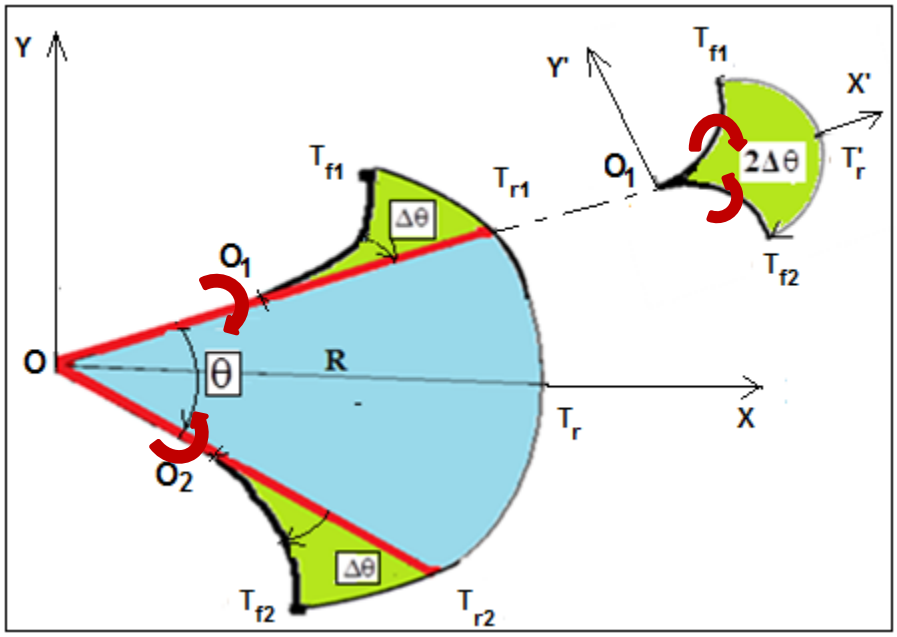

Fig. 6.7 Relative angular rotation of flexible flapping plates

The total distance d_{TF} travelled by the tip of the flexible flapping plate over a complete cycle includes a bulk displacement of the whole plate over a distance of $R(2\theta)$ and an additional displacement of the tip only of $R'(2\times 2\Delta\theta)$, evaluated using equation (6.40).

$$d_{TF} = R(2\theta) + R'(4\Delta\theta) \tag{6.40}$$

Where

R = characteristic length of plate, m
$R' = OO_1$ = plate portion of major deformations, m
θ = stroke angle described by rigid plate, rad.
$\Delta\theta$ = extra angular displacement of the tip of flexible plate, rad

Assuming $R' = R/2$, the total displacements of the tips of rigid d_{TF} and flexible d_{TR} plates over a complete flapping cycle are given respectively by equation (6.41) and (6.42) and the additional

displacement Δd_{TF} performed by the tip of flexible plates is given by equation (6.43) which is the difference between both displacements.

$$d_{TF} = 2R(\theta + \Delta\theta) \tag{6.41}$$

$$d_{TR} = 2R\Delta\theta \tag{6.42}$$

$$\Delta d_{TF} = 2R\Delta\theta \tag{6.43}$$

The flow around flexible flapping plates requires particular attention because its geometry changes with the stroke angle and vortex shedding occurs each time the tip of the plate accelerates or decelerates. Since the tip of flexible plates travels a longer distance compared to rigid counterparts, an opportunity is provided for further heat dissipation from their surface. A sectional cut across the center of the plate, perpendicular to the axis of rotation as shown in Fig. 6.8 illustrates the deformation of the tip of the flexible plate. It is observed that the center of the shedding vortex is brought closer to the center of the plate's surface. Therefore, the penetration depth of the vortex inside the boundary layer over the surface of the flexible plate is increased because the center of the vortex is relocated closer to the axis of rotation of the plate over a distance Δd compared to rigid counterparts. As a result, the area S_f swept by the tip vortex from the flexible plate is greater than the equivalent area S_r from the rigid equivalent. An illustration of the deformed tip of the flexible plate is provided in Fig. 6.9 showing how the straight segment RT_r along the surface of the rigid plate became an arc of circle RT_f for the flexible equivalent. Therefore, the detached flow from the surface of the flexible plate is offered an additional opportunity to impact again the plate's surface during the shedding of the vortex. Conversely, the separated flow from rigid plates completely leaves the surface as illustrated in Fig.6.9.

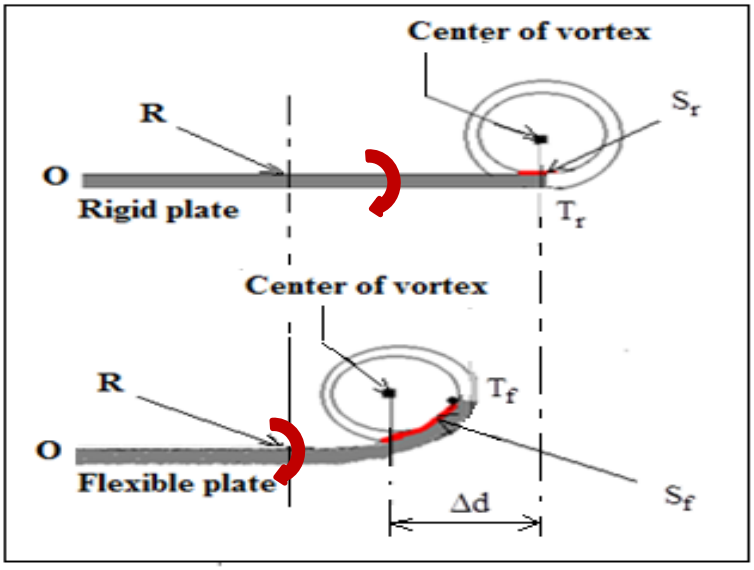

Fig. 6.8 Comparative analysis of vortex shedding between rigid and flexible plates

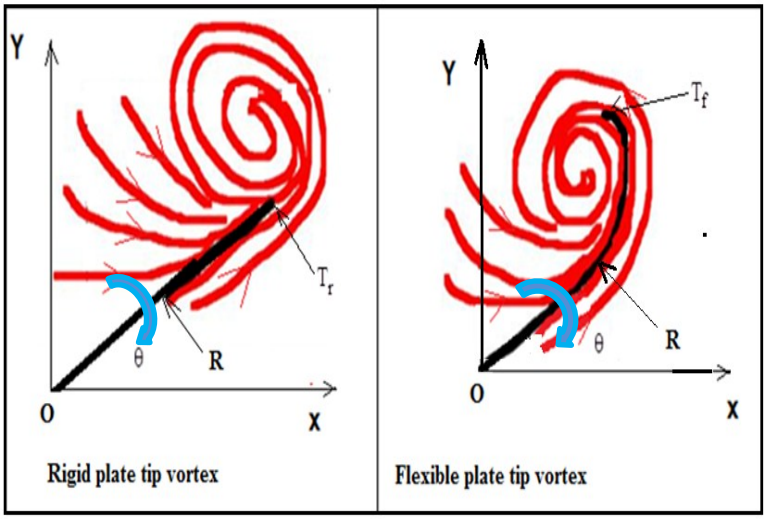

Fig. 6.9 Deforming tip of flexible plates compared to rigid ones within the flapping cycle

In conclusion, besides the fact that the tip of the flexible plate travels a longer arc length, it provides larger interaction area between the vortex and the plate's boundary layer compared to the rigid counterpart. As a result, a significant amount of fluid is separated from the boundary layer during the shedding of the tip vortex, promoting heat transfer from the surface of the flexible plate.

6.4 Discussion of the surface thermal characteristics induced by flapping plates

6.4.1 Introduction

In the current research, the flapping plate is heated at constant flux q'' on both sides. Therefore, in the close vicinity of its surface, the energy equation for incompressible fluid in equation (6.44) is used for the calculation of the surface temperature distribution [72].

$$\rho C_p \frac{DT}{Dt} = \nabla \cdot (k\nabla T) + q''' + \mu\Phi \tag{6.44}$$

Where Φ the general dissipation function expressed in Cartesian coordinates system is given by equation (6.45).

$$\begin{aligned}\Phi = 2&\left[\left(\frac{\partial u}{\partial x}\right)^2 + \left(\frac{\partial v}{\partial y}\right)^2 + \left(\frac{\partial w}{\partial z}\right)^2\right] \\ &+ \left[\left(\frac{\partial u}{\partial y} + \frac{\partial v}{\partial x}\right)^2 + \left(\frac{\partial v}{\partial z} + \frac{\partial w}{\partial y}\right)^2 + \left(\frac{\partial w}{\partial x} + \frac{\partial u}{\partial z}\right)^2\right] \\ &- \frac{2}{3}\left(\frac{\partial u}{\partial x} + \frac{\partial v}{\partial y} + \frac{\partial w}{\partial z}\right)^2\end{aligned} \tag{6.45}$$

Where

T = surface temperature, ^{o}C
u, v, w = components of the velocity in x, y, and z directions, m/s
q''' = internal energy generated by the plate, W
t = time, s
ρ = fluid density, kg/m^3
μ = dynamic viscosity of fluid, $kg/s-m$
C_p = specific heat of the fluid, $J/kg-^{o}C$
k = thermal conductivity of the fluid, $W/m-^{o}C$

The energy equation can be simplified using few assumptions applied to the model, which are: constant thermal conductivity, no internal energy generation and neglecting viscous dissipation.

Therefore, the energy equation is reduced to equation (6.49) expressed in the Cartesian coordinates system.

$$\rho C_p\left(\frac{\partial T}{\partial t}+u\frac{\partial T}{\partial x}+v\frac{\partial T}{\partial y}+w\frac{\partial T}{\partial z}\right)=k\left(\frac{\partial^2 T}{\partial x^2}+\frac{\partial^2 T}{\partial y^2}+\frac{\partial^2 T}{\partial z^2}\right) \tag{6.49}$$

A constant heat flux q'' is applied to the surface of the moving plate and the temperature distribution is determined using a 3D computational simulation of the flow over several flapping cycles with FLUENT 6.3. To check the improvement of the local surface heat transfer coefficient due to the rotational oscillating motion of the plate, computational investigation results are compared to free convection analytical solution.

6.4.2 Surface convection over rotationally oscillating plates

a) Correlation between flow field and surface temperature distribution induced by a rotationally oscillating heated plate.

In this paragraph, the results of computational and experimental investigations of the flow induced by rotationally oscillating heated plates obtained in chapters 5 and 6 are compared with the objective to discuss the impact of the flow field on the surface temperature distribution of the moving model. The plate is rotated in the vertical position at a rate of 2 rad/s and a heat flux $q'' = 540 W/m^2$ is applied to its surface. Both vertical and horizontal positions are considered here in order to facilitate the comparison of surface thermal data recorded at specific points (P1, P2, P3, P4, P5, and P6) as shown in Fig. 6.10. According to Views A, B, and C of Fig. 6.11, the 2D velocity pathlines and the 3D velocity vectors, resulting from FLUENT simulation, agree with the flow visualization photograph, on the existence of tip vortices observed during the rotational oscillations of the plate.

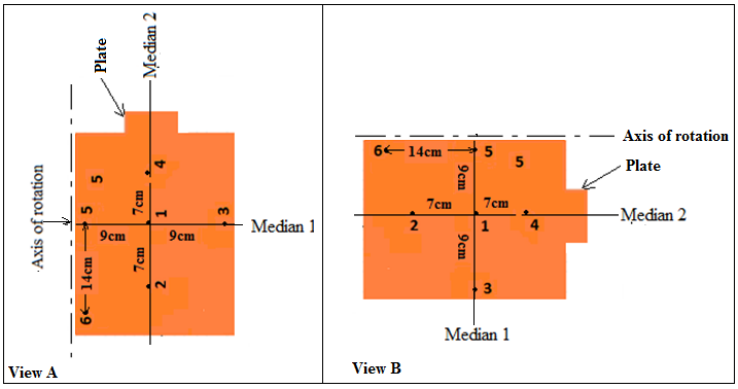

Fig. 6.10 Sketch of the rotating plate with characteristics tracking location

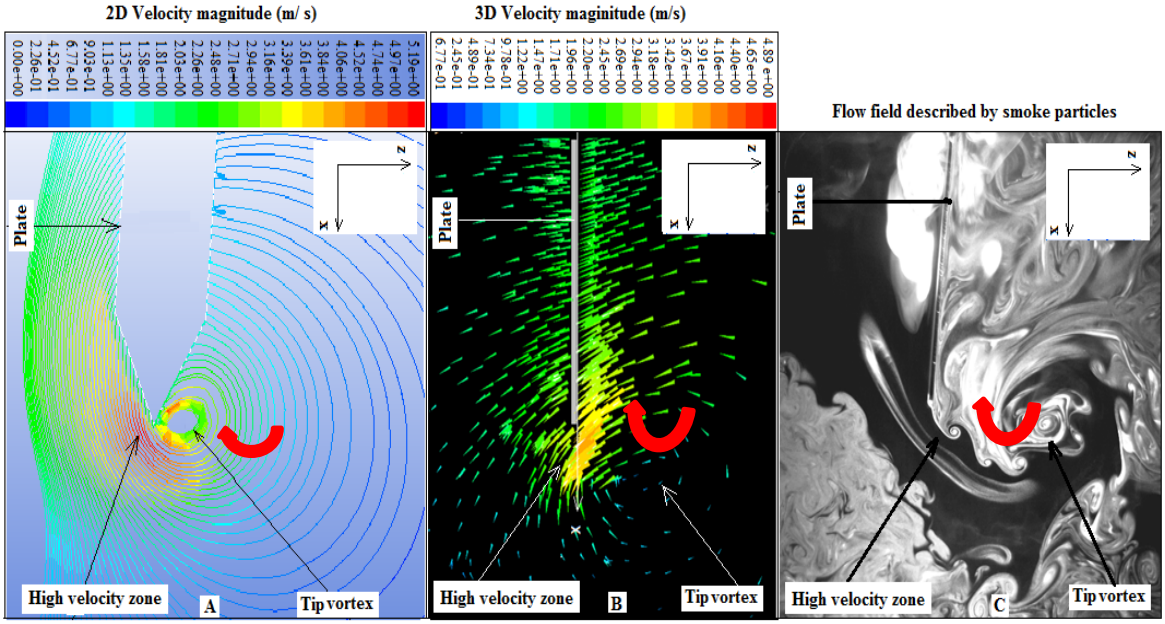

Fig. 6.11 Tip vortex induced by the rotationally oscillating plate at the onset of the upstroke motion

The flow path lines colored by velocity magnitudes in View A obtained from simulations of the flow with FLUENT agree with the symmetrical flow field about the y axis, resulting from the experimental investigation in view B of Fig. 6.12. Due to the forming and shedding vortices, the impact of the flow field can be seen in the symmetrical temperature map in View C of the same figure. The symmetrical surface temperature distribution (View C of Fig.6.12) is made of a higher temperature region (Points 1, 2, 4 and 5) and a cooler zone (Points 3 and 6), separated by a U shape boundary. Overall, one can see the impact of

tip vortices discussed in Fig. 6.11, in the improvement of the heat transfer from the surface of the rotating plate.

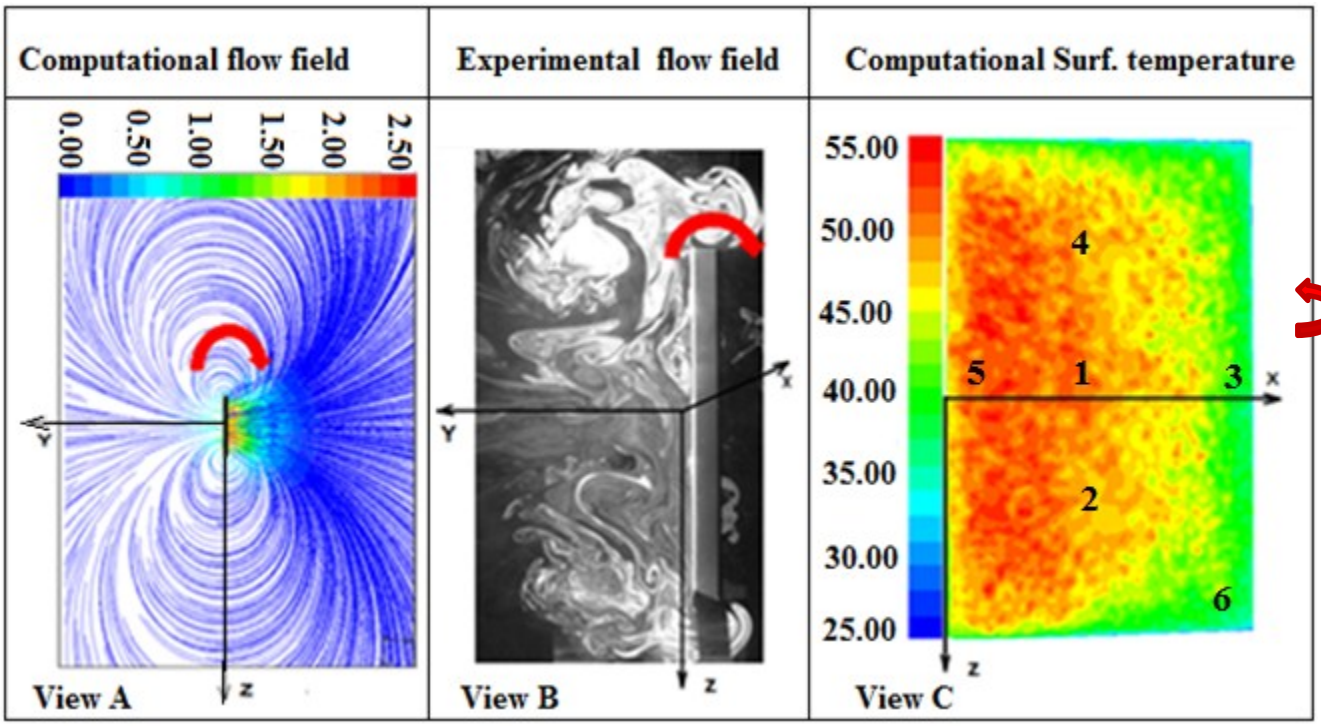

Fig. 6.12 Impact of the flow field on the surface temperature distribution of a rotationally oscillating plate at 2rad/s heated at a constant flux of 540W/m^2

b) Experimental vs. computational transient surface temperature induced by the rotational oscillating motion of a flat plate

In this paragraph, the plate's local surface temperature distributions are compared for computational and experimental transient solutions, when the plate is subject to rotationally oscillating motion. Temperature profiles obtained from both methods are correlated over a time period of 50 seconds for a surface heat flux of $q" = 540 W/m^2$, as shown in Fig.6.13. At first sight, all local temperature curves look analogous. For both experimental and computational results, the distribution of the surface temperature is preserved: the lowest heat transfer coefficient is noticeable at the center of the plate and the highest in the corner.

Although computational results are carried over a very short period of time, temperature results from both methods agree in an acceptable average range less than 5%.

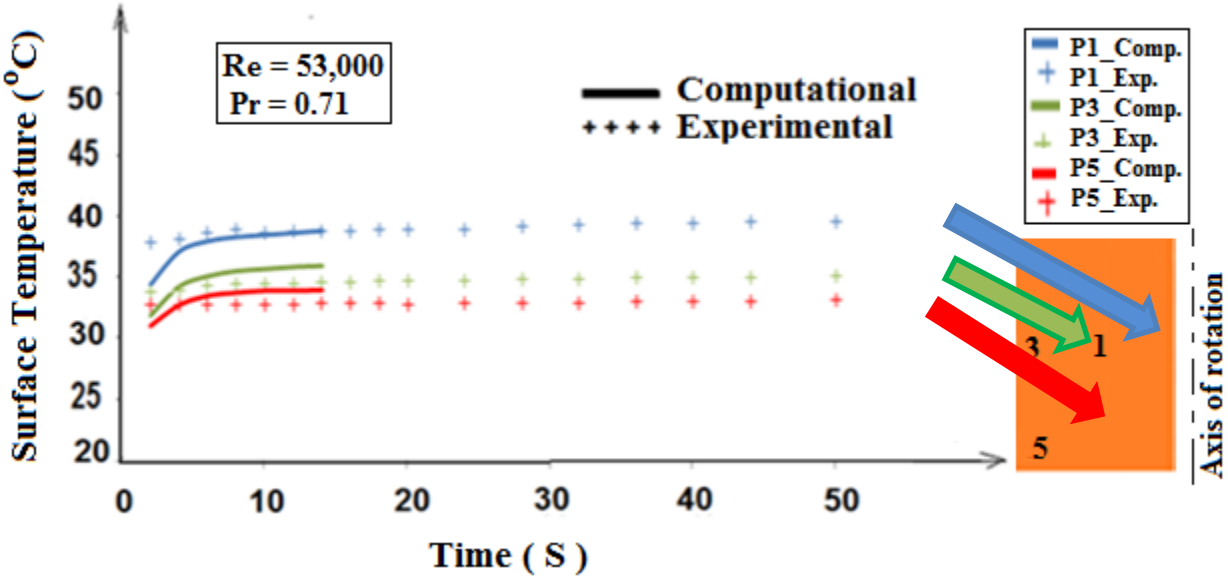

Fig. 6.13 Experimental vs. computational surface temperature induced by the rotational oscillating motion of a flat plate at 2 rad/s with a surface heat flux of 540W/m^2

6.5 Conclusion of discussion of the flow induced by rotationally oscillating heated plates flapping plates

In conclusion, the surface temperature of a plate heated at constant flux always increases with time but with a decreasing slope before reaching an asymptotic profile at steady state. Although the computational simulation over the rotationally oscillating heated plate is performed over a shorter period of time, the result matches experimental findings in the similarity of the profiles. Overall, forced convection heat transfer provides higher cooling rate compared to free convection. Moreover, the cooling rate is enhanced when the plate is subject to a rotationally oscillating motion.

Signicant dimensionless parameters such as the Reynolds number, the Stokes number and the reduced frequency provide preliminary information about the nature of the flow induced by

rotationally oscillating plates. The results of both experimental and computational investigations of the flow induced by flapping plates have revealed the presence of tip vortices, responsible for a symmetrical distribution of the flow and thermal characteristics over the plate's surface and heat transfer enhancement in the vicinity of the free edges. Our discussion in this chapter has lead to investigate a few ways to improve the heat transfer rate from flapping surfaces. Conclusions from present study have shown that forced convection due to rotationally oscillating motion is an excellent method to improve the cooling rate of hot surfaces because the leading edge in this case includes all other edges, except for the fixed one about which the rotation of the plate occurs. Moreover, better cooling rates are obtained with flexible materials compared to rigid counterparts because the interaction between the shedding vortex and the boundary layer of the plate's surface is improved further. However, additional investigations with more complex geometrical shapes will give more insight and interest in the study of flapping heated plates.Therefore, the next chapter will discuss a biological application observed in the flapping pinna of large mammals such as the African elephant.

CHAPTER 7: HEAT TRANSFER FROM THE ELEPHANT'S PINNAE

7.1 Introduction

Studies have shown that large mammals like African elephants produce a significant amount of metabolic heat due to the large size of their bodies [73, 74] as illustrated in Fig.7.1. These animals can generate up to 5.12kW of heat [75] during their daily motions. Their body energy is estimated to be 10 times larger than the heat dissipated by humans performing physical work, which is only 440W [76]. The question is the technique used by these mammals to deal with such a substantial amount of heat generated. A literature review indicates that surface convection from the body of the elephant cannot be the primary mechanism for the animal's heat loss [35]. However, due to the high surface to volume ratio of their pinna, made of a large network of blood vessels, previous work has hypothesized that ear flapping, should be the principal thermoregulatory mechanism for elephants. Therefore, to deal with their excess heat, African elephants flap their pinnae, which are the visible portions of their ears as shown in Fig.7.2, for comfort**.**

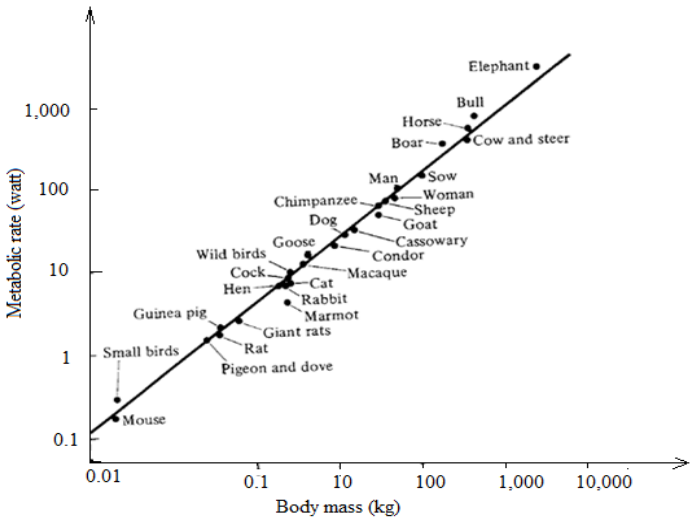

Fig. 7.1. Metabolic rates for mammals and birds plotted against body mass logarithmic coordinates [73].

against body mass logarithmic coordinates [73].

Fig. 7.2 African Elephant in Mikumi National Park in the savannah [77]

The current research is carried out to investigate the impact of ear flapping on the animal's overall heat dissipation. The objective of the study is to confirm previous work and extend the results of earlier researchers using different methods for the investigation of the flow and the thermal characteristics induced by a rotationally oscillating model of elephant pinna. First, a computational simulation of the flow and the thermal characteristics in the vicinity of a full-size flapping model of 120cm x 90cm using the software package FLUENT 6.3 is performed. Then, the flow field is visualized with smoke particles followed by the tracking of the pinna's local temperature with J-type thermocouples installed at preferred locations on its surface. The experimental results are compared to the flow and the temperature profiles obtained from the simulation with FLUENT. Rigid and flexible models are tested in order to understand the influence of the flexural strength of the material in the enhancement of the heat transfer from the pinna. To check the validity of experimental and computational findings of this research, results are compared to data from literature.

7. 2 Computational investigation of the flow induced by a medium size elephant pinna with FLUENT 6.3

The flow induced by a 5 mm-thick full-size rigid model of elephant pinna of 1.2 m x 0.9 m, rotationally oscillating at a rate of 2 rad/s about the z axis, is simulated with FLUENT 6.3. In a semi-spherical domain meshed with tetrahedral elements, the dynamic mesh method is used to account for the moving boundary of the geometry in Fig. 7.3. Similar to the flat plate experiment in the present study, the user-defined function written in the C programming language is used to move the model from 0° to a 90° angle about its fixed edge. A constant heat flux of 375W/m^2 is applied to both faces of the model during its oscillating motion in a flow domain at atmospheric pressure. Of interest is the study of the flow and the thermal characteristics in the vicinity of the model.

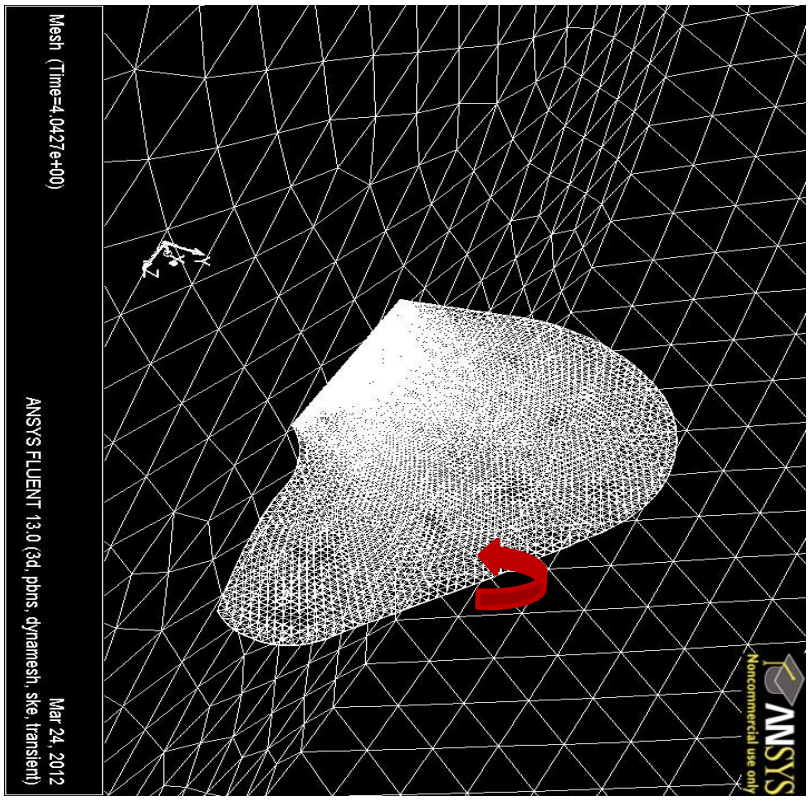

Fig. 7. 3 Picture of an elephant pinna in the computational flow domain

7.2.1 Analysis of the flow induced by a flapping elephant ear

A sectional view of the model in the flow domain, perpendicular to the axis of rotation, with an angular position of 10° is presented in Fig. 7.4. Path lines around the moving model exhibit a peak velocity magnitude of 9m/s recorded at the tip, which is larger than the tip velocity $v = 1.6\text{m/s}$ calculated based on solid body rotation:

$$V = \omega \times r = (2\text{rad/s}) \times (0.9\text{m}) = 1.8\text{m/s}$$

A horizontal section is made through the center of the model along segment AB as illustrated in the left view of Fig. 7.4. The presence of a shedding tip vortex behind the moving model is evidenced at point B in the right View. Moreover, a sectional view parallel to the axis of rotation along a vertical segment AB, illustrated in Fig. 7. 5 is used for further investigations of the flow field. Path lines on the right indicate that the formation and the shedding of vortices occur in all directions. Points A and B enable to visualize a quasi-symmetrical, highly three-dimensional flow pattern.

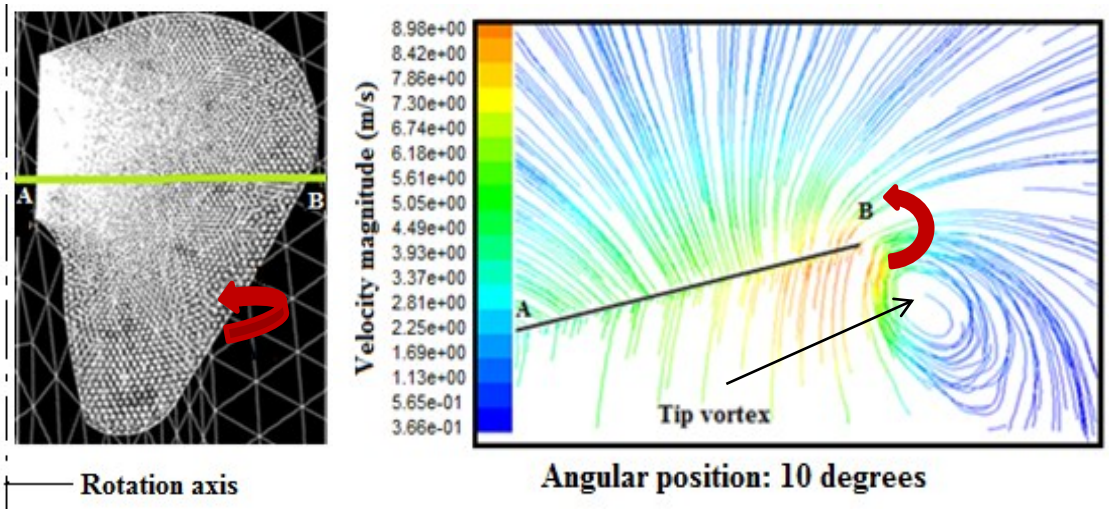

Fig. 7.4. Upstroke motion at 10° angle. Left view: horizontal section of pinna normal to axis of rotation. Right view: flow path lines induced by the model colored by velocity magnitude

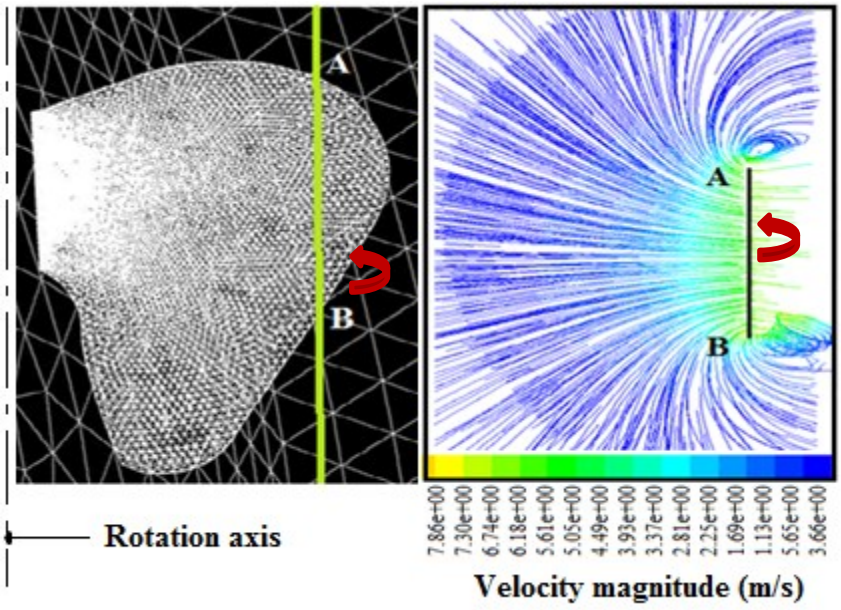

Fig. 7.5. Upstroke motion at 10° angle. Left view: Path lines at a 10° angle. Right view: Plane section of path lines parallel to axis of rotation

The flow domain colored by the contour of static pressure in Fig. 7.6 can be divided into two important zones: (1) a higher pressure zone in front of the moving model, where a peak value of 89.2 Pa (above atmospheric pressure) is recorded; and (2) a low-pressure region behind, evidencing a wake with a pressure value of 162Pa (below the atmospheric pressure). Such a static pressure is responsible for the acceleration of fluid particles moving at a maximum velocity of 12.2m/s as shown by the contours in Fig. 7.7.

At higher angles of attack within the flapping cycle, the pressure distribution over the surface of the model in Fig. 7. 8 shows curves of high pressure values in the vicinity of the center of the pinna. However, on line 4, the edges of the model are characterized by lower static pressure. In addition, the peak value of the shear stress (375Pa) recorded on line 4 is indicator of fluid rotation at the tip of the moving model in Fig. 7. 9. The analysis of lines 1 through 4 in both figures 7.8 and 7.9 shows that shear stress and static pressure vary in opposite directions. Fluid

particles are engaged in the formation of vortices in regions of higher shear stress or lower static pressure at the free edges of the model. This explains the peak velocity value of the fluid at the tip of the model in Fig. 7.7.

The direct consequence of the flow field on the surface temperature of the moving model is predictable in such a way that the convection rate at the tip will be improved compared to zones between the center and regions on the face, located in the vicinity of the axis of rotation.

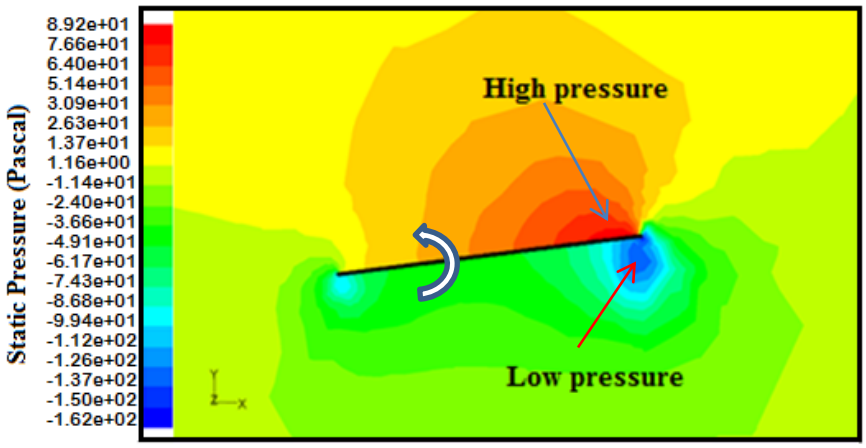

Fig. 7.6 Starting upstroke pressure contours at a 10° angle

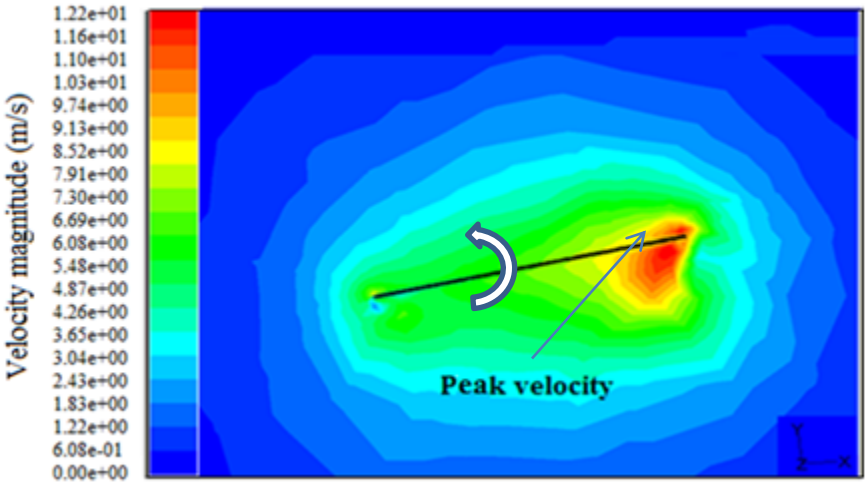

Fig. 7.7 Upstroke velocity contours at a 10° angle

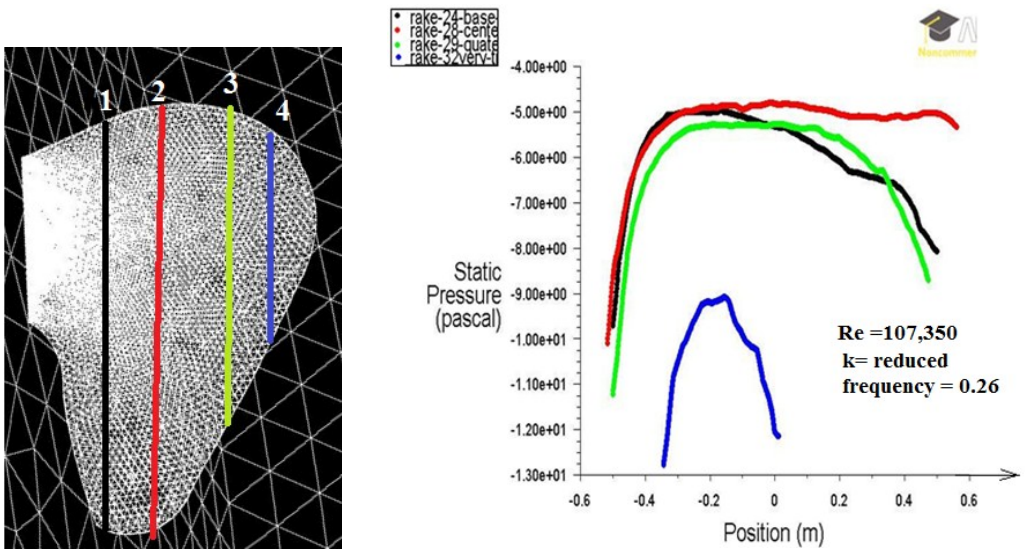

Fig. 7.8 Static pressure distribution over the surface of the elephant ear along vertical lines. Left: lines across model. Right: static pressure profiles

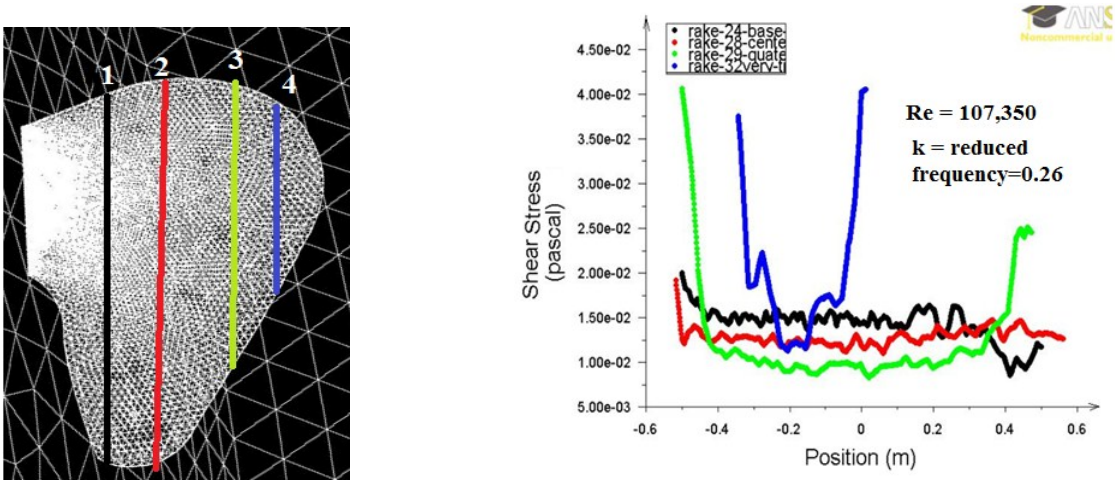

Fig. 7.9 Spatial distribution of shear stress over the surface of the elephant pinna along vertical lines Left: lines across model. Right: Shear stress profiles

7.2.2 Temperature field investigation over a flapping elephant pinna

a) Local temperature distribution over the pinna's surface

The temperature distribution over the surface of the moving model of the elephant pinna, obtained by the computational investigation is compared to experimental data from literature in Fig. 7.10. It is observed from the results of both methods that the center region of the pinna is characterized by peak temperatures values at points A and B, compared to lower temperature

magnitudes ranging from 34°C to 35°C recorded in the peripheral zones at D, F and G. The higher temperature data observed at the center of the pinna's surface are due to the presence of the stagnation pressure discussed earlier in the study of the flow field illustrated by Fig. 7.8.

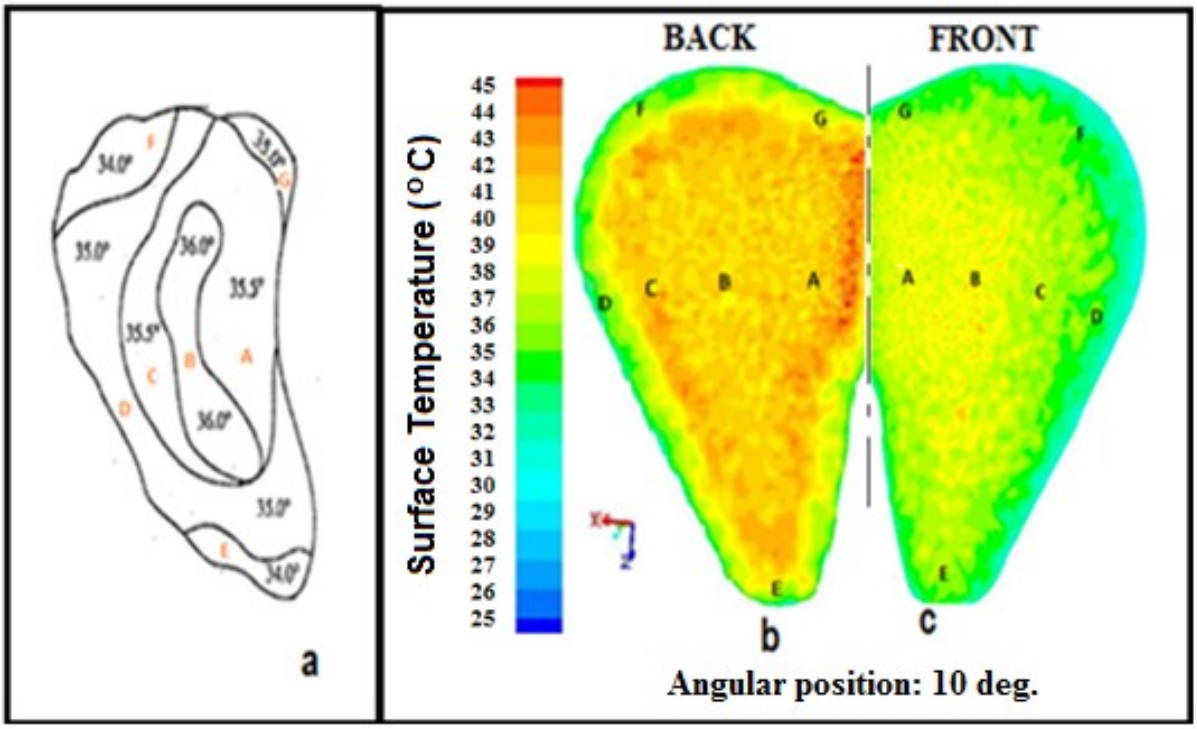

Fig. 7.10 Comparative analysis of elephant ear's surface temperature: (a) data from literature, (b) and (c) data from computational investigation with ANSYS /FLUENT 6.3

Additionally, the local surface temperature collected from the computational investigation in Table 7.1 indicates that the back face is warmer than the front. The temperature gap between the front and the back faces is highlighted by the plot in Fig. 7.11. Moreover, it is observed a similarity in the distribution of the local temperature over both faces, across the surface of the pinna. Overall, from the temperature values collected in Table 7.2, it is easy to establish a correlation between data from literature and computational temperature results. The average surface temperature difference evaluated between data from both methods is only 0.8 percent.

Table 7.1
Temperature distribution over the elephant pinna (°C)

	Zones	Lit_Front	Comp_Front	Comp_Back
A	Base	35	37	42
B	Center	36	39	41
C	Mid-Edge	35	36	41
D	Tip-Edge	35	32	34
E	Bot-Edge	34	34	36
F	Tip/top-Ed	34	33	36
G	Base-Edge	35	35	39

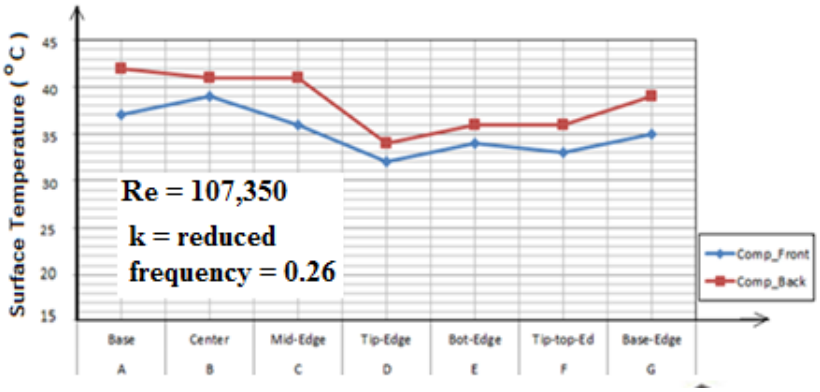

Fig. 7.11 Computational front vs. back local surface temperature over elephant pinna

Table 7.2
Computational vs. Experimental data from literature
Elephant pinna local surface temperature (°C)

	Zones	Lit_Data	Comp_Data	ΔT
A	Base	35	37	2
B	Center	36	39	**3**
C	Mid-Edge	35	36	1
D	Tip-Edge	34	32	2
E	Bot-Edge	34	34	**0**
F	Tip/top-Ed	34	33	1
G	Base-Edge	35	35	**0**

b) Transient local temperature over a flapping elephant pinna

A tracking of the surface temperature is carried at the tip of the flapping model of the elephant pinna, over 4 consecutive cycles as shown in Fig. 7.12. In this case, the local surface temperature increases during a transient unsteady periodic phase. According to a similar study performed earlier with the flat plate model, the unsteady transient phase is followed by a steady periodic region when steady state is reached. Again in Fig. 7.13, a constant temperature gap between a cooler front and a warmer back face is observed as discussed earlier in this paragraph. These results match well with the prediction made by Benedict et al. in 1921 [42], stating that the back of the pinna is warmer than the front.

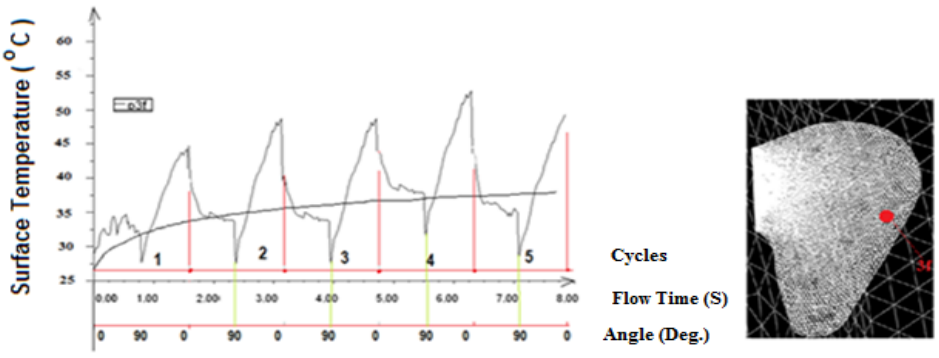

Fig. 7.12 Transient Temperature over a model elephant pinna for a flux 375W/m^2

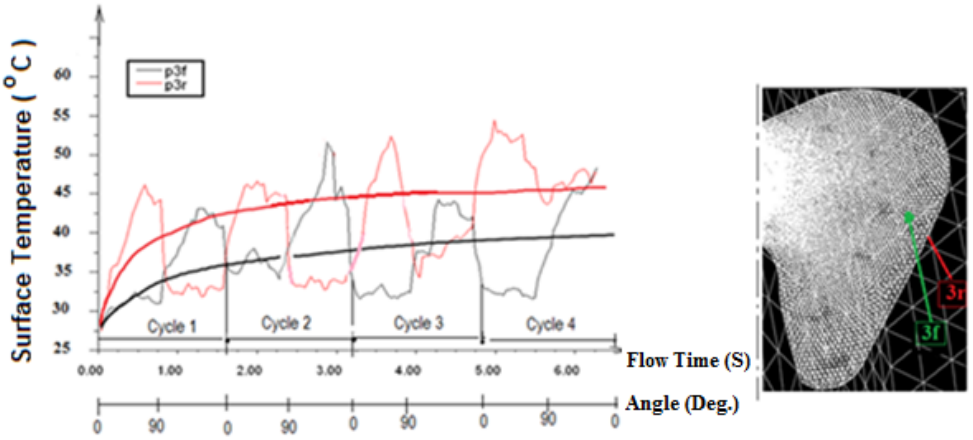

Fig. 7.13 Tracking front and back surface temperature over model elephant pinna

Finally, temperature profiles along parallel lines made on the surface of the studied model, in the vertical and horizontal directions as illustrated respectively in Figs. 7.14 and 7.15 indicate large temperature gradients in the vicinity of the edges of the pinna. These gradients between the center and the peripheral zones of the pinna's surface are more visible along the blue and the green lines in Fig. 7.14, which is confirmed by the local heat transfer coefficient distribution in Fig. 7.16. Such results explain the observation of large fluctuations of blood flow made by Benedict et al. at the tip of their studied model [42]. In conclusion, the coolest zones on the surface are located in the vicinity of the tip of the model, due to the shedding of vortices regardless of the direction of rotation and the face being analyzed. However, saying that the back face is warmer than the front is equivalent to the statement that the cooling rate is a function of the direction of rotation of the pinna. But overall, literature data and computational results agree upon the fact that heat flows from the center region to peripheral zones. Still, the experimental investigation is required before any valid conclusion about the temperature distribution over the flapping heated model of the elephant pinna.

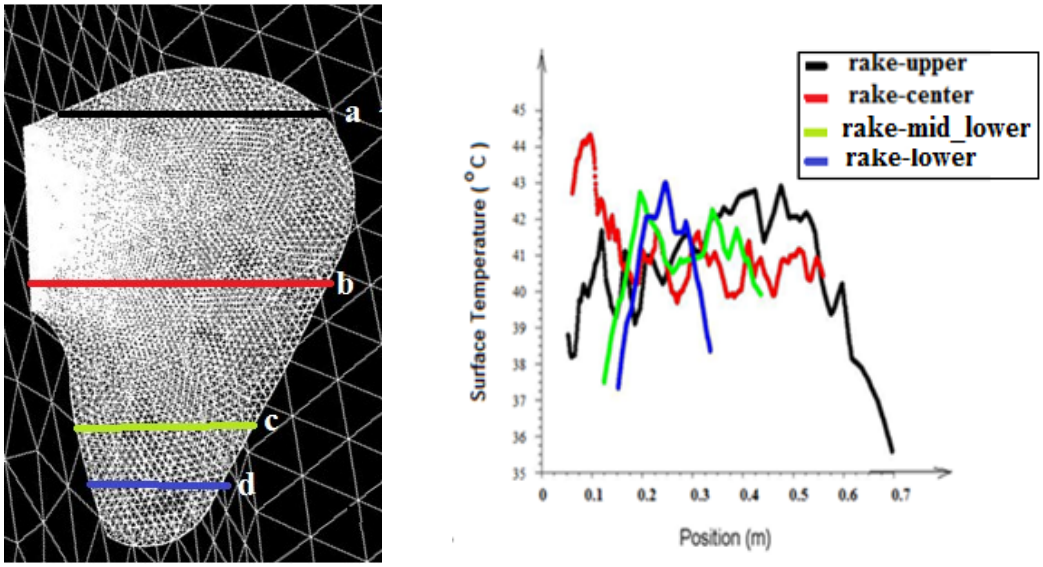

Fig. 7.14 Surface temperature distribution along horizontal lines across a model elephant pinna. Left: lines across model. Right: temperature profiles.

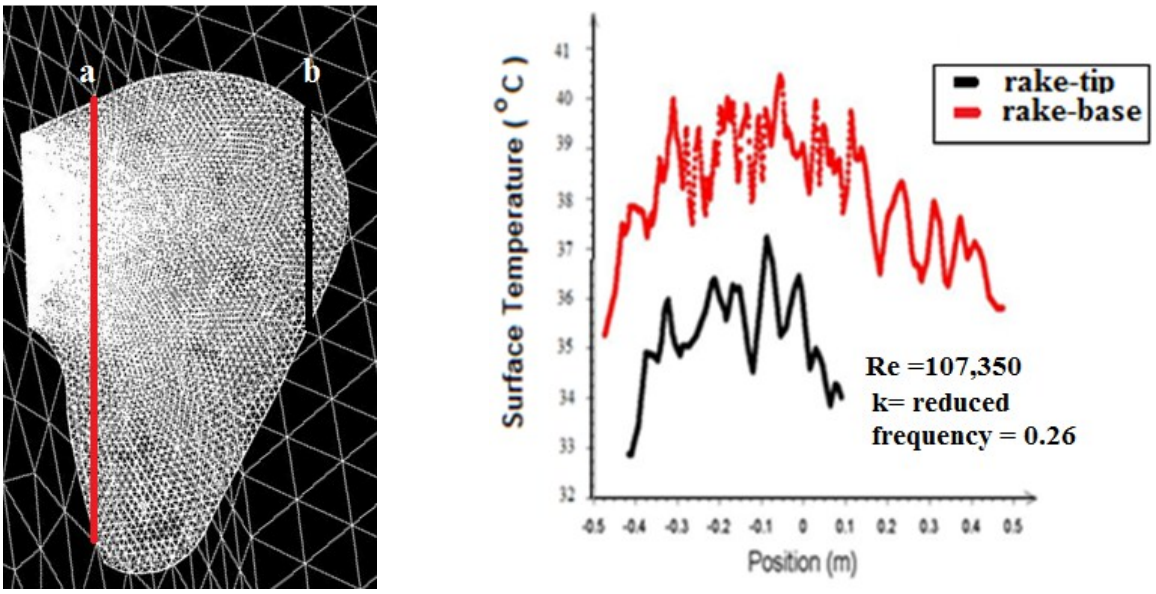

Fig. 7.15 Surface temperature distribution along vertical lines across a model elephant pinna. Left: lines across model. Right: temperature profiles

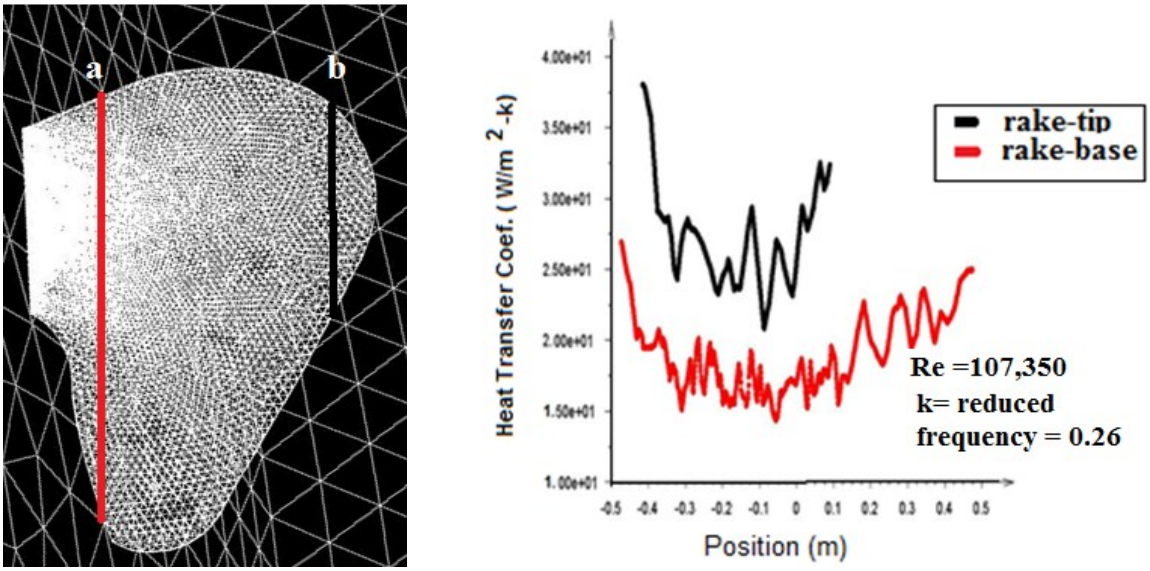

Fig. 7.16 Local surface heat transfer coefficient distribution along vertical lines across a model elephant pinna. Left: lines across model. Right: heat coefficient profiles

7.3 Experimental study of the flow around two models of flapping elephant pinnae

The experimental setup of the flapping elephant pinna test in Fig. 7.17 is composed of 2 different components: the apparatus of a total height of 120 cm, described with the drawings in Paragraph 9.2 of the Appendix, stands vertically mounted on a 140 cm-tall metallic support. The supporting

table is also used to carry the components of the mechanism such as the electrical box, batteries and accessories. A 7.6cm-diameter PVC pipe, centered on the vertical axis of the mechanism, connects the smoke machine to a 49cm- tall synthetic container, which plays the role of a smoke reservoir for the flow visualization experiment. An opening of 25cm x18cm is created across the wooden base support for the release of smoke particles to the flow visualization testing area. The whole experimental setup is equipped with 4 wheels made of synthetic polymer that allow the mechanism to be carried to any location where a power chord can be connected to a 110V source for the experimental investigation.

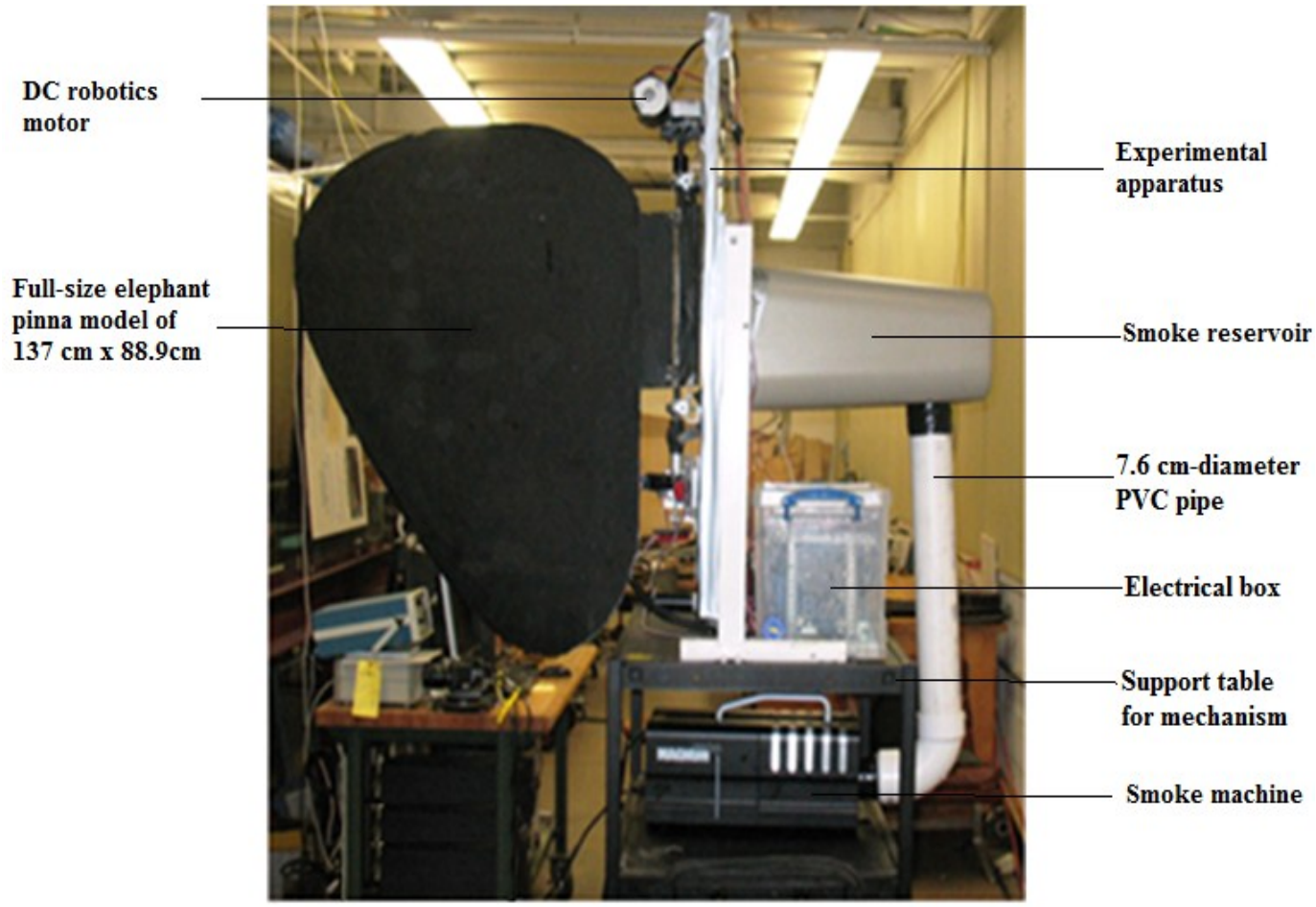

Fig. 7.17 Experimental setup of the flapping elephant pinna test with a full-sized rigid model of 137cm x 88.9cm

For the visualization of the flow around the model, a rigid cardboard with the shape like an elephant ear is performed using smoke particles. The setup in Fig. 7.17 utilizes a full-size model of 137cm x 88.9 cm in size; however, due to a few constraints related to the testing area, only the model of 55 cm x 48cm in Fig. 7.18 will be fully investigated. Analogous to the flat plate experiment in Chapter 6, a high-power laser sheet illuminates the imaging section flow visualization. In this experiment, the model rotates 20 flaps per minute over total amplitude of 90° about a fixed edge.

The complete setup of the experiment in Fig. 7.18, which is 2.60 m-tall, fits in an open space of 25m in length with a sectional area of about $4\text{m} \times 4\text{m}$ where a high-speed camera is used to observe the details of the flow field.

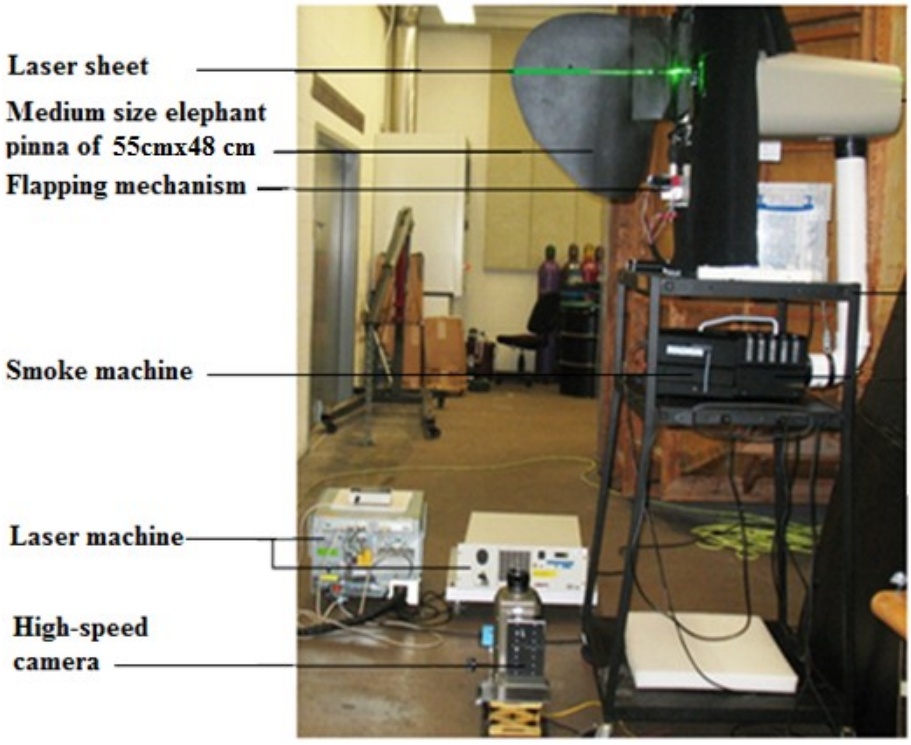

Fig. 7.18 Smoke flow visualization setup for a full size (55cm x 48cm) elephant pinna

7.3.1 Visualization of the flow induced by two models of elephant pinna

a) Flow field induced by a flapping rigid elephant pinna

Starting with the rigid model of pinna, the imaging section is chosen parallel to the axis of rotation of the moving device (as shown in View A of Fig. 7.19), to allow the visualization of the flow in the vertical direction. The flow picture in View B of Fig. 7.19 is dominated by large vortices that form and shed progressively throughout the cycle. At end strokes, these vortices detach suddenly when the model comes to a complete stop, before stroke reversal. View A of Fig. 7.20 shows a light sheet perpendicular to the axis of rotation. The sheet allows the visualization of a tip vortex interacting with the boundary layer on the back surface of the moving model in view B. We can visibly see the counterclockwise motion of the pinna, opposed to the clockwise bulk flow of fluid particles around the edges. These particles mix with the incoming impinging jet of new and fresh fluid behind the moving device to form the tip vortex.

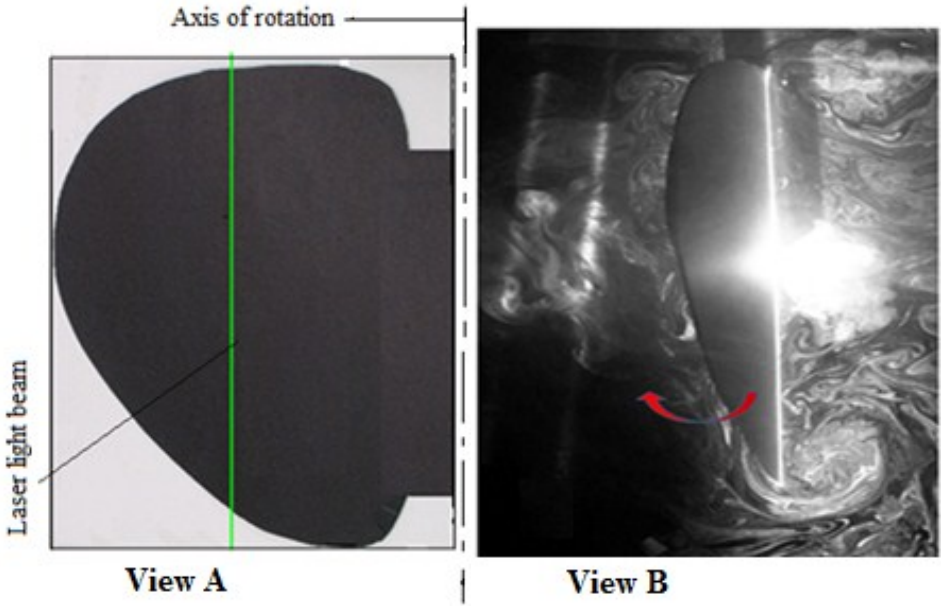

Fig. 7.19 Flow visualization with smoke in the longitudinal direction: View A: Flapping elephant model illuminated with laser sheet. View B: Flapping elephant model evidencing vortices

vortices

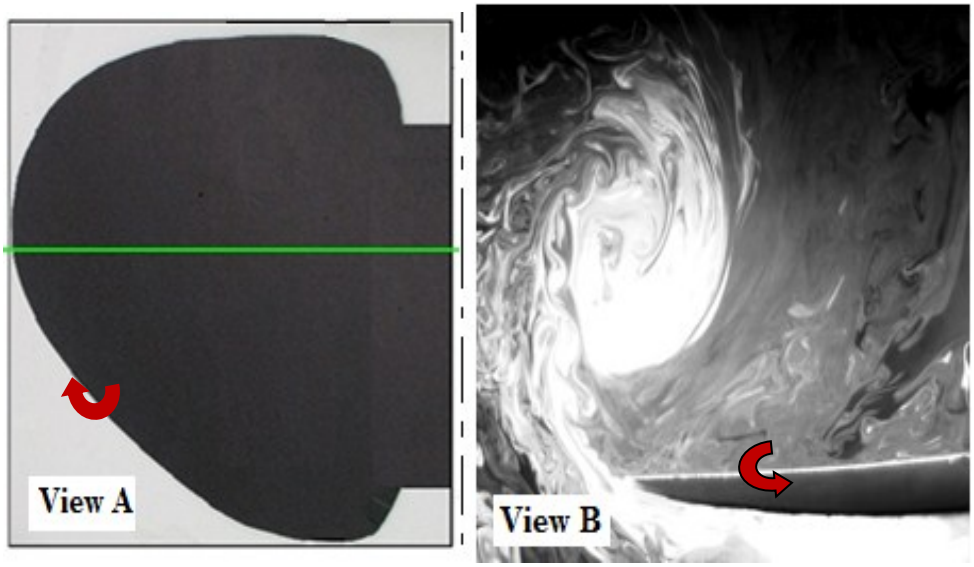

Fig. 7.20 Flow visualization with smoke in the radial direction: View A: Flapping elephant model illuminated with laser sheet. View B: Flapping elephant model evidencing vortices

The flow visualization results viewed from a sectional cut of the flow field through the center of the full size elephant pinna in Fig. 7.21 exhibits a large spiral-shape tip vortex with its center moving away from the surface of the model as its diameter grows with the stroke angle as shown in Fig. 7.22. The increase in the diameter of the vortex tube leads to better interaction with the boundary layer on the model's surface.

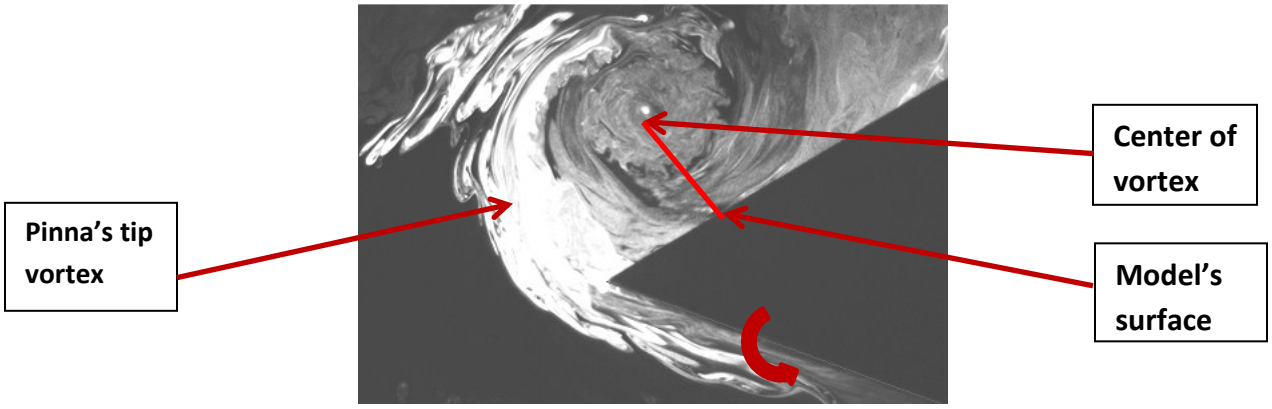

Fig. 7.21 Flow visualization around a real size flapping elephant pinna at the beginning of the down stroke motion at 20^{o} - Angle from the horizontal position

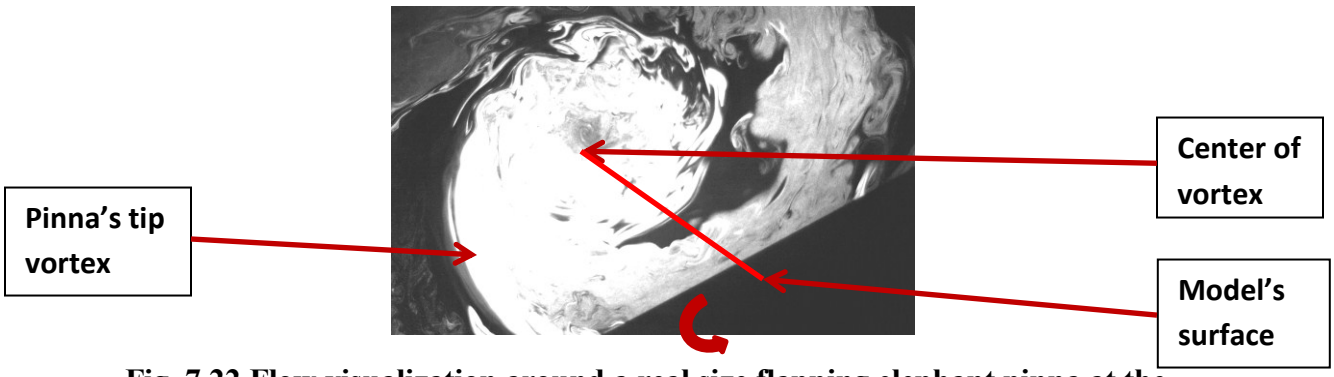

Fig. 7.22 Flow visualization around a real size flapping elephant pinna at the beginning of the down stroke at 30^{o} -Angle from the horizontal position

Using experimental results from the medium size model, the dynamics of vortices are illustrated in Fig. 7.23 in 4 different steps of a size of 10° angle during the flapping cycle, from the onset of the down stroke motion to the end of the stroke. The development of vortices starts with a circular shape at the tip, far away from the center of the model. At Stage 1, fluid particles move quickly around the edge of the model from the front to the back face during the acceleration phase of the moving device. The diameter of the vortex increases by half at Stage 2 after an additional angular rotation of the model of about 10°. A combination of front and back flows participates in the formation of the boundary layer over the back surface, with an increasing thickness at Stage 3 after a stroke angle of 20°. At the same time, the center of the vortex moves gradually with a growing diameter, from the tip towards the center of the model. At that stage, the spinning fluid interacts with the edge of the boundary layer with a penetration depth that grows with the diameter of the vortex. The end of the stroke at Stage 4 is described by a size augmentation of the vortex in a way to increase the magnitude of generated shear forces due to the viscosity of the fluid. These forces participate actively in reducing the thickness of the boundary layer during the shedding of the vortex created by the rigid model. However, the use of

a flexible material for the flapping experiment seems to be a more realistic approach for the experimental investigation of the flow around flapping elephant pinnae.

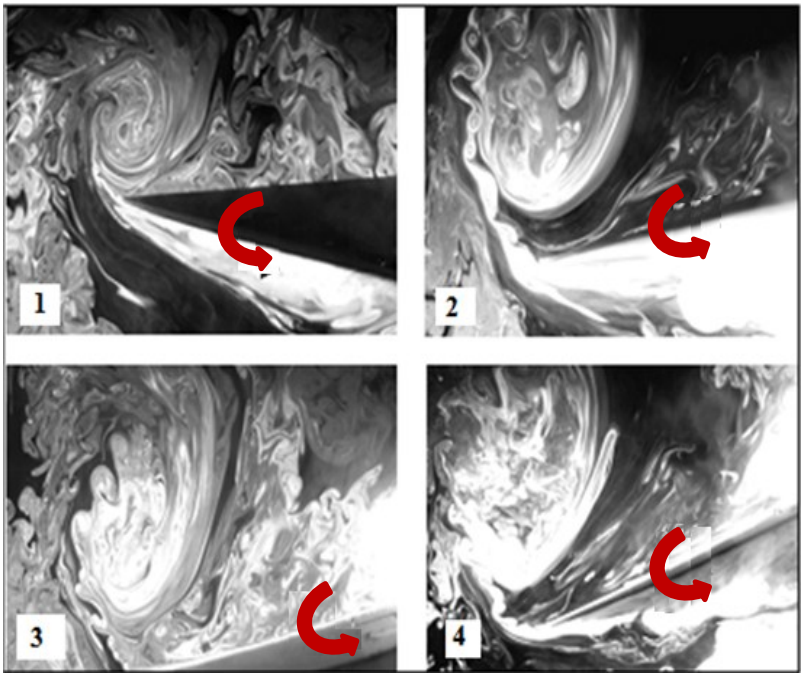

Fig. 7.23 Bottom view of vortex undergoing a cycle for rigid elephant pinna

b) Flow induced by a flapping flexible elephant pinna

In this experiment, the rigid model of the elephant pinna is replaced by a 55cm x 48cm piece of leather, which is a flexible material of a Young's modulus estimated to 0.25 GPA.

As we learned from the results of flexible plates in chapter 6, the tip of the model does not stop immediately at end strokes like rigid counterparts. Instead, it travels an additional angle due to flexure. Because of the backward curving of the model in motion, the vortex covers a larger portion of the pinna even beyond the centroid of the rear face. The center of the vortex visualized in Fig. 7.24 is brought closer to the center of the moving surface. During their rotation, fluid particles from the outer layer of the vortex are then offered more opportunity to remove fluid located on the upper edge of the boundary layer of the model.

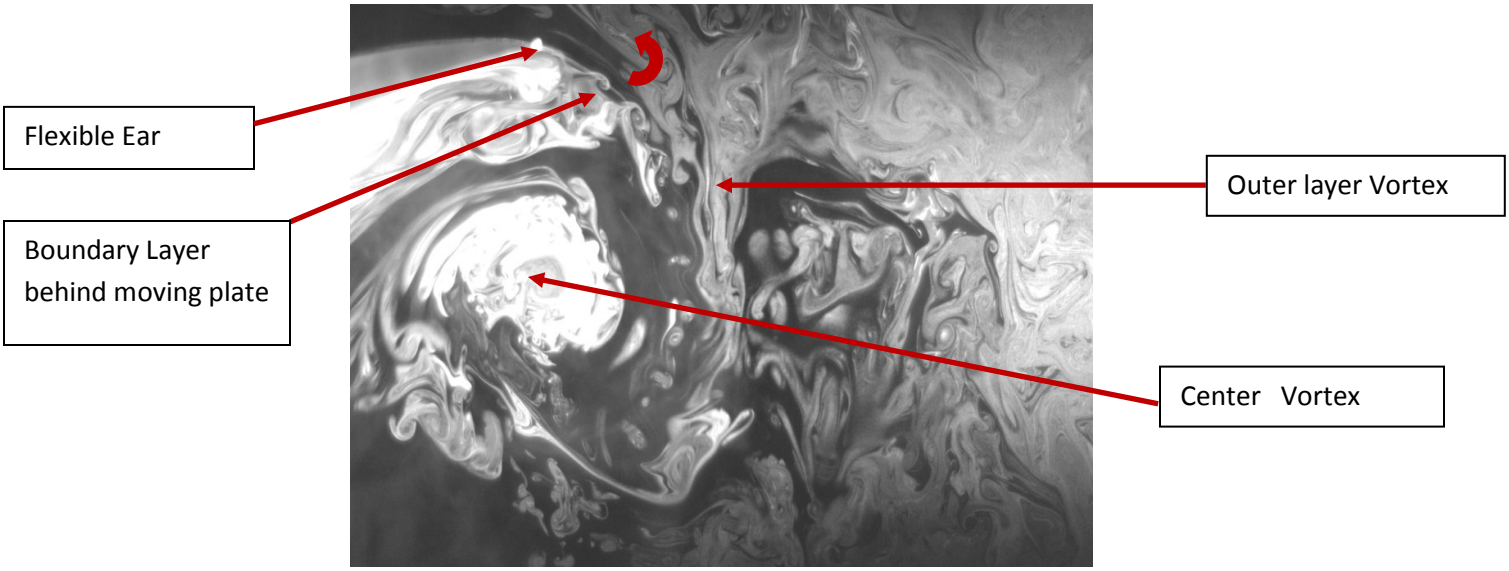

Fig. 7.24 Upstroke motion. Vortex behind moving flexible elephant ear

A sectional view of the flow field induced by the flexible model of the elephant pinna is displayed in Fig. 7.25, during the down stroke motion. Here, the forming of the vortex is facilitated by the slight backward bending of the material of the pinna. The deformation of the model is favored by the opposing pressure drag. As we can visualize in Fig. 7.25A, the vortex is approaching the tip of the pinna; and in Fig. 7.25B, the vortex already reached the tip and is about to switch to the opposite side of the model during supination. As a result, the end portions of the model's surface are laminated by the bulk motion of the fluid involved in the formation and the shedding of the tip vortex. Such behavior of fluid particles participates effectively in the enhancement of the heat loss from the surface. Now the flow is visualized during the upstroke motion, along 2 parallel view segments AB and A'B' across the pinna as shown in Fig. 7.26, measuring respectively 355mm and 432mm. Along both segments discussed earlier, the tip vortex in Fig. 7.27 describes the same behavior, with an overall increase in size from AB to A'B'.

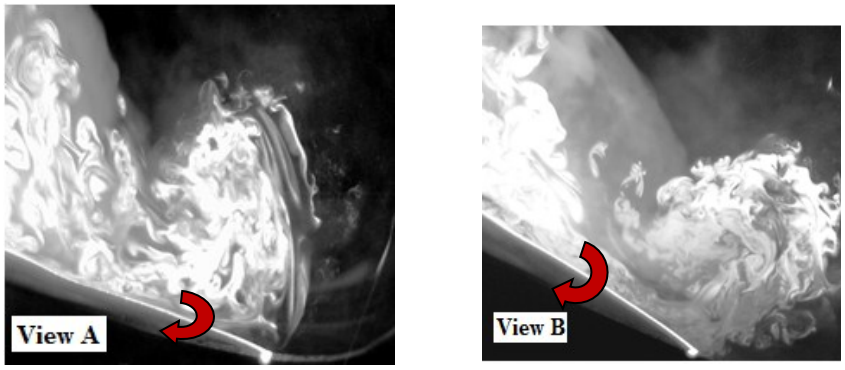

Fig. 7.25 Down stroke detaching flow at 20 flaps/minutes for flexible pinna at 356 mm. View A: Preliminary shedding vortex. View B: Shedding vortex

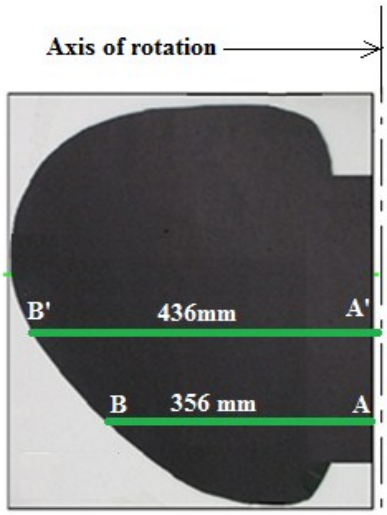

Fig. 7.26 Sectional view across the pinna along 2 horizontal segments of 356 mm and 432 mm

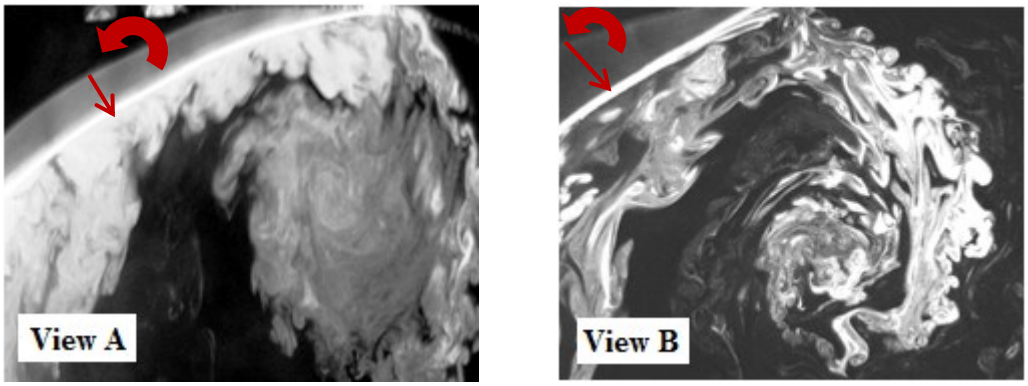

Fig. 7.27 Sectional view of upstroke detaching flow at 20 flaps/min a) View along segment of 356 mm b) View along segment of 432 mm

The dynamics of the forming vortices are tracked in both sectional views over three consecutive time steps with an angular step size of 15° as shown in Fig. 7. 28. First, we notice that the size of the vortex grows with the radius of the section. At a larger radius of the flexible model, the vortices flatten even further, increasing the area of shear surfaces and, at the same time, the shear stress within fluid layers.

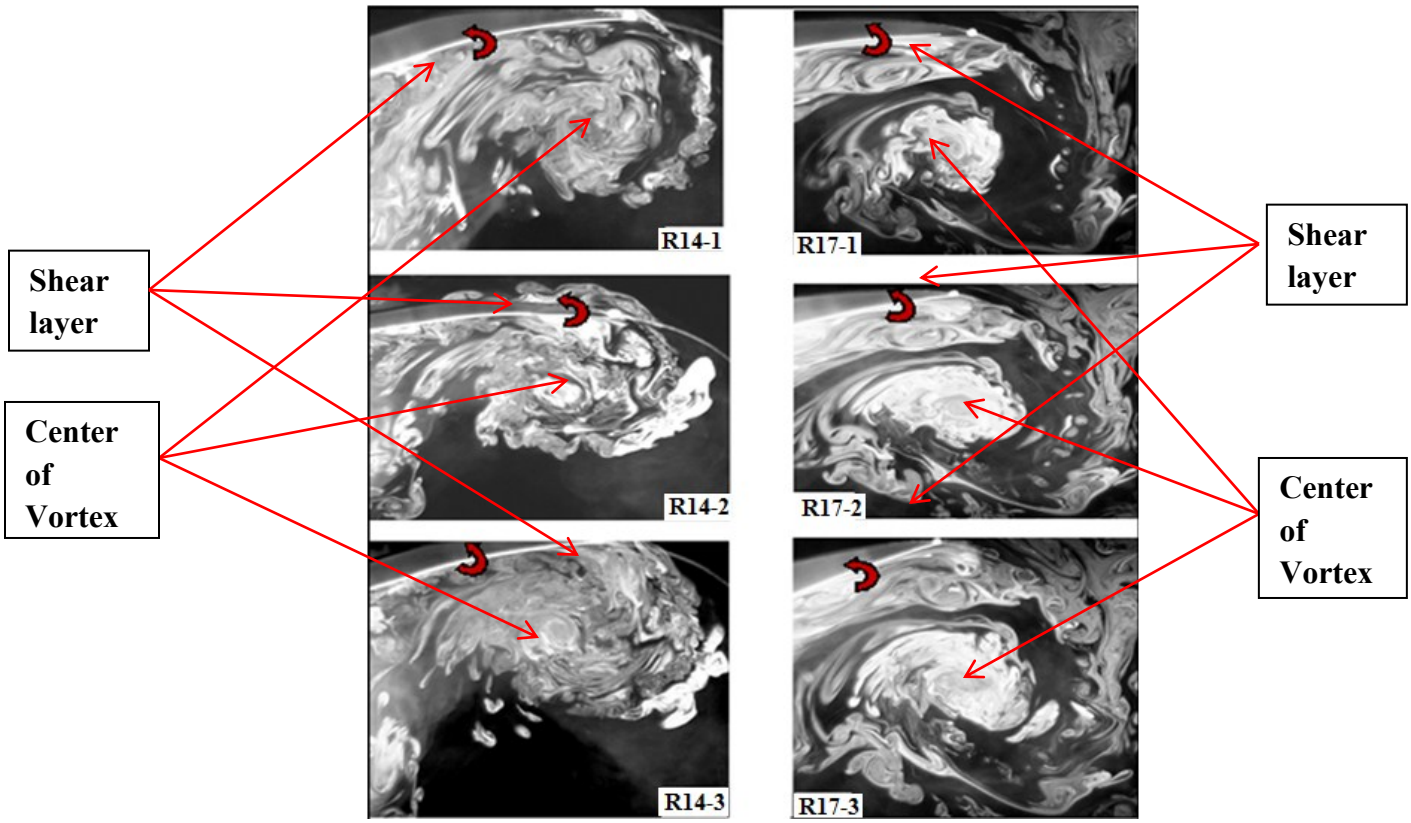

Fig. 7. 28 Upstroke: development of the tip vortex over 3 time steps for 2 different sectional views along segments measuring 356mm (AB) and 432mm (A'B').

In conclusion, the experimental investigation of the flow induced by the flapping pinna facilitates visualizing a highly unsteady flow field dominated by shedding vortices that will influence the distribution of the aerodynamics and the thermal characteristics over the surface of the model. According to the flow visualization results, using a flexible material is likely to create more shear

layers over the surface of the plate, improving further the heat transfer rate. However, an experimental investigation of the thermal characteristics needs to be performed for effective conclusions on the cooling rate of flapping elephant pinnae.

7.3.2 Analysis of the surface temperature of flapping elephant pinna

The medium size model in Fig. 7.29, made of cardboard, is used for the experimental investigation of the surface temperature distribution over the flapping elephant pinna. Five circular silicone rubber heaters of 7.6cm-diameter, of the type S RFR-3/2 from Omega Engineering, are cemented over a thin layer of leather which is directly attached to the surface of the pinna with a high temperature double sided tape. Furthermore, J- type thermocouples are attached to the center of each heater for the measurement of the surface temperature, which is checked with digital thermometers. The heaters are displayed 15 cm and 20cm apart respectively in the horizontal and the vertical positions as illustrated in the left view of Fig. 7.29. The same data acquisition system with the mat lab code in Paragraph 9.3.3 of the Appendix is used for the measurement of the surface temperature, assisted by a desktop computer. A constant heat flux $q'' = 375 W/m^2$ is applied to the surface of the elephant pinna; the heat loss through the leather can be neglected. For the forced convection experiment, the rigid model of the pinna is rotated in the vertical position as shown in the right view of Fig. 7. 29, in a surrounding ambient at 25.5°C

the vertical position as shown in the right view of Fig. 7. 29, in a surrounding ambient at 25.5°C

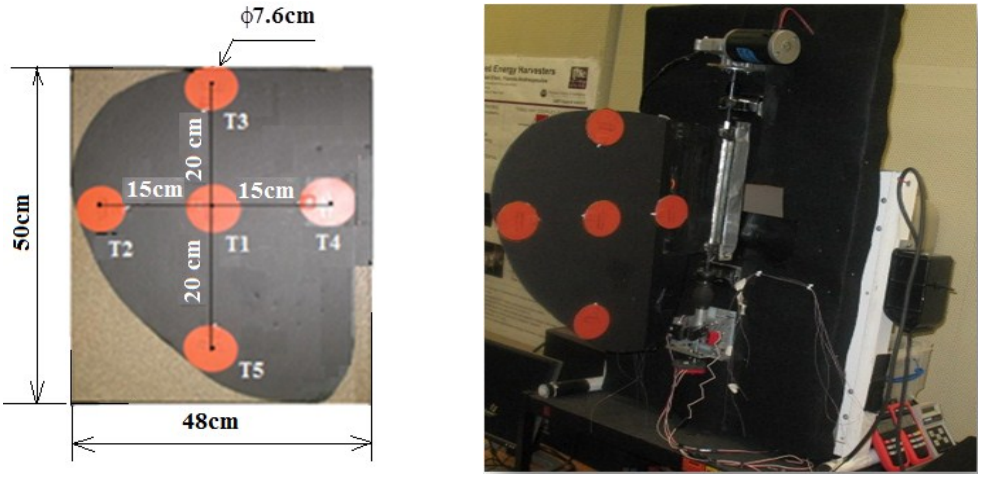

Fig.7.29 Elephant pinna model equipped with silicone rubber heaters. Left view: Layout of heating elements. Right view: Experimental setup

a) Free convection vs. forced convection surface temperature

A free convection experiment is conducted first for the investigation of the temperature distribution over the heated model's surface. Next, forced convection tests at 2 different flapping frequencies of 20 flaps/min and 35 flaps/min are performed. For each experiment, the surface temperature is monitored over a period of 1800s using the data acquisition system described earlier in chapter 6. In free convection, temperature readings at the 3 points T3, T1 and T5, located on the same vertical line in Fig. 7.30 indicate an increasing magnitude from the bottom to the top of the model. Temperature readings across the pinna's center at T2, T1, and T4 should indicate values in the same range because they are located at the same altitude. However, the reading at T4 is out of range, due to high circulation of ambient air through the opening created for the flow visualization experiment.

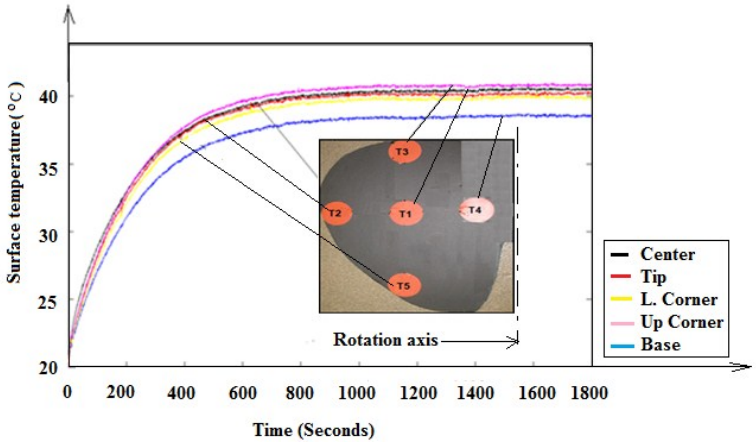

Fig. 7.30 Free convection analysis of the surface of a rigid model elephant pinna

In forced convection, the local temperature distribution over the model's surface is different from the free convection results; the highest value is located at the center of the model as shown in Fig. 7.31 while lower values are read in the corner of the flapping model. Free and forced convection results are compared using a bar graph in Fig. 7.32 for an applied heat flux of $375 W/m^2$. The local free convection temperature is higher at all locations compared to forced convection results. Consequently, the heat transfer coefficients in Fig. 7.33 indicate a favorable cooling rate when the pinna is subject to forced convection.

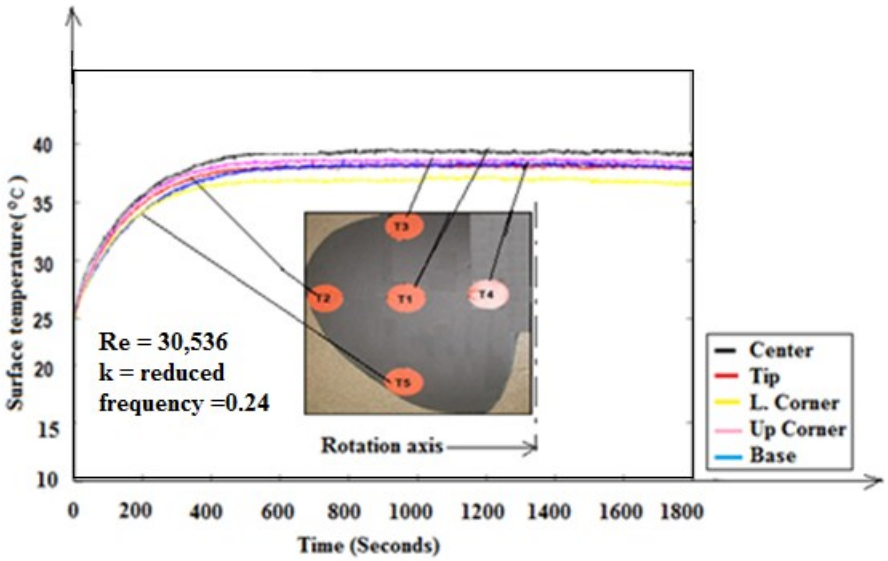

Fig. 7.31 Forced convection temperature for a rigid model pinna flapping at 35 flaps/min

Fig. 7.31 Forced convection temperature for a rigid model pinna flapping at 35 flaps/min

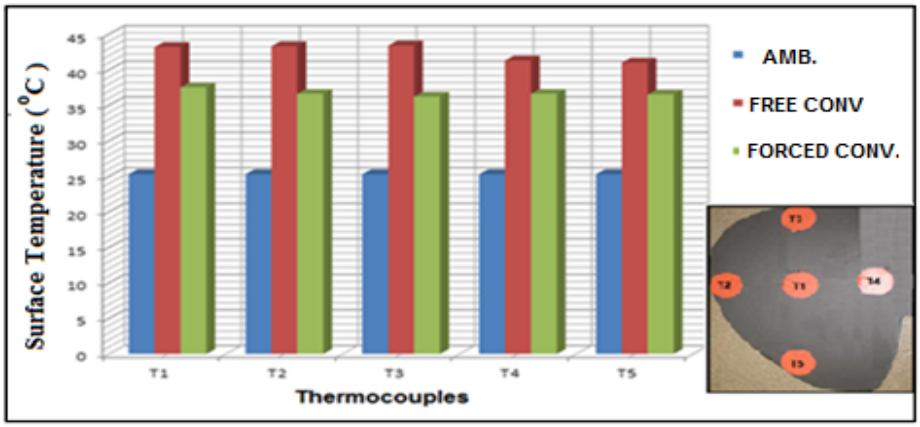

Fig. 7.32 Free convection vs. forced convection local surface temperature distribution

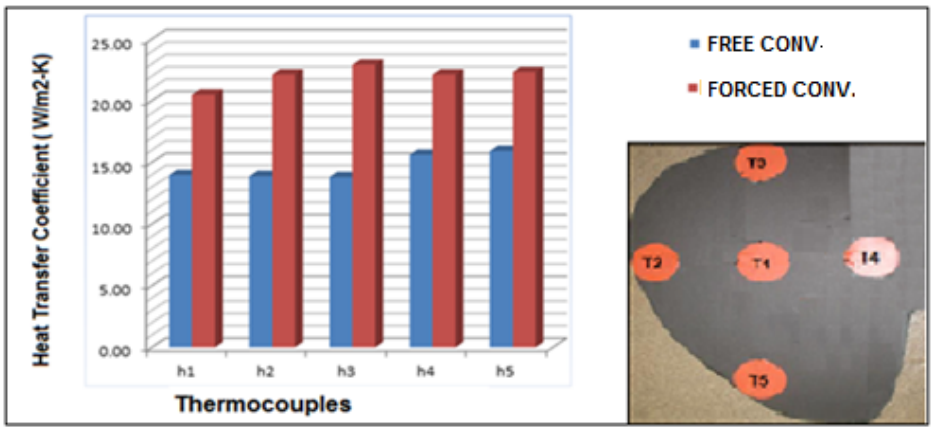

Fig. 7.33 Free convection vs. forced convection local heat transfer coefficient distribution

b) Forced convection at 20flaps/min vs. 35 flaps/min

Now the rigid model is tested for 2 different flapping rates (20 flaps/min and 35 flaps/min) to investigate the impact on the thermal characteristics keeping the same boundary conditions for free and forced convections. The resulting thermal characteristics are organized in Table 7.3, and plotted in Figs.7. 34 and 7.35. The analysis of experimental results indicates that the cooling rate is lowered when the flapping rate is increased from 20 flaps/min to 35 flaps/min, leading to the enhancement of the heat transfer rate.

enhancement of the heat transfer rate.

Table 7.3
Surface thermal characteristics for rigid eleph. pinna 20 flaps/min vs. 35 flaps/min for a heat flux of 375 W/m^2

Thermocouples	T1	T2	T3	T4	T5
Temperature _Ambient (°C)	24.80	24.70	24.70	24.60	25.30
Temperature _Rigid_pinna at 20 flaps/mn (°C)	41.40	39.10	39.40	39.70	39.40
Temperature _Rigid_pinna at 35 flaps/mn (°C)	37.50	36.60	36.20	36.60	36.50
Heat Coef_Rigid_pinna at 20 flaps/mn (W/m^2- K)	22.59	26.04	25.51	24.83	26.60
Heat Coef_Rigid_pinna at 35 flaps/mn (W/m^2- K)	29.53	31.51	32.61	31.25	33.48

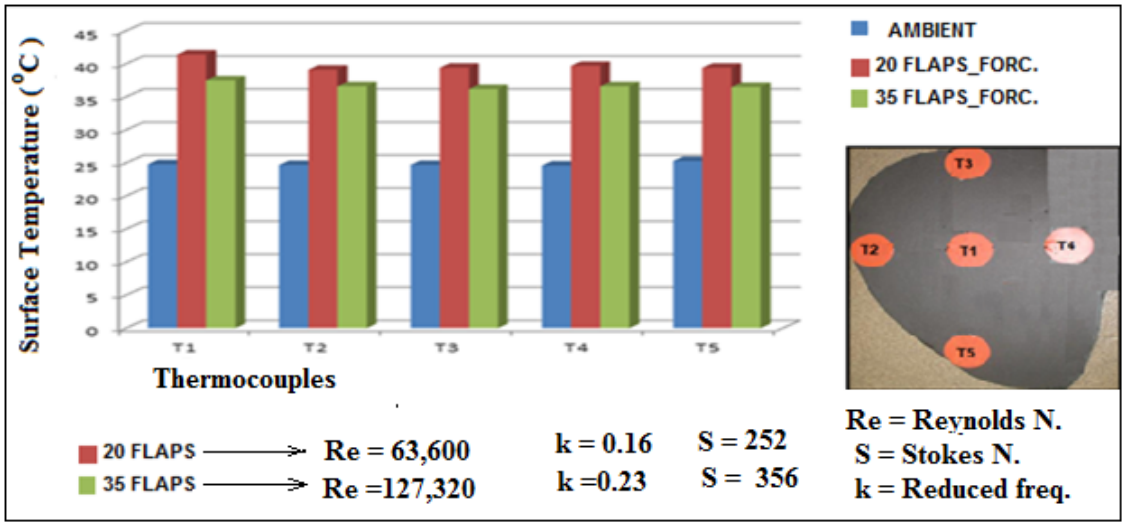

Fig. 7.34 Local surface temperature over rigid model: 20 flaps vs. 35 flaps/min

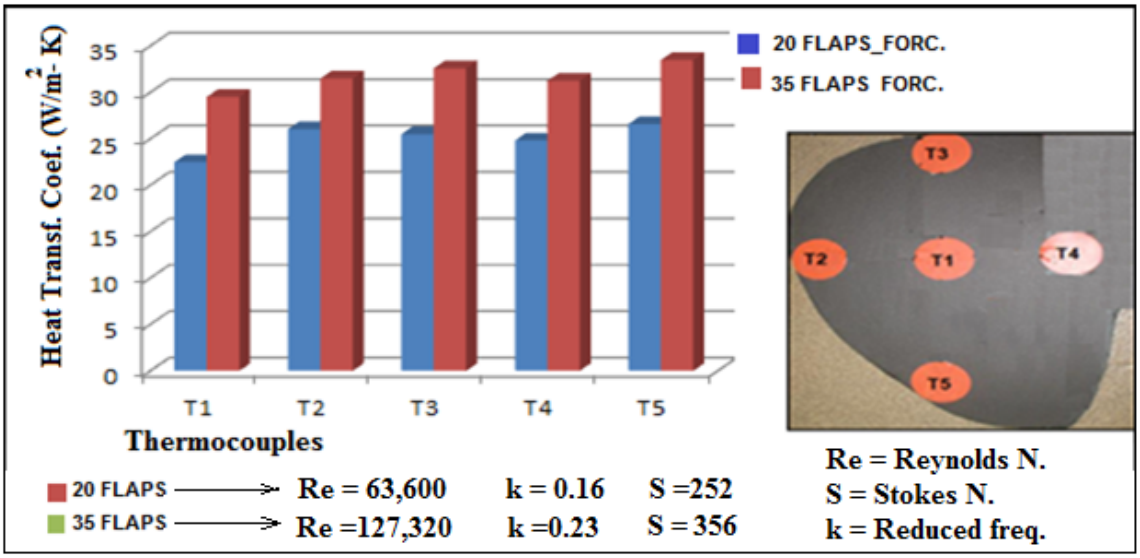

Fig. 7.35 Local heat transfer coefficient for rigid model: 20 flaps/min vs. 35 flaps/min

c) Rigid vs. flexible forced convection surface temperature

In real life, the elephant pinna is not rigid, but flexible. In the following experiment, a model made of a flexible material is tested to investigate the relative changes in the thermal characteristics. Therefore, the rigid model is replaced by a flexible equivalent, made of leather and the boundary conditions are kept the same as previous. The experimental investigation is performed with a flapping rate of 20 flaps/min followed by another testing where the rate is increased to 35 flaps/min. Results are organized in Tables 7.4 and 7.5, and plotted in Figs. 7.36 through 7.39. For both flapping rates of 20 and 35 flaps/min, the flexible model indicates an improved cooling rate based on the local temperature distributions in Figs. 7.36 and 7.37. The same results are confirmed by the local heat transfer coefficients in Figs. 7.38 and 7.39.

Table 7.4

Surface thermal characteristics of rigid vs flexible elephant pinna heated at 375 W/m^2 flapping at rate of 20flaps/min

Thermocouples	T1	T2	T3	T4	T5
Temperature _Ambient (°C)	25.30	25.30	25.30	25.30	25.30
Temperature _Rigid_pinna (°C)	41.40	39.10	39.40	39.70	39.40
Temperature _Flexible_pinna (°C)	39.90	37.80	36.10	35.20	39.30
Heat Coef_Rigid_pinna (W/m^2-K)	23.29	27.17	26.60	26.04	26.60
Heat Coef_RigidFlexible_pinna (W/m^2-K)	25.68	30.00	34.72	37.88	26.79

Table 7.5

Surface thermal characteristics of rigid vs flexible elephant pinna heated at 375 W/m^2 flapping at rate of 35flaps/ min

Thermocouples	T1	T2	T3	T4	T5
Temperature _Ambient (°C)	25.30	25.30	25.30	25.30	25.30
Temperature _Rigid_pinna (°C)	37.50	36.60	36.20	39.60	36.50
Temperature _Flexible_pinna (°C)	35.30	33.30	32.60	32.80	34.80
Heat Coef_Rigid_pinna (W/m^2-K)	30.74	33.19	34.40	26.22	33.48
Heat Coef_RigidFlexible_pinna (W/m^2-K)	37.50	46.88	51.37	50.00	39.47

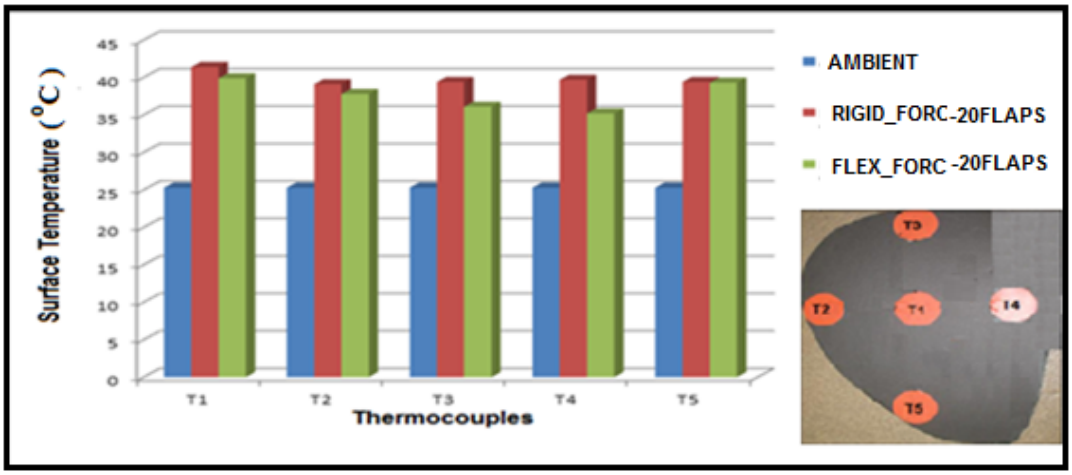

Fig. 7.36 Local temperature at 20flaps/min rigid vs. flexible ear

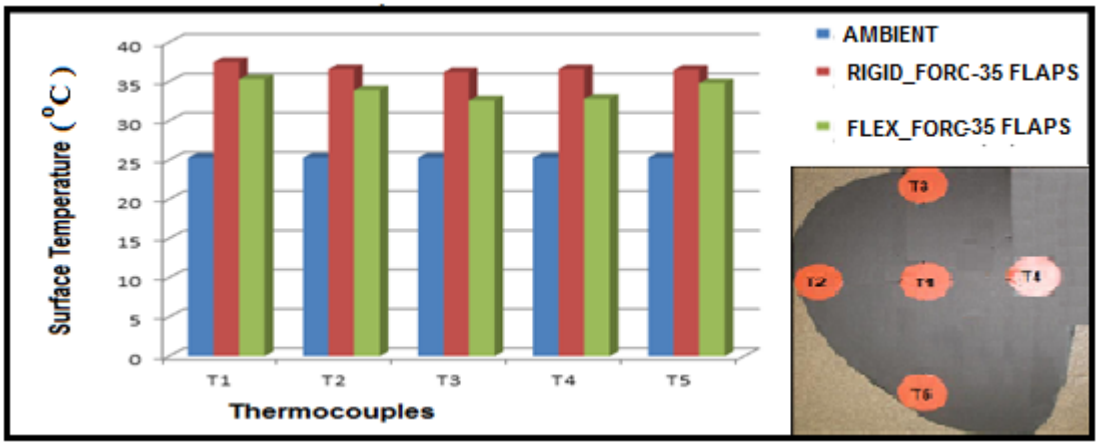

Fig. 7.37 Local temperature at 35flaps/min rigid vs. flexible ear

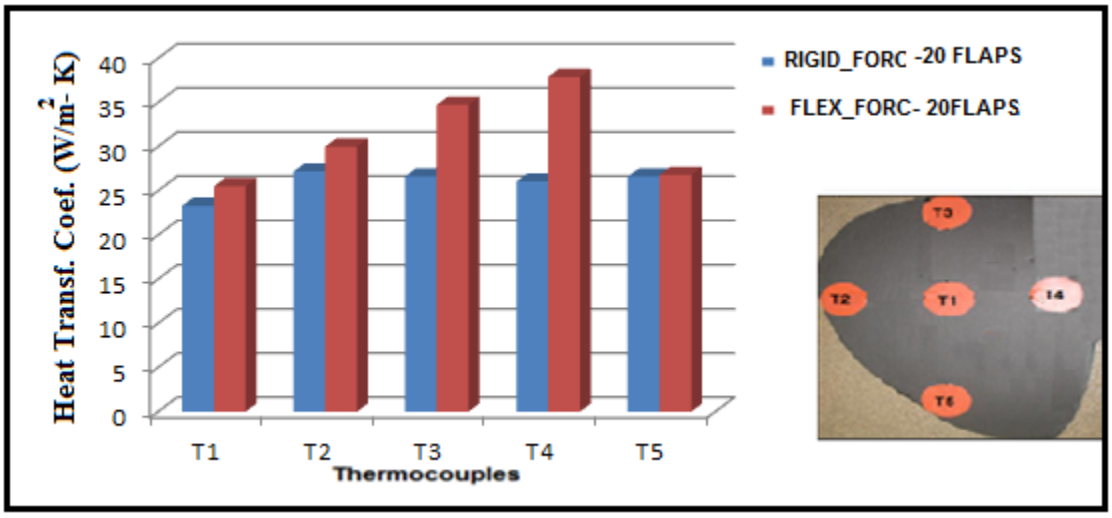

Fig. 7.38 Local heat transfer coefficient at 20flaps/min: rigid vs. flexible ear

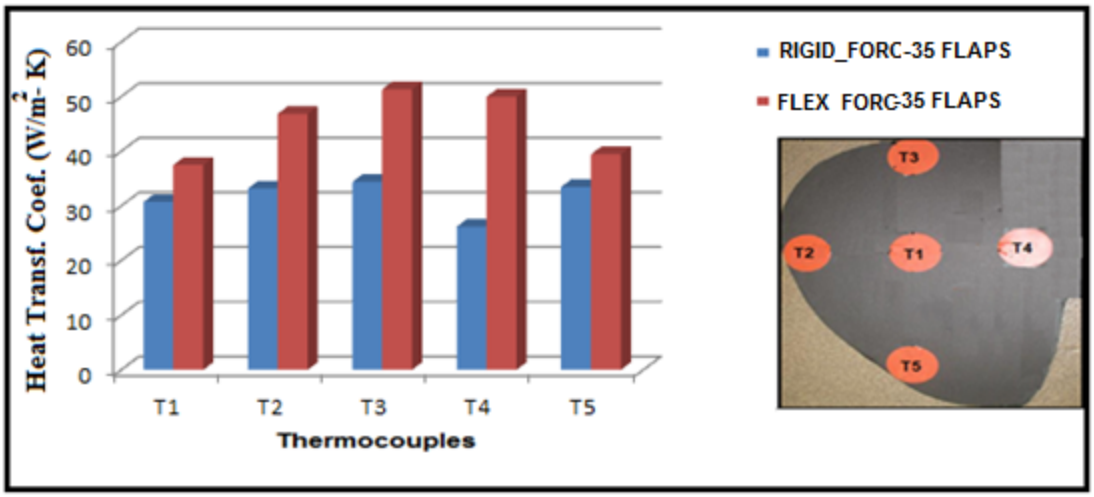

Fig. 7.39 Local heat transfer coefficient at 35flaps/min: rigid vs. flexible ear

7.4 Discussion of the flow and the thermal characteristics around flapping Elephant pinnae

The flow induced by the flapping model of the elephant pinna is characterized by forming and shedding vortices in the vicinity of the tip: In Fig. 7.40, a nearly symmetrical distribution of velocity path lines is visualized in the left view along a cross-section made through the center of the pinna, along segment AB as shown in the right view. The tip vortex is also visualized at point B in Fig. 7.41 with path lines colored by velocity magnitudes that can reach 9 m/s behind the moving elephant pinna. The dimensionless parameters used to describe the flow and the shedding of vortices are respectively the Reynolds number Re and the Stokes number S defined in equations (7.1) and (7.2):

$$\mathrm{Re} = \frac{U_r L}{\nu} \tag{7.1}$$

$$S = \sqrt{\frac{\omega L^2}{\nu}} \tag{7.2}$$

Where

$U_r = \omega \times L = \text{tip velocity}, 1.8\text{m/s}$
$\omega =$ angular rotation speed$= 2$ rad/s
$L =$ characteristics dimension $= 0.9\text{m}$
$\nu =$ kinematic viscosity $= 15.08 \times 10^{-6}\ \text{m}^2/\text{s}^2$

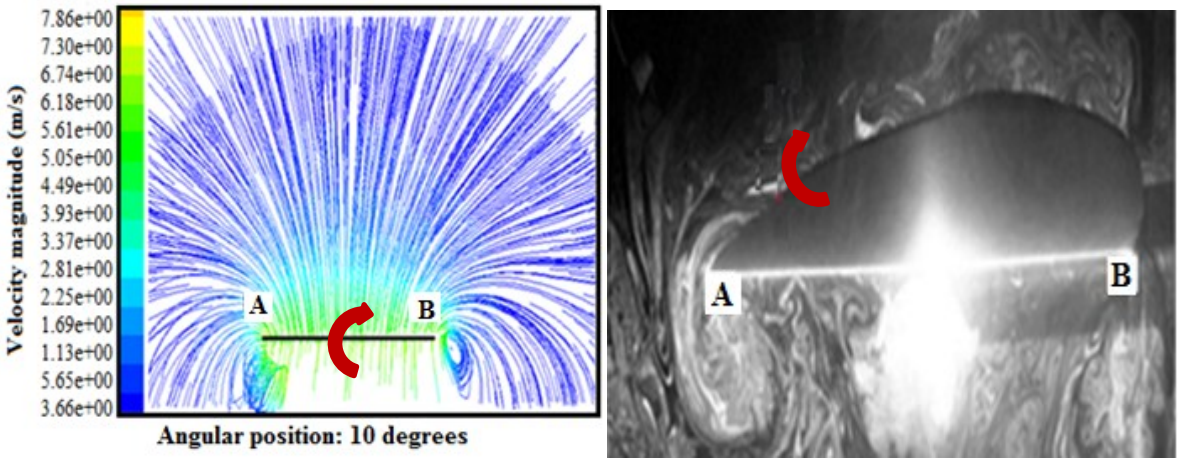

Fig. 7.40 Upstroke motion at 10° angle. Left view: Side vortex evidenced by computational path lines. Right view: Side vortex evidenced by experimental flow visualization

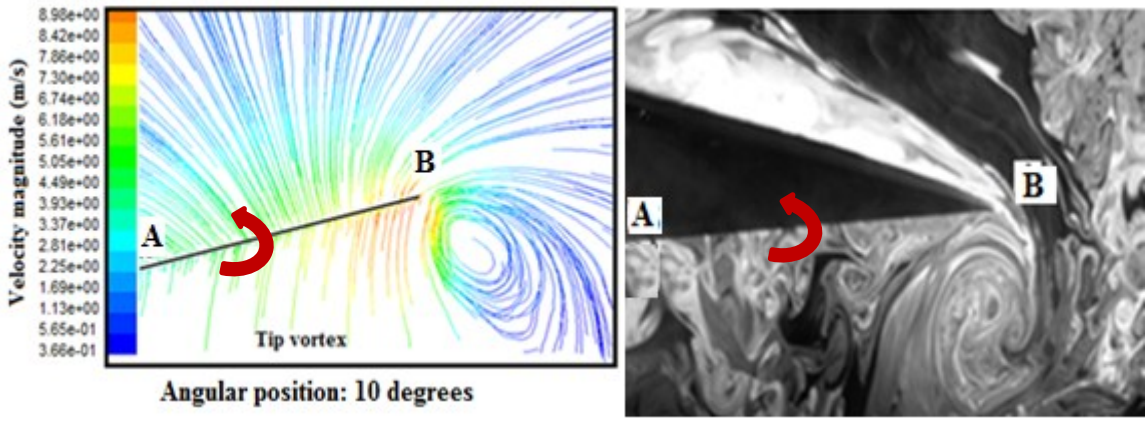

Fig. 7.41 Upstroke motion at 10° angle. Left view: Tip vortex evidenced by computational results. Right view: Tip vortex evidenced by experimental flow visualization

In this study, the shedding of vortices presents similarities with the escape of the vortex ring described by Holman et al. [78] in the formation criterion for a synthetic jet, defined in equation (7.3). In reality, the induced flow velocity magnitude provided by the computational results in Fig. 7.41 can reach a critical value $U_c = 8.9 m/s$. Therefore, vortex shedding occurs if the ratio of the Reynolds number to the square of the Stokes number is larger than a constant K, defined by the jet formation criterion:

$$\frac{Re}{S^2} > K \qquad (7.3)$$

where K is a constant ≈ 1

$$Re = \frac{U_c \times L}{\nu} = \frac{(8.9\text{m/s}) \times (0.9\text{m})}{15.08 \times 10^{-6}} = 531{,}167$$

$$S = \sqrt{\frac{\omega L^2}{\nu}} = \sqrt{\frac{(2\text{rad/s}) \times (0.9\text{m/s})^2}{15.08 \times 10^{-6}}} = 327.76$$

$$K = (\frac{U_c \times L}{\nu})/(\frac{\omega \times L^2}{\nu}) = \frac{U_c}{\omega \times L} = \frac{8.9\text{m/s}}{(2\text{rad/s}) \times (0.9\text{m})} = 4.94 > 1$$

The study of the flow field around the flapping elephant pinna shows that the visualization results with smoke particles illustrated in the right views of Figs.7.42 and 7.43 match well with the computational pathlines colored by the velocity magnitude in the left. From the nature of the flow, it is easy to predict that shedding vortices significantly influence the distribution and the magnitudes of the local surface temperature, making free edges cooler than the central zone of the pinna.

Because the tip moves a longer distance than the base, which is driven by the same angular rotation, it will move faster, resulting in a higher cooling rate at the corresponding edges. The surface temperature values in Table 7.6 and plotted in Fig. 7.43 and Fig. 7.44 demonstrate an acceptable agreement between experimental and theoretical findings with a slight discrepancy between the results from both methods due to experimental errors related to the readings of thermocouples from the surface of the model.

thermocouples from the surface of the model.

Table 7.6
Theoretical vs. Experimental elephant pinnae's surface temperature (°C)

Zones		Lit_Data	Theo_Comp	Exp_Rigid.	Exp_Flex.
A	Base	35.5	38.2	39.7	35.2
B	Center	36.0	39.5	41.4	39.9
D	Tip-Edge	35.0	34.2	39.1	37.8
E	Bot-Edge	34.0	34.5	39.4	39.3
F	Tip_Top-Edge	34.0	34.5	39.4	36.1

Curves in Fig. 7.43 indicate a similarity in the distribution of the surface temperature over the pinna with a large gradient between the center and the tip. The maximum temperature is recorded in the central zone regardless of the method used, with a barely noticeable variation at the edges. Normally, the temperature magnitude should decrease across the surface, from the axis of rotation to the tip of the pinna. Here, the base is slightly cooler than the center zone of the surface due to a small gap of 10 mm, left intentionally between the fixed edge of the model and the wooden-base support of the flapping mechanism in the design of the apparatus. The average experimental pinna's surface temperature is higher by 10 % compared to theoretical results due to the smaller size of the model tested. However, the distribution of the local surface temperature is similar for both methods.

According to Fig. 7.44, the cooling rate of the pinna is significantly improved with flexible models compared to rigid counterparts due to the oval shape of vortices that offers more interacting shearing surfaces within the boundary layer.

interacting shearing surfaces within the boundary layer.

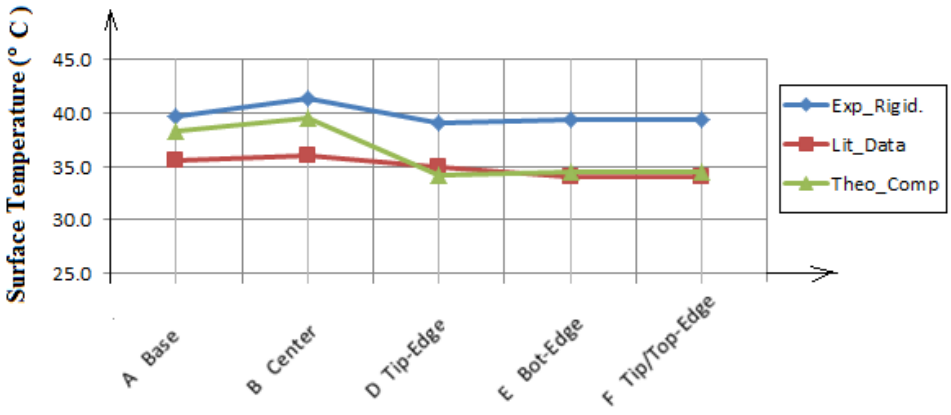

Fig. 7.42. Comparative analysis of elephant pinna's surface temperature.

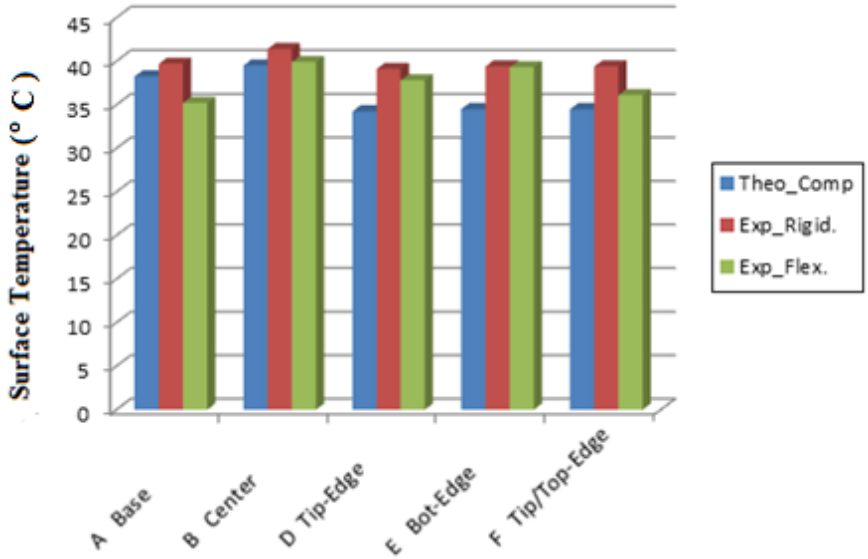

Fig. 7.43. Comparative analysis of elephant pinna's surface temperature.

7.5 Conclusion on the heat transfer from the elephant pinna

The investigation of the flow around a flapping elephant pinna is performed in this research to study the relevance of ear flapping used by the animal for heat dissipation. First, a computational investigation of the flow is simulated with FLUENT 6.3 to analyze the flow and the thermal characteristics over the flapping elephant Pinna. The experimental apparatus introduced earlier

in the study of the rotationally oscillating heated plate is reset and operated to visualize the flow field induced by the flapping pinna with smokes particles. Using the data acquisition system of the flapping plate experiment discussed earlier, the temperature distribution over the pinna is tracked with thermocouples over several cycles. It is interesting to note from experimental and theoretical results that vortices are formed progressively and shed at end cycles leading to substantial decrease in the surface temperature in the vicinity of the tip, while peak temperature magnitudes are observed between the central zone and the base of the pinna's surface. Moreover, the amount of heat loss is improved significantly using a flexible pinna by up to 30 percent According to the experimental investigation, the tracking of the local surface temperature over several cycles has revealed asymptotic temperature profiles over 200 seconds when steady state is reached. Therefore, current research agrees with the statement made by previous researchers [36] who concluded that the flapping of the pinna should be the main thermoregulatory mechanism of the body temperature of large animals such as African elephants.

CHAPTER 8: CONCLUSION AND FUTUR WORK

A computational investigation of the flow induced by a rotationally oscillating rectangular flat plate of $0.2\text{m} \times 0.3\text{m}$ at a rate of $2\text{rad}/\text{s}$ about a fixed edge is performed with the software package FLUENT 6.3. The results of the transient simulation of the flow using the dynamic mesh method have shown a three dimensional flow structure dominated by the presence of strong tip vortices. The analysis of velocity pathlines and pressure contours indicate a hook-shaped vortex tube that grows with the stroke angle and shed from the surface of the plate at the free edges during supination. A robotic mechanism is designed for the control of the frequency and the amplitude of oscillations over several cycles. A visualization of the flow induced by the oscillating model with smoke particles has shown a three dimensional, unsteady flow field, confirming the dynamics of vortices throughout the flapping cycles of the rotating plate. Both theoretical and experimental results agree that the forming and the shedding of tip vortices occur principally at end cycles, triggered by the impulsive motion of the plate. The spatial distribution of flow parameters in the vicinity of the rotating plate indicates the existence of stagnation pressure in the center region of the face and a wake at the free edges behind the plate. The resulting flow induced aerodynamics characteristics, the drag and the lift are used in several applications today for the design of flying or swimming engineering vehicles, motivated by biological systems. However, of interest is the impact of the shedding vortices on the distribution of the local temperature over the surface of the flapping plate. A three dimensional computational solution using FLUENT 6.3 with a constant heat flux q'' applied to both faces enabled to track the variation of the surface temperature over several flapping cycles. To check the validity of the computational results, a data acquisition system utilizing a MATLAB

program, provides transient temperature maps recorded by J-type thermocouples attached to the surface of the moving plate.

The simulation of several cycles has shown a rise of the local temperature over the plate's surface through a transient periodic phase, before reaching an asymptotic profile at steady state. According to theoretical and experimental results, the highest cooling rate is observed at the free edges where tip vortices interact with the plate's boundary layer during their shedding from the surface.

Similar to the flow characteristics over the surface of the rotational oscillating plates, the correlation of temperature results obtained from both computational and experimental investigations indicate a symmetrical distribution of the local temperature over the surface of the flapping plate. Moreover, results from both methods match with an error which is less than 5%.

Additional experimental investigations of the flow induced by flexible flapping heated plates have provided higher cooling rates compared to rigid counterparts because the flexibility of the material allows further interaction between the tip vortex and the boundary layer of the surface. Overall, the local heat transfer coefficient over the surface of an oscillating plate increases with several parameters: the distance from the center of the surface, the orientation of the surface, the stroke angle, the frequency of rotation of the plate, the size of the shedding vortex and the flexural strength of the material used to design the plate.

A biological application of current research found in the the flapping of the elephant pinna has confirmed the results obtained with the flat plate model. Moreover, the investigation of a flexible model has indicated an improvement of the heat transfer coefficient by 30% compared to rigid counterparts, due to the flexibility of the material. In conclusion, the asymptotic temperature

profile obtained at steady state after several flapping cycles despite the continuous heat flux applied to the surface is typical example of temperature regulation. Therefore, the flapping of the pinna observed in large mammals like African elephants is the principal mechanism used by these animals for heat dissipation for thermal comfort.

Overall, this research project has provided relevant results confirming and extending previous work, using different approaches for the investigation of the flow field and the thermal characteristics induced by rotational oscillating plates. The heat transfer results obtained in this research will be used in future work for the determination of the local Nusselt number distribution over the plate's surface. The Nusselt number will be used to develop a correlation equation for predicting heat transfer characteristics over the surface of heated flapping plates. The findings in the current research give more insight in the study of the flow and the thermal characteristics over rotationally oscillating heated surfaces. However, additional investigations need to be performed for further understanding of the physics behind the phenomenon of flapping used to explain biological systems, and also to develop challenging engineering applications.

The three dimensional simulation of the thermal characteristics induced by rotational oscillating plates with FLUENT 6.3 needs to be extended over several more cycles for better conclusion between experimental and theoretical results. Moreover, a full investigation of the flow and the thermal characteristics over the surface of flexible models of the elephant pinna seems to be a more realistic approach in the study of the elephant's thermoregulatory system. The impact of the flexural strength of the material on the enhancement of surface thermal characteristics should be investigated.

CHAPTER 9: APPENDIX

9.1: Tables

Table 9.1
Specifications for carbon fiber [61]

PROPERTY		Typical Values RO4003	Typical Values RO4350	Units
Dielectric Constant @10 GHz		3.38 ± 0.05	3.48 ± 0.05	–
Thermal Coefficient of ε_r @ 0 to 100°C		+40	+50	ppm/°C
Dissipation Factor @10 GHz		0.0027	0.0040	–
Youngs Modulus	X	3700 (25,510)		kpsi (MPa)
	Y	3900 (26,889)	1664 (11,473)	
Volume Resistivity		1.7×10^{10}	1.2×10^{10}	Mohm•cm
Surface Resistivity		4.2×10^{9}	5.7×20^{9}	Mohm
Moisture Absorption		0.06	0.06	%
Dimensional Stability	X,Y	<0.3	<0.5	mm/m
Specific Gravity 23°C		1.8	1.9	–
Peel Strength		1.1 (6.4)	0.9 (5.3)	N/m (pli)
Thermal Conductivity		0.64	0.62	W/m/°K
Coefficient of Thermal Expansion @ 0 to 100°C	X	11	14	ppm/°C
	Y	14	16	
	Z	46	50	
Glass Transition (Tg)		>280	>280	°C
UL Flammability Rating		NO	94-VO	–

Availability:
Standard Thicknesses:
RO4350: 0.0066"(0.168mm), 0.010" (0.254mm), 0.020" (0.508mm), 0.030" (0.762mm), 0.060" (1.524mm)
RO4003: 0.008" (0.203mm), 0.020" (0.508mm), 0.032" (0.813mm), 0.060" (1.524mm)
Standard Sheet Sizes: 24" X18" (610 X 457mm), 12" X18" (305 X 457mm)
Standard Copper Cladding: 1/2 oz (17µm) and 1 oz (35µm) electrodeposited copper.

9.2. Engineering drawing of the parts of the flapping mechanism.

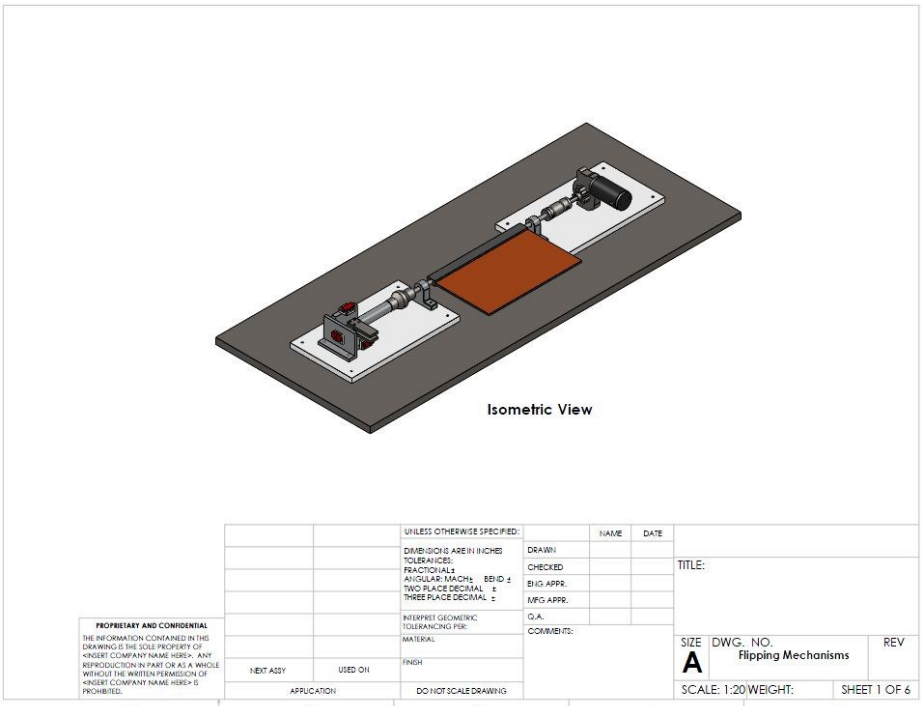

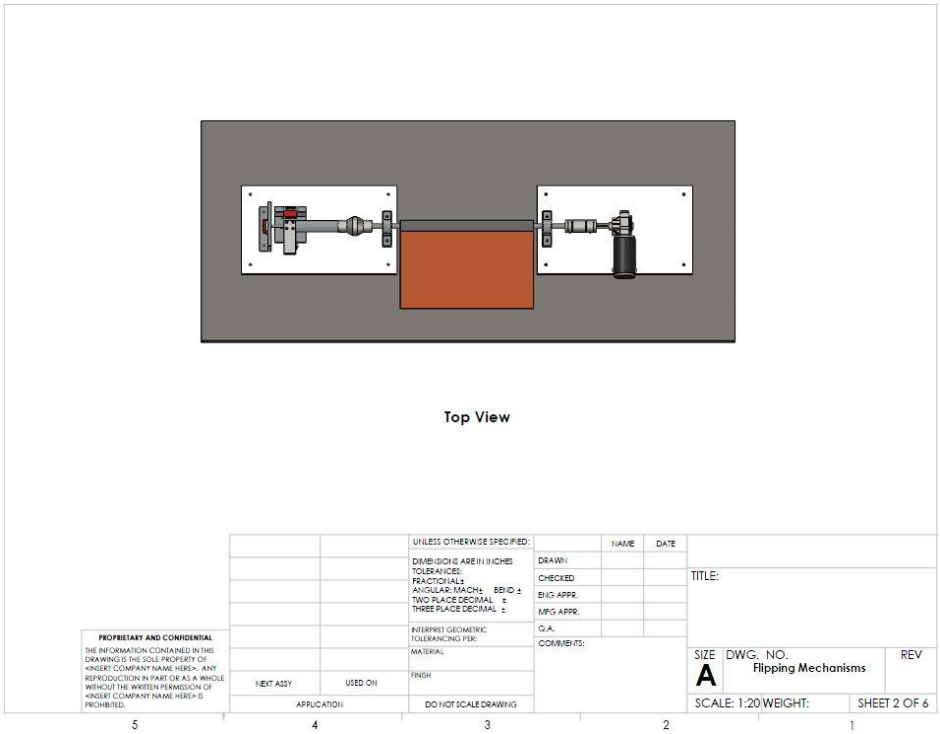

Fig. 9.1 Assembly drawing of flapping mechanism

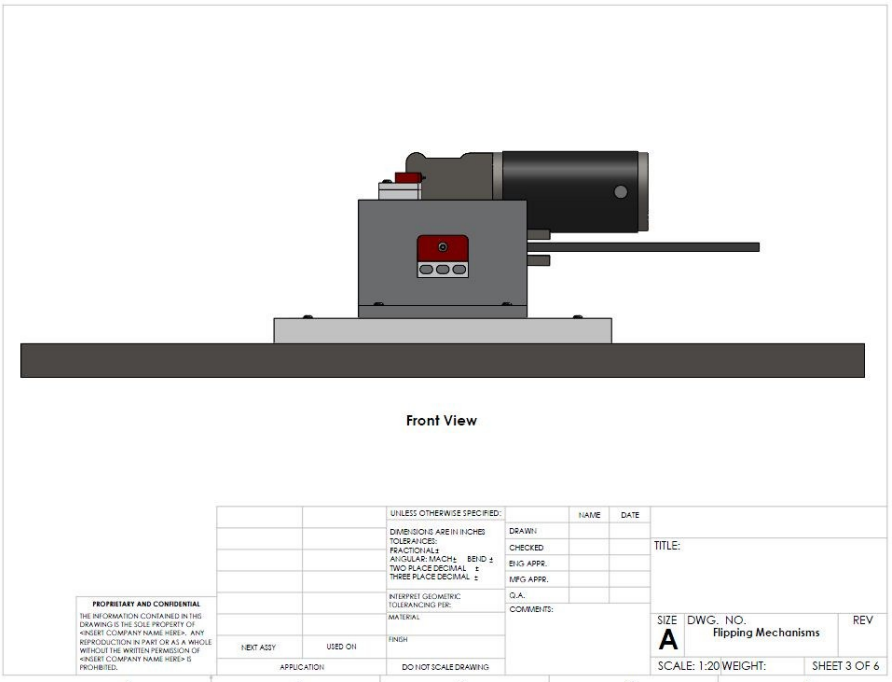

Front View

		UNLESS OTHERWISE SPECIFIED:		NAME	DATE
		DIMENSIONS ARE IN INCHES TOLERANCES: FRACTIONAL ± ANGULAR: MACH ± BEND ± TWO PLACE DECIMAL ± THREE PLACE DECIMAL ±	DRAWN		
			CHECKED		TITLE:
			ENG APPR.		
			MFG APPR.		
		INTERPRET GEOMETRIC TOLERANCING PER:	Q.A.		
		MATERIAL	COMMENTS:		SIZE A DWG. NO. Flipping Mechanisms REV
NEXT ASSY	USED ON	FINISH			
APPLICATION		DO NOT SCALE DRAWING			SCALE: 1:20 WEIGHT: SHEET 3 OF 6

PROPRIETARY AND CONFIDENTIAL
THE INFORMATION CONTAINED IN THIS DRAWING IS THE SOLE PROPERTY OF <INSERT COMPANY NAME HERE>. ANY REPRODUCTION IN PART OR AS A WHOLE WITHOUT THE WRITTEN PERMISSION OF <INSERT COMPANY NAME HERE> IS PROHIBITED.

5 4 3 2 1

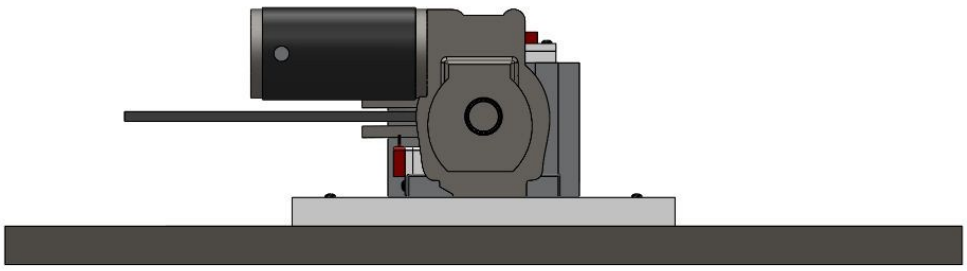

Back View

		UNLESS OTHERWISE SPECIFIED:		NAME	DATE
		DIMENSIONS ARE IN INCHES TOLERANCES: FRACTIONAL ± ANGULAR: MACH ± BEND ± TWO PLACE DECIMAL ± THREE PLACE DECIMAL ±	DRAWN		
			CHECKED		TITLE:
			ENG APPR.		
			MFG APPR.		
		INTERPRET GEOMETRIC TOLERANCING PER:	Q.A.		
		MATERIAL	COMMENTS:		SIZE A DWG. NO. Flipping Mechanisms REV
NEXT ASSY	USED ON	FINISH			
APPLICATION		DO NOT SCALE DRAWING			SCALE: 1:20 WEIGHT: SHEET 4 OF 6

PROPRIETARY AND CONFIDENTIAL
THE INFORMATION CONTAINED IN THIS DRAWING IS THE SOLE PROPERTY OF <INSERT COMPANY NAME HERE>. ANY REPRODUCTION IN PART OR AS A WHOLE WITHOUT THE WRITTEN PERMISSION OF <INSERT COMPANY NAME HERE> IS PROHIBITED.

5 4 3 2 1

Fig. 9.2 Assembly drawing of flapping mechanism; Front and Back Views

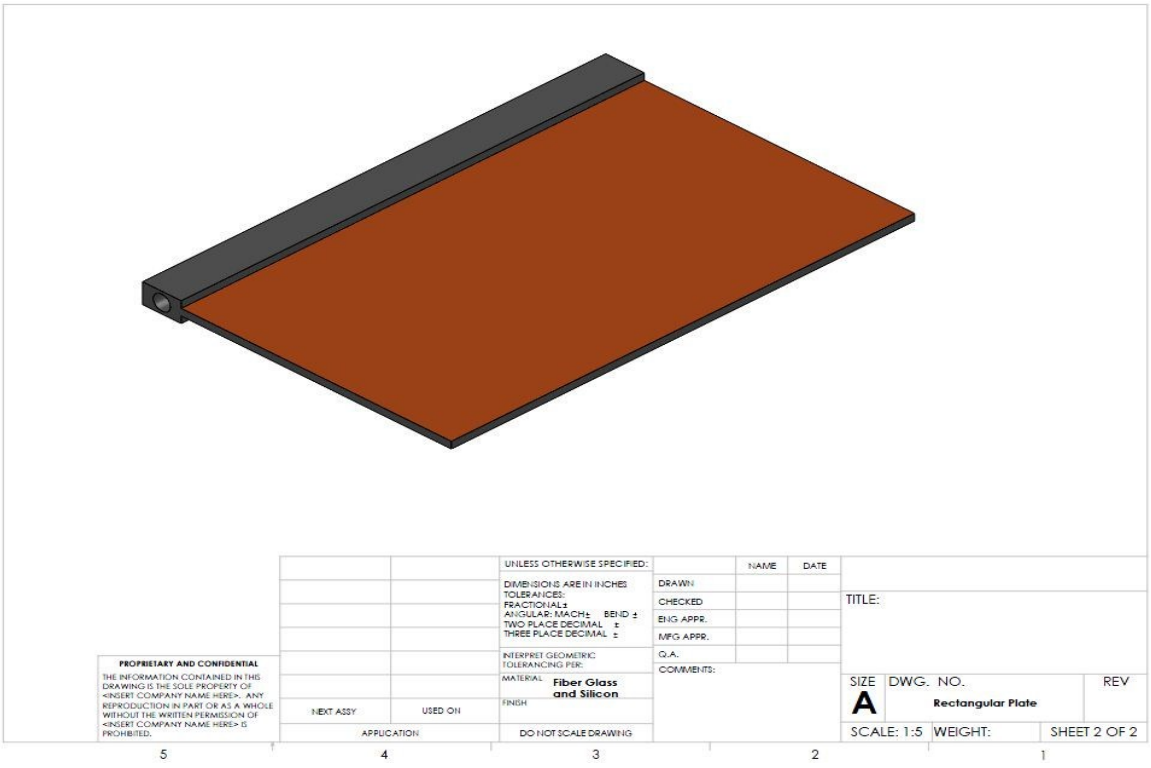

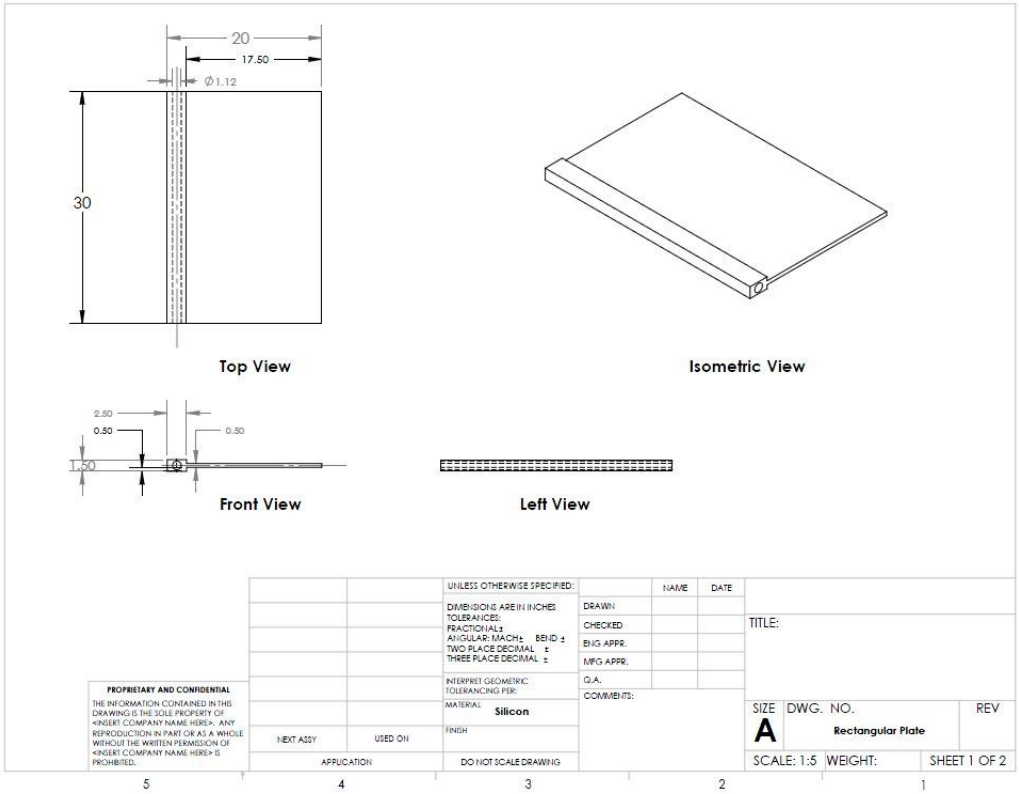

Fig. 9.3 Rectangular plate

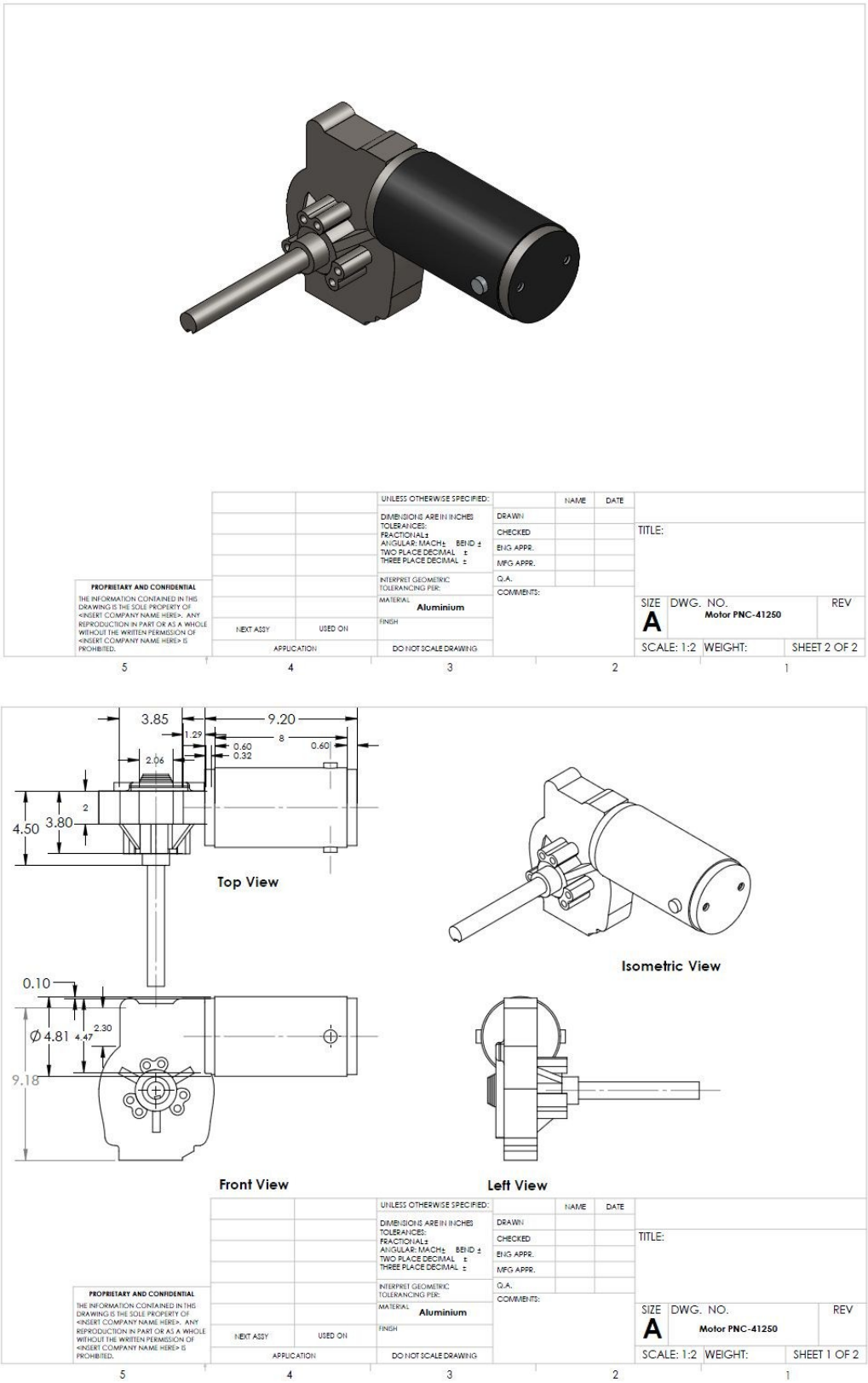

Fig. 9.4 NPC Robotics DC motor

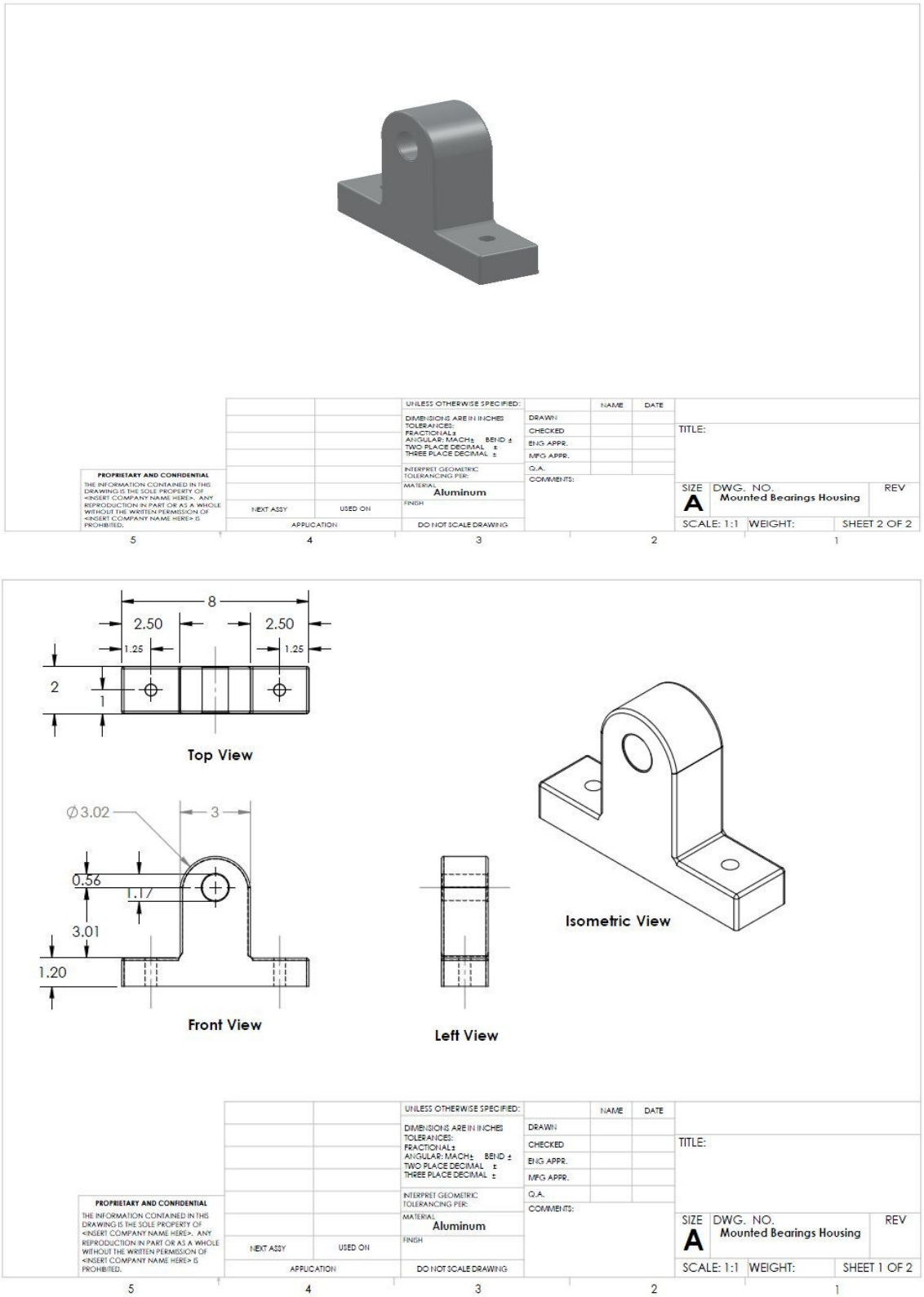

Fig. 9.5 Housing of mounted bearing

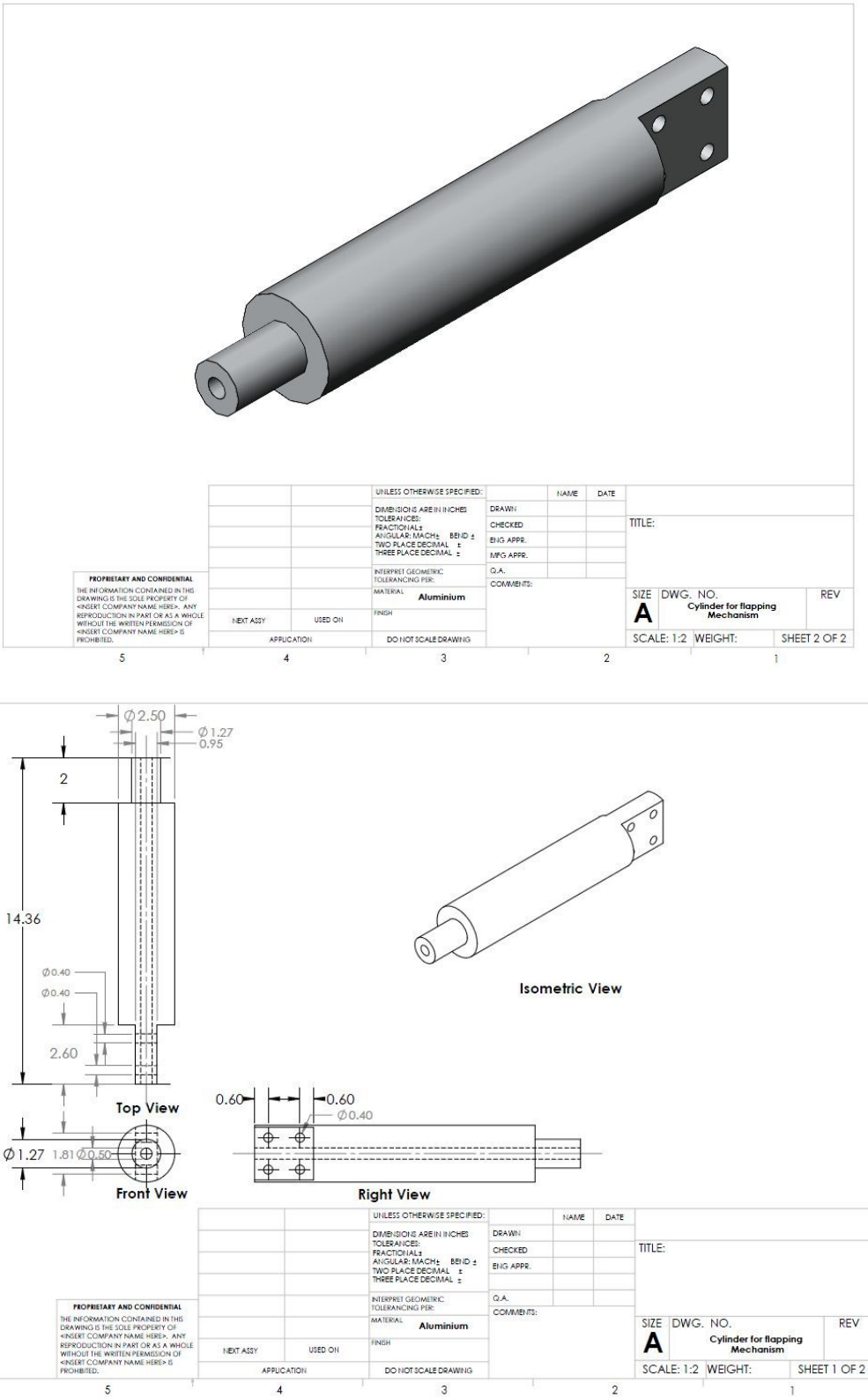

Fig. 9.6 Aluminum support cylinder for flapping mechanism

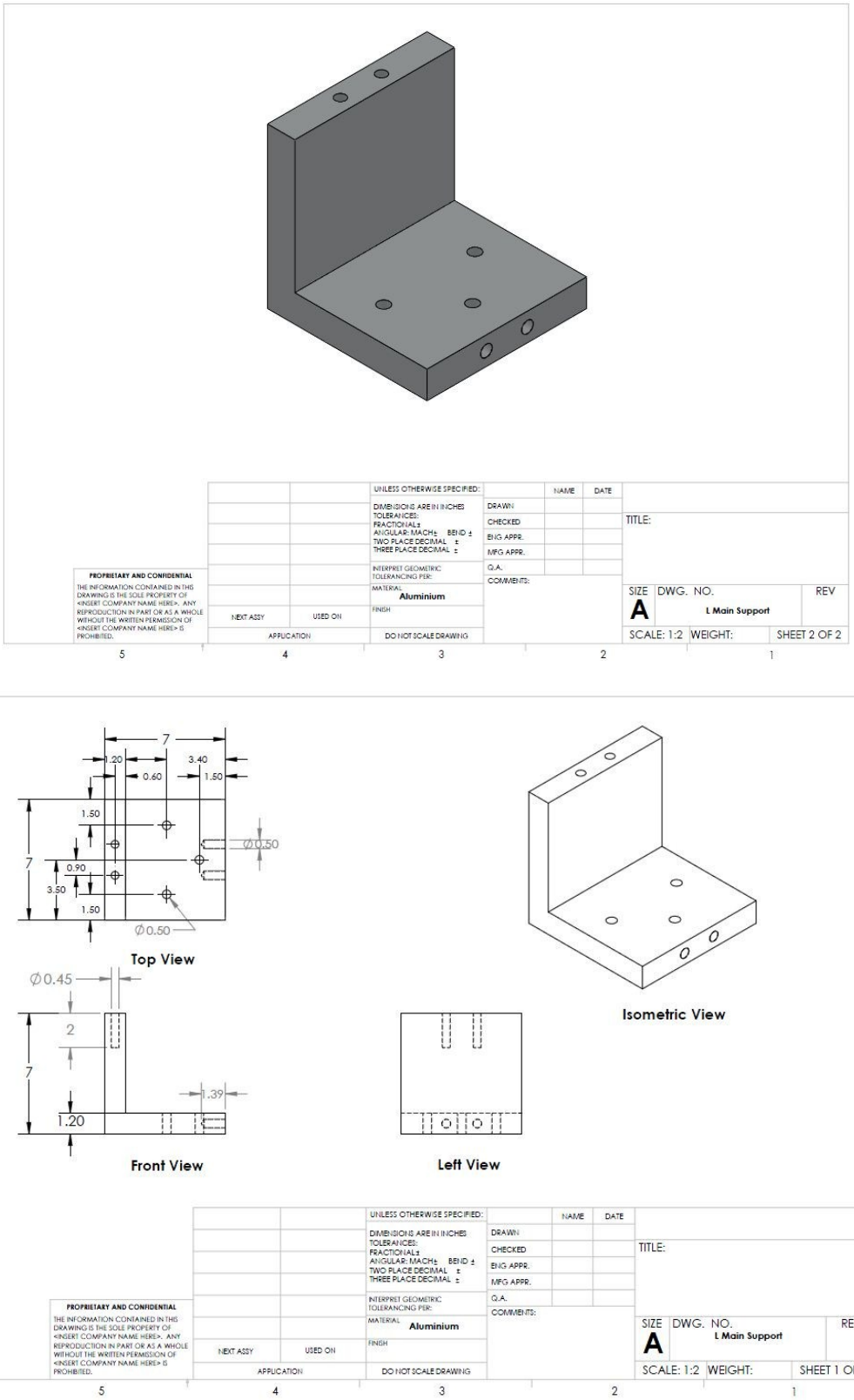

Fig. 9.7 L-shape main support for flapping mechanism

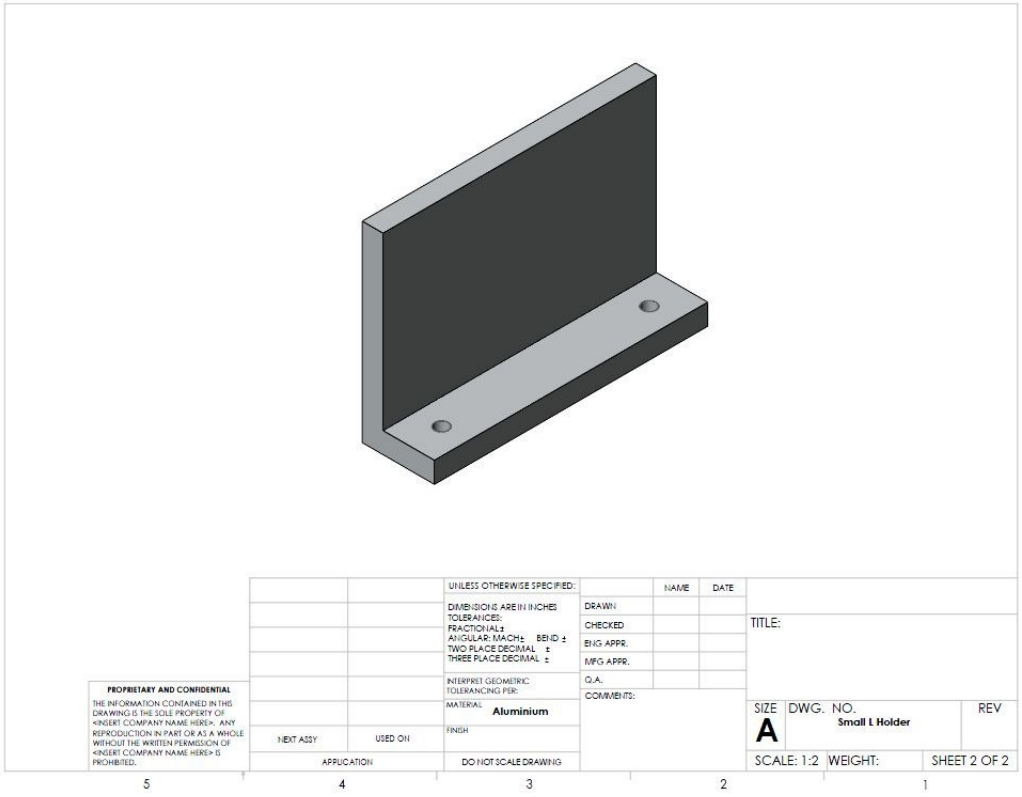

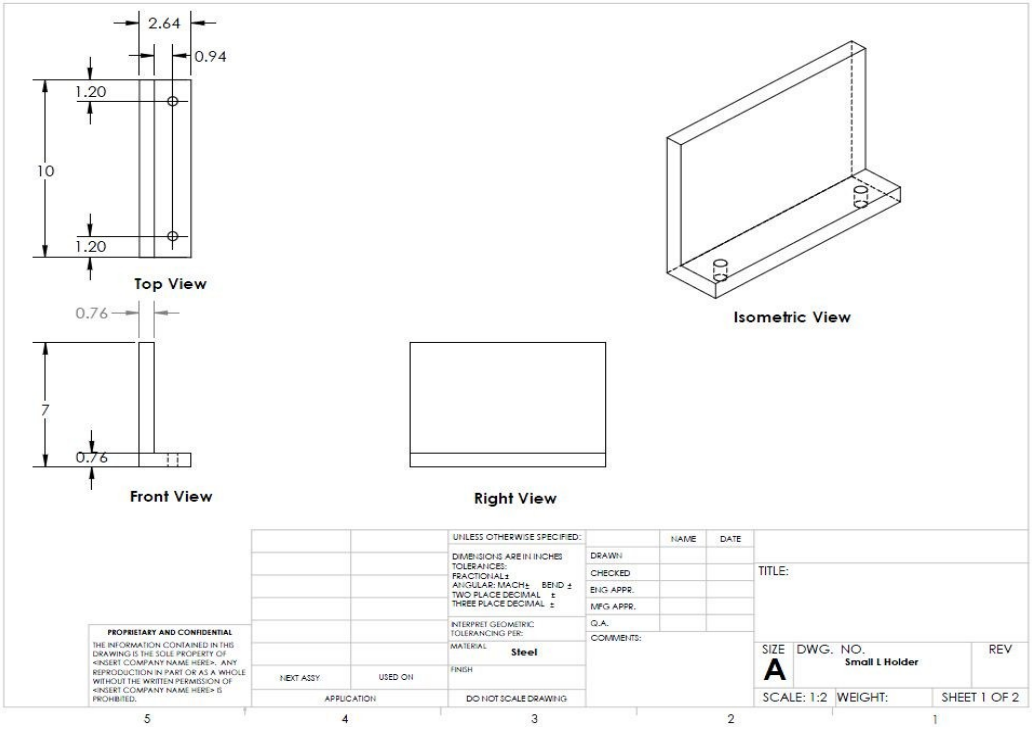

Fig. 9.8 L- shape small holder for flapping mechanism

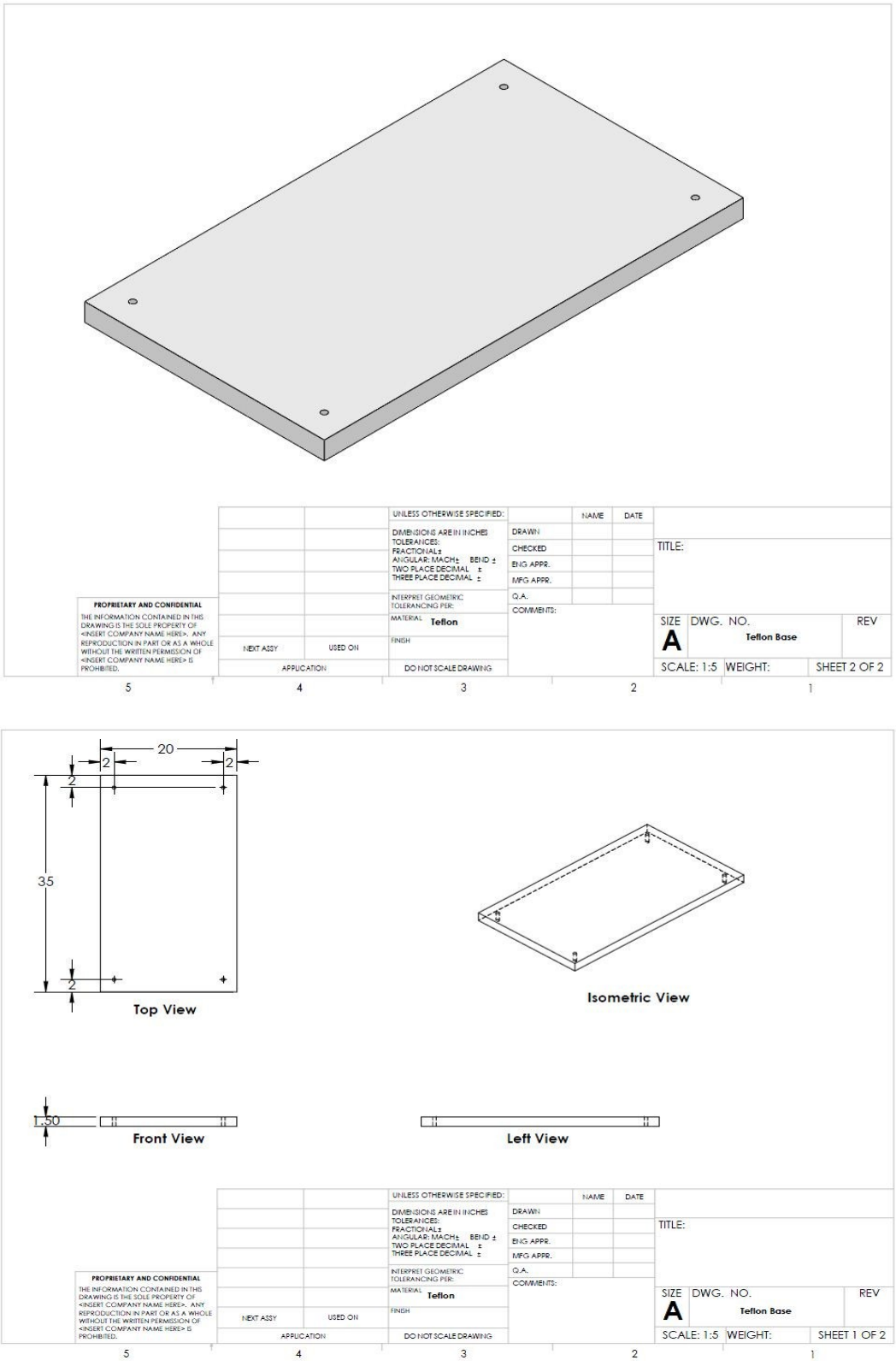

Fig. 9.9 Teflon base for flapping mechanism

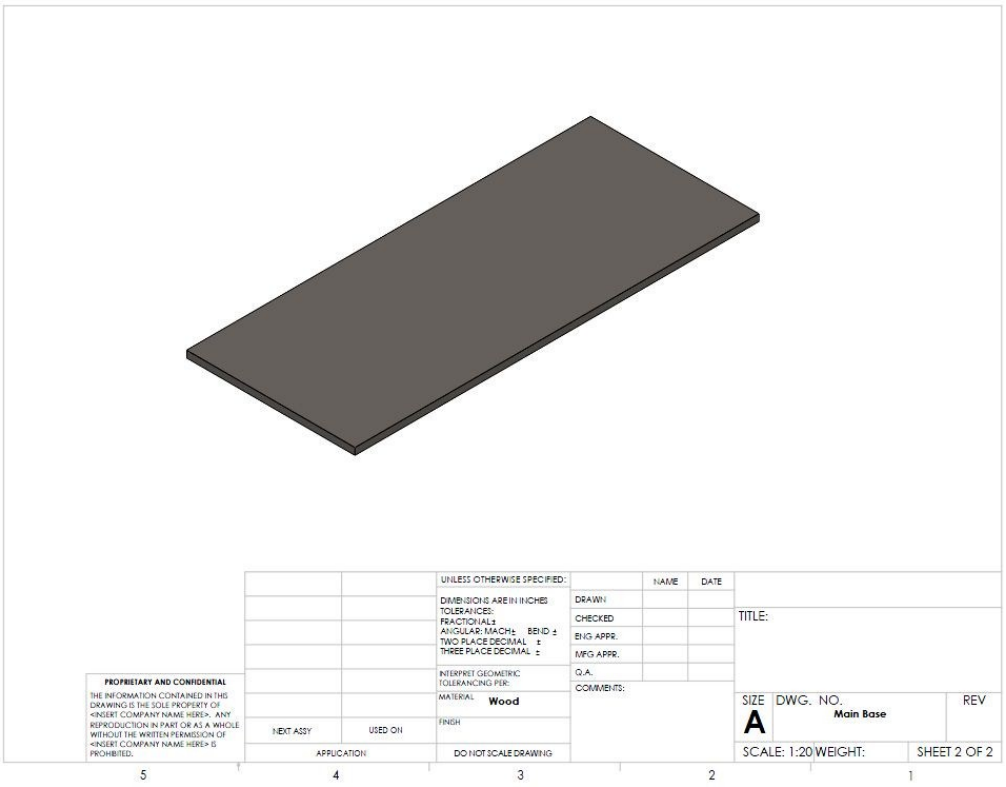

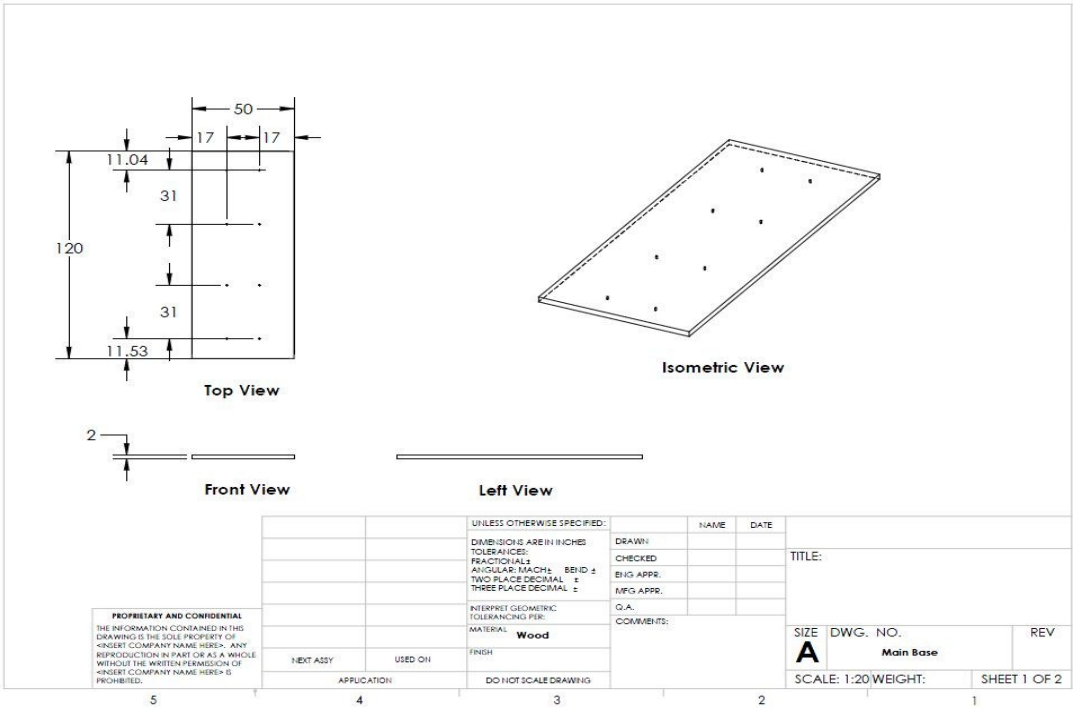

Fig. 9.10 Main wooden base support for apparatus

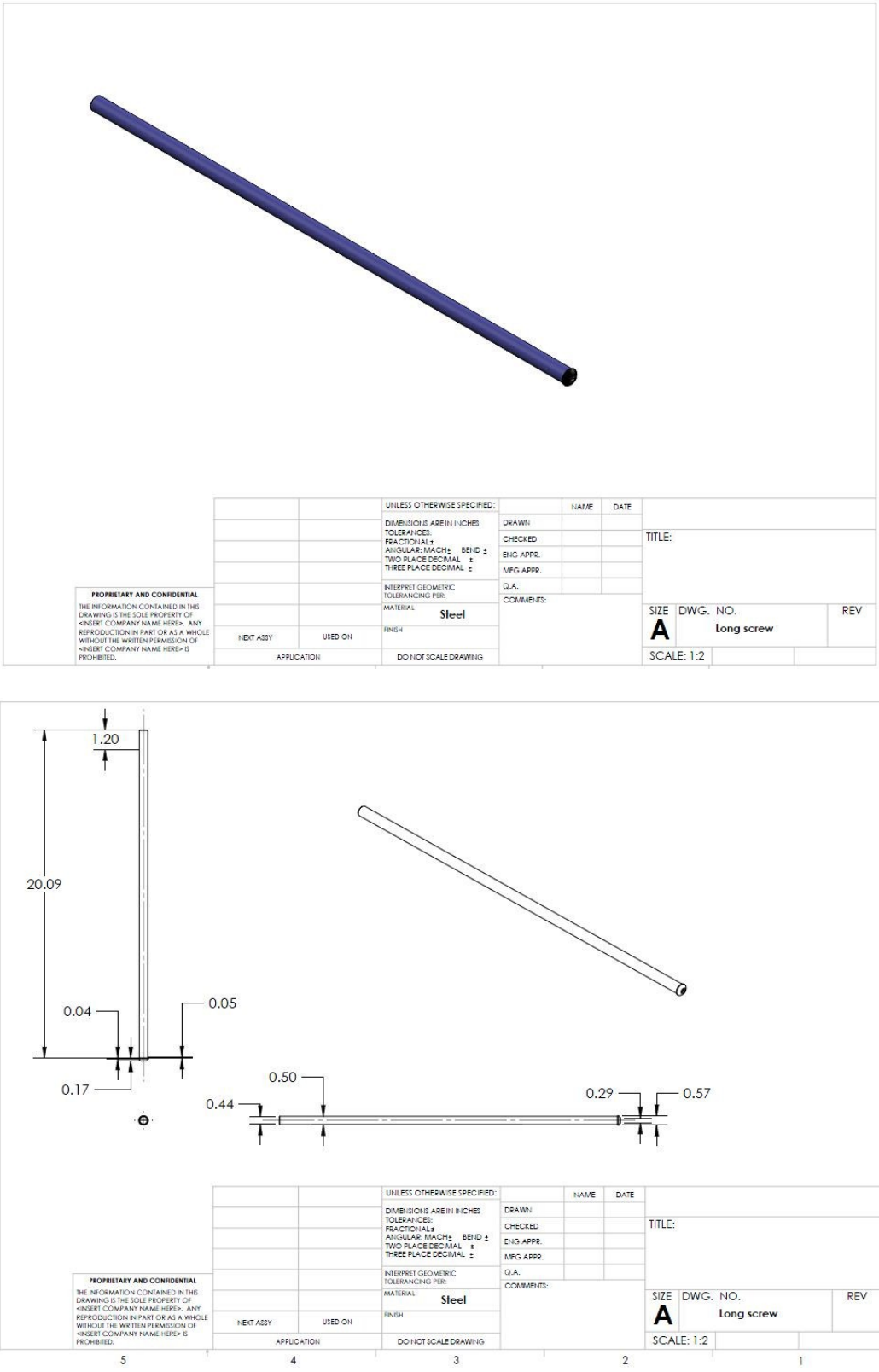

Fig. 9.11 Long screw for flapping mechanism

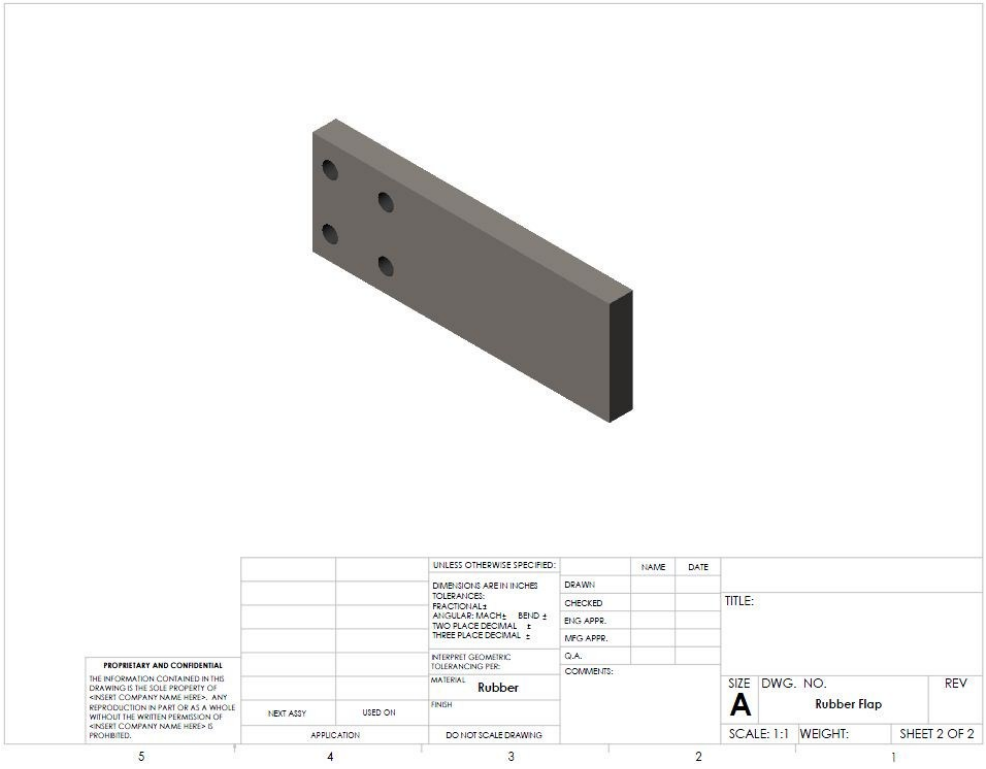

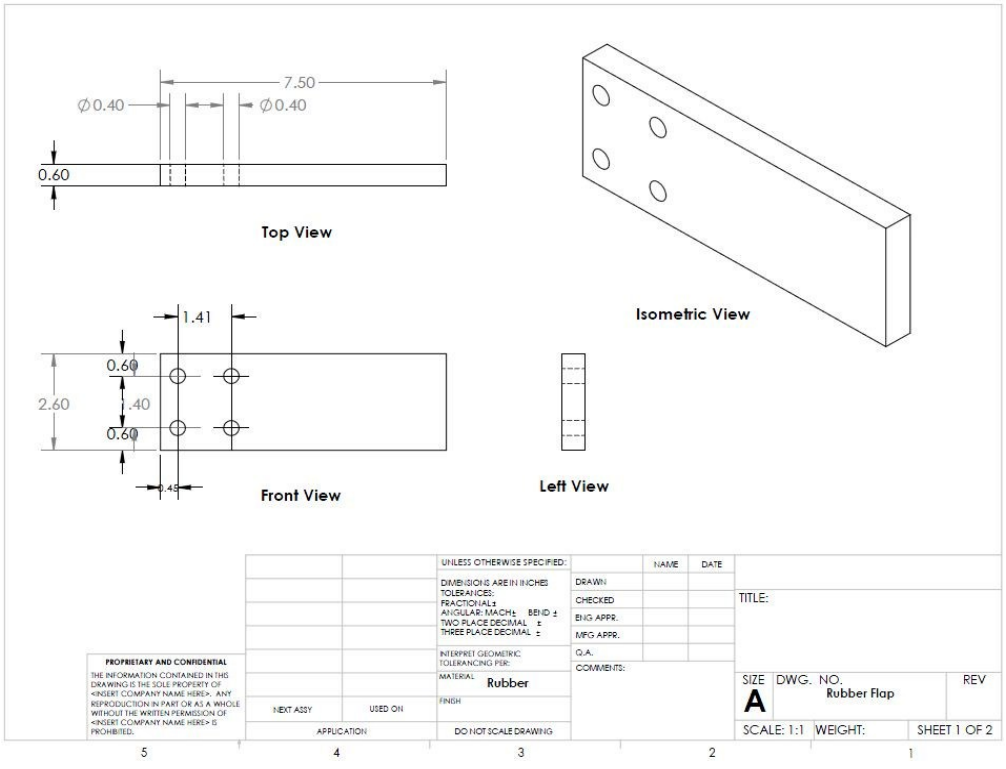

Fig. 9.12 Rubber flap for flapping mechanism

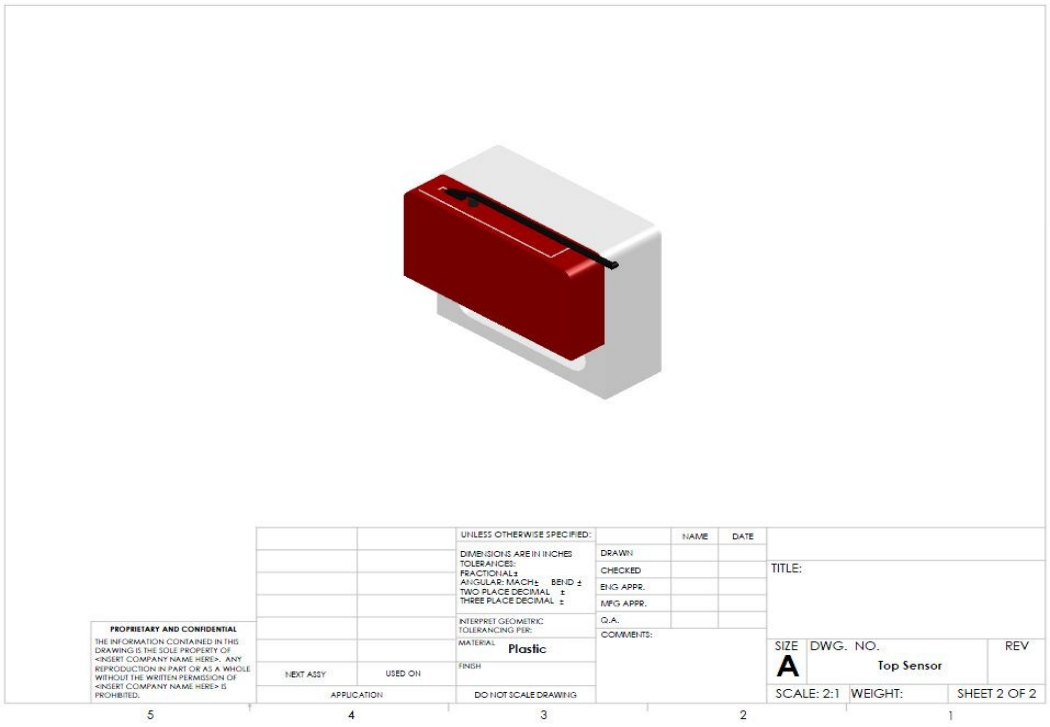

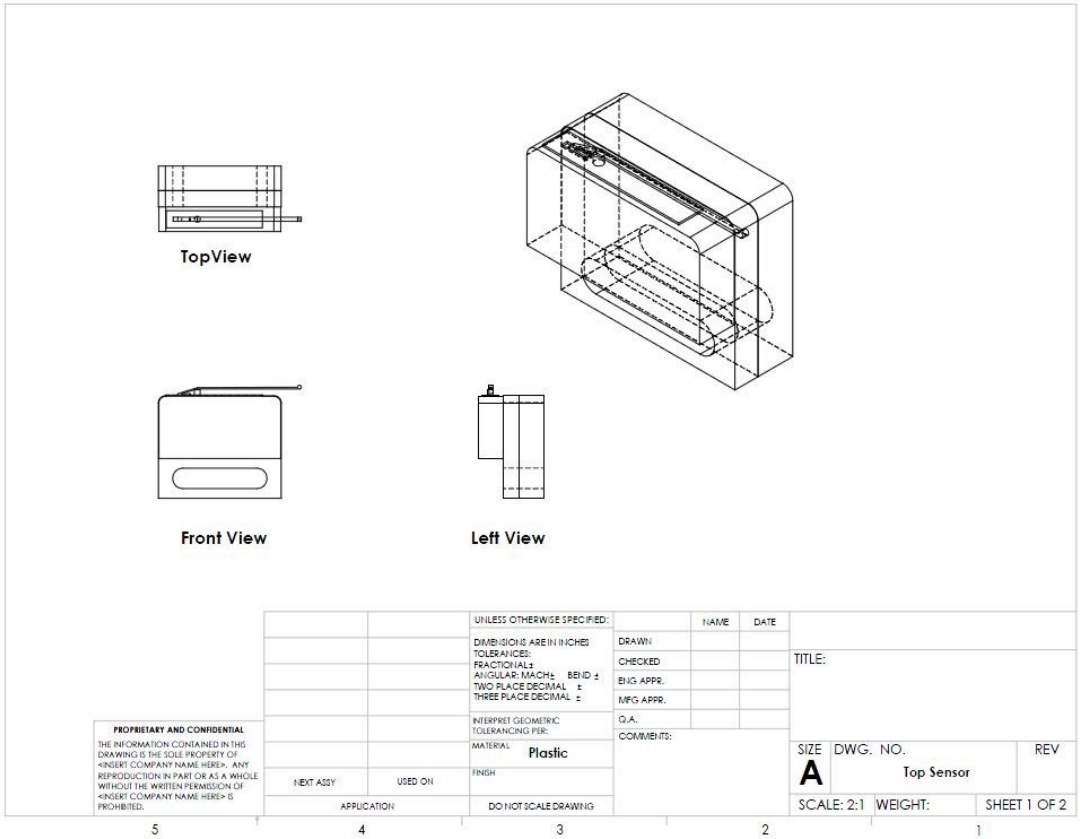

Fig. 9.13 Top limiting switch for flapping mechanism

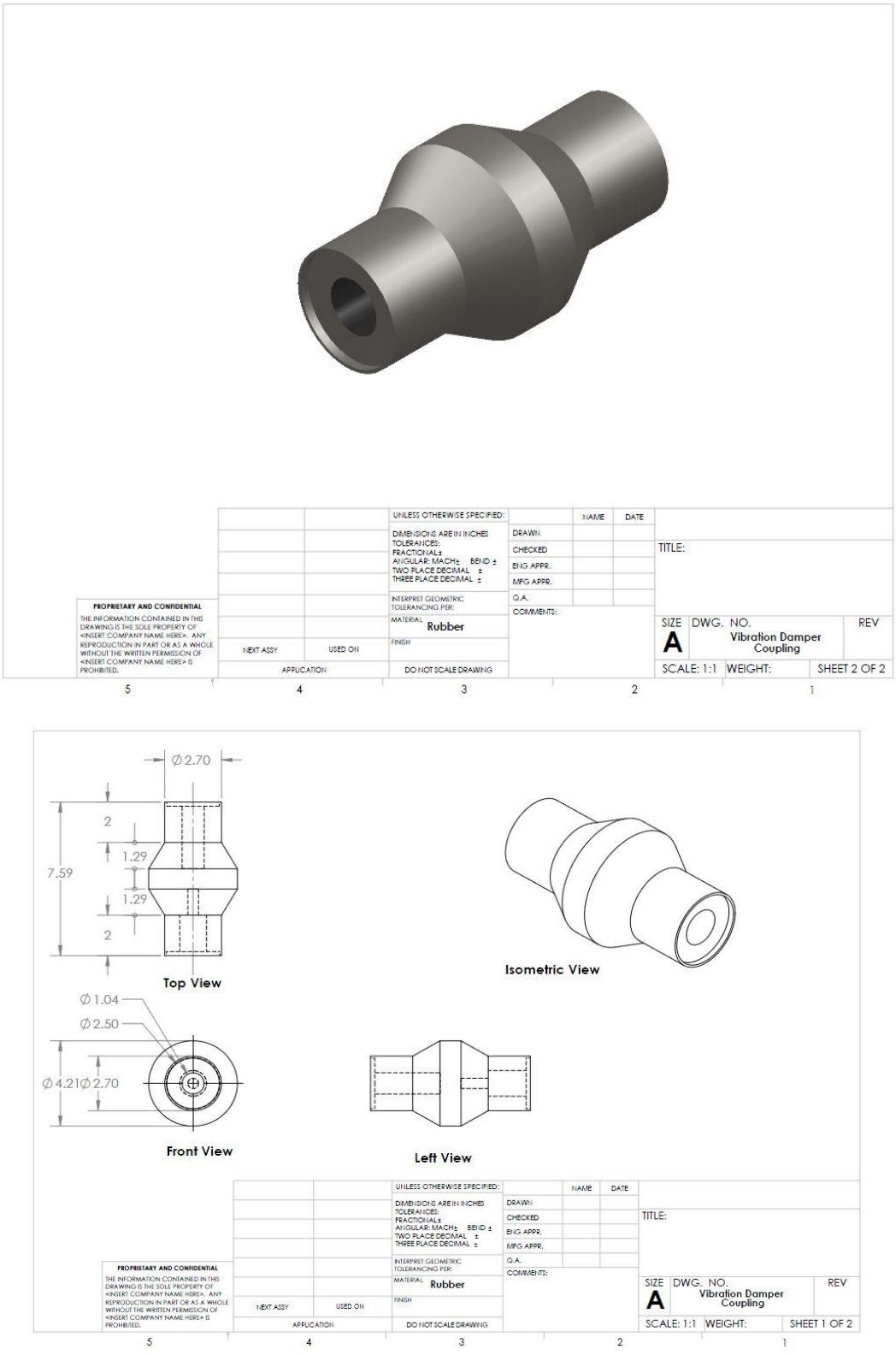

Fig. 9.14 Vibration damper coupling for flapping mechanism

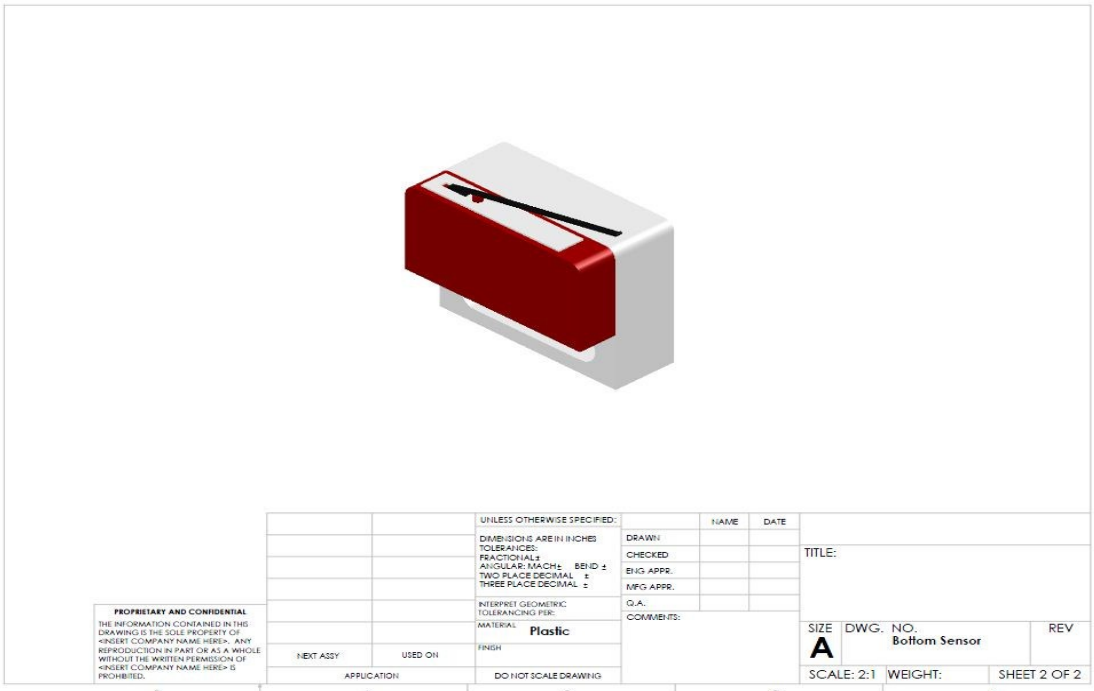

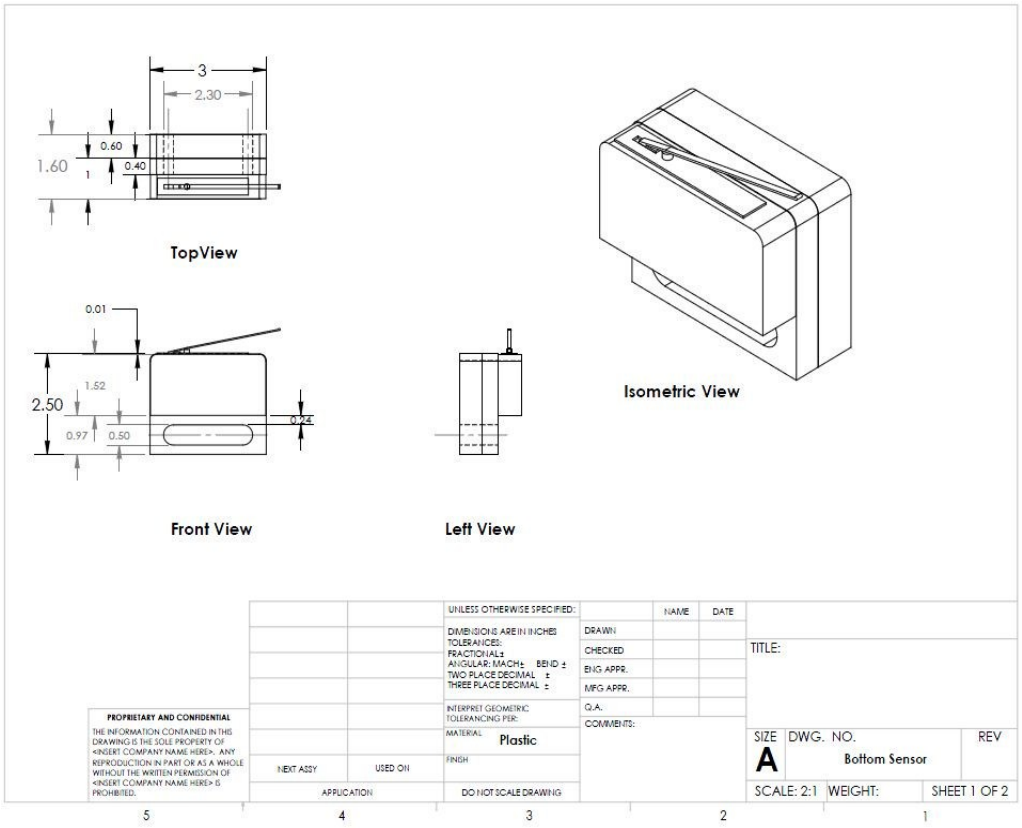

Fig. 9.15 Bottom limiting switch for flapping mechanism

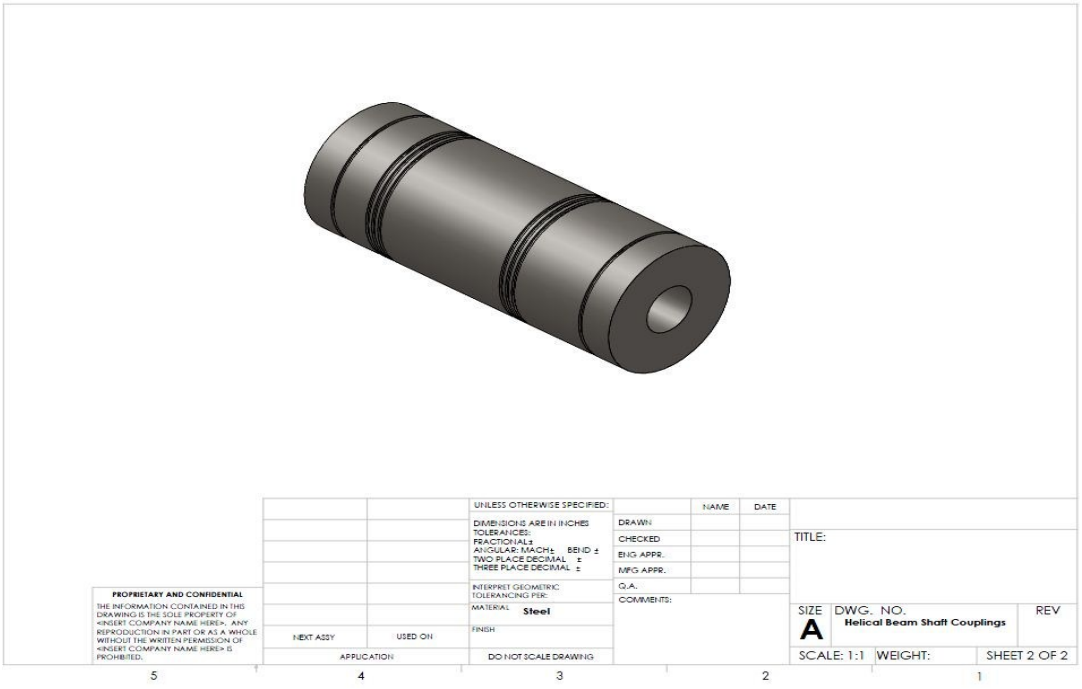

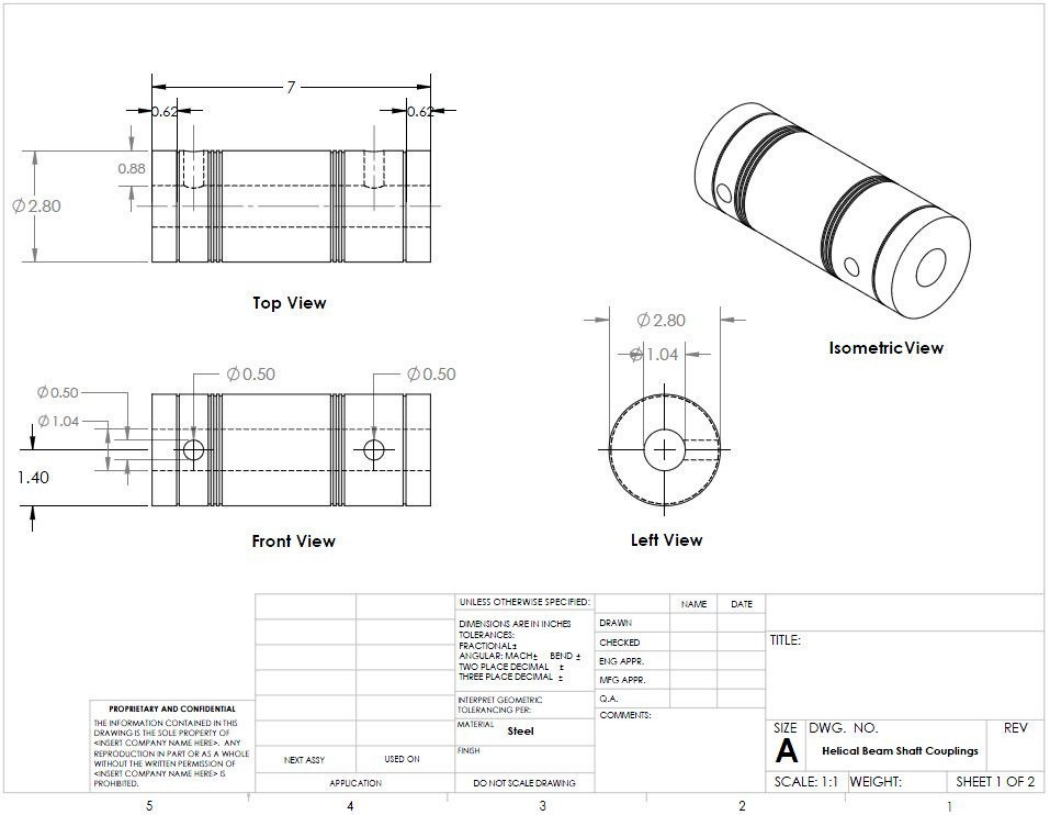

Fig. 9.16 Helical beam shaft coupling for flapping mechanism

9.3. Programming Codes

9.3.1 User defined function for Computational Investigation written in C++

```
*Open the user defined function library*/
#include "udf.h"

/*External declarations*/
#define VCG 0.96
#define Angle_start 0
DEFINE_CG_MOTION (plate,dt,vel,omega,time,dtime)
{
        /*declare the data types or variables*/
        Thread *t;
        real x[ND_ND];
        real VCGX, VCGY, WZ;
        real X0, Y0, r,  X1, Y1,fp;
        /*set the velocities due the flow motion to
        zero, since they are not used to compute the
        force on the wing, do anything else*/
        NV_S(vel, =, 0.0);
        NV_S(omega, =, 0.0);
        /*Set the condition to perform calculations if there
        is any data ready.*/
        if (!Data_Valid_P ())
        return;
        t = DT_THREAD (dt);
        /*Computation condition to stop the model
        before a period of 280 seconds. One can choose to
        stop the model at any other time when he writes his
        own program. The assignments are inside the if
        statement.*/
        if (time < 0.19625)
                {
                r = 0.12;
                X0 =0.0;
                Y0 =0.0;
                /* CYCLE_1 The angular velocity is 5730 deg/s or
                /*8 rad/s*/
                WZ =  8;
                VCGX = -VCG * sin(WZ * time);
                VCGY = VCG * cos(WZ * time);
                X1 = X0 + VCGX * dtime;
                Y1 = Y0 + VCGY * dtime;
                vel[0]=VCGX;
                vel[1]=VCGY;
                }
        if (time > 0.19625*1)
                {
                WZ =   -8;
```

```
            VCGX = -VCG * sin(WZ * time);
            VCGY = VCG * cos(WZ * time);
            X1 = X0 + VCGX * dtime;
            Y1 = Y0 + VCGY * dtime;
            vel[0]=VCGX;
            vel[1]=VCGY;
            }
if (time > 0.19625*2)
            {
            WZ =   8;
            VCGX = -VCG * sin(WZ * time);
            VCGY = VCG * cos(WZ * time);
            X1 = X0 + VCGX * dtime;
            Y1 = Y0 + VCGY * dtime;
            vel[0]=VCGX;
            vel[1]=VCGY;
            }
if (time > 0.19625*3)
            {
            WZ =   -8;
            VCGX = -VCG * sin(WZ * time);
            VCGY = VCG * cos(WZ * time);
            X1 = X0 + VCGX * dtime;
            Y1 = Y0 + VCGY * dtime;
            vel[0]=VCGX;
            vel[1]=VCGY;
            }
if (time > 0.19625*4)
            {
            WZ =   8;
            VCGX = -VCG * sin(WZ * time);
            VCGY = VCG * cos(WZ * time);
            X1 = X0 + VCGX * dtime;
            Y1 = Y0 + VCGY * dtime;
            vel[0]=VCGX;
            vel[1]=VCGY;
                        }

if (time > 0.19625*5)
            {
            WZ =   -8;
            VCGX = -VCG * sin(WZ * time);
            VCGY = VCG * cos(WZ * time);
            X1 = X0 + VCGX * dtime;
            Y1 = Y0 + VCGY * dtime;
            vel[0]=VCGX;
            vel[1]=VCGY;
                        }
if (time > 0.19625*6)
            {
            WZ =   8;
```

```
            VCGX = -VCG * sin(WZ * time);
            VCGY = VCG * cos(WZ * time);
            X1 = X0 + VCGX * dtime;
            Y1 = Y0 + VCGY * dtime;
            vel[0]=VCGX;
            vel[1]=VCGY;
                        }
if (time > 0.19625*7)
            {
            WZ =   -8;
            VCGX = -VCG * sin(WZ * time);
            VCGY = VCG * cos(WZ * time);
            X1 = X0 + VCGX * dtime;
            Y1 = Y0 + VCGY * dtime;
            vel[0]=VCGX;
            vel[1]=VCGY;
                        }
if (time > 0.19625*8)
            {
            WZ =   8;
            VCGX = -VCG * sin(WZ * time);
            VCGY = VCG * cos(WZ * time);
            X1 = X0 + VCGX * dtime;
            Y1 = Y0 + VCGY * dtime;
            vel[0]=VCGX;
            vel[1]=VCGY;
                        }
if (time > 0.19625*9)
            WZ =   -8;
            VCGX = -VCG * sin(WZ * time);
            VCGY = VCG * cos(WZ * time);
            X1 = X0 + VCGX * dtime;
            Y1 = Y0 + VCGY * dtime;
            vel[0]=VCGX;
            vel[1]=VCGY;
                        }
if (time > 0.19625*10)
            {
            WZ =   8;
            VCGX = -VCG * sin(WZ * time);
            VCGY = VCG * cos(WZ * time);
            X1 = X0 + VCGX * dtime;
            Y1 = Y0 + VCGY * dtime;
            vel[0]=VCGX;
            vel[1]=VCGY;
                        }
if (time > 0.19625*11)
            {
            WZ =   -8;
            VCGX = -VCG * sin(WZ * time);
            VCGY = VCG * cos(WZ * time);
```

```
            X1 = X0 + VCGX * dtime;
            Y1 = Y0 + VCGY * dtime;
            vel[0]=VCGX;
            vel[1]=VCGY;
                        }
if (time > 0.19625*12)
            {
            WZ =   8;
            VCGX = -VCG * sin(WZ * time);
            VCGY = VCG * cos(WZ * time);
            X1 = X0 + VCGX * dtime;
            Y1 = Y0 + VCGY * dtime;
            vel[0]=VCGX;
            vel[1]=VCGY;
                        }
if (time > 0.19625*13)
            {
            WZ =   -8;
            VCGX = -VCG * sin(WZ * time);
            VCGY = VCG * cos(WZ * time);
            X1 = X0 + VCGX * dtime;
            Y1 = Y0 + VCGY * dtime;
            vel[0]=VCGX;
            vel[1]=VCGY;
                        }
if (time > 0.19625*14)
            {
            WZ =   8;
            VCGX = -VCG * sin(WZ * time);
            VCGY = VCG * cos(WZ * time);
            X1 = X0 + VCGX * dtime;
            Y1 = Y0 + VCGY * dtime;
            vel[0]=VCGX;
            vel[1]=VCGY;
                        }
if (time > 0.19625*15)
            {
            WZ =   -8;
            VCGX = -VCG * sin(WZ * time);
            VCGY = VCG * cos(WZ * time);
            X1 = X0 + VCGX * dtime;
            Y1 = Y0 + VCGY * dtime;
            vel[0]=VCGX;
            vel[1]=VCGY;
                        }
if (time > 0.19625*16)
            {
            WZ =   8;
            VCGX = -VCG * sin(WZ * time);
            VCGY = VCG * cos(WZ * time);
            X1 = X0 + VCGX * dtime;
```

```
                Y1 = Y0 + VCGY * dtime;
                vel[0]=VCGX;
                vel[1]=VCGY;
                        }
        if (time > 0.19625*17)
                {
                WZ =   -8;
                VCGX = -VCG * sin(WZ * time);
                VCGY = VCG * cos(WZ * time);
                X1 = X0 + VCGX * dtime;
                Y1 = Y0 + VCGY * dtime;
                vel[0]=VCGX;
                vel[1]=VCGY;
                        }
        else
                {
                printf("Model stopped, Time limit is reached");
                }
        /*Display or output functions*/
        Message("Time = %f,  CG_xposition = %f,  CG_yposition = %f\n", time, X1,
Y1);
        /* Assign to the center of gravity. The assignment will
        be used to move the flat plate about its center of gravity
        and a fixed coordinate system.*/
        x[0] = X1;
        x[1] = Y1;
        omega[2] = WZ;
}
```

9.3.2 Program for experimental simulation of flapping motion with Easy C language.

a) Robotics Program flow chart for experimental investigation

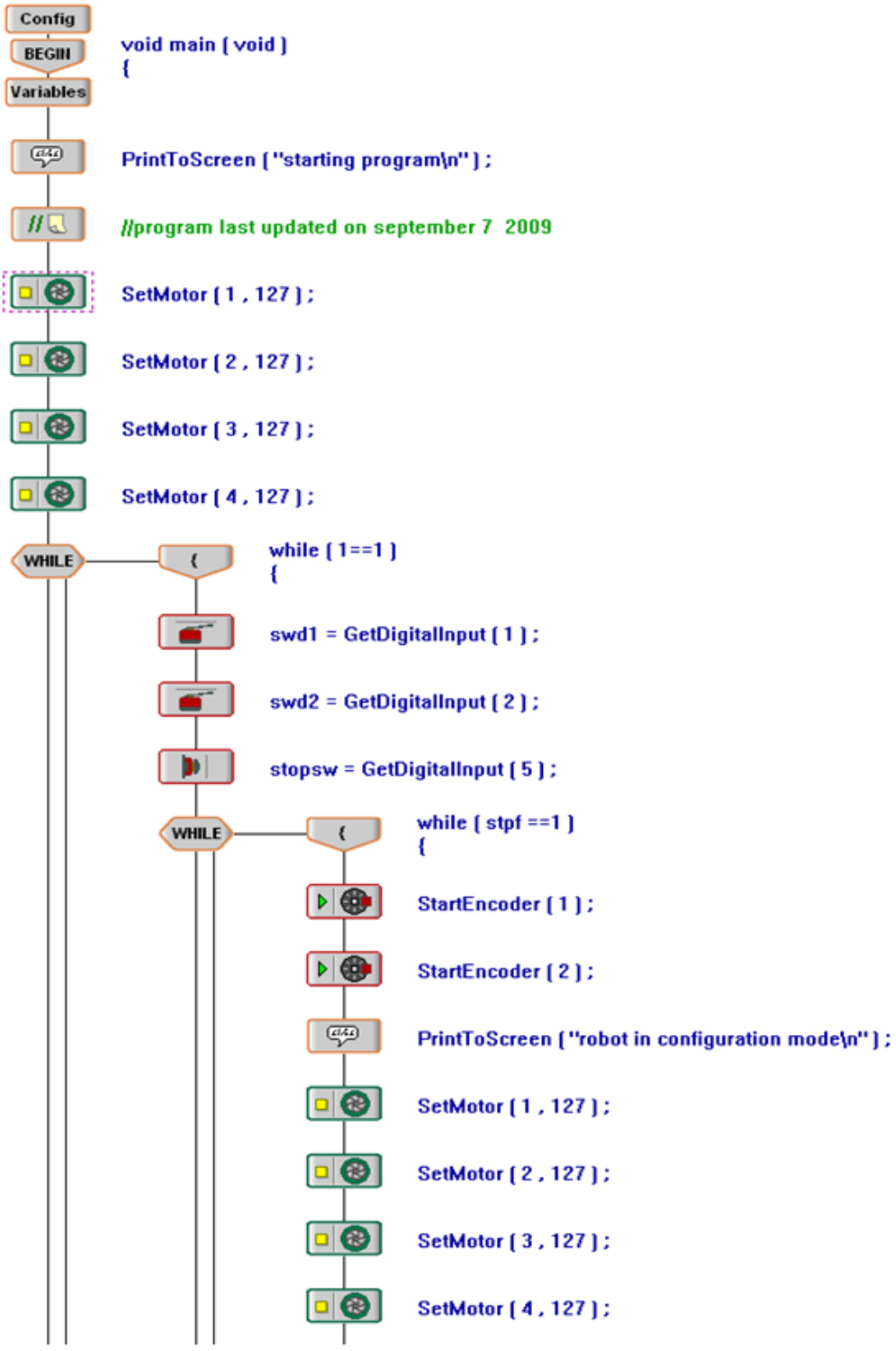
Config
BEGIN
Variables
void main (void)
{
PrintToScreen ("starting program\n") ;
//program last updated on september 7 2009
SetMotor (1 , 127) ;
SetMotor (2 , 127) ;
SetMotor (3 , 127) ;
SetMotor (4 , 127) ;
WHILE
{
while (1==1)
{
swd1 = GetDigitalInput (1) ;
swd2 = GetDigitalInput (2) ;
stopsw = GetDigitalInput (5) ;
WHILE
{
while (stpf ==1)
{
StartEncoder (1) ;
StartEncoder (2) ;
PrintToScreen ("robot in configuration mode\n") ;
SetMotor (1 , 127) ;
SetMotor (2 , 127) ;
SetMotor (3 , 127) ;
SetMotor (4 , 127) ;

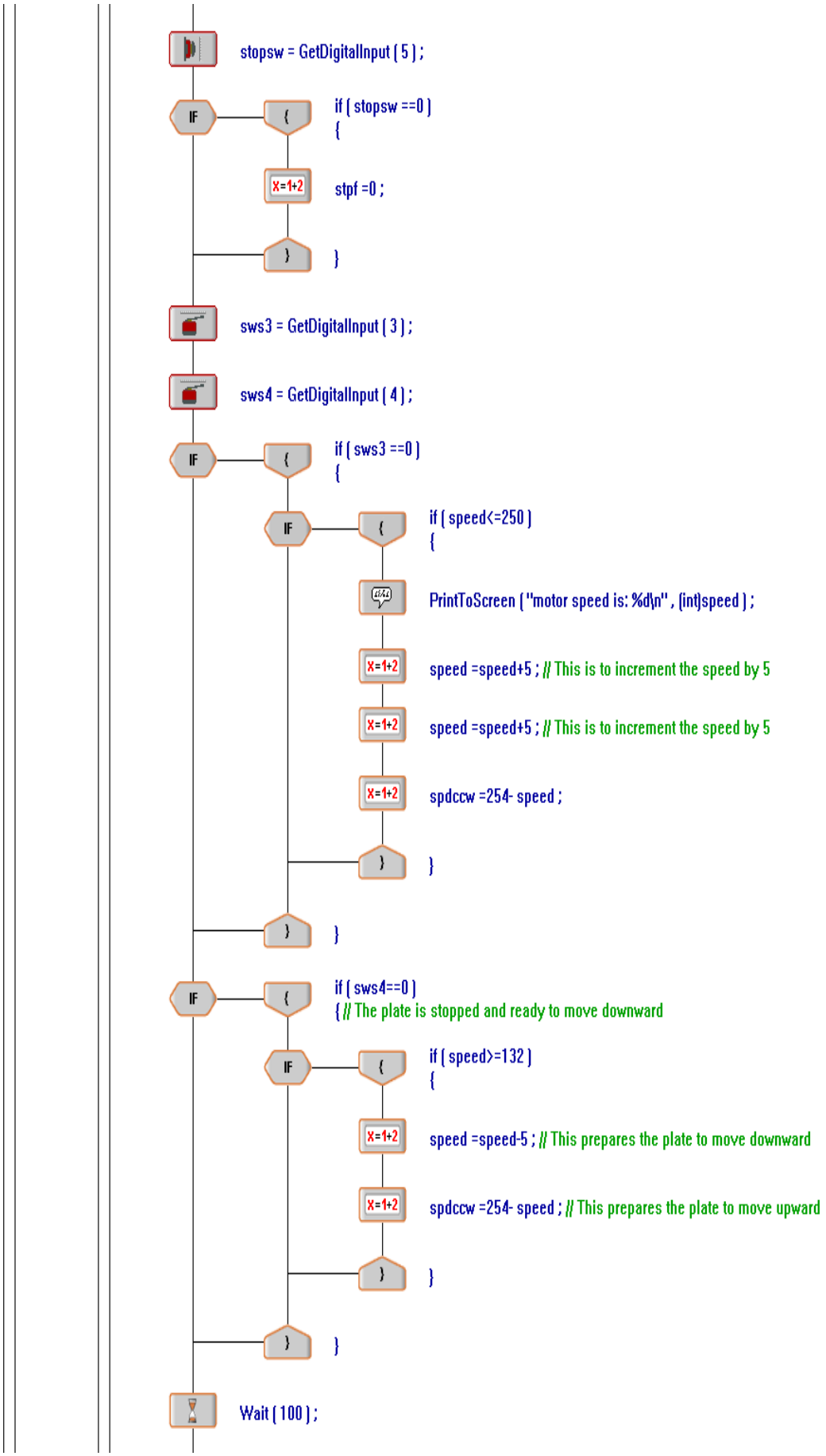
stopsw = GetDigitalInput (5) ;
IF
{
if (stopsw ==0)
{
X=1+2
stpf =0 ;
}
}
sws3 = GetDigitalInput (3) ;
sws4 = GetDigitalInput (4) ;
IF
{
if (sws3 ==0)
{
IF
{
if (speed<=250)
{
PrintToScreen ("motor speed is: %d\n" , (int)speed) ;
X=1+2
speed =speed+5 ; // This is to increment the speed by 5
X=1+2
speed =speed+5 ; // This is to increment the speed by 5
X=1+2
spdccw =254- speed ;
}
}
}
IF
{
if (sws4==0)
{ // The plate is stopped and ready to move downward
IF
{
if (speed>=132)
{
X=1+2
speed =speed-5 ; // This prepares the plate to move downward
X=1+2
spdccw =254- speed ; // This prepares the plate to move upward
}
}
}
Wait (100) ;

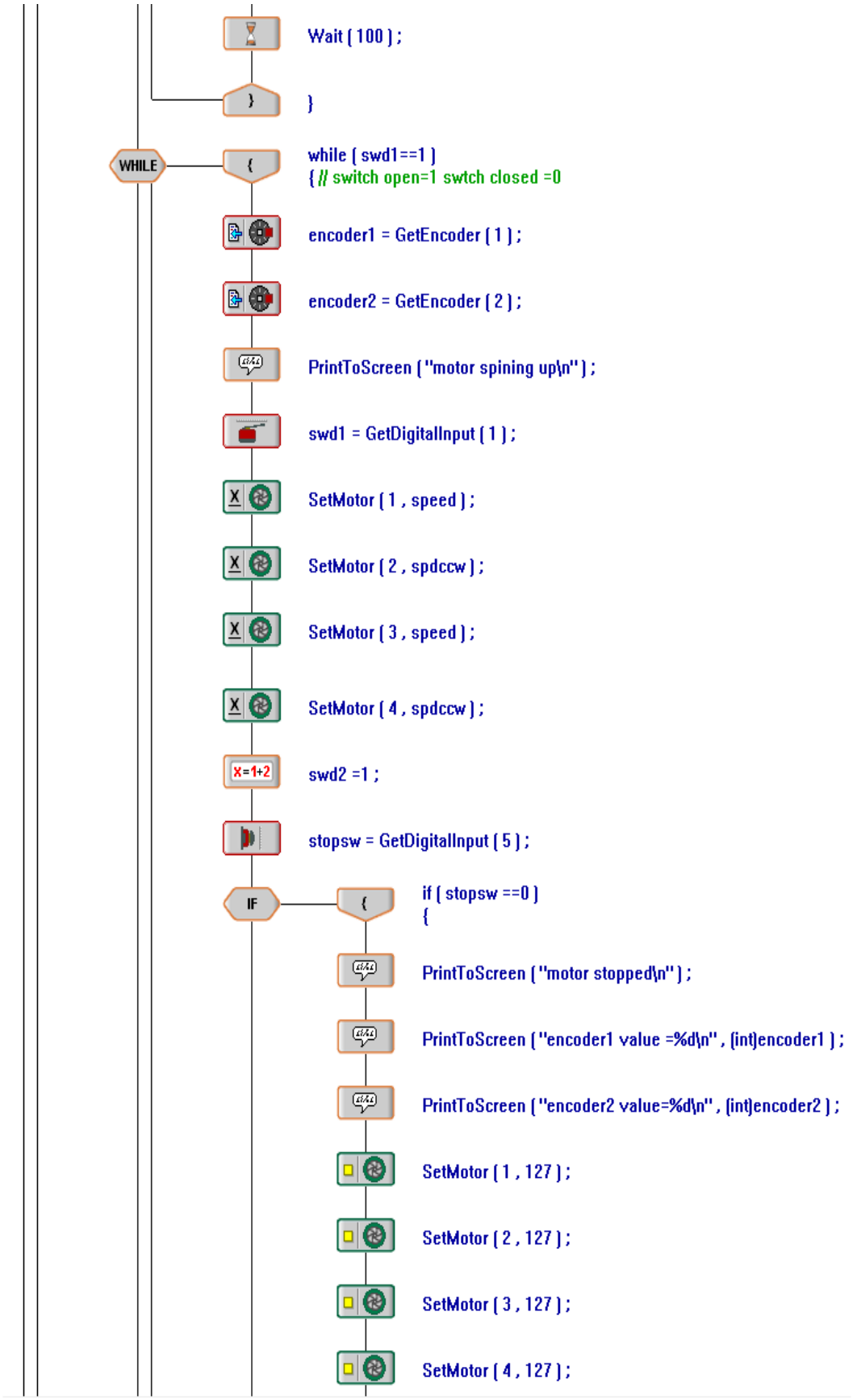
Wait (100) ;
}
WHILE
while (swd1==1)
{ // switch open=1 swtch closed =0
encoder1 = GetEncoder (1) ;
encoder2 = GetEncoder (2) ;
PrintToScreen ("motor spining up\n") ;
swd1 = GetDigitalInput (1) ;
SetMotor (1 , speed) ;
SetMotor (2 , spdccw) ;
SetMotor (3 , speed) ;
SetMotor (4 , spdccw) ;
X=1+2
swd2 =1 ;
stopsw = GetDigitalInput (5) ;
IF
if (stopsw ==0)
{
PrintToScreen ("motor stopped\n") ;
PrintToScreen ("encoder1 value =%d\n" , (int)encoder1) ;
PrintToScreen ("encoder2 value=%d\n" , (int)encoder2) ;
SetMotor (1 , 127) ;
SetMotor (2 , 127) ;
SetMotor (3 , 127) ;
SetMotor (4 , 127) ;

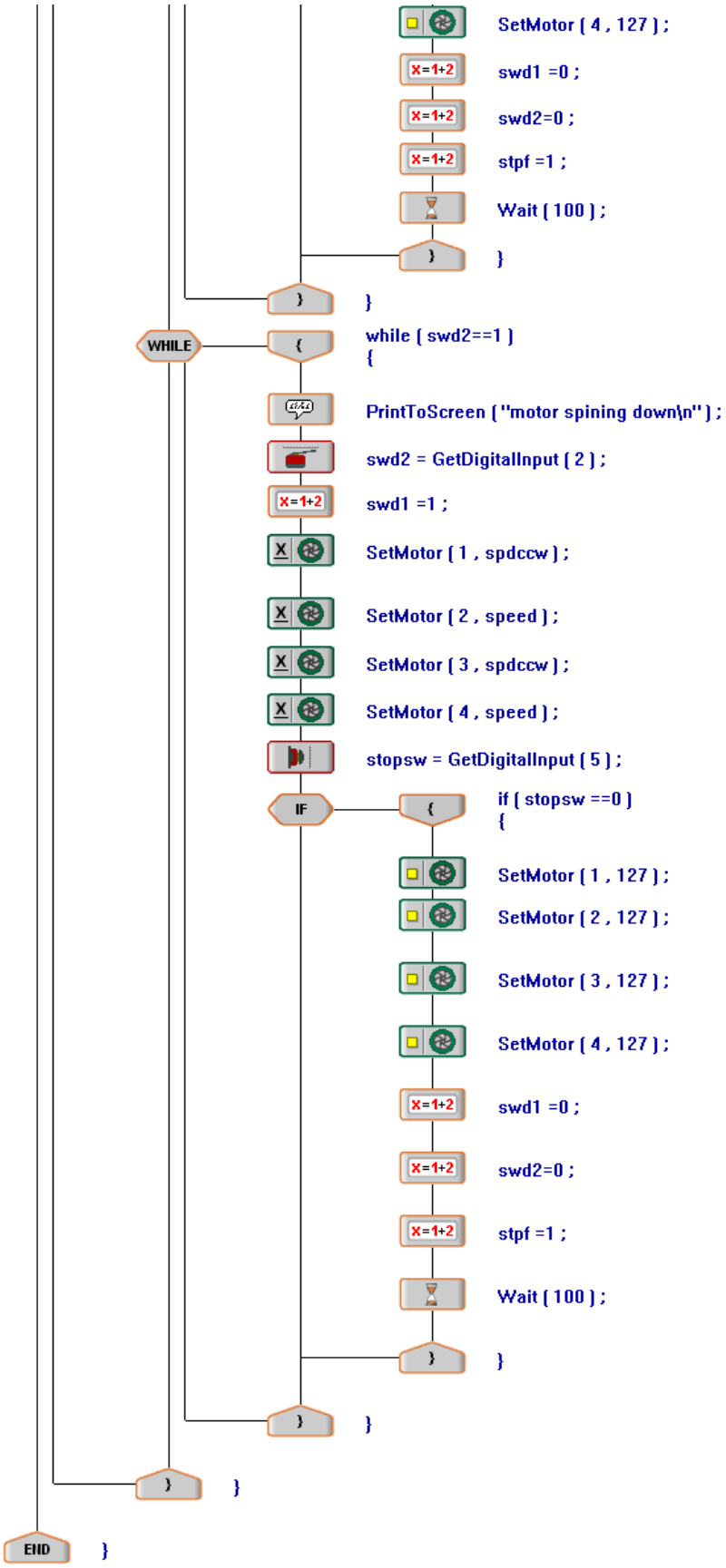
SetMotor (4 , 127) ;
swd1 =0 ;
swd2=0 ;
stpf =1 ;
Wait (100) ;
}
}
WHILE
while (swd2==1)
{
PrintToScreen ("motor spining down\n") ;
swd2 = GetDigitalInput (2) ;
swd1 =1 ;
SetMotor (1 , spdccw) ;
SetMotor (2 , speed) ;
SetMotor (3 , spdccw) ;
SetMotor (4 , speed) ;
stopsw = GetDigitalInput (5) ;
IF
if (stopsw ==0)
{
SetMotor (1 , 127) ;
SetMotor (2 , 127) ;
SetMotor (3 , 127) ;
SetMotor (4 , 127) ;
swd1 =0 ;
swd2=0 ;
stpf =1 ;
Wait (100) ;
}
}
}
}
END
}

b) Robotics Program code for experimental investigation

```
#include "Main.h"

void main ( void )
{
    int swd1 = 1; // switch direction of rotation
    int swd2 = 1; // switch direction of rotation
    int sws3 = 1; // increase speed
    int sws4 = 1; // decrease speed
    int stopsw = 1; // stop / engage system
    int stpf = 1; // 1= stop 0= rotate
    int speed = 127;
    int spdccw = 127;
    int encoder1 = 0;
    int encoder2 = 0;

    PrintToScreen ( "starting program\n" ) ;
    //program last updated on september 7  2009
    SetMotor ( 1 , 127 ) ;
    SetMotor ( 2 , 127 ) ;
    SetMotor ( 3 , 127 ) ;
    SetMotor ( 4 , 127 ) ;
    while ( 1==1 )
    {
        swd1 = GetDigitalInput ( 1 ) ;
        swd2 = GetDigitalInput ( 2 ) ;
        stopsw = GetDigitalInput ( 5 ) ;
        while ( stpf ==1 )
        {
            StartEncoder ( 1 ) ;
            StartEncoder ( 2 ) ;
            PrintToScreen ( "robot in configuration mode\n" ) ;
            SetMotor ( 1 , 127 ) ;
            SetMotor ( 2 , 127 ) ;
            SetMotor ( 3 , 127 ) ;
            SetMotor ( 4 , 127 ) ;
            stopsw = GetDigitalInput ( 5 ) ;
            if ( stopsw ==0 )
```

```
38              {
39                  stpf =0 ;
40              }
41              sws3 = GetDigitalInput ( 3 ) ;
42              sws4 = GetDigitalInput ( 4 ) ;
43              if ( sws3 ==0 )
44              {
45                  if ( speed<=250 )
46                  {
47                      PrintToScreen ( "motor speed is: %d\n" , (int)speed ) ;
48                      speed =speed+5 ; // This is to increment the speed by 5
49                      spdccw =254- speed ;
50                  }
51              }
52              if ( sws4==0 )
53              { // The plate is stopped and ready to move downward
54                  if ( speed>=132 )
55                  {
56                      speed =speed-5 ; // This prepares the plate to move downward
57                      spdccw =254- speed ; // This prepares the plate to move upward
58                  }
59              }
60              Wait ( 100 ) ;
61          }
62          while ( swd1==1 )
63          { // switch open=1 swtch closed =0
64              encoder1 = GetEncoder ( 1 ) ;
65              encoder2 = GetEncoder ( 2 ) ;
66              PrintToScreen ( "motor spining up\n" ) ;
67              swd1 = GetDigitalInput ( 1 ) ;
68              SetMotor ( 1 , speed ) ;
69              SetMotor ( 2 , spdccw ) ;
70              SetMotor ( 3 , speed ) ;
71              SetMotor ( 4 , spdccw ) ;
72              swd2 =1 ;
73              stopsw = GetDigitalInput ( 5 ) ;
74              if ( stopsw ==0 )
```

```
75              {
76                  PrintToScreen ( "motor stopped\n" ) ;
77                  PrintToScreen ( "encoder1 value =%d\n'
78                  PrintToScreen ( "encoder2 value=%d\n"
79                  SetMotor ( 1 , 127 ) ;
80                  SetMotor ( 2 , 127 ) ;
81                  SetMotor ( 3 , 127 ) ;
82                  SetMotor ( 4 , 127 ) ;
83                  swd1 =0 ;
84                  swd2=0 ;
85                  stpf =1 ;
86                  Wait ( 100 ) ;
87              }
88          }
89          while ( swd2==1 )
90          {
91              PrintToScreen ( "motor spining down\n" ) ;
92              swd2 = GetDigitalInput ( 2 ) ;
93              swd1 =1 ;
94              SetMotor ( 1 , spdccw ) ;
95              SetMotor ( 2 , speed ) ;
96              SetMotor ( 3 , spdccw ) ;
97              SetMotor ( 4 , speed ) ;
98              stopsw = GetDigitalInput ( 5 ) ;
99              if ( stopsw ==0 )
100             {
101                 SetMotor ( 1 , 127 ) ;
102                 SetMotor ( 2 , 127 ) ;
103                 SetMotor ( 3 , 127 ) ;
104                 SetMotor ( 4 , 127 ) ;
105                 swd1 =0 ;
106                 swd2=0 ;
107                 stpf =1 ;
108                 Wait ( 100 ) ;
109             }
110         }
111     }
112 }
```

9.3.3 Code written in Mat lab for temperature data acquisition

```
% DATA ACQUISITION CODE

functionThermoDAQ(Freq,Duration)
clear all
clc
Freq=100;
Duration=(100); %Measured in secs
globalai
ai=analoginput('nidaq');
ai.InputType='differential';
addchannel(ai,[0:7]);
ai.Channel(1).InputRange=[-5,5];
ai.Channel(1).SensorRange=[-5,5];
ai.Channel(1).UnitsRange=[-5,5];
ai.Channel(1).Units='Celsius';
ai.Channel(2:8).InputRange=[0,0.01];
set(ai,'SampleRate',Freq)
ActualRate = get(ai,'SampleRate')
DataNum=ActualRate*Duration;
set(ai,'SamplesPerTrigger',DataNum);
figure(1)
set(gcf,'doublebuffer','on');
subplot(8,1,1), P1 = plot(zeros(DataNum,1)); grid on
subplot(8,1,2), P2 = plot(zeros(DataNum,1)); grid on
subplot(8,1,3), P3 = plot(zeros(DataNum,1)); grid on
subplot(8,1,4), P4 = plot(zeros(DataNum,1)); grid on
subplot(8,1,5), P5 = plot(zeros(DataNum,1)); grid on
subplot(8,1,6), P6 = plot(zeros(DataNum,1)); grid on
subplot(8,1,7), P7 = plot(zeros(DataNum,1)); grid on
subplot(8,1,8), P8 = plot(zeros(DataNum,1)); grid on
%Start the data acquisition
start(ai)
whileai.SamplesAcquired< Duration*ActualRate
data = peekdata(ai, ai.SamplesAcquired);
set(P1, 'ydata', data(:,1));
set(P2, 'ydata', data(:,2));
set(P3, 'ydata', data(:,3));
set(P4, 'ydata', data(:,4));
set(P5, 'ydata', data(:,5));
set(P6, 'ydata', data(:,6));
set(P7, 'ydata', data(:,7));
set(P8, 'ydata', data(:,8));
drawnow;
end
time(1:1)=0;
exp_data=getdata(ai);
fori=1:Freq*Duration-1;
time(i+1,1)=time(i,1)+1/Freq;
end
all_data=[time,exp_data];
```

9.3 f J-Thermocouples written in
M

```
%PLOTING AND FILTERING CODE
clear all
clc
xmin =  0.0;
xmax = 10.0;
ymin = -0.002;
ymax =  0.002;

ambient_temperature=23.33;
ice_temperature=0;
DeltaTemperature=ambient_temperature;

s1=load('CalibTall_ambient2.txt');
s2=load('Ice_TC1.txt');
s3=load('Ice_TC2.txt');
s4=load('Ice_TC3.txt');
s5=load('Ice_TC4.txt');
s6=load('Ice_TC5.txt');
s7=load('Ice_TC6.txt');

t=s1(:,1);
TC1Amb=mean(s1(:,3));
TC2Amb=mean(s1(:,4));
TC3Amb=mean(s1(:,5));
TC4Amb=mean(s1(:,6));
TC5Amb=mean(s1(:,7));
TC6Amb=mean(s1(:,8));

TC1Aice=mean(s2(:,3));
TC2Aice=mean(s3(:,4));
TC3Aice=mean(s4(:,5));
TC4Aice=mean(s5(:,6));
TC5Aice=mean(s6(:,7));
TC6Aice=mean(s7(:,8));

format long

Calibration_TC1=(TC1Amb-TC1Aice)/DeltaTemperature
Calibration_TC2=(TC2Amb-TC2Aice)/DeltaTemperature
Calibration_TC3=(TC3Amb-TC3Aice)/DeltaTemperature
Calibration_TC4=(TC4Amb-TC4Aice)/DeltaTemperature
Calibration_TC5=(TC5Amb-TC5Aice)/DeltaTemperature
Calibration_TC6=(TC6Amb-TC6Aice)/DeltaTemperature

```

9.3.5 Filtering and plotting program for temperature data written in Mat lab

clear all

```
clc
xmin =  0.0;
xmax = 100.0;
ymin = -0.002;
ymax =  0.002;

s1=load('Fall_4motors3.txt');
s2=load('Fall_4motors1.txt');

t=s1(:,1);

TC1Aoff=s1(:,3);
TC2Aoff=s1(:,4);
TC3Aoff=s1(:,5);
TC4Aoff=s1(:,6);
TC5Aoff=s1(:,7);
TC6Aoff=s1(:,8);
TC1A=TC1Aoff-mean(TC1Aoff);
TC2A=TC2Aoff-mean(TC2Aoff);
TC3A=TC3Aoff-mean(TC3Aoff);
TC4A=TC4Aoff-mean(TC4Aoff);
TC5A=TC5Aoff-mean(TC5Aoff);
TC6A=TC6Aoff-mean(TC6Aoff);

Tc1Ref=TC1Aoff-TC6Aoff;
Tc2Ref=TC2Aoff-TC6Aoff;
Tc3Ref=TC3Aoff-TC6Aoff;
Tc4Ref=TC4Aoff-TC6Aoff;
Tc5Ref=TC5Aoff-TC6Aoff;

TC1Aoff;
TC2Aoff;
TC3Aoff;
TC4Aoff;
TC5Aoff;
TC6Aoff;

mean(TC1Aoff);
mean(TC2Aoff);
mean(TC3Aoff);
mean(TC4Aoff);
mean(TC5Aoff);
mean(TC6Aoff);
```

```
TC1Ooff=s2(:,3);
TC2Ooff=s2(:,4);
TC3Ooff=s2(:,5);
TC4Ooff=s2(:,6);
TC5Ooff=s2(:,7);
TC6Ooff=s2(:,8);

TC1O=TC1Ooff-mean(TC1Ooff);
TC2O=TC2Ooff-mean(TC2Ooff);
TC3O=TC3Ooff-mean(TC3Ooff);
TC4O=TC4Ooff-mean(TC4Ooff);
TC5O=TC5Ooff-mean(TC5Ooff);
TC6O=TC6Ooff-mean(TC6Ooff);

%fnorm = normalized frequency
%fcut: cut-off freq. Play around and put a reasonable value(not too high or
%low
%sampling rate
% butter: for butterworth filter
%4: The order of the filter. Keep it in the limit.
% high: highpass, cuts frequencies before cutoff
%low:lowpass cuts frequencies above cutoff
%Vraw: row signal
%Vfilt: filtered signal

rate=100
Fcut=0.94
fnorm=Fcut/(rate/2);
[b,a]=butter(4,fnorm,'low');
TCfil1=filtfilt(b,a, TC1A);
TCfil2=filtfilt(b,a, TC2A);
TCfil3=filtfilt(b,a, TC3A);
TCfil4=filtfilt(b,a, TC4A);
TCfil5=filtfilt(b,a, TC5A);
TCfil6=filtfilt(b,a, TC6A);

%Offsetting filtered signals
TC1ARS=TCfil1 + mean(TC1Aoff);
TC2ARS=TCfil2 + mean(TC2Aoff);
TC3ARS=TCfil3 + mean(TC3Aoff);
TC4ARS=TCfil4 + mean(TC4Aoff);
TC5ARS=TCfil5 + mean(TC5Aoff);
TC6ARS=TCfil6 + mean(TC6Aoff);
```

```
% TC1ARS=abs((TCfil1 + mean(TC1Aoff))/(4.73260833563e-005));
TC1ARS=(TCfil1 + mean(TC1Aoff))/4.73260833563e-005;
TC2ARS=(TCfil2 + mean(TC2Aoff))/4.73260833563e-005;
TC3ARS=(TCfil3 + mean(TC3Aoff))/5.662478877622406e-005;
TC4ARS=(TCfil4 + mean(TC4Aoff))/5.149055499999976e-005;
TC5ARS=(TCfil5 + mean(TC5Aoff))/5.696497699300743e-005;
TC6ARS=(TCfil6 + mean(TC6Aoff))/4.243551746853123e-005;


%[bb,aa]=cheby1(2,0.9,0.00305);
% [bb,aa] = cheby1(2,0.9 0.05,'high');
% TCfil=filter(b,a,TC6A);
figure(1)
subplot(2,6,1)
plot(t,TC1A,'r');
axis([xminxmaxyminymax]);
title('TC1')
ylabel('oC)')
xlabel('Time(s)')

subplot(2,6,2)
plot(t,TC2A,'r');
axis([xminxmaxyminymax]);
title('TC2')
ylabel('oC)')
xlabel('Time(s)')

subplot(2,6,3)
plot(t,TC3A,'r');
axis([xminxmaxyminymax]);
title('TC3')
ylabel('oC)')
xlabel('Time(s)')

subplot(2,6,4)
plot(t,TC4A,'r');
axis([xminxmaxyminymax]);
title('TC4')
ylabel('oC)')
xlabel('Time(s)')

subplot(2,6,5)
plot(t,TC5A,'r');
axis([xminxmaxyminymax]);
```

```
title('TC5')
ylabel('Temperature (oC))')
xlabel('Time(s)')

subplot(2,6,6)
plot(t,TC6A,'r');
axis([xminxmaxyminymax]);
title('TC6')
ylabel('Temperature (oC))')
xlabel('Time(s)')

subplot(2,6,7)
plot(t(1:10000),TC1O,'r');
axis([xminxmaxyminymax]);
title('TC1')
ylabel('Temperature (oC))')
xlabel('Time(s)')

subplot(2,6,8)
plot(t(1:10000),TC2O,'r');
axis([xminxmaxyminymax]);
title('TC2')
ylabel('Temperature (oC))')
xlabel('Time(s)')

subplot(2,6,9)
plot(t(1:10000),TC3O,'r');
axis([xminxmaxyminymax]);
title('TC3')
ylabel('Temperature (oC))')
xlabel('Time(s)')

subplot(2,6,10)
plot(t(1:10000),TC4O,'r');
axis([xminxmaxyminymax]);
title('TC4')
ylabel ('Temperature (oC))')
xlabel('Time(s)')

subplot(2,6,11)
plot(t(1:10000),TC5O,'r');
axis([xminxmaxyminymax]);
title('TC5')
ylabel('Temperature (oC))')
```

```
xlabel('Time(s)')

subplot(2,6,12)
plot(t(1:10000),TC6O,'r');
axis([xminxmaxyminymax]);
title('TC6')
ylabel('Temperature (oC))')
xlabel('Time(s)')

figure(2)
subplot(1,2,1);
plot (t(1:10000),TC6A(1:10000));
axis([xminxmaxyminymax]);
title ('Unfiltered signal')
ylabel('Temperature (V))')
xlabel ('Time(s)')

subplot(1,2,2);
plot (t(1:10000),TCfil6(1:10000));
axis([xminxmaxyminymax])
title ('Filtered signal')
ylabel('Temperature (V))')
xlabel ('Time(s)')

figure(3)
plot (t(1:9999),TC6A(1:9999),'b',t(1:9999),TCfil6(1:9999),'r');
axis([xminxmaxyminymax]);

figure(4)
subplot(1,6,1)
plot (t(1:9999),TC1ARS(1:9999));
axis([0 100 0 200]);
title('TC1')
ylabel('Temperature (oC)')
xlabel('Time(s)')

subplot(1,6,2)
plot (t(1:9999),TC2ARS(1:9999));
axis([0 100 0 200]);
title('TC2')
ylabel('Temperature (oC)')
xlabel('Time(s)')

subplot(1,6,3)
```

```
plot (t(1:9999),TC3ARS(1:9999));
axis([0 100 0 200]);
title('TC3')
ylabel('Temperature (oC)')
xlabel('Seconds')

subplot(1,6,4)
plot (t(1:9999),TC4ARS(1:9999));
axis([0 100 0 200]);
title('TC4')
ylabel('Temperature (oC)')
xlabel('Time(s)')

subplot(1,6,5)
plot (t(1:9999),TC5ARS(1:9999));
axis([0 100 0 200]);
title('TC5')
ylabel('Temperature (oC)')
xlabel('Time(s)')

subplot(1,6,6)
plot (t(1:9999),TC6ARS(1:9999));
axis([0 100 0 200]);
title('TC6')
ylabel('Temperature (oC)')
xlabel('Time(s)')
```

9.4. Flow equations and derivations

9.4.1 Derivation of the Stokes number using the x-momentum equation

Dimensionless variables in (9.1) are combined with the x-momentum equation in (9.2) to derive equation (9.3) .The latter equation can be rearranged to yield (9.4) using $T = 2\pi/\omega$ where ω is the angular velocity of the plate. Dividing (9.4) through by U^2/L yields (9.5) which is rewritten in (9.6). Finally, setting $U = \omega L$ in equation (9.6), the momentum equation is written with a new parameter S called the Stoke number in (9.7).

Dimensionless variables $$t^* = \frac{t}{T}; x^* = \frac{x}{L}; y^* = \frac{y}{L}; u^* = \frac{u}{U}; v^* = \frac{v}{U} \text{ and } p^* = \frac{p}{\rho U^2} \quad (9.1)$$

2D X-momentum: $$\frac{\partial u}{\partial t} + u\frac{\partial u}{\partial x} + v\frac{\partial u}{\partial y} = -\frac{1}{\rho}\frac{\partial p}{\partial x} + \nu\left[\frac{\partial^2 u}{\partial x^2} + \frac{\partial^2 u}{\partial y^2}\right] \quad (9.2)$$

$$\frac{1}{2\pi}\cdot\frac{U^2}{L}\cdot\frac{\partial u^*}{\partial t^*} + \frac{U^2}{L}\cdot\left(u^*\cdot\frac{\partial u^*}{\partial x^*} + u^*\cdot\frac{\partial u^*}{\partial y^*}\right) = -\frac{U^2}{L}\cdot\frac{\partial p^*}{\partial x^*} + \frac{\nu U}{L^2}\cdot\left(\frac{\partial^2 u^*}{\partial {x^*}^2} + \frac{\partial^2 u^*}{\partial {y^*}^2}\right) \quad (9.3)$$

$$\frac{1}{2\pi}\cdot\frac{\partial u^*}{\partial t^*} + \left(u^*\cdot\frac{\partial u^*}{\partial x^*} + u^*\cdot\frac{\partial u^*}{\partial y^*}\right) = -\frac{\partial p^*}{\partial x^*} + \frac{\nu}{UL}\cdot\left(\frac{\partial^2 u^*}{\partial {x^*}^2} + \frac{\partial^2 u^*}{\partial {y^*}^2}\right) \quad (9.4)$$

$$\frac{1}{2\pi}\cdot\frac{\partial u^*}{\partial t^*} + \left(u^*\cdot\frac{\partial u^*}{\partial x^*} + u^*\cdot\frac{\partial u^*}{\partial y^*}\right) = -\frac{\partial p^*}{\partial x^*} + \frac{\nu}{\omega L^2}\cdot\left(\frac{\partial^2 u^*}{\partial {x^*}^2} + \frac{\partial^2 u^*}{\partial {y^*}^2}\right) \quad (9.5)$$

$$\frac{1}{2\pi}\cdot\frac{\partial u^*}{\partial t^*} + \left(u^*\cdot\frac{\partial u^*}{\partial x^*} + u^*\cdot\frac{\partial u^*}{\partial y^*}\right) = -\frac{\partial p^*}{\partial x^*} + \frac{1}{S^2}\cdot\left(\frac{\partial^2 u^*}{\partial {x^*}^2} + \frac{\partial^2 u^*}{\partial {y^*}^2}\right) \quad (9.6)$$

9.4.2 Transformation of the momentum equation into the vorticity transport equation.

The vorticity transport equation can be derived from the momentum equation [93] in (9.8) using the vector identity in (9.9). Multiplying the resulting differentiated equation by ε_{pqi} yields (9.10). This result is simplified in (9.11) to give (9.12) which can be expressed in symbolic form in equation (9.13).

$$\partial_o v_i + v_j \partial_j v_i = -\frac{1}{\rho}\partial_i p + \nu \partial_j \partial_j v_i \tag{9.8}$$

$$v_j \partial_j v_i = \partial_i (\frac{1}{2} v_j v_j) + \varepsilon_{ijk} \omega_j v_k \tag{9.9}$$

$$\partial_o (\varepsilon_{pqi} \partial_q v_i) + \varepsilon_{pqi} \partial_q \partial_i (\frac{1}{2} v_j v_j) + \varepsilon_{pqi} \partial_q (\varepsilon_{ijk} \omega_j v_k) = -\frac{1}{\rho} \varepsilon_{pqi} \partial_q \partial_i p + \nu \varepsilon_{pqi} \partial_j \partial_j \partial_q v_i \tag{9.10}$$

$$\varepsilon_{pqi} \varepsilon_{ijk} \partial_q (\omega_j v_k) = \partial_k (\omega_p v_k) - \partial_j (\omega_j v_p) = v_k \partial_k \omega_p - \omega_j \partial_i v_p \tag{9.11}$$

$$\partial_o \omega_i + v_j \partial_i \omega_i = \omega_j \partial_j v_i + \nu \partial_j \partial_j \omega_i \tag{9.12}$$

$$\frac{D\omega}{Dt} = \omega \cdot \nabla v + \nu \nabla^2 \omega \tag{9.13}$$

BIBLIOGRAPHY

1. Tytell, E. D. and G. V. Launder, "The Hydrodynamics of Eel Swimming. I. Wake Structure," J. Exp. Biol. Vol. 207, 2004, pp. 1825-1841.

2. Sane, S. P., "The Aerodynamics of Insect Flight," J. Exp. Biol. Vol. 206, 2003, pp. 4191-4208.

3. Spedding, G.R., "The Wake of a Kestrel (Falco Tinnunculus) in Flapping flight," J. Exp. Biol. Vol. 127, 1987, pp. 59-78.

4. Craig, A. and J. Larochelle, "The Cooling Power of Pigeon Wings," J. Exp. Biol. Vol. 155, 1991, pp.193-202.

5. Jensen, M., "Biology and Physics of Locust Flight. III. The Aerodynamics of Locust Flight," Proc. R. Soc. Lond. B, Vol. 239, 1956, pp. 511-552.

6. Weis-Fogh, T., "Biology and Physics of Locust Flight. IV. Notes on Sensory Mechanisms in Locust Flight," Proc. R. Soc. London B, Vol. 239, 1956, pp. 553-584.

7. Wang, J. Z., "Vortex Shedding and Frequency Selection in Flapping Flight," J. Fluid Mech. Vol. 410, 2000, pp. 321-341.

8. Oshima, K. and Y. Oshima, "Lift Generation due to Vortex Shedding," Proc. Symp. Mech. SF., Feb. 1983.

9. Wang, J. Z., "The Role of Drag in Insect Hovering," J. Exp. Biol., Vol. 207, 2004, pp. 4147-4155.

10. Singh, K., "Why do Fish Swim and Birds Fly?" Math. Conf., Univ. Cambridge Oct. 7, 2007.

11. http://thundafunda.com/free-wallpaper/boats-vietnam-photos/attachment/tiger-swallowtail-butterfly-backgrounds-pictures.

12. Mariappa, D., *Anatomy and Histology of the Indian Elephant*. Indira Pub. House, Oak Park, 1986.

13. Phillips, P.K. and J.E. Heath, "Heat Exchange by the Pinna of the African Elephant (Loxodonta Africana)," Comp. Biochemist. Physiol., A, Vol.101, 1992, 693-699.

14. Phillips, P.K. and J. E. Heath, "Heat Loss in Dumbo: a Theoretical Approach, "J. Therm. Biol., Vol. 26, 2001, pp. 117-120.

15. http://animals.nationalgeographic.com/animals/mammals/african-elephant

16. Lesage, F., N. Hamel, X. Huang, W. Yuan, M. Khalid and P. Zdunich, "Initial Investigation on the Aerodynamic Performance of Flapping Wings for Nano Air Vehicles," Tech. Memo., DRDC TM 2007-550.RDDC Val Cartier, Canada, February 2008

17. Licht, S., F. Hover and M.S. Triantafillou, "Design of a Flapping Foil Underwater Vehicle," Int. Symp., April 20-23, 2004, pp. 311- 316.

18. Ellington, C.P. "The Novel Aerodynamics of Insect Flight: Applications to Micro-Air Vehicles," Depart. Zool., Univ. of Cambridge, Downing Street, 1999.

19. Liu, H., "Leading-Edge Vortices of Flapping and Rotary Wings at Low Reynolds Number," Program. Astronaut. Aero. Vol. 195, 2001, pp. 34-43.

20. Pesavento, U., and Z. J. Wang, "Flapping Wing Can Save Aerodynamics Power Compared to Steady Flight," Am. Phys. Soc., and PRL 103, 118102, 2009.

21. Zibikowski, R., K. Knowles, C. B. Pedersen and C. Galinski, "Some Aeromechanical Aspects of Insect-Like Flapping in Hover," J. Aerosp. Eng., Vol. 218, 2004, part G.

22. George, R. B., M. B. Colton, C. A. Mattson, and S. L. Thomson "A Differentially Driven Flapping Wing Mechanism for Force Analysis and Trajectory Optimization", Int. J. MAV, Vol. 4 · Number 1 · March 2012.

23. http://nanopatentsandinnovations.blogspot.com/2011/11/darpas-hummingbird-nano-air-vehicle-and.html.

24. Viieru D., Albertani R., Shyy W. and Ifju P.G., 2005, "Effect of Tip Vortex on Wing Aerodynamics of Micro Aerial Vehicles," J. Aircraft, Vol. 42, No. 6, pp. 1530-1536.

25. Shan, H., L. Jiang, C. Liu, M. Love, B. Maines, "Numerical Study of Passive and Active Flow Separation Control over a NACA0012 Airfoil," Technical Report, 2007-03.

26. Gentry, M.C. and A. M. Jacobi, "Heat Transfer Enhancement by Delta-Wing Vortex Generators on a Flat Plate: Vortex Interactions with the Boundary Layer," Exp. Therm. Fluid Sci., Vol.14, 1997, pp. 231-242.

27. Zhu, Q. and Z. Peng, "Mode Coupling and Flow Energy Harvesting by a Flapping Foil," Phys. Fluids, Vol. 21, 033601.

28. Akaydin, H. D., N. Elvin and Y. Andreopoulos, "Wake of a Cylinder: a Paradigm for Energy Harvesting with Piezoelectric Materials," Exp. Fluids, Vol. 49, 2010, pp. 291-304.

29. Guglielmini, L., P. Blondeaux and V. Giovanna, "A Simple Model of Propulsive Oscillating Foils," Ocean Eng., Vol. 31, 2004, pp. 883-899.

30. Lin, C.–S., C. Hwu and W.-B. Young, "The Thrust and Lift of an Ornithopter's Membrane Wings with Simple Flapping Motion," Aerosp. Sci. Technol., Vol.10, 2006, pp. 111-119.

31. Datta, A. K., *Biological and Bioenvironmental Heat and Mass Transfer,* Marcel Dekker, New York, 2002.

32. Wright P.G.., "Why do Elephant Flap their Ears?*"* S. Afr. J. Zool., Vol.19, 1984, pp. 266-269.

33. Benedict, F.G." The Physiology of the Elephant" Carnegie Institute, Washington DC, 1936.

34. Moran, J. M. and N. H. Shapiro, Fundamentals of Engineering Thermodynamics, 5th Edition. Wiley, New York, 2004.

35. Williams, T. M., "Heat Transfer in Elephants: Thermal Partitioning Based on Skin Temperature Profile," J. of Zool., Vol. 222, 1989, pp. 235-245.

36. Kinahan, A. A., R. Inge-moller, P. W. Baterman, A. Kotze, and M. Scantlebury, "Body Temperature Daily Rhythm Adaptations in African Savanna Elephants (Loxodonta Africana)," Physiol. Behav., Vol. 92, 2007, pp. 560-565.

37. Weissenbock, N., "Thermoregulation of African (Loxodonta Africana) and Asian (Elephas maximus) Elephants: Heterothermy as an Adaptation of Living in Hot Climates," Doctoral thesis, Nat. Sci., June 2010.

38. Heffner, R.; Heffner, H.; Stichman, N. "Role of the Elephant Pinna in Sound Localization", Animal Behav. Vol. 30, 1982, pp. 628-630.

39. Garstang, M.," Long-Distance, Low-Frequency Elephant Communication," J Comp. Physiol., A, Vol. 190, 2004, pp. 791–805.

40. Vanitha, V. and N. Baskaran, "Seasonal and Roofing Material Influence on the Thermoregulation by Captive Asian Elephants and its Implications for Captive Elephant Welfare" J. IUCN/SSC Asian Elephant Specialist Group, Vol. 33, 2010, pp. 35-40, Tamil Nadu, India.

41. Sikes, S.K. "*The Natural History of the African Elephant"* Elsevier Ltd., New York, 1971.

42. Benedict, F. G., E. L., Fox and M. L., Baker "The Surface Temperature of the Elephant, the Rhinoceros and Hippotamus," Am. J. Physiol. Vol. 56, 1921, pp.464-474.

43. Ward, S., J. M. V. Rayner, U. Moller, D. M. Jackson, W. Nachtigall and J. R. Speakman, "Heat Transfer from Starlings Sturnus Vulgaris during Flight," J. Exp. Biol.,Vol. 202, 1999, pp.1589-1602.

44. Jiji, L. M., *Heat Convection*, 1st ed. Springer, New York, 2006.

45. Karo, T., H. Nakatani and E. Hatayama, "The Flow by a Rotational Oscillation of the Flat Plate," J. Jpn. Soc. Mech. Eng., Issue 510, Vol.55, 1989, pp. 398-403.

46. Liu, H. and K. Kawachi, "A Numerical Study of Insect Flight," J. Comput. Phys. Vol.146, 1998, pp.124-156.

47. Ho, S., H. Nassef, N. Pornsinsirirak, Y. C. Tai and C. M. Ho, "Unsteady Aerodynamics and Flow Control for Flapping Wing Flyers," Prog. Aerosp. Sci., Vol. 39, 2003, pp. 635–681.

48. Minotti, F. O., "Unsteady Two Dimensional Theory of a Flapping Wing," Phys. Rev. E, 66, 051907, 2002.

49. Dickinson, M. H. and K. G. Gotz, "Unsteady Aerodynamic Performance of Model Wings at Low Reynolds Number," J. Exp. Biol. Vol.174, 1993, pp. 45-64.

50. Lind, J. R. and B. Abedian, "Transient Heat Transfer Effects from a Flapping Wing," Proc. COMSOL Mutiphys. User's Conf., Boston, 2005.

51. Adkins, D. and Y. Y. Yan, " CFD Simulation of Fish-like Body Moving in Viscous Liquid," J. Bionic Eng., Vol.3, 2006, pp. 147-153.

52. Moffat, H. K. and B. R. Duffy, "Similarity Solution and their Limitations," J. Fluid Mech., Vol. 96, 1980, pp. 299-313.

53. FLUENT 6.3, *FLUENT Documentation*, 2005.

54. Fox, R. W. and A. T. McDonald, Introduction *to Fluid Mechanics*, 5th ed., Wiley, New York, 1998.

55. Erdma, A. G. and G. N. Sandor, *Mechanism Design*, 2nd ed., Analysis and Synthesis, Vol. 1, Prentice Hall, New Jersey, 1991.

56. Ugural, A. C. and S. K. Fenster, *Advanced Strength and Applied Elasticity*, 3rd ed. Prentice Hall, New Jersey, 1995.

57. http://www.robotmarketplace.com/products/NPC-41250.html

58. http://www.mcmaster.com/#flexible-shaft-couplings/=km8xih

59. http://www.education.rec.ri.cmu.edu/products/teaching_robotc_cortex/reference/shaft_ig.pdf

60. http://content.vexrobotics.com/docs/ifi-v884-users-manual-9-25-06.pdf

61. http://www.rogerscorporation.com/mwu/pdf/ro4000ds_4.pdf

62. http://www.watlow.com/products/heaters/flexible-silicone-heaters.cfm?famid

63. http://www.artisan-scientific.com/75047.htm.

64. Suryadi, A., T. Ishii and S. Obi, "Stereo PIV measurement of a finite, flapping rigid plate in hovering condition," Exp. Fluids, Vol. 49, 2010, pp. 447-460.

65. Tang J., Viieru D. and Shyy W., 2006, "Effects of Reynolds Number and Stroke Amplitude on Hovering Aerodynamics," rev. 45th AIAA Aerosp. Sci. Mtg. and Exhib. Reno NV, Jan. 2007.

66. YAO, T. and T. WU, "Hydromechanics of swimming propulsion. Part 1. Swimming of a two-dimensional flexible plate at variable forward speeds in an inviscid fluid", J. Fluid Mech., Vol. 46, 1971, pp. 337-355 Great Britain.

67. Anono, H., S. K. Chimakurthi, P. Wu, E. Sallstron, B.K. Stanford, C. E. S. Cesnik, P. Ifju, L. Ukeiley and W. Shyy, "A Computational and Experimental Study of Flexible Flapping Wing Aerodynamics," 48th AIAA Aerosp. Sci. Mtg. Incl. New Horiz. FR. and Aerosp. Expo. 4-7 Jan. 2010, Orlando, Florida.

68. Braza, M. and K. Hourigan, "Unsteady Separated Flows and their Control," Proc. IUTAM Symp., Corfu, Greece, 18-22 June 2007.

69. Viieru, D., J. Tang, Y. Lian, H. Liu, and W. Shyy, "Flapping and Flexible Wing Aerodynamics of Low Reynolds Number Flight Vehicles", 44th AIAA Aerosp. Sci. Mtg. and Exhib. 9 - 12 January 2006, Reno, Nevada.

70. Panton R. L. *Incompressible Flow,* 1st ed., Austin Texas1995.

71. Ishihara, D., Y. Yamashita, T. Horie, S.Yoshiday, and T.Niho, "Passive maintenance of high angle of attack and its lift generation during flapping translation in crane fly wing," J. Exp. Biol., Vol. 212, 2009, pp. 3882-3891.

72. Bejan, A., *Convection Heat Transfer*, 3rd ed., Wiley, New York, 2003.

73. http://homepage.psy.utexas.edu/homepage/class/Psy355D/metabolic.pdf

74. Laursen, B., and M. Bekoff, "Loxodonta Africana", A. S.M, Mammalian Sp., Vol.92,1978, pp.1-8.

75. Koffi, M.; J. Latif, and Y. Andreopoulos. "Why Do Elephants Flap Their Ears? "A. P. S., 62nd Ann. Mtg. APS DFD, Nov. 22-24, 2009.

76. Cengel, Y. A. and M. A. Boles, *Thermodynamics: An Engineering Approach*, 6th Edition

77. http://www.newworldencyclopedia.org/entry/Elephant.

78. Holman, R., Y. Utturkar, R. Mittal†, Barton L. Smith‡ L. Cattafesta, "Formation Criterion for Synthetic Jets," AIAA J. Vol. 43, 2005.